

SPIN AND ORBITAL DYNAMICS OF CLOSE-IN
GIANT PLANET SYSTEMS AND STELLAR
BINARIES

A Dissertation

Presented to the Faculty of the Graduate School

of Cornell University

in Partial Fulfillment of the Requirements for the Degree of

Doctor of Philosophy

by

Kassandra Renata Anderson

August 2019

© 2019 Kassandra Renata Anderson

ALL RIGHTS RESERVED

SPIN AND ORBITAL DYNAMICS OF CLOSE-IN GIANT PLANET SYSTEMS

AND STELLAR BINARIES

Kassandra Renata Anderson, Ph.D.

Cornell University 2019

Hot Jupiters (giant planets with orbital periods less than 10 days) and warm Jupiters (giant planets with orbital periods between 10-300 days) are major topics in exoplanetary dynamics, with unresolved puzzles regarding their dynamical histories and migration. Many observed systems show hints of a dynamically-active past, such as large stellar spin-orbit misalignments (obliquities) in hot Jupiter systems, and substantial eccentricities in warm Jupiter systems. Some stellar binaries present similar puzzles as close-in exoplanets, including a range of eccentricities and obliquities. This dissertation explores the spin and orbital evolution of close-in giant exoplanets and binaries due to the presence of an external companion. A third body may perturb the orbit of the planet or binary, leading to secular changes in eccentricity and inclination. Alongside the secular evolution of the orbit, an oblate star experiences a torque from the planet or binary companion, leading to precession of the spin axis and obliquity evolution. This dissertation explores such spin-orbit dynamics in a variety of contexts: (1) I conduct a population synthesis of hot Jupiter migration in stellar binaries due to Lidov-Kozai cycles, and present the resulting distributions of spin-orbit misalignment angles and formation efficiencies. (2) Considering both hot and warm Jupiter systems with external planetary companions, I identify the requirements for the outer planet to generate dramatic obliquity growth through a secular spin-orbit resonance, which may be encountered as

the host star spins down due to magnetic braking. (3) I consider stellar binaries with a tertiary companion, and identify the system architectures in which the tertiary may affect the obliquities of the inner binary members. (4) I consider how an inclined circumbinary disk may excite obliquities in stellar binaries. In addition to spin-orbit dynamics, this dissertation also explores two different mechanisms for exciting eccentricities in warm Jupiter systems, due to secular perturbations from inclined companions, and in-situ scattering.

BIOGRAPHICAL SKETCH

Kassandra Anderson was born in Oakland CA and grew up in Ann Arbor MI. In her teenage years she developed a strong interest in science, especially in astronomy and physics. She completed her undergraduate studies at the University of Michigan, and received her B.S. in Physics in 2012. While at the University of Michigan, Kassandra began undergraduate research in astronomy and completed her senior thesis on exoplanet dynamics. She remained in Ann Arbor for an additional year following graduation to continue her research, working on photoevaporation of protoplanetary disks. In August 2013, she moved to Ithaca NY to pursue a PhD in Astronomy, working with Professor Dong Lai on dynamics of giant exoplanets and stellar binaries. In September 2019, Kassandra will move to Princeton NJ to begin a Lyman Spitzer, Jr. Postdoctoral Fellowship at Princeton University. Besides astronomy, Kassandra's interests and hobbies include sewing, knitting, ballet and other dance forms, cooking, and of course cats. One day she plans to adopt two cats and name them Lidov and Kozai, in honor of the Lidov-Kozai effect, which appears repeatedly throughout this dissertation.

To my mother, for her unwavering support, enthusiasm, and encouragement of
my endeavors.

ACKNOWLEDGEMENTS

First and foremost I thank my advisor Dong Lai for the countless hours spent mentoring me and helping me to develop as a scientist. My success thus far is in no small part due to Dong's support and tutelage over the years. I am extremely fortunate to have had the opportunity for research collaboration with such an energetic and enthusiastic scientist.

Next, I thank the members of my thesis committee, Terry Herter, Richard Lovelace, and Lisa Kaltenegger for their time, feedback, and support.

My undergraduate mentors Fred Adams and Nuria Calvet were instrumental in developing my research skills. I am grateful to them for their time, limitless patience, and for instilling the confidence in me to pursue a PhD in astronomy.

I have enjoyed collaborating with Cornell graduate students Natalia Storch, Michael Pu, and Michelle Vick. In addition, I appreciate many stimulating science discussions with members of Dong's group over the years, including Ryan Miranda, Diego Muñoz, Michael Pu, Natalia Storch, Jean Teyssandier, Michelle Vick, and J.J. Zanazzi.

I thank Fred Adams and Phil Nicholson for interesting discussions, and for their support of my postdoc applications. I also thank Nikole Lewis for advice on writing postdoc proposals. I gratefully acknowledge support from the Cornell University Fellowship, the NSF Graduate Research Fellowship, and the NASA Earth & Space Science Graduate Fellowship.

I thank my family for their encouragement and support. And finally, my friends in Ithaca have made the past six years a truly wonderful experience, and I am especially grateful to Ryan, Paul, Michelle, Maryame, Sam, Tyler, and Jean.

TABLE OF CONTENTS

Biographical Sketch	iii
Dedication	iv
Acknowledgements	v
Table of Contents	vi
List of Tables	ix
List of Figures	x
1 Introduction	1
2 Formation and stellar spin-orbit misalignment of hot Jupiters from Lidov-Kozai oscillations in stellar binaries	12
2.1 Introduction	12
2.2 Formulation	17
2.2.1 Spin Evolution due to Stellar Quadrupole	19
2.3 LK Migration and Stellar Spin Evolution: Analytical Results	23
2.3.1 LK Oscillations: Range of Eccentricity and Freezing of Oscillations	23
2.3.2 Migration Rate: Upper Limit and Estimate	28
2.3.3 Evolution of Planet Spin During LK Cycles with Tidal Friction	31
2.3.4 Limiting Eccentricity and Necessary Conditions for Planet Migration and Disruption	34
2.3.5 Freezing of Spin-Orbit Angle	40
2.4 Paths Toward Misalignment	43
2.4.1 Effects of Varying Stellar Spin Rate	44
2.4.2 Effects of Varying Inclination	45
2.4.3 Effects of the Backreaction Torque from the Stellar Quadrupole on the Orbit	47
2.5 Population Synthesis	54
2.5.1 Setup and Computational Procedure	54
2.5.2 Quadrupole Results	58
2.5.3 Octupole Results: Fixed Binary Eccentricity and Separation	62
2.5.4 General Results for a Range of Binary Separations, Eccentricities, and Planet Semi-major Axes	67
2.5.5 Dependence on Tidal Dissipation Strength	76
2.5.6 Primordial Misalignment	81
2.6 Conclusion	84
2.6.1 Summary of Results	84
2.6.2 Discussion	88

3	Teetering Stars: Resonant Excitation of Stellar Obliquities by Hot and Warm Jupiters with External Companions	93
3.1	Introduction	93
3.2	Setup & Classification of Dynamical Behavior	97
3.3	Spin-Orbit Dynamics when S_* $\ll L_1$	103
3.3.1	Cassini States & Phase Space Structure	105
3.3.2	Spin-Orbit Resonance and Separatrix Crossing	107
3.4	Spin-Orbit Dynamics for Comparable S_* and L_1	111
3.4.1	Cassini States for Finite S_*/L_1 and an Evolution Example .	113
3.4.2	Results for HJs and WJs with External Companions . . .	117
3.5	Summary & Discussion	121
4	Moderately Eccentric Warm Jupiters from Secular Interactions with Exterior Companions	127
4.1	Introduction	127
4.2	Secular Interactions of Warm Jupiters With Distant Planet Companions	132
4.2.1	Setup and Method	132
4.2.2	Coplanar Systems	134
4.2.3	Coplanar Systems With Modest Initial Eccentricity . . .	139
4.2.4	Moderately Inclined Companions	141
4.2.5	General Inclinations: Lidov-Kozai Cycles	142
4.3	Observed WJ Systems with Exterior Companions	149
4.3.1	Sample Description and Method	149
4.3.2	Fiducial Experiment	150
4.3.3	Additional Numerical Experiments	153
4.4	Suppression of Eccentricity Oscillations by Close Rocky Neighbors	157
4.5	Summary & Discussion	159
5	In-Situ Scattering of Warm Jupiters	165
5.1	Introduction	165
5.2	Scattering Experiments	171
5.2.1	Setup & Canonical Parameters	171
5.2.2	Scattering Outcomes	172
5.2.3	Properties of One and Two-Planet Systems and Parameter Exploration	175
5.2.4	In-Situ Scattering of Four Planets	186
5.3	Comparison with Observations	187
5.3.1	Eccentricities	189
5.3.2	Spacing and Mutual Inclinations of Two-Planet Systems .	193
5.3.3	Relative Numbers of One and Two-Planet Systems	194
5.4	Summary of Results and Discussion	197

6 Eccentricity and Spin-Orbit Misalignment in Short-Period Stellar Binaries as a Signpost of Hidden Tertiary Companions	202
6.1 Introduction	202
6.2 Lidov-Kozai Cycles in Triples with Comparable Angular Momentum and Short-Range Forces	206
6.2.1 Setup and Equations	206
6.2.2 Range of Inclinations Allowing Eccentricity Excitation . .	212
6.2.3 Maximum and Limiting Eccentricities	216
6.2.4 Constraints on Hidden Tertiary Companions from Inner Binary Eccentricities	217
6.2.5 Eccentricity Excitation in Coplanar Systems	224
6.3 Spin-Orbit Dynamics in Systems Undergoing LK Oscillations . .	225
6.4 Numerical Experiments	230
6.4.1 Setup and Computational Procedure	230
6.4.2 Equal Mass Inner Binary	233
6.4.3 Unequal Mass Inner Binary: Octupole Results	237
6.5 Application: DI Herculis	242
6.6 Conclusion	245
6.6.1 Summary of Key Results	245
6.6.2 Discussion	250
7 Spin-Orbit Misalignments in Stellar Binaries with Circumbinary Disks: Application to DI Herculis	252
7.1 Introduction	252
7.2 Obliquity Excitation in Stellar Binaries	253
7.2.1 Torques and Mutual Precession	253
7.2.2 Cassini States	255
7.2.3 Relevant Timescales	257
7.2.4 Importance of Spin Feedback	260
7.3 Effects of Accretion onto the Binary	262
8 Conclusion and Future Work	271
A Orbital & Spin Secular Equations of Motion	273
A.0.1 Lidov-Kozai Oscillations	273
A.0.2 Spin Evolution Due to the Stellar Quadrupole	275
A.0.3 Pericenter Precession Due to Short Range Forces	276
A.0.4 Dissipative Tides in the Planet	277
A.0.5 Stellar Spin-down due to Magnetic Braking	278
B LK Maximum Eccentricity for Non-zero Initial Eccentricity	279
C Treatment of Planet-Planet Collisions	283
D Discrete Mixture Model for Planet Eccentricities	286

LIST OF TABLES

2.1	Definitions of variables, along with the canonical value used in this chapter (if applicable), and dimensionless form.	20
2.2	Input parameters and results of the calculations presented in Sections 2.5.2 and 2.5.3.	67
2.3	Same format as Table 2.2, but showing results for the full population synthesis calculations in Sections 2.5.4, 2.5.5, and 2.5.6. . .	68
4.1	Various sets of numerical experiments involving observed WJs with outer planetary companions (see Sections 4.3.2, 4.3.3, and Fig. 4.9).	154
5.1	Initial conditions, scattering outcomes, and final eccentricities for the different sets of simulations.	176
5.2	Scattering outcomes and properties of the two-planet systems at the end of “Phase 2” of the integration.	177
5.3	Scattering outcomes and properties of the one-planet systems at the end of “Phase 2” of the integration.	177
5.4	Properties of both one and two-planet systems from 4-planets	177

LIST OF FIGURES

2.1	Semi-major axis a (top), eccentricity (middle), and inclination θ_{lb} (bottom) as functions of time, showing the evolution until the planetary orbit has decayed and circularized.	25
2.2	Condition for freezing of LK oscillations, $\Delta j/j_{\max}$ as a function of a	29
2.3	Planet spin period as a function of time, for the same parameters shown in Fig. 2.1.	35
2.4	Same as Figure 2.3, but showing only three LK cycles, once the planet spin has achieved the “Kozai spin equilibrium”.	36
2.5	“Kozai spin equilibrium rate” rate ($\Omega_{p,eq}$, solid curve), as a function of e_{\max} , the maximum eccentricity attained in an LK cycle.	37
2.6	Boundaries in $(a_0, a_{b,\text{eff}})$ parameter space for migration and tidal disruption.	41
2.7	Examples of chaotic evolution for three values of the stellar spin period, neglecting the feedback torque from the stellar quadrupole on the orbit.	48
2.8	Examples of possible non-chaotic evolution of the spin-orbit angle, depending on the stellar spin rate.	49
2.9	The final spin-orbit angle as a function of the adiabaticity parameter.	50
2.10	Examples of possible evolution of the spin-orbit angle, depending on the initial inclination.	51
2.11	Final spin orbit misalignments as a function of the initial inclination, for various combinations of planet mass and (constant) stellar spin period.	52
2.12	Time evolution for two systems with very similar initial inclinations, illustrating the bimodality in the final misalignment angle.	53
2.13	Same as Fig. 2.11, but including feedback from the stellar quadrupole on the orbit.	54
2.14	Final distributions of spin-orbit angles for circularized hot Jupiters.	61
2.15	Same as Fig. 2.14, except for an F-type host star.	63
2.16	Same as Fig. 2.14, except that $e_b = 0.8$, and $a_b = 333.33$ AU.	65
2.17	Distributions of final spin-orbit misalignments for various binary eccentricities.	66
2.18	Parameter space producing HJs, tidally disrupted planets, and non-migrating planets around G stars.	73
2.19	Parameter space producing tidally disrupted planets and HJs for the calculations presented in Fig. 2.18.	77
2.20	Final stellar obliquities and orbital periods for the systems shown in Figure 2.18 that resulted in HJs.	78
2.21	Same as Fig. 2.20, but showing results for planets around F stars.	79

2.22	Cumulative distributions of migration times.	80
2.23	Effects of varying tidal dissipation strength on the distribution of final HJ orbital periods.	82
2.24	Effects of varying tidal dissipation strength on the distributions of final spin-orbit misalignments.	83
2.25	Same as Figure 2.24, but showing results for planets around F stars.	84
2.26	The effect of primordial misalignment on distributions of final spin-orbit misalignments.	85
3.1	Parameter space for resonant excitation of the stellar obliquity to be possible.	104
3.2	Cartoon illustration of the Cassini state configuration.	108
3.3	Cassini states $\theta_{1,2,3,4}$ versus $\eta = g /\alpha$, with fixed $I = 20^\circ$	109
3.4	Spin evolution with slowly increasing η , for a system with $S_*/L_1 \ll 1$, so that $I = \text{constant}$ (as discussed in Section 3).	110
3.5	Solid curve: Average value of θ following resonant excitation, as calculated from the area of the separatrix.	112
3.6	Generalized Cassini state obliquities as a function of the coupling parameter.	114
3.7	Example of resonant obliquity excitation for a system with finite S_* and L_1	116
3.8	Obliquity excitation as a function of perturber semi-major axis, showing various initial inclinations.	119
3.9	Parameter survey of obliquity excitation and inclination decay in systems consisting of a host star, a HJ or WJ, and an external perturber.	122
4.1	Maximum eccentricity of the WJ as a function of a_{out} , for various masses and eccentricities of the outer planet.	137
4.2	Contours of $\dot{\varpi}_{\text{in}}/\dot{\varpi}_{\text{out}} = 1$	138
4.3	Minimum value of ε_{oct} required to raise the eccentricity of the WJ.	140
4.4	e_{max} versus a_{out} for various initial inclinations.	143
4.5	Maximum eccentricity e_{max} , in terms of (I_0, a_{out}) parameter space, for various outer planet masses and eccentricities.	147
4.6	Same numerical experiments as depicted in Fig. 4.5, but showing the fraction of the total integration time that the WJ spends with e above	148
4.7	Constraints on the required mutual orbital inclination of observed WJs with external companions	151
4.8	Large set of numerical integrations of observed WJ systems with external companions, with inclinations and orbital angles randomly sampled	156

4.9	Comparison of the various experiments (see Table 4.1) involving observed WJs with external companions.	157
4.10	Maximum mass of m' that allows eccentricity oscillations of m_1 (due to m_2), as a function of a'/a	160
5.1	Fraction of one, two, and three-planet systems as a function of time for the <code>fiducial</code> set of simulations.	173
5.2	Two-planet systems, along with the observed WJ systems with external giant planet companions.	179
5.3	One-planet systems, along with observed “solitary WJs” (without any identified giant planet companions).	180
5.4	Scattering outcomes, fractions of one and two-planet systems, and average eccentricities for the <code>fiducial</code> set of calculations. .	183
5.5	Dependence of two-planet system properties on the initial semi-major axis of the innermost planet of the initial three-planet system.	184
5.6	Eccentricities of WJ systems, illustrating the dependence on planet masses.	186
5.7	Properties of two-planet systems produced from 4-planets, along with those from <code>fiducial</code> for reference.	188
5.8	Radial velocity semi-amplitude versus orbital period for the outer planet.	192
5.9	The effect of imposing an RV cut on the eccentricity distributions of one and two-planet systems.	193
6.1	The “window” of inclinations that allow LK oscillations.	213
6.2	The maximum eccentricity of the inner binary, versus the initial inclination I_0	218
6.3	Limiting eccentricity e_{lim} and critical inclination $I_{0,\text{lim}}$, as a function of $(a_{\text{out}}/a_{\text{in}})\bar{m}_2^{-1/3}$	220
6.4	Curves in (I_0, a_{out}) parameter space able to produce a given value of e_{max}	221
6.5	Effective perturber distance required to generate a limiting eccentricity e_{lim} , as labeled, as a function of the inner binary orbital period.	223
6.6	Maximum eccentricity e_{max} for coplanar ($I = 0$) hierarchical triple systems, versus the outer binary semi-major axis.	226
6.7	Maximum spin-orbit angle and eccentricity of the inner binary as a function of the adiabaticity parameter.	235
6.8	Orbital parameters $a_{\text{out,eff}} = a_{\text{out}}\sqrt{1 - e_{\text{out}}^2}$ versus a_{in} for the same sets of triples as in Fig. 6.7.	236
6.9	Maximum eccentricity achieved over the integration timespan, compared to the algebraically-determined quadrupole estimate.	239

6.10	Maximum eccentricity e_{\max} achieved over the integration timespan, compared to the analytically determined (quadrupole) limiting eccentricity e_{\lim}	240
6.11	Same experiment as depicted in Fig. 6.7, except that the inner binary has unequal mass.	241
6.12	Similar to Fig. 6.4, but applied to the DI Herculis system.	246
6.13	Required effective separation versus mass of a tertiary companion in the DI Herculis system, to generate the large inferred spin-orbit misalignment of the primary member.	247
7.1	Relevant frequencies as a function of disk mass in units of the binary mass.	259
7.2	Relevant ratios and precession frequencies.	260
7.3	Example of obliquity and inclination evolution (θ_{sb} and θ_{bd}) for the canonical parameters.	262
7.4	“Final” obliquity (top panel) and binary-disk inclination (bottom panel) after the disk has lost the majority of its initial mass. . . .	263
7.5	Similar to Fig. 7.3, illustrating how the combination of spin feedback and accretion torques can dramatically reduce the final obliquity.	265
7.6	Similar to Figs. 7.3 and 7.5, showing the effects of including both N_{bd} and N_{sb}	267
7.7	Parameter space allowing sustained obliquity excitation.	268
7.8	“Final” obliquity and binary-disk inclination, obtained when $t = 10t_{\text{disk}}$	269
7.9	Similar to Fig. 7.7, illustrating how differing binary and disk properties widen or narrow the available parameter space for sustained obliquity excitation.	270
B.1	e_{\max} , in terms of η and $\cos I_0$, for various combinations of e_0 and ω_0	281
B.2	Maximum and minimum eccentricities as a function of initial inclination, for various initial eccentricities e_0 and phase angles ω_0	282
C.1	Properties of scattering outcomes, showing that most collisions are grazing.	285
D.1	Estimated parameters of the mixing model discussed in Appendix D.	288

CHAPTER 1

INTRODUCTION

Hot Jupiters (giant planets with orbital periods less than about ten days) have served as a major topic in exoplanetary science following the discovery of the first hot Jupiter by Mayor & Queloz in 1995. Over twenty subsequent years of exoplanet observations have revealed a rich variety of planetary systems and architectures, including a sample of several hundred hot Jupiters. Although hot Jupiters are intrinsically rare, with an occurrence rate of only $\sim 1\%$ (e.g. Wright et al., 2012), such planets continue to be of great interest, given their extreme environments and with no analogue in the solar system. In recent years, warm Jupiters (giant planets with orbital periods roughly between 10 and 300 days) have gained considerable attention alongside hot Jupiters.

Many unresolved puzzles involving hot and warm Jupiters remain, especially regarding their formation and migration histories. Some recent work has considered the possibility of forming hot Jupiters in-situ (Boley et al., 2016; Batygin et al., 2016), but given the conditions so close to the star, most formation studies consider the scenario in which hot Jupiters formed farther away, at locations of \sim several AU, and subsequently undergo inward migration, arriving at a final orbital period of several days. Planet migration comes two distinct flavors. One possibility is disk-driven migration, in which planets are transported inwards due to torques from the protoplanetary disk (e.g. Lin et al., 1996; Tanaka et al., 2002; Kley, & Nelson, 2012; Baruteau et al., 2014). The second possibility is high-eccentricity migration, in which the planet's eccentricity is excited to an extreme value ($e \gtrsim 0.9$) by a stellar or planetary companion(s), so that tides raised on the planet at pericenter distances shrink and eventually circularize

the orbit. High-eccentricity migration itself comes in several distinct flavors depending on the details of the eccentricity excitation, including excitation from an inclined companion due to Lidov-Kozai cycles (Lidov, 1962; Kozai, 1962) or other secular perturbations (Wu & Murray, 2003; Fabrycky & Tremaine, 2007; Naoz et al., 2012; Petrovich, 2015a,b; Anderson et al., 2016; Muñoz et al., 2016; Hamers et al., 2017; Vick et al., 2019), scatterings (possibly combined with secular interactions) (Rasio & Ford, 1996; Nagasawa et al., 2008; Nagasawa, & Ida, 2011; Beaugé & Nesvorný, 2012), and secular chaos (Lithwick & Naoz, 2011; Lithwick, & Wu, 2014; Teyssandier et al., 2019). See also Dawson, & Johnson (2018) for a recent review. Despite the fact that giant planet migration is one of the oldest theory problems in the field of exoplanets, no general consensus has been reached as to which migration mechanism (if any) is responsible for producing the majority of hot Jupiters. Warm Jupiters raise similar questions regarding their formation and migration. Whether hot and warm Jupiters share the same formation/migration histories is still an open question.

Theories of planet formation and migration must be able to account for several observational features of the hot and warm Jupiter samples. For example, many hot Jupiter systems are observed to have an orbital axis that is misaligned with respect to the spin-axis of the host star, or equivalently, an orbital plane that is misaligned with respect to the stellar equator (e.g. Hébrard et al., 2008; Narita et al., 2009; Winn et al., 2009; Triaud et al., 2010; Albrecht et al., 2012a; Moutou et al., 2011). The majority of these measurements have been obtained from Rossiter-McLaughlin observations (Rossiter, 1924; McLaughlin, 1924), in which a transiting planet induces an anomaly in the radial velocity signature as it periodically blocks red-shifted and blue-shifted portions of the stellar disk. The shape of the anomaly depends on the inclination of the host star's spin axis,

and as a result, the sky-projected spin-orbit misalignment (also referred to as obliquity) may be determined (Winn et al., 2005). Nearly 100 hot Jupiters have obliquity constraints, revealing a large population of aligned systems, but many significantly misaligned systems, some of which are retrograde, or intriguingly close to 90° (Simpson et al., 2011; Albrecht et al., 2012b; Addison et al., 2013). At present, warm Jupiter stellar obliquities are mostly un-probed, but the situation is expected to change in the coming years, enabled, for example, by *TESS* mission discoveries amenable to follow-up radial velocity observations.

High-eccentricity migration is a natural mechanism for producing large stellar obliquities. Alongside the extreme eccentricities generated (as required to induce orbital decay), planetary inclinations are frequently excited as well. Perhaps even more importantly, spin-orbit coupling between the migrating planet and oblate host star can lead to large obliquity excitation. The amount of angular momentum stored in the planetary orbit usually exceeds (or at least is comparable to) that of the host star. The direction of the stellar spin may thus be drastically altered under some circumstances due to torques from the planet. The complex, and often chaotic spin-orbit dynamics that ensue often play the dominant role in determining final obliquities (Storch et al., 2014; Storch & Lai, 2015; Storch et al., 2017). In contrast, disk-driven migration predicts low stellar obliquities, provided that the disk is aligned with the stellar spin axis. As a result, hot Jupiters with large stellar obliquities are traditionally attributed to formation through a high-eccentricity migration channel.

However, this elegant paradigm for inferring hot Jupiter migration histories using stellar obliquities is complicated by several factors. For example, low obliquities do not necessarily imply a disk migration history, because tides

raised by the planet on the host star may erase initially large obliquities. Indeed, a well-known correlation between obliquities and stellar effective temperatures exists, with hot Jupiters orbiting cool stars having low obliquities and hot Jupiters orbiting hot stars tending to have high obliquities (Winn et al., 2010, 2017; Muñoz, & Perets, 2018). This trend is qualitatively consistent with tidal realignment in systems with cool host stars due to convective envelopes, although note that the tidal realignment scenario suffers from some uncertainties and inconsistencies (e.g. Lai, 2012). As another complication, various works have investigated the possibility of tilting the protoplanetary disk itself relative to the stellar spin axis. Such primordial misalignments may allow for in-situ formation or disk-migration to result in high obliquities, albeit with varying degrees of success (Bate et al., 2010; Foucart & Lai, 2011; Lai et al., 2011; Batygin, 2012; Batygin & Adams, 2013; Lai, 2014; Spalding & Batygin, 2014; Fielding et al., 2015; Zanazzi & Lai, 2018). Given these results, exactly what obliquities inform us about planetary migration history is not obvious.

Besides hot Jupiter obliquities, another observational feature in the sample of close-in giant planets is a substantial population of eccentric warm Jupiters. Many different mechanisms have been proposed in exciting warm Jupiter eccentricities. Some mechanisms involve eccentricity excitation after formation/arrival at a short-period orbit, such as planet scattering, planet-disk interactions, or secular perturbations. A major proposed explanation for warm Jupiter eccentricities is high-eccentricity migration (Dong et al., 2014; Dawson & Chiang, 2014; Petrovich & Tremaine, 2016). In the context of high-eccentricity migration, warm Jupiters are caught in the act of inward migration, eventually to become hot Jupiters on circular orbits. However, although high-eccentricity migration can readily form hot Jupiters, it suffers from some difficulties and

observational inconsistencies in forming warm Jupiters, and eccentricity excitation following formation/arrival at sub-AU distances may be more promising in explaining the observations.

Together, these two observational features of close-in giant planets (hot Jupiter obliquities and warm Jupiter eccentricities), constitute the major motivation for the studies in this dissertation. The primary goal of this thesis is to better understand the dynamical and migration histories of hot and warm Jupiters, by studying a variety of processes for raising eccentricities and stellar obliquities. A secondary theme of this dissertation involves stellar binaries. The existence of close main-sequence stellar binaries present similar puzzles as close-in giant planets. Short-period stellar binaries are thought to have previously undergone migration, either due to tidal dissipation and circularization of an eccentric orbit, or within a gaseous disk. Similar to giant planets, several close stellar binaries exhibit spin-orbit misalignments (Albrecht et al., 2009, 2014; Sybilska et al., 2018); whether such spin-orbit misalignments are primordial or arose after the binary formed is unknown. This dissertation considers two different mechanisms for raising obliquities in stellar binaries, starting with initially aligned spin and orbital axes.

Most of this dissertation considers the secular (orbit-averaged) evolution of hierarchical triple systems, consisting of an “inner binary” (a planet and host star or a stellar binary), and a distant planetary or stellar companion orbiting the center of mass of the inner system (referred to as the “outer binary”). Secular perturbations allow the orbital eccentricities and/or inclinations to evolve, but leave the semi-major axes unchanged. Several chapters of this dissertation focus on a particular type of secular behavior, known as the Lidov-Kozai effect (Lidov,

1962; Kozai, 1962). In this scenario, a highly inclined tertiary ($\gtrsim 40^\circ$) causes the eccentricity and inclination of the inner binary to periodically oscillate, often to extreme values. Combined with additional physical ingredients, such as stellar spin-orbit coupling and tidal dissipation allows for a rich variety of applications in the context of giant planets and stellar binaries.

All of the studies in this dissertation involving hot and warm Jupiters explore the dynamical effects of one or more additional planetary companions, or a binary stellar companion. Searches for both planetary and stellar companions in observed hot and warm Jupiter systems have been conducted. Knutson et al. (2014) searched for radial velocity signatures from distant companions in systems known to host hot Jupiters, and estimated a companion occurrence rate of $\sim 50\%$ (corrected for sample incompleteness), for companion masses in the range $\sim 1 - 13M_J$ and separations $\sim 1 - 20$ AU. By direct imaging, Ngo et al. (2015) performed a similar survey for stellar mass companions, and found an occurrence rate of $48 \pm 9\%$ for companions at separations $\sim 50 - 2000$ AU; this is larger than 24%, the fraction of binaries (of the same separation range) among solar-type field stars (Raghavan et al., 2010). Taken together, Ngo et al. (2015) suggested a total companion fraction (including stars and planets) of $\sim 70\%$ for systems hosting hot Jupiters. Using a combination of adaptive optics imaging and radial velocity, Wang et al. (2015) searched for stellar companions in systems containing *Kepler* Objects of Interest, focusing on gas giant planets with orbital periods ranging from a few days to hundreds of days. They found that the stellar multiplicity fraction of companions with separations between 20 and 200 AU is a factor of ~ 2 higher for stars hosting a giant planet, compared to a control sample with no planet detections. Focusing on giant planet companions to hot, warm, and cold Jupiters, Bryan et al. (2016) found companion

occurrence rates of 50% for warm Jupiters and up to 80% for hot Jupiters. In addition, there is a growing number of systems with well-characterized orbits for the companion, especially for warm Jupiters (see, e.g. Table 1 of Antonini et al., 2016, for a recent compilation of warm Jupiters with external companions). Collectively, these works demonstrate that distant external companions to close-in giant planets are common, highlighting the importance of the dynamical studies presented in this dissertation.

Next, I provide a brief summary of each chapter.

Chapter 2 studies high-eccentricity migration of giant planets in stellar binary systems. An inclined stellar perturber may periodically excite the eccentricity (through Lidov-Kozai cycles) of a planet initially located at several AU from its host star, leading to spin-orbit coupling and tidal dissipation during pericenter passages. Together, these physical effects may lead to inward migration and formation of a hot Jupiter with a misaligned orbit with respect to the host star’s spin axis. I conduct an extensive population synthesis study, including the quadrupole and octupole gravitational potential from the stellar companion, mutual precession of the host stellar spin axis and planet orbital axis, tidal dissipation in the planet, and stellar spin-down of the host star due to magnetic braking. I consider a range of planet masses and initial orbital architectures, different properties for the host star, and varying degrees of tidal dissipation. The fraction of systems that result in hot Jupiters depends on planet mass and stellar type. Based on the observed occurrence rate of hot Jupiters, and the estimated occurrence rate of giant planets and stellar binaries, I deduce that Lidov-Kozai cycles from stellar companions may have produced at most $\sim 10\% - 20\%$ of the observed hot Jupiters. This mechanism does not produce

any appreciable numbers of warm Jupiters, due to extremely rapid inward migration once the planet has reached sub-AU distances from the host star. The final distribution of stellar obliquities depends somewhat on stellar and planetary masses, but usually exhibits a distinct bimodal structure.

Chapter 3 studies a mechanism for exciting stellar obliquities for systems hosting a close-in planet (either a hot or warm Jupiter) with an external, modestly inclined companion. Spin-orbit misalignment may be excited due to a secular resonance, occurring when the precession rate of the stellar spin axis (driven by the inner planet) becomes comparable to the nodal precession rate of the inner planet (driven by the companion). Due to the spin-down of the host star via magnetic braking, this resonance may be achieved during the star's main-sequence lifetime for a wide range of planet masses and orbital architectures. Obliquity excitation is accompanied by a decrease in mutual inclination between the inner planet and perturber, and can thus erase high inclinations. For hot Jupiters, the stellar spin axis is strongly coupled to the orbital axis, and obliquity excitation by a giant planet companion requires a strong perturber, usually located within 1-2 AU. For warm Jupiters, the spin and orbital axes are more weakly coupled, and the resonance may be achieved for distant giant planet perturbers (at several to tens of AU). Since warm Jupiters have a high occurrence rate of distant planetary companions with appropriate properties for resonant obliquity excitation, stellar obliquities in warm Jupiter systems may be common, particularly for warm Jupiters orbiting cool stars that have undergone significant spin-down.

In Chapter 4 I examine the possibility of forming eccentric warm Jupiters due to secular interactions with exterior giant planet companions. Starting with

a warm Jupiter in a circular orbit (consistent with either in-situ formation or disk migration), I quantify the necessary conditions (in terms of the eccentricity, semi-major axis and inclination) for external perturbers of various masses to secularly raise warm Jupiter eccentricities. Eccentricity growth may arise from a highly inclined companion (through Lidov-Kozai cycles), or from an eccentric coplanar or low-inclination companion (through apsidal precession resonances). I also consider the sample of eccentric warm Jupiters with characterized external giant planet companions, and for each system, identify the range of mutual inclinations needed to generate the observed eccentricity. For most systems, I find that relatively high inclinations (typically $\gtrsim 50^\circ$) are needed so that Lidov-Kozai cycles are induced; the observed outer companions are typically not sufficiently eccentric to generate the observed inner planet eccentricities in a low-inclination configuration. The results of this chapter place constraints on possibly unseen external companions to eccentric warm Jupiters. Observations that probe mutual inclinations of giant planet systems will help clarify the origin of eccentric warm Jupiters and the role of external companions.

Chapter 5 considers a non-secular avenue of forming eccentric warm Jupiters, due to in-situ formation of several unstable giant planets in nearly circular orbits, followed by planet-planet scattering. Similar to Chapter 4, this setup is consistent with either in-situ formation or disk migration. Most previous N-body scattering experiments have focused on “cold” Jupiters at several AU, where scattering results in ejections, efficiently exciting the eccentricities of surviving planets. In contrast, scattering at sub-AU distances results in a mixture of collisions and ejections, so that the final eccentricities of surviving planets is unclear. I conduct scattering experiments for a range of planet masses

and initial spacing, including the effects of general relativistic apsidal precession, and systematically catalogue the scattering outcomes and properties of surviving planets. Scattering produces comparable numbers of one-planet and two-planet systems, and I compare the properties of these systems with observed WJs. Two-planet systems arise exclusively through planet-planet collisions, tend to have low eccentricities/inclinations, quite compact configurations, and are inconsistent with many of the observed WJs with characterized external companions. One-planet systems arise through a combination of ejections and collisions, resulting in much higher eccentricities. The observed eccentricity distribution of solitary warm Jupiters is consistent with roughly half or more of systems having undergone in-situ scattering, and the remaining experiencing a quiescent history.

Motivated by observed stellar binaries with a range of eccentricities and spin-orbit misalignments, Chapter 6 studies the secular spin-orbit evolution of stellar triples. If the tertiary is inclined with respect to the inner binary, Lidov-Kozai cycles in concert with spin-orbit coupling may occur, leading to eccentricity excitation, and under some circumstances, spin-orbit misalignment. I derive the requirements that the tertiary companion must satisfy in order to raise the eccentricity and obliquity of the inner binary. Through numerical integrations of the secular octupole-order equations of motion, coupled with the spin precession of the oblate primary star due to the torque from the secondary, I obtain a simple, robust condition for producing spin-orbit misalignment in the inner binary: In order to excite appreciable obliquity, the precession rate of the stellar spin axis must be smaller than the orbital precession rate due to the tertiary companion. This yields quantitative requirements on the mass and orbit of the tertiary. I also present new analytic expressions for the maximum eccentricity

and range of inclination allowing eccentricity excitation (the “Lidov-Kozai window”) for stellar triples with arbitrary masses, and including the non-Keplerian potentials introduced by general relativity, stellar tides and rotational bulges. The results of this chapter can be used to place constraints on unobserved tertiary companions in binaries that exhibit high eccentricity and/or spin-orbit misalignment, and will be helpful in guiding efforts to detect external companions around stellar binaries. As an application, I consider the eclipsing binary DI Herculis in which both the primary and secondary have $\sim 90^\circ$ sky-projected obliquities, and identify the requirements that a tertiary companion must satisfy to produce the observed misalignment.

In Chapter 7 I discuss another mechanism for exciting stellar obliquities, due to the presence of a circumbinary disk. An inclined disk introduces precession of the binary orbital axes around the disk angular momentum axis; meanwhile the oblate stars themselves experience torques and precess around the binary orbital axis. As the disk disperses, the system may be trapped into a spin-orbit resonance, causing the obliquity to grow to large values. In some circumstances, the obliquities may approach 90° . I identify the the disk and binary properties required for large obliquity growth, and apply the problem to the eclipsing binary DI Herculis, finding that the large observed obliquities may have been generated by a massive circumbinary disk (of order the binary mass).

In Chapter 8 I summarize and discuss some possible future avenues for research.

CHAPTER 2

**FORMATION AND STELLAR SPIN-ORBIT MISALIGNMENT OF HOT
JUPITERS FROM LIDOV-KOZAI OSCILLATIONS IN STELLAR
BINARIES**

2.1 Introduction

The growing sample of close-in giant planets (hot Jupiters, hereafter HJs) continues to yield surprises. These planets (with orbital periods of ~ 3 days) could not have formed *in situ*, given the large stellar tidal gravity and radiation fields close to their host stars, and must have formed beyond a few AUs and migrated inward. The recent discoveries of many HJs with orbital angular momentum axes that are misaligned with respect to their host star's spin axis (e.g. Hébrard et al., 2008; Narita et al., 2009; Winn et al., 2009; Triaud et al., 2010; Albrecht et al., 2012a; Moutou et al., 2011) has stimulated new studies on the dynamical causes behind such configurations. The presence (or lack) of such misalignment in an HJ system serves as a probe of the planet's dynamical history, and can potentially constrain the planet's migration channel. Therefore, understanding the dynamics behind spin-orbit misalignments is an important endeavor.

HJ systems with low spin-orbit misalignments are commonly thought to have arisen from smooth disk-driven migration, thereby preserving an initially low stellar obliquity. In contrast, systems with high misalignments must have

This chapter is adapted from Anderson et al. (2016)

undergone a more disruptive high-eccentricity migration, in which the eccentricity becomes excited to a large value, with subsequent orbital decay due to dissipative tides raised on the planet by the host star. This assumption has been challenged recently with the suggestion of a “primordial misalignment” (Bate et al., 2010; Foucart & Lai, 2011; Lai et al., 2011; Thies et al., 2011; Batygin, 2012; Batygin & Adams, 2013; Lai, 2014; Spalding & Batygin, 2014; Fielding et al., 2015), in which the protoplanetary disk itself becomes tilted with respect to the stellar spin and planets subsequently form and smoothly migrate within the misaligned disk, resulting in close-in planets with large stellar obliquities. Collectively, these works show that much remains to be done in disentangling the various possible dynamical histories of HJs.

High-eccentricity migration requires either one or more additional planets in the system, or the presence of a stellar binary companion. In the former case, the eccentricity excitation can be caused by strong planet-planet scatterings (Rasio & Ford, 1996; Chatterjee et al., 2008; Ford & Rasio, 2008; Jurić & Tremaine, 2008), and various forms of secular interactions, such as secular chaos with at least three giant planets (Wu & Lithwick, 2011) and interactions between two modestly eccentric coplanar planets (Petrovich, 2015a), or, most likely, a combination of both (Nagasawa et al., 2008; Beaugé & Nesvorný, 2012). In the case of a stellar companion, high eccentricity is achieved from “Lidov-Kozai” (LK) oscillations (Lidov, 1962; Kozai, 1962), in which an inclined stellar companion pumps up the planet’s eccentricity to values close to unity; during the brief high eccentricity phases, dissipative tides within the planet cause orbital decay and inward migration, eventually resulting in a planet with an orbital period of a few days (e.g. Wu & Murray, 2003; Fabrycky & Tremaine, 2007; Naoz et al., 2012; Petrovich, 2015b). Note that LK oscillations with tidal dissipation from

stellar companions have also been invoked to explain the existence of tight inner binaries in stellar triple systems (e.g. Mazeh & Shaham, 1979; Eggleton & Kiseleva-Eggleton, 2001; Fabrycky & Tremaine, 2007; Naoz & Fabrycky, 2014).

To assess the feasibility of HJ formation from the dynamical effects of distant perturbers, searches for both planetary and stellar companions in HJ systems have been conducted. Knutson et al. (2014) searched for radial velocity signatures from distant companions in systems known to host HJs, and estimated a companion occurrence rate of $\sim 50\%$ for HJ systems (corrected for sample incompleteness), for companion masses in the range $\sim 1 - 13M_J$ and separations $\sim 1 - 20$ AU. By direct imaging, Ngo et al. (2015) performed a similar survey for stellar mass companions, and found an occurrence rate of $48 \pm 9\%$ for companions at separations $\sim 50 - 2000$ AU; this is larger than 24%, the fraction of binaries (of the same separation range) among solar-type field stars (Raghavan et al., 2010), suggesting that the presence of a stellar companion increases the likelihood of HJ formation. Taken together, Ngo et al. (2015) suggested a total companion fraction (including stars and planets) of $\sim 70\%$ for systems hosting HJs. Using a combination of adaptive optics imaging and radial velocity, Wang et al. (2015) searched for stellar companions in systems containing *Kepler* Objects of Interest, focusing on gas giant planets with orbital periods ranging from a few days to hundreds of days. They found that the stellar multiplicity fraction of companions with separations between 20 and 200 AU is a factor of ~ 2 higher for stars hosting a giant planet, compared to a control sample with no planet detections. Since many of the objects in their sample are HJs, this highlights the potential role of companion stars in the formation of close-in giant planets.

Despite these optimistic companion fractions, some aspects of HJ formation

via LK oscillations remain problematic. Assuming steady-state formation of HJs, high-eccentricity migration implies the presence of giant planets at wide orbital separations and large eccentricities, with $a \sim$ several AU and $e \gtrsim 0.9$ (“super-eccentric migrating Jupiters,” Socrates et al., 2012). However, this class of planets is not observed (Dawson et al., 2015). Whether this apparent lack of ultra-eccentric giant planets is due to the majority of HJs being formed from disk-driven migration, or whether our understanding of high-eccentricity migration needs to be revised remains to be determined. In addition, the discovery that a significant fraction of HJs have giant planet companions at a few AU’s (Knutson et al., 2014), including a number of systems with full orbit solutions for the companions (e.g. Feng et al., 2015; Becker et al., 2015; Neveu-VanMalle et al., 2015), and the observed stellar-metallicity trend of giant planet eccentricities (Dawson & Murray-Clay, 2013), suggest that LK oscillations driven by stellar companions may not account for the majority of the observed HJ population. Regardless, these issues clearly highlight the need for a better understanding of all channels of HJ formation.

In this paper, we focus on HJ formation in stellar binaries through LK oscillations with tidal dissipation, and present the results of a large-scale population synthesis. Initial population studies of HJ formation by the LK mechanism included the leading order (quadrupole) gravitational potential of the binary companion on the planet’s orbit (Fabrycky & Tremaine, 2007; Wu et al., 2007; Correia et al., 2011). Naoz et al. (2012) incorporated the octupole potential of the binary (Ford et al., 2000), and showed that the octupole terms could alter the outcome of the population synthesis (e.g., they claimed that the efficiency of HJ production can be significantly increased due to increases in the maximum eccentricity). Taking a slightly different approach, Petrovich (2015b) conducted

a thorough octupole-level population synthesis study, focusing on the steady-state distributions of the planet’s orbital elements. He showed that the octupole potential leads to a significant increase in the fraction of tidally disrupted planets. Both Naoz et al. (2012) and Petrovich (2015b) have presented results for the distribution of the stellar obliquities of HJs formed in this scenario, showing a broad spread in the spin-orbit misalignment angles (from $\sim 20^\circ$ to $\sim 140^\circ$). Thus far, all population studies have focused on a single planet mass ($1M_J$) and limited stellar spin properties. However, in a recent paper (Storch et al., 2014), we showed that gravitational interaction between the planet and its oblate host star can lead to chaotic evolution of the stellar spin axis during LK cycles, and this evolution depends sensitively on the planet mass and stellar rotation period. The chaotic spin dynamics arises from secular spin-orbit resonances and related resonance overlaps (Storch & Lai 2015). In the presence of tidal dissipation, the complex spin evolution can leave an imprint on the final spin-orbit misalignment angles. Thus, the result of Storch et al. (2014) shows that the stellar spin properties and the planet mass can have a strong effect on the distribution of stellar obliquities in HJ systems produced by the LK mechanism. The goal of the present paper is to expand upon this previous work by running a large ensemble of numerical simulations with varying planet masses and stellar mass and spin properties. We perform a thorough survey of the parameter space and examine a range of planetary semi-major axes, binary separations, inclinations, and eccentricities. We show that, not only the spin-orbit misalignments are affected by stellar types and planet masses, but also the various outcomes of the planets (HJ formation and tidal disruption) are strongly influenced by the properties of the planets and host stars. We also present a number of new analytical calculations and estimates to help understand our numerical population syn-

thesis results.

This paper is organized as follows. In Section 2.2, we describe the problem setup and present the secular equations of motion that govern the evolution of the system. Section 2.3 presents several analytical results for understanding the dynamics of the planet’s orbit and stellar spin evolution – these results will be useful for interpreting the numerical calculations of later sections. In Section 2.4, we investigate the properties of the stellar spin evolution, and illustrate the various possible paths of generating spin-orbit misalignments. Section 2.5 presents our population synthesis calculations. We first discuss results (with and without octupole effects) for a given value of binary separation and initial planet semi-major axis (Sections 2.5.2-2.5.3; Table 2). The most general population synthesis results are presented in Sections 2.5.4-2.5.5 (Table 3). We conclude in Section 2.6 with a summary of results and discussion of their implications.

2.2 Formulation

We consider a hierarchical triple system, consisting of an inner binary (host star and planet) of masses M_* and M_p , with a distant, inclined outer (stellar) companion M_b . The planet and binary companion have semi-major axes a and a_b respectively, with $a/a_b \ll 1$. We include the secular gravitational perturbations on the planet from the outer companion to octupole order in the disturbing potential, along with spin-orbit coupling between the oblate host star and planet, tidal dissipation within the planet, and periastron precession due to various short-range forces (General Relativity, and rotational and tidal distortions of the planet). We ignore the perturbations from the inner binary (M_* and M_p) on the

outer binary (M_* and M_b). The planetary orbit is characterized by the unit vectors $(\hat{\mathbf{L}}, \hat{\mathbf{e}})$, where $\hat{\mathbf{L}}$ is normal to the orbital plane (in the direction of the angular momentum vector \mathbf{L}) and $\hat{\mathbf{e}}$ is in the direction of the eccentricity vector \mathbf{e} . Similarly, the orbit of the outer binary is characterized by the unit vectors $(\hat{\mathbf{L}}_b, \hat{\mathbf{e}}_b)$. The invariant plane is determined by the outer binary angular momentum axis $\hat{\mathbf{L}}_b$. The secular equations of motion for the planetary orbit take the forms

$$\frac{d\mathbf{L}}{dt} = \left. \frac{d\mathbf{L}}{dt} \right|_{LK} + \left. \frac{d\mathbf{L}}{dt} \right|_{SL} + \left. \frac{d\mathbf{L}}{dt} \right|_{Tide}, \quad (2.1)$$

and

$$\frac{d\mathbf{e}}{dt} = \left. \frac{d\mathbf{e}}{dt} \right|_{LK} + \left. \frac{d\mathbf{e}}{dt} \right|_{SL} + \left. \frac{d\mathbf{e}}{dt} \right|_{SRF} + \left. \frac{d\mathbf{e}}{dt} \right|_{Tide}, \quad (2.2)$$

where we are including contributions from the binary companion that give rise to Lidov-Kozai (LK) oscillations, spin-orbit coupling between the host star spin S_* and L (SL), dissipative tides (Tide) within the planet, and periastron precession due to short-range forces (SRFs). Explicit forms for each term are given in Appendix A.

Note that the “LK” term from the binary companion consists of two pieces: a quadrupole term, and an octupole term. The quadrupole has a characteristic timescale for LK oscillations t_k , given by

$$\frac{1}{t_k} = \frac{M_b}{M_{\text{tot}}} \frac{a^3}{a_{b,\text{eff}}^3} n = \left(\frac{2\pi}{10^6 \text{yr}} \right) \frac{\bar{M}_b \bar{a}^{3/2}}{\bar{M}_{\text{tot}}^{1/2} \bar{a}_{b,\text{eff}}^3}, \quad (2.3)$$

where $a_{b,\text{eff}} \equiv a_b \sqrt{1 - e_b^2}$, and $n = \sqrt{GM_{\text{tot}}/a^3}$ is the planetary mean motion. The octupole term has a relative “strength” ε_{oct} (compared to the quadrupole contribution), given by

$$\varepsilon_{\text{oct}} = \frac{M_* - M_p}{M_* + M_p} \frac{a}{a_b} \frac{e_b}{1 - e_b^2}. \quad (2.4)$$

(See Table 2.1 for a summary of various physical quantities and their normalized forms used throughout the paper.) In terms of the unit vector $\hat{\mathbf{L}}$, the effect of the

binary companion is to induce precession of $\hat{\mathbf{L}}$ around $\hat{\mathbf{L}}_b$, with simultaneous nutation. The rate of change of $\hat{\mathbf{L}}$ due to the quadrupole potential of the binary companion is given by

$$\begin{aligned}\Omega_L &= \left| \frac{d\hat{\mathbf{L}}}{dt} \right|_{\text{LK,Quad}} \\ &= [(\Omega_{\text{pl}} \sin \theta_{\text{lb}})^2 + \dot{\theta}_{\text{lb}}^2]^{1/2},\end{aligned}\quad (2.5)$$

where $\Omega_{\text{pl}} = \dot{\Omega}$, the precession rate of the classical orbital node Ω , and θ_{lb} (defined as $\cos \theta_{\text{lb}} = \hat{\mathbf{L}} \cdot \hat{\mathbf{L}}_b$) is the angle between the planet orbital axis $\hat{\mathbf{L}}$ and the binary axis $\hat{\mathbf{L}}_b$. The first term in Eq. (2.5) represents precession of $\hat{\mathbf{L}}$ around the binary axis $\hat{\mathbf{L}}_b$, and the second term represents nutation of $\hat{\mathbf{L}}$. An approximate expression for Ω_L as a function of e and θ_{lb} is (see Appendix)

$$\Omega_L \simeq \frac{3(1+4e^2)}{8t_k \sqrt{1-e^2}} |\sin 2\theta_{\text{lb}}|. \quad (2.6)$$

(Note that Eq. (2.6) is exact at $e = 0$ and the maximum eccentricity.) At zero eccentricity the expression becomes

$$\begin{aligned}\Omega_L|_{e=0} &= \frac{3}{4t_k} \cos \theta_{\text{lb}} \sin \theta_{\text{lb}} \\ &\simeq 4.71 \times 10^{-6} \text{yr}^{-1} \frac{\bar{M}_b \bar{a}^{3/2}}{\bar{M}_{\text{tot}}^{1/2} \bar{a}_{b,\text{eff}}^3} \cos \theta_{\text{lb}} \sin \theta_{\text{lb}}.\end{aligned}\quad (2.7)$$

2.2.1 Spin Evolution due to Stellar Quadrupole

The oblate host star has angular momentum $\mathbf{S}_* = I_* \Omega_* \hat{\mathbf{S}}_*$, where $I_* = k_* M_* R_*^2$ is the moment of inertia, with $k_* \simeq 0.1$ for a solar-type star (Claret & Gimenez, 1992), Ω_* is the stellar spin frequency (with period $P_* = 2\pi/\Omega_*$), and $\hat{\mathbf{S}}_* = \mathbf{S}_*/S_*$ is the unit vector along the spin axis. The stellar rotational distortion generates a quadrupole moment, thus introducing a torque between the star and planet.

Table 2.1: Definitions of variables, along with the canonical value used in this chapter (if applicable), and dimensionless form.

Quantity	Dimensionless/Normalized Form
Vector Quantities	
Planet orbital angular momentum \mathbf{L}
Planet eccentricity vector \mathbf{e}
Binary orbital angular momentum \mathbf{L}_b
Binary eccentricity vector \mathbf{e}_b
Stellar spin angular momentum \mathbf{S}_*
Planetary spin angular momentum \mathbf{S}_p
Physical Properties	
Stellar mass M_*	$\bar{M}_* = M_*/M_\odot$
Stellar radius R_*	$\bar{R}_* = R_*/R_\odot$
Planet mass M_p	$\bar{M}_p = M_p/M_J$
Planet radius R_p	$\bar{R}_p = R_p/R_J$
Binary companion mass M_b	$\bar{M}_b = M_b/M_\odot$
Inner binary total mass $M_{\text{tot}} \equiv M_* + M_p$	$\bar{M}_{\text{tot}} = M_{\text{tot}}/M_\odot$
Spin & Structure Properties	
Spin-orbit angle θ_{sl} (defined by $\cos \theta_{\text{sl}} = \hat{\mathbf{L}} \cdot \hat{\mathbf{S}}_*$)
Stellar moment of inertia constant k_* ($I_* = k_* M_* R_*^2$)	$\bar{k}_* = k_*/0.1$
Planet moment of inertia constant k_p ($I_p = k_p M_p R_p^2$)	$\bar{k}_p = k_p/0.25$
Stellar rotational distortion coefficient k_{q*} (see Sec. 2.2.1)	$\bar{k}_{q*} = k_{q*}/0.05$
Planet rotational distortion coefficient k_{qp} (see Sec. 2.2.1)	$\bar{k}_{qp} = k_{qp}/0.17$
Stellar spin period $P_* = 2\pi/\Omega_*$	$\bar{P}_* = P_*/\text{day}$
Planet spin period $P_p = 2\pi/\Omega_p$	$\bar{P}_p = P_p/\text{day}$
Tidal Properties	
Planet tidal Love number k_{2p}	$\bar{k}_{2p} = k_{2p}/0.37$
Tidal lag time Δt_L
Tidal enhancement factor χ ($\Delta t_L = 0.1\chi\text{sec}$)
Orbital Properties	
Planet semi-major axis a	$\bar{a} = a/\text{AU}$
Planet eccentricity e
Planet inclination θ_{lb} (relative to outer binary, defined by $\cos \theta_{\text{lb}} = \hat{\mathbf{L}} \cdot \hat{\mathbf{L}}_b$)
Outer binary semi-major axis a_b	$\bar{a}_b = a_b/100\text{AU}$
Outer binary eccentricity e_b
Effective outer binary semi-major axis $a_{b,\text{eff}} \equiv a_b \sqrt{1 - e_b^2}$	$\bar{a}_{b,\text{eff}} = a_{b,\text{eff}}/100\text{AU}$
Orbital mean motion $n = \sqrt{GM_{\text{tot}}/a^3}$

This results in mutual precession of \mathbf{S}_* and \mathbf{L} around the total angular momentum $\mathbf{J} = \mathbf{L} + \mathbf{S}_*$ (we ignore the small contribution to \mathbf{J} due to the planet spin, see Section 2.3.3). The star also spins down via magnetic braking: we adopt the Skumanich law (Skumanich, 1972), with $d\Omega_*/dt \propto -\Omega_*^3$. The stellar spin evolution thus has two contributions, and is given by

$$\begin{aligned} \frac{d\mathbf{S}_*}{dt} &= \left. \frac{d\mathbf{S}_*}{dt} \right|_{\text{SL}} + \left. \frac{d\mathbf{S}_*}{dt} \right|_{\text{MB}} \\ &= \Omega_{\text{ps}} \hat{\mathbf{L}} \times \mathbf{S}_* - \alpha_{\text{MB}} I_* \Omega_*^3 \hat{\mathbf{S}}_*, \end{aligned} \quad (2.8)$$

where the first term describes the precession of \mathbf{S}_* around \mathbf{L} (SL), and the second term describes the spin-down due to magnetic braking (MB), with the efficiency parameter α_{MB} . In this paper we set $\alpha_{\text{MB}} = 1.5 \times 10^{-14}$ yr to model solar-mass (type G) stars, and $\alpha_{\text{MB}} = 1.5 \times 10^{-15}$ yr to model more massive ($1.4M_\odot$, type F) stars, as in Barker & Ogilvie (2009). This is consistent with observed stellar rotation periods, with massive stars spinning more rapidly on average (McQuillan et al., 2014), and more sophisticated stellar spin-down models (see Bouvier 2013 for a review).

The precession frequency of \mathbf{S}_* around \mathbf{L} , Ω_{ps} , is given by

$$\begin{aligned}\Omega_{\text{ps}} &= -\frac{3GM_p(I_3 - I_1)\cos\theta_{\text{sl}}}{2a^3j^3S_*} = -\frac{3}{2}\frac{k_{q*}}{k_*}\frac{M_p}{M_*}\frac{R_*^3}{a^3}\frac{\Omega_*}{j^3}\cos\theta_{\text{sl}} \\ &\simeq -1.64 \times 10^{-7} \text{yr}^{-1}\frac{\bar{k}_{q*}\bar{M}_p\bar{R}_*^3}{\bar{k}_*\bar{P}_*\bar{M}_*\bar{a}^3}\frac{\cos\theta_{\text{sl}}}{j^3},\end{aligned}\quad (2.9)$$

where the stellar spin-orbit angle θ_{sl} is defined by $\cos\theta_{\text{sl}} = \hat{\mathbf{L}} \cdot \hat{\mathbf{S}}_*$, $j = \sqrt{1 - e^2}$, and the stellar quadrupole moment $(I_3 - I_1)$ is related to the spin frequency via $(I_3 - I_1) = k_{q*}M_*R_*^2\hat{\Omega}_*^2$. Here $\hat{\Omega}_* = \Omega_*(GM_*/R_*^3)^{-1/2}$ is the stellar rotation rate in units of the breakup frequency, and k_{q*} is a “rotational distortion coefficient” (we adopt the canonical value $k_{q*} = 0.05$ in this paper; Claret & Gimenez 1992).² The stellar quadrupole also affects the planet’s orbit through a backreaction torque, and precession of the pericenter (see Section 2.4.3 and Appendix A).

As discussed in Storch et al. (2014), qualitatively distinct types of behavior for the stellar spin axis arise, depending on the ratio of the stellar spin precession rate $|\Omega_{\text{ps}}|$ to the nodal precession rate due to the binary companion $|\Omega_L|$ (see Eqs. [6.35] and [2.5]):

²Note that k_{q*} is related to the apsidal motion constant κ , the Love number k_2 , and the J_2 parameter by $k_{q*} = 2\kappa/3 = k_2/3$ and $J_2 = k_{q*}\hat{\Omega}_*^2$.

If $|\Omega_{\text{ps}}| \ll |\Omega_L|$ throughout the LK cycle, the stellar spin axis effectively precesses around the binary axis $\hat{\mathbf{L}}_b$, so that the angle between $\hat{\mathbf{S}}_*$ and $\hat{\mathbf{L}}_b$ is nearly constant. We refer to this as the “non-adiabatic” regime.

On the other hand, if $|\Omega_{\text{ps}}| \gtrsim |\Omega_L|$ throughout the LK cycle, the stellar spin axis is strongly coupled to the evolution of the orbital axis. Two different types of behavior can occur in this “adiabatic regime”: (i) The stellar spin axis $\hat{\mathbf{S}}_*$ essentially follows the orbital axis $\hat{\mathbf{L}}$, with $\theta_{\text{sl}} \sim \text{constant}$. For systems that begin with $\hat{\mathbf{S}}_*$ and $\hat{\mathbf{L}}$ aligned ($\theta_{\text{sl},0} = 0^\circ$), the spin-orbit angle remains relatively small ($\theta_{\text{sl}} \lesssim 30^\circ$) throughout the evolution. (ii) The spin-orbit angle is initially small, but gradually increases towards the end of the evolution when the planet semi-major axis has decayed appreciably due to tidal dissipation. In this situation, the final misalignment angle settles to a final value $\theta_{\text{sl,f}} < 90^\circ$. We term this behavior “adiabatic advection” and will discuss it in Section 2.4 (see also Storch & Lai 2015).

Finally, if during the LK cycle, $|\Omega_{\text{ps}}| \sim |\Omega_L|$, secular resonances develop, and overlapping resonances can lead to complex, and often chaotic behavior of the stellar spin axis. The spin-orbit angle θ_{sl} may cross 90° , and a wide distribution of final misalignment angles is possible. Note that θ_{sl} can also cross 90° in the non-adiabatic regime, but the addition of secular resonances in the trans-adiabatic regime leads to much more complex evolution than the non-adiabatic regime.

To help characterize the dynamics, we introduce an “adiabaticity parameter” \mathcal{A} :

$$\mathcal{A} \equiv \left| \frac{\Omega_{\text{ps}}}{\Omega_L} \right|. \quad (2.10)$$

This parameter will be used throughout the paper to help characterize the spin-

orbit dynamics. In general, \mathcal{A} is a strong function of eccentricity and time. At the start of the evolution (so that $e \approx 0$)

$$\mathcal{A}_0 \equiv \left| \frac{\Omega_{\text{ps}}}{\Omega_L} \right|_{e=0} = 0.07 \frac{\bar{k}_{q\star} \bar{M}_p \bar{M}_{\text{tot}}^{1/2} \bar{R}_{\star}^3 \bar{a}_{b,\text{eff}}^3}{\bar{k}_{\star} \bar{M}_{\star} \bar{M}_b \bar{a}^{9/2} \bar{P}_{\star}} \left| \frac{\cos \theta_{\text{sl},0}}{\sin 2\theta_{\text{lb},0}} \right|. \quad (2.11)$$

2.3 LK Migration and Stellar Spin Evolution: Analytical Results

Before presenting our detailed population synthesis calculations, we discuss some general properties of LK migration and stellar spin evolution. These will be useful for understanding the results of later sections. Readers interested in the full population synthesis and observational implications are referred to Section 2.5.

2.3.1 LK Oscillations: Range of Eccentricity and Freezing of Oscillations

Figure 2.1 gives a “canonical” example of the formation of an HJ due to LK oscillations with tidal dissipation. For simplicity, this example neglects the feedback of the stellar spin on the orbit. Here we set the binary eccentricity $e_b = 0$, so that the octupole-level perturbation from the binary companion vanishes. The planet starts with initial semi-major axis $a_0 = 1.5$ AU, and eccentricity $e_0 = 0.01$, and then undergoes cyclic excursions to maximum eccentricity e_{max} , with accompanying oscillations in the inclination θ_{lb} (recall that $\cos \theta_{\text{lb}} = \hat{\mathbf{L}} \cdot \hat{\mathbf{L}}_b$), between the initial (maximum) $\theta_{\text{lb},0} = 85^\circ$ and minimum (occurring at $e = e_{\text{max}}$)

$\theta_{lb,max} \approx 53^\circ$. Note that short-range forces (SRFs) cause $\theta_{lb,max} > 40^\circ$ here, in contrast to planets subject only to LK oscillations (without SRFs). As the planetary orbit decays, the range of eccentricity oscillations becomes smaller. The example shows that before the oscillations freeze, e_{max} is approximately constant in time, while the minimum eccentricity e_{min} steadily increases toward e_{max} . Eventually, when a is sufficiently small, the LK oscillations freeze, and the planet undergoes “pure” orbital decay/circularization governed by tidal dissipation, at nearly constant angular momentum.

As is well recognized in previous work (e.g. Holman et al., 1997; Wu & Murray, 2003; Fabrycky & Tremaine, 2007; Liu et al., 2015), SRFs play an important role in determining the maximum eccentricity e_{max} in LK cycles. The range of eccentricity oscillations during the LK migration can also be understood from the effects of SRFs, as we discuss below. As in the example depicted in Fig. 2.1, we ignore the stellar spin feedback on the planetary orbit, as well as octupole-level perturbations from the binary companion.

In the absence of tidal dissipation, the evolution of the planetary orbit is governed by two conservation laws. The first, which is related to the component of the angular momentum along the binary axis, is the well-known “Kozai constant”, given by

$$K = j \cos \theta_{lb}, \quad \text{where } j = \sqrt{1 - e^2}. \quad (2.12)$$

The second conserved quantity is the energy per unit mass, which in secular form is given by (e.g. Fabrycky & Tremaine, 2007; Liu et al., 2015)

$$\Phi = \Phi_{\text{Quad}} + \Phi_{\text{GR}} + \Phi_{\text{Tide}} + \Phi_{\text{Rot}}, \quad (2.13)$$

where the subscripts “Quad”, “GR”, “Tide”, and “Rot” denote contributions from the binary companion (to quadrupole order), General Relativity, static tidal

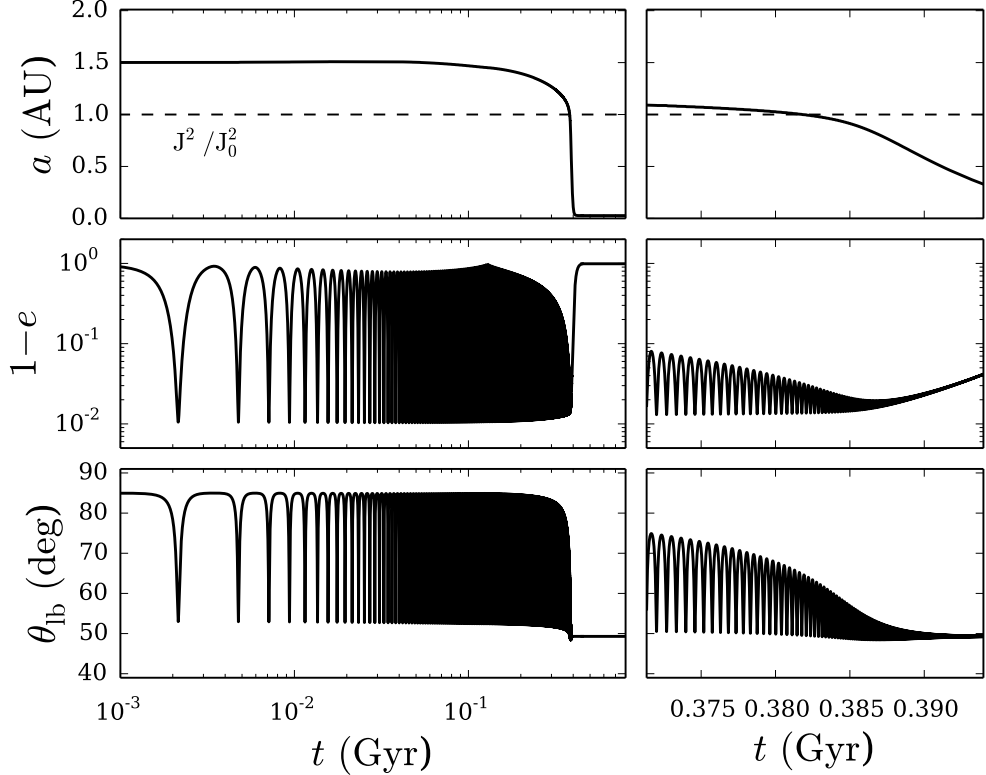


Figure 2.1: Semi-major axis a (top), eccentricity (middle), and inclination θ_{lb} (bottom) as functions of time, showing the evolution until the planetary orbit has decayed and circularized (left panels, with logarithmic scale on the x-axis), as well as a zoomed-in version showing the suppression of LK oscillations and tidal decay (right panels, with linear scale on the x-axis). As the orbit decays, the maximum eccentricity of each LK cycle is approximately constant, while the minimum eccentricity steadily increases, until eventually the LK cycles are completely suppressed due to the effects of short-range forces. The dashed line shows that the angular momentum projected along the binary axis \hat{L}_b (defined by Eq. [2.20]) is conserved throughout the evolution. Parameters are $M_p = 5M_J$, $a_0 = 1.5$ AU, $a_b = 200$ AU, $e_b = 0$, $\theta_{lb,0} = 85^\circ$. The other parameters assume their canonical values, as defined in Table 2.1.

deformation of the planet, and the rotational deformation of the planet. In terms of the planet's eccentricity (e), inclination (θ_{lb}), and argument of pericenter (ω), the energy (per unit mass) from the binary companion takes the form

$$\Phi_{\text{Quad}} = \frac{\Phi_0}{8} (1 - 6e^2 - 3K^2 + 15e^2 \sin^2 \theta_{\text{lb}} \sin^2 \omega), \quad (2.14)$$

where

$$\Phi_0 = \frac{GM_b a^2}{a_{b,\text{eff}}^3}. \quad (2.15)$$

The remaining energy terms due to SRFs can be written as

$$\begin{aligned} \Phi_{\text{GR}} &= -\varepsilon_{\text{GR}} \frac{\Phi_0}{j}, \\ \Phi_{\text{Tide}} &= -\varepsilon_{\text{Tide}} \frac{\Phi_0}{15} \frac{1 + 3e^2 + 3e^4/8}{j^9}, \\ \Phi_{\text{Rot}} &= -\varepsilon_{\text{Rot}} \frac{\Phi_0}{3j^3}, \end{aligned} \quad (2.16)$$

where we have defined dimensionless parameters ε_{GR} , $\varepsilon_{\text{Tide}}$ and ε_{Rot} that quantify the “strengths” of the SRFs:

$$\varepsilon_{\text{GR}} \equiv \frac{3GM_{\text{tot}}^2 a_{b,\text{eff}}^3}{M_b a^4 c^2} \simeq 0.03 \frac{\bar{M}_{\text{tot}}^2 \bar{a}_{b,\text{eff}}^3}{\bar{M}_b \bar{a}^4}, \quad (2.17)$$

$$\begin{aligned} \varepsilon_{\text{Tide}} &\equiv \frac{15k_{2p} M_{\star} M_{\text{tot}} a_{b,\text{eff}}^3 R_p^5}{M_b M_p a^8} \\ &\simeq 1.47 \times 10^{-7} \frac{\bar{M}_{\star} \bar{M}_{\text{tot}} \bar{a}_{b,\text{eff}}^3 \bar{R}_p^5}{\bar{M}_b \bar{M}_p \bar{a}^8}, \end{aligned} \quad (2.18)$$

$$\begin{aligned} \varepsilon_{\text{Rot}} &\equiv \frac{3k_{qp} \hat{\Omega}_p^2}{2} \frac{M_{\text{tot}}}{M_b} \left(\frac{R_p}{a} \right)^2 \left(\frac{a_{b,\text{eff}}}{a} \right)^3 \\ &\simeq 8.48 \times 10^{-4} \bar{k}_{qp} \left(\frac{P_p}{1\text{day}} \right)^{-2} \frac{\bar{M}_{\text{tot}} \bar{R}_p^5 \bar{a}_{b,\text{eff}}^3}{\bar{M}_p \bar{M}_b \bar{a}^5}. \end{aligned} \quad (2.19)$$

(see Table 2.1 for definitions of k_{2p} and k_{qp}).

With tidal dissipation included, the semi-major axis is no longer constant. We expect that the first conservation law, Eq. (2.12) is replaced by

$$J = \sqrt{a(1 - e^2)} \cos \theta_{\text{lb}} = \sqrt{a} j \cos \theta_{\text{lb}}. \quad (2.20)$$

Figure 2.1 shows that J is indeed conserved to high precision throughout the LK migration. With $a \neq \text{constant}$, the energy expression, Eq. (2.14) is no longer conserved. However, since the timescale for tidal dissipation (see Section 2.3.2, Eq. [2.32]) is much longer than the timescale for LK oscillations (Eq. [2.3]), the energy is very nearly constant over a single LK cycle.

As seen from Fig. 2.1, during the oscillatory phase of the LK migration, the maximum eccentricity of each LK cycle $e_{\max} \approx \text{constant}$, while the minimum eccentricity steadily increases, so that the range of eccentricity variation narrows (see right panels of Fig. 2.1). The inclination at maximum eccentricity, $\theta_{lb,max}$, is also nearly constant. For given e_{\max} and $\theta_{lb,max}$, the minimum eccentricity e_{\min} can be determined using the two (approximate) conservation laws, giving

$$\begin{aligned} \frac{3}{4}e_{\min}^2 &= \frac{3}{8}e_{\max}^2(2 - 5\sin^2\theta_{lb,max}) \\ &+ \left[\frac{\varepsilon_{GR}}{j} + \frac{\varepsilon_{Tide}}{15j^9} \left(1 + 3e^2 + \frac{3e^4}{8} \right) + \frac{\varepsilon_{Rot}}{3j^3} \right] \Big|_{e_{\min}}^{e_{\max}}. \end{aligned} \quad (2.21)$$

Here we have used the fact that the maximum eccentricity occurs when $\omega = \pi/2$ or $3\pi/2$, while the minimum eccentricity occurs at $\omega = 0$ or π (provided that ω is in the circulating, rather than librating regime). For reasonable values of the planetary rotation rate (see Section 2.3.3), the SRF effect due to the rotational bulge can be neglected compared to the tidal effect.

We can now determine the condition for the suppression (freezing) of LK oscillations. Since the freezing occurs at e_{\max} close to 1, it is more appropriate to consider the freezing of j . For $\Delta j \equiv j_{\min} - j_{\max} = \sqrt{1 - e_{\min}^2} - \sqrt{1 - e_{\max}^2} \ll j_{\max}$, we find that

$$\frac{\Delta j}{j_{\max}} \approx \frac{15}{8} \sin^2\theta_{lb,max} \left(\frac{\varepsilon_{GR}}{j_{\max}} + \frac{21}{8} \frac{\varepsilon_{Tide}}{j_{\max}^9} \right)^{-1}. \quad (2.22)$$

(Note that the subscript “max” indicates the value at maximum eccentricity.)

As a decreases, both ε_{GR} and $\varepsilon_{\text{Tide}}$ increase rapidly, which leads to the decrease of Δj . The fact that $\theta_{\text{lb},\max}$ is nearly constant (see Fig. 2.1), along with conservation of J (see Eq. [2.20]), together imply that $j_{\max} \propto a^{-1/2}$. For $\varepsilon_{\text{GR}}/j_{\max} \gtrsim (21/8)\varepsilon_{\text{Tide}}/j_{\max}^9$, or

$$j_{\max} \gtrsim \left(\frac{21\varepsilon_{\text{Tide}}}{8\varepsilon_{\text{GR}}} \right)^{1/8} = 0.245 \frac{\bar{R}_p^{5/8}}{\bar{M}_p^{1/8} \bar{a}^{1/2}}, \quad (2.23)$$

the GR term dominates, and we have

$$\frac{\Delta j}{j_{\max}} \simeq 0.1 \frac{\bar{M}_b}{\bar{M}_{\star}^2 \bar{a}_{b,\text{eff}}^2} \left(\frac{a}{0.3 \text{ AU}} \right)^4 \left(\frac{j_{\max}}{0.2} \right) \sin^2 \theta_{\text{lb},\max}. \quad (2.24)$$

When equation (2.23) is not satisfied, the tidal term dominates, and we have

$$\frac{\Delta j}{j_{\max}} \simeq 0.01 \frac{\bar{M}_b \bar{M}_p}{\bar{M}_{\star}^2 \bar{a}_{b,\text{eff}}^3} \left(\frac{a}{0.5 \text{ AU}} \right)^8 \left(\frac{j_{\max}}{0.2} \right)^9 \sin^2 \theta_{\text{lb},\max}. \quad (2.25)$$

Figure 2.2 shows $\Delta j/j_{\max}$ as a function of a using Eq. (2.22) (where j_{\max} has been calculated from Eq. [2.20]), for the same system parameters as depicted in Fig. 2.1, and three values of $\theta_{\text{lb},0}$. We see that $\Delta j/j_{\max}$ decreases with decreasing a , as SRFs increasingly suppress the LK oscillations.

2.3.2 Migration Rate: Upper Limit and Estimate

For a given a and e , the orbital decay rate (using weak friction tidal theory) takes the form (Alexander, 1973; Hut, 1981)

$$\left(\frac{1}{a} \frac{da}{dt} \right)_{\text{Tide}} = -\frac{1}{t_a} \frac{1}{j^{15}} \left[f_1(e) - j^3 f_2(e) \frac{\Omega_p}{n} \right], \quad (2.26)$$

where the dimensionless functions of eccentricity f_1 and f_2 are defined in Eqs. (A.18) and (A.19). The timescale t_a is given by

$$\begin{aligned} \frac{1}{t_a} &= 6k_{2p}\Delta t_L \frac{M_{\star}}{M_p} \left(\frac{R_p}{a} \right)^5 n^2 \\ &\approx \frac{7.3 \times 10^{-21}}{\text{yr}} \chi \bar{k}_{2p} \frac{\bar{M}_{\star} \bar{M}_{\text{tot}}}{\bar{M}_p} \frac{\bar{R}_p^5}{\bar{a}^8}, \end{aligned} \quad (2.27)$$

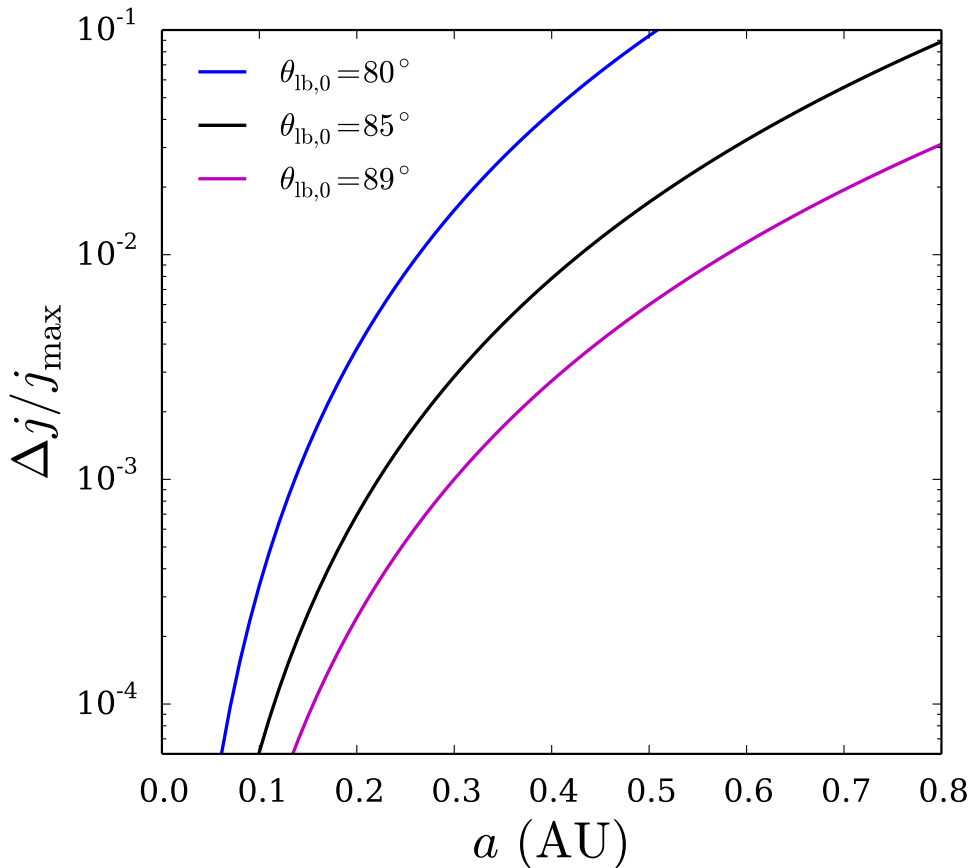


Figure 2.2: Condition for freezing of LK oscillations, $\Delta j/j_{\max}$ as a function of a using Eq. (2.22) (where we assumed $\Delta j/j_{\max} \ll 1$), where $j_{\max} = \sqrt{1 - e_{\max}^2}$ has been calculated from Eq. (2.20), with the assumption that $\theta_{lb,\max} \sim \theta_{lb,0}$. We have chosen three values of $\theta_{lb,0}$, as labeled, and all other parameters the same as in Fig. 2.1. As a decreases (so that ε_{GR} and ε_{Tide} increase), SRFs limit the eccentricity variation, causing Δj to decrease.

where Δt_L is the lag time, k_{2p} is the tidal Love number, and we have introduced a tidal enhancement factor χ (relative to Jupiter), defined such that $\Delta t_L = 0.1\chi$ sec. Our canonical value is $\chi = 10$. It is convenient to introduce the quantity

$$a_F \equiv a(1 - e_{\max}^2), \quad (2.28)$$

because a_F varies by at most $\sim 20\%$ during the inward migration of a planet undergoing LK cycles. Note that a_F is approximately equivalent to the final (“circularized”) semi-major axis of the planet. To produce HJs, we require $a_F \lesssim 0.05$ AU (i.e. orbital periods less than ~ 4 days).

For a given value of the planetary spin rate Ω_p , the maximum decay rate occurs for $e = e_{\max}$ (see Section 2.3.3 for a discussion of our treatment of the planetary spin). Setting $\Omega_p \simeq 0$ for simplicity, the maximum decay rate is

$$\begin{aligned} \left| \frac{1}{a} \frac{da}{dt} \right|_{\text{Tide,max}} &= \frac{1}{t_a} \frac{f_1(e_{\max})}{j_{\max}^{15}} \\ &\approx \frac{2.52 \times 10^{-9}}{\text{yr}} \chi \bar{k}_{2p} \frac{\bar{M}_{\text{tot}} \bar{M}_* \bar{R}_p^5}{\bar{M}_p \bar{a}^{1/2}} \left(\frac{\bar{a}_F}{0.05} \right)^{-15/2}. \end{aligned} \quad (2.29)$$

Non-zero values of the planetary spin rate Ω_p would slightly modify the numerical coefficient in Eq. (2.29).

Eq. (2.29) overestimates the actual LK migration rate, since the planet spends only a small fraction of time near high eccentricity during an LK cycle. We can estimate the time spent in the vicinity of e_{\max} as follows. Neglecting SRFs, the planet’s argument of pericenter ω evolves according to

$$\frac{d\omega}{dt} = \frac{3}{4t_k \sqrt{1-e^2}} [2(1-e^2) + 5 \sin^2 \omega (e^2 - \sin^2 \theta_{\text{lb}})]. \quad (2.30)$$

Near maximum eccentricity, ω centers around $\pi/2$ or $3\pi/2$, with width of $\Delta\omega \sim 1$ radian (see, e.g. Holman et al., 1997, Fig. 3). Thus, the second term in Eq. (2.30) is of order unity and the first term is negligible, so that the time spent near e_{\max}

can be approximated by

$$\Delta t(e_{\max}) \sim t_k \sqrt{1 - e_{\max}^2}. \quad (2.31)$$

Thus, the actual orbital decay rate during LK migration is roughly

$$\begin{aligned} \left| \frac{1}{a} \frac{da}{dt} \right|_{\text{Tide,LK}} &\sim \left| \frac{1}{a} \frac{da}{dt} \right|_{\text{Tide,max}} (1 - e_{\max}^2)^{1/2} \\ &\simeq \frac{5.6 \times 10^{-10}}{\text{yr}} \chi \bar{k}_{2p} \frac{\bar{M}_{\text{tot}} \bar{M}_* \bar{R}_p^5}{\bar{M}_p \bar{a}} \left(\frac{\bar{a}_F}{0.05} \right)^{-7} \end{aligned} \quad (2.32)$$

(see also Petrovich 2015b for a more detailed exploration of the LK migration rate). Since the main-sequence lifetime of a solar-type star is $\sim 10^{10}$ yr, inward migration resulting in HJ formation requires that $a_F \lesssim 0.05$ AU.

2.3.3 Evolution of Planet Spin During LK Cycles with Tidal Friction

Similar to the spin axis of the host star, the spin axis of the oblate planet $\hat{\mathbf{S}}_p$ (where the spin angular momentum is $\mathbf{S}_p = S_p \hat{\mathbf{S}}_p$) precesses around the orbital axis $\hat{\mathbf{L}}$ according to

$$\frac{d\hat{\mathbf{S}}_p}{dt} = \Omega_{\text{prec},p} \hat{\mathbf{L}} \times \hat{\mathbf{S}}_p, \quad (2.33)$$

where the precession rate $\Omega_{\text{prec},p}$ is given by

$$\begin{aligned} \Omega_{\text{prec},p} &= -\frac{3}{2} \frac{k_{qp}}{k_p} \frac{M_*}{M_p} \frac{R_p^3}{a^3} \frac{\Omega_p}{j^3} \cos \theta_p \\ &\simeq -2.69 \times 10^{-4} \text{yr}^{-1} \frac{\bar{k}_{qp} \bar{M}_* \bar{R}_p^3}{\bar{k}_p \bar{M}_p \bar{a}^3} \frac{\cos \theta_p}{j^3}, \end{aligned} \quad (2.34)$$

with $\cos \theta_p = \hat{\mathbf{S}}_p \cdot \hat{\mathbf{L}}$ (see Table 1 for definitions and canonical values of all other quantities). We can define a planetary “adiabaticity parameter” $\mathcal{A}_{p,0}$ (analogous to the stellar adiabaticity parameter \mathcal{A}_0 , see Eq. [2.11]), where

$$\mathcal{A}_{p,0} \equiv \left| \frac{\Omega_{\text{prec},p}}{\Omega_L} \right|_{e=0} \simeq 57.1 \frac{\bar{k}_{qp} \bar{M}_* \bar{M}_{\text{tot}}^{1/2} \bar{R}_p^3 \bar{a}_{b,\text{eff}}^3}{\bar{k}_p \bar{M}_p \bar{M}_b \bar{a}^{9/2} \bar{P}_p} \left| \frac{\cos \theta_p}{\cos \theta_{\text{lb}} \sin \theta_{\text{lb}}} \right|. \quad (2.35)$$

Clearly, for all plausible parameters, $\mathcal{A}_{p,0} \gg 1$, provided that the planetary obliquity θ_p is not too close to 90° . The planetary spin axis is thus always in the adiabatic regime (see Section 2.2.1), with the planetary spin orbit angle $\theta_p \approx$ constant.

We thus treat the direction of the planetary spin axis as always being aligned with the orbital axis $\hat{\mathbf{L}}$, and the spin magnitude $S_p = k_p M_p R_p^2 \Omega_p$ evolves only due to tidal dissipation. After averaging over the periastron precession (e.g. Alexander, 1973; Hut, 1981; Correia et al., 2011), the evolution of S_p is governed by the expression

$$\left(\frac{1}{S_p} \frac{dS_p}{dt} \right)_{\text{Tide}} = -\frac{1}{2t_a} \frac{L}{S_p} \frac{1}{j^{13}} \left[j^3 f_5(e) \frac{\Omega_p}{n} - f_2(e) \right], \quad (2.36)$$

where f_2 and f_5 are functions of eccentricity, defined in Eqs. (A.19) and (A.22). The magnitude of the orbital angular momentum evolves according to $(dL/dt)_{\text{Tide}} = -(dS_p/dt)_{\text{Tide}}$.

A fiducial example of the planetary spin behavior is shown in Fig. 2.3, for the same parameters as in Fig. 2.1. The planet spin period is initialized to $P_p = 10$ hours, and exhibits complex behavior, as it tidally evolves while under the external forcing of the binary companion. During the low- e phase of each LK cycle, the planet spin magnitude remains nearly constant, and then undergoes a rapid “jump” (with $|\Delta P_p|/P_p \ll 1$) during the high- e phases. After many LK cycles, a state of near equilibrium is reached, so that the spin period at low eccentricity returns to nearly the same value after the high- e “jump” (see Fig. 2.4). As the LK cycles begin to be suppressed due to orbital decay, the range of eccentricity narrows (see Section 2.3.1), and the spin period gradually decreases. Once the LK cycles are completely suppressed, the spin period increases and eventually settles to a final value $P_p \simeq 38$ hours, synchronized with the final orbital period

of the planet.

We can understand the behavior of the planetary spin under the influence of LK cycles as follows. The timescale for planetary spin variation due to tidal dissipation is (see Eq. [2.36])

$$t_{\text{spin}} = \left| \frac{\dot{S}_p}{\ddot{S}_p} \right| \sim \frac{S_p}{L} t_a j^{13} \\ \simeq 2.9 \times 10^3 \text{yr} \frac{\bar{k}_p}{\bar{k}_{2p}\chi} \frac{\bar{M}_p \bar{a}^{15/2}}{\bar{M}_\star^2 \bar{M}_{\text{tot}}^{1/2} \bar{R}_p^3} \left(\frac{P_p}{1\text{day}} \right)^{-1} \left(\frac{j}{0.1} \right)^{12}. \quad (2.37)$$

This is much less than the orbital decay circularization timescale due to tides, $t_{\text{circ}} \sim t_a j^{13}$, or the orbital decay time ($\sim t_a j^{15}$) for all values of a and e . Therefore, in the absence of an external perturber (i.e. when the system is governed purely by tidal dissipation), the planetary spin reaches a state of pseudo-synchronization, with

$$\Omega_{p,\text{eq}} = \Omega_{p,\text{pseudo}} = \frac{f_2(e)}{j^3 f_5(e)} n. \quad (2.38)$$

The situation is very different when the planet undergoes LK oscillations driven by an external perturber. The time the planet spends around eccentricity e in each LK cycle is of order $\Delta t_k \sim t_k \sqrt{1 - e^2}$ (see Eqs. [2.3] and [2.31]). Note that the spin evolution timescale t_{spin} (see Eq. [2.37]) depends strongly on eccentricity. During the low-eccentricity phase of the LK cycle, $t_{\text{spin}} \gg \Delta t_k$, so that the spin magnitude remains constant. However, during the brief high-eccentricity phase, t_{spin} can be comparable to Δt_k , and the planetary spin magnitude undergoes a small “jump” $\Delta\Omega_p$. Assuming $|\Delta\Omega_p|/\Omega_p \ll 1$, this jump can be calculated from

$$\frac{\Delta\Omega_p}{\Omega_p} \simeq - \int_{-t_k/2}^{t_k/2} \frac{1}{2t_a j^{13}} \frac{L}{S_p} \left[j^3 f_5(e) \frac{\Omega_p}{n} - f_2(e) \right] dt, \quad (2.39)$$

where $e = e(t)$, and the time integration covers a single LK cycle centered around the eccentricity maximum. On timescales much longer than t_k but

shorter than the orbital decay time, the spin rate approaches a constant value $\Omega_{p,\text{eq}}$, the “Kozai spin equilibrium,” such that $\Delta\Omega_p = 0$. For “canonical” system parameters ($M_p = 1M_J$, $a_0 = 1.5\text{AU}$, $a_b = 200\text{AU}$), and varying initial inclination (corresponding to varying e_{\max}), we determine $\Omega_{p,\text{eq}}$ by adjusting the initial planetary spin rate, integrating for a single LK cycle, and iterating until $\Delta\Omega_p = 0$ in Eq. (2.39). The results are depicted in Figure 2.5. We see that the Kozai spin equilibrium differs from the pseudo-synchronized value at e_{\max} , with the ratio $\Omega_{p,\text{eq}}/\Omega_{p,\text{pseudo}}(e_{\max}) \approx 0.8$.

2.3.4 Limiting Eccentricity and Necessary Conditions for Planet Migration and Disruption

When the octupole potential from the binary companion is neglected, the maximum eccentricity e_{\max} attained by the planet in LK cycles can be determined by the conservation laws discussed in Section 2.3.1. If the initial eccentricity of the planet is close to zero and the initial inclination is $\theta_{\text{lb},0}$, we find (Liu et al. 2015):

$$\begin{aligned} \varepsilon_{\text{GR}} \left(\frac{1}{j_{\max}} - 1 \right) + \frac{\varepsilon_{\text{Tide}}}{15} \left(\frac{1 + 3e_{\max}^2 + \frac{3}{8}e_{\max}^4}{j_{\max}^9} - 1 \right) \\ + \frac{\varepsilon_{\text{Rot}}}{3} \left(\frac{1}{j_{\max}^3} - 1 \right) = \frac{9e_{\max}^2}{8j_{\max}^2} \left(j_{\max}^2 - \frac{5}{3} \cos^2 \theta_{\text{lb},0} \right). \end{aligned} \quad (2.40)$$

The limiting eccentricity e_{\lim} is achieved at $\theta_{\text{lb},0} = 90^\circ$. For $e_{\max} \simeq 1$, we have

$$\frac{\varepsilon_{\text{GR}}}{j_{\lim}} + \frac{7\varepsilon_{\text{Tide}}}{24j_{\lim}^9} \simeq \frac{9}{8}, \quad (2.41)$$

where

$$j_{\lim} \equiv (1 - e_{\lim}^2)^{1/2}, \quad (2.42)$$

and we have neglected the effect associated with the planetary rotational bulge (since it is generally smaller than the tidal term).

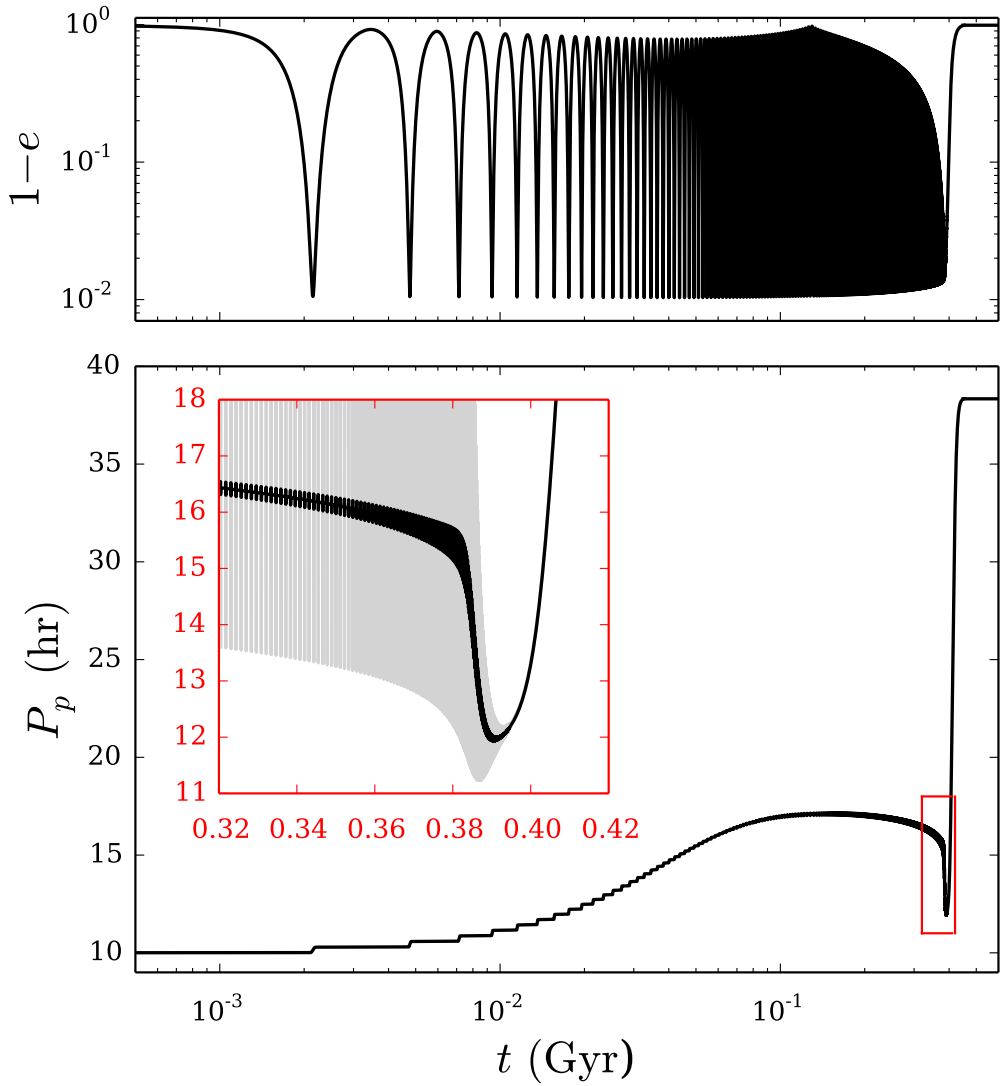


Figure 2.3: Planet spin period as a function of time, for the same parameters shown in Fig. 2.1. For reference, we also show the variation of the orbital eccentricity $1 - e$ (top panel). The planet spin remains constant during the low-eccentricity phase of each LK cycle, and undergoes a rapid “jump” during the brief high-eccentricity phase. The bottom panel shows P_p over the entire evolution (until the LK cycles are suppressed and the semi-major axis decays to the final value), and the inset shows a zoomed-in portion of the spin evolution, as indicated by the red-boxed region ($0.32 \text{ Gyr} \lesssim t \lesssim 0.42 \text{ Gyr}$). On timescales much longer than t_k , but shorter than the orbital decay time, the spin period reaches “Kozai spin equilibrium” (see text). As the LK oscillations are suppressed (see Section 2.3.1), the equilibrium spin period approaches the pseudo-synchronized value (Eq. 2.38), drawn in light-grey in the inset panel.

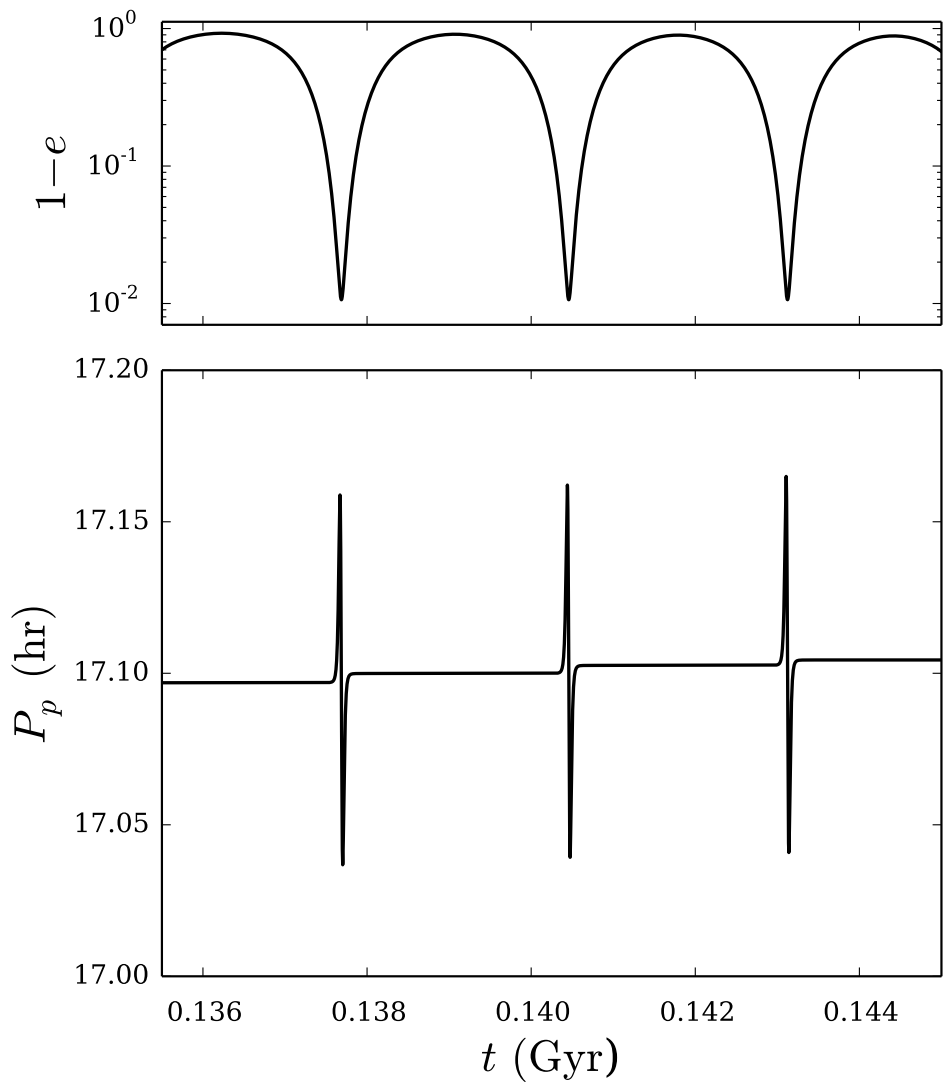


Figure 2.4: Same as Figure 2.3, but showing only three LK cycles, once the planet spin has achieved the “Kozai spin equilibrium” (see text).

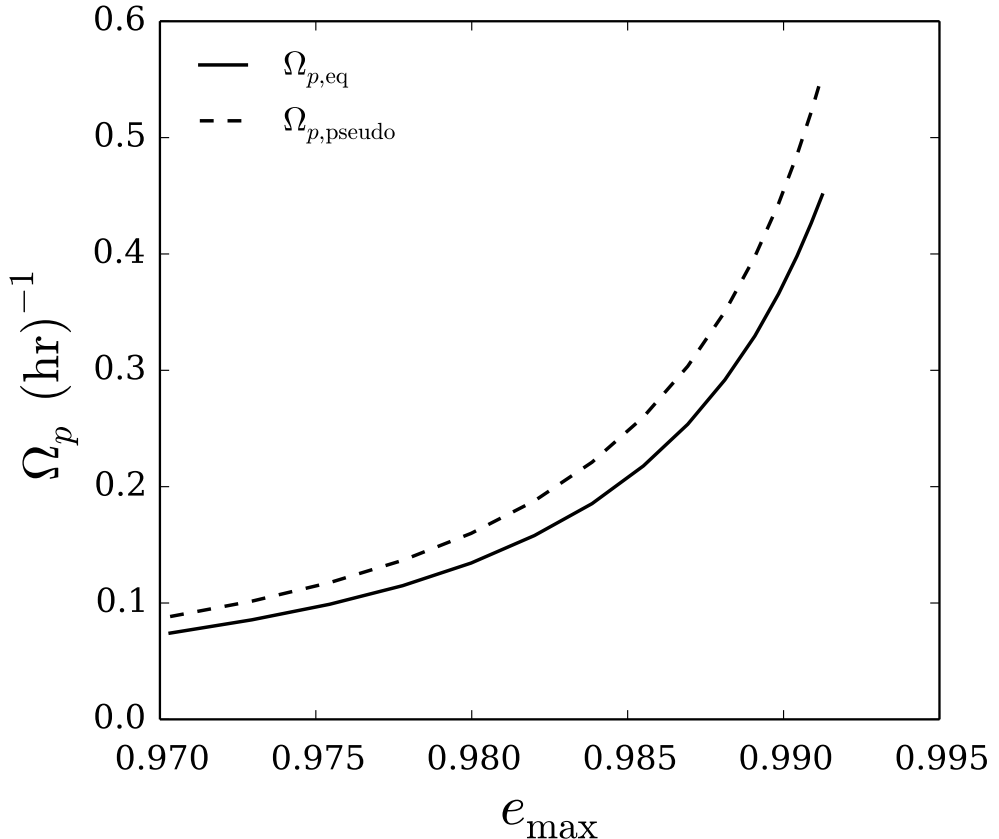


Figure 2.5: “Kozai spin equilibrium rate” rate ($\Omega_{p,\text{eq}}$, solid curve), as a function of e_{\max} , the maximum eccentricity attained in an LK cycle. For comparison, we also plot the pseudo-synchronized rate at e_{\max} ($\Omega_{p,\text{pseudo}}$, dashed curve). We vary the maximum eccentricity by varying the initial inclination $\theta_{\text{lb},0}$, and integrate a set of simplified equations for a single LK cycle (accounting for pericenter precession due to GR and static tides, but neglecting the precession due to planetary rotation). We further ignore orbital decay. Parameters are $M_p = 1M_J$, $a = 1.5\text{AU}$, $a_b = 200\text{AU}$, $e_b = 0$.

When the octupole potential is included, the “Kozai constant” K [Eq. (2.12)] is no longer a constant of motion, thus Eq. (2.40) is not valid. Nevertheless, Liu et al. (2015) show that the limiting eccentricity, as determined by Eq. (6.26) still provides an upper limit to the achievable eccentricity in the LK cycles in the presence of SRFs. The effect of the octupole potential is to make the planet undergo occasional excursion into e_{lim} even when $\theta_{\text{lb},0} \neq 90^\circ$. In general, e_{lim} can be attained for a range of $\theta_{\text{lb},0}$ centered around 90° , with the range becoming wider as the octupole parameter ε_{oct} increases (see Eq. [2.4]).

For a given set of system parameters $(M_\star, M_b, M_p, R_p, a, a_b, e_b)$, Eq. (6.26) determines the limiting eccentricity (or limiting periastron distance $a_{p,\text{lim}} \equiv a[1 - e_{\text{lim}}]$)

$$0.021 \frac{\bar{M}_\star^2 \bar{a}_{b,\text{eff}}^3}{\bar{M}_b \bar{a}_{p,\text{lim}}^{1/2} \bar{a}^{3.5}} + 1.89 \times 10^{-9} \frac{\bar{M}_\star^2 \bar{a}_{b,\text{eff}}^3 \bar{R}_p^5}{\bar{M}_b \bar{M}_p \bar{a}_{p,\text{lim}}^{4.5} \bar{a}^{3.5}} = \frac{9}{8}, \quad (2.43)$$

where we have used Eqs. (2.17) and (2.18). For $j_{\text{lim}} \gtrsim j_{\text{lim},c}$, where

$$j_{\text{lim},c}^2 = \left(\frac{7\varepsilon_{\text{Tide}}}{24\varepsilon_{\text{GR}}} \right)^{1/4} = 3.46 \times 10^{-2} \frac{\bar{R}_p^{5/4}}{\bar{M}_p^{1/4} \bar{a}}, \quad (2.44)$$

the GR effect dominates SRFs, and we have

$$j_{\text{lim}}^2 = 1 - e_{\text{lim}}^2 = 7.1 \times 10^{-4} \left(\frac{\bar{M}_\star^2 \bar{a}_{b,\text{eff}}^3}{\bar{M}_b \bar{a}^4} \right)^2. \quad (2.45)$$

For $j_{\text{lim}} \leq j_{\text{lim},c}$, tides dominate the SRF, and we have

$$j_{\text{lim}}^2 = 1 - e_{\text{lim}}^2 = 2.25 \times 10^{-2} \left(\frac{\bar{M}_\star^2 \bar{R}_p^5 \bar{a}_{b,\text{eff}}^3}{\bar{M}_b \bar{M}_p \bar{a}^8} \right)^{2/9}. \quad (2.46)$$

As discussed in Section 2.3.2, for a planet to migrate, its pericenter distance a_p must be sufficiently small, so that tidal dissipation can damp and circularize the orbit within a few Gyrs. We therefore require $a_{p,\text{lim}} \lesssim a_{p,\text{crit}}$, where $a_{p,\text{crit}}$ is the maximum pericenter distance needed to circularize the orbit within a specified

time frame. Note that $a_{p,\text{crit}}$ depends on the tidal dissipation strength, and therefore is a fuzzy number. However, for reasonable tidal dissipation strengths, and circularization times of a few Gyr or less, $a_{p,\text{crit}} \simeq 0.025$ AU (so that $a_F \lesssim 0.05$ AU). Setting $a_{p,\text{lim}} \lesssim a_{p,\text{crit}}$, a necessary condition for LK migration is

$$\bar{a}_{b,\text{eff}} \lesssim 2.03 \bar{a}^{7/6} \left(\frac{a_{p,\text{crit}}}{0.025 \text{AU}} \right)^{1/6} \left(\frac{\bar{M}_b}{\bar{M}_\star^2} \right)^{1/3} \times \left[1 + 0.23 \frac{\bar{R}_p^5}{\bar{M}_p} \left(\frac{a_{p,\text{crit}}}{0.025 \text{AU}} \right)^{-4} \right]^{-1/3}. \quad (2.47)$$

Note that this is a necessary, but not sufficient condition, because as discussed above, the outer binary must be sufficiently inclined in order for a planet to achieve e_{lim} .

The planet is tidally disrupted if the planet's periastron distance is less than the tidal radius (e.g. Guillot et al., 2011)

$$r_{\text{Tide}} = 2.7 f R_p \left(\frac{M_\star}{M_p} \right)^{1/3}, \quad (2.48)$$

where $f \sim 1$ (we set $f = 1$ for all calculations in this paper). Setting $a_{p,\text{lim}} \leq r_{\text{Tide}}$, we obtain a necessary condition for tidal disruption:

$$\bar{a}_{b,\text{eff}} \leq 1.81 \bar{a}^{7/6} (f \bar{R}_p)^{1/6} \left(\frac{\bar{M}_\star}{\bar{M}_p} \right)^{1/18} \left(\frac{\bar{M}_b}{\bar{M}_\star^2} \right)^{1/3} \times \left(1 + \frac{3.54 \bar{R}_p \bar{M}_p^{1/3}}{f^4 \bar{M}_\star^{4/3}} \right)^{-1/3}. \quad (2.49)$$

Note that since the tidal disruption radius (Eq. [2.48]) is not a precisely defined quantity (the coefficient f has uncertainties, and it depends on the planetary mass-radius relation, which can vary widely for giant planets), there are associated uncertainties in the disruption condition in Eq. (2.49).

Figure 2.6 delineates the parameter space in terms of the initial planet semi-major axis a_0 and effective binary separation $a_{b,\text{eff}}$ for migration and disruption,

as determined from Eqs. (2.47) and (2.49) for various planetary masses. For a given planet mass, the parameter space can be divided into a “Migration Impossible” zone, a “HJ Formation” zone, and a “Disruption Possible” zone. Migration is possible below the solid line when the planet is sufficiently inclined relative to the binary, while below the dashed line, tidal disruption is possible. The “HJ Formation” zone, the region between the solid and dashed lines, narrows substantially with decreasing planet mass, implying that HJ production efficiency should decline with decreasing planet mass. Finally, note that while HJs are never able to form above the solid line, they do occasionally form below the dashed line, for systems where the mutual inclination is not high enough to result in tidal disruption. Therefore, while the upper boundary (solid line) of the HJ formation zone is robust, the lower boundary is somewhat uncertain. However, the vast majority of HJs will reside in the region between the solid and dashed lines.

Further discussion of the planet migration and disruption fractions can be found in Section 2.5.4.

2.3.5 Freezing of Spin-Orbit Angle

The evolution of the spin-orbit angle θ_{sl} is complex. Here we examine how θ_{sl} is frozen into its final value near the end of the LK migration.

As shown in Storch & Lai (2015) (hereafter SL15), the dynamics of the stellar spin axis $\hat{\mathbf{S}}_*$ relative to the planet’s orbital axis $\hat{\mathbf{L}}$ depends on three dimension-

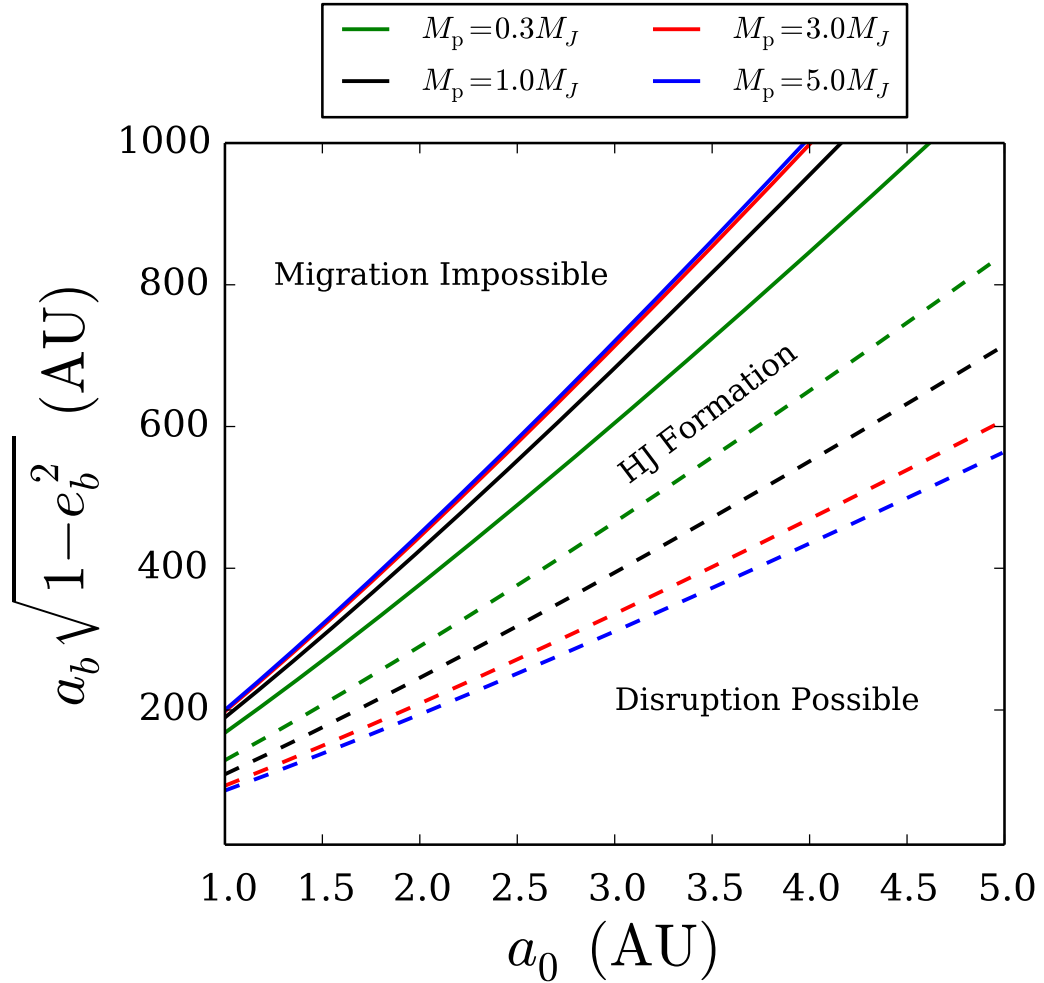


Figure 2.6: Boundaries in $(a_0, a_{b,\text{eff}})$ parameter space for migration (solid lines), and tidal disruption (dashed lines). The migration and disruption boundaries are determined by Eq. (2.47) (with $a_{p,\text{crit}} = 0.025$ AU) and Eq. (2.49) (with $f = 1$) for several planet masses (as indicated by the color). For each planet mass, migration is impossible (for all initial planet-outer binary inclinations) above the solid line, and tidal disruption is impossible above the dashed line. Below the solid (dashed) line, migration (disruption) is possible (depending on the binary inclination), but not guaranteed. HJ formation only occurs below the solid line, and is usually, but not always, confined to the region between the solid and dashed lines.

less ratios

$$\epsilon\beta = -\frac{\Omega_{\text{pl}}}{\alpha} \sin \theta_{\text{lb}}, \quad (2.50)$$

$$\epsilon\gamma = \frac{\dot{\theta}_{\text{lb}}}{\alpha}, \quad (2.51)$$

$$\epsilon\psi = -\frac{\Omega_{\text{pl}}}{\alpha} \cos \theta_{\text{lb}}, \quad (2.52)$$

where we have defined the function α via

$$\Omega_{\text{ps}} = -\alpha \cos \theta_{\text{sl}}, \quad (2.53)$$

and the dimensionless parameter ϵ is defined by

$$\epsilon = \left| \frac{\Omega_{\text{pl}}}{\alpha} \right|_{e=0}. \quad (2.54)$$

The parameter ϵ is related to the “adiabaticity parameter” \mathcal{A}_0 [see Eq. (2.11)] by $\epsilon = \mathcal{A}_0^{-1} |\cos \theta_{\text{sl},0} / \sin \theta_{\text{lb},0}|$. In general β, γ, ψ are strong functions of time, with the period given by the LK period of the eccentricity variation (when neglecting the feedback effect of the stellar spin on the orbit and the dissipative effect). They can be decomposed into various Fourier components, each giving rise to a resonance (see SL15). Near the end of LK migration, the amplitude of the eccentricity oscillation becomes small (see Section 2.3.1). So when θ_{sl} begins to freeze, the dynamics of $\hat{\mathbf{S}}_*$ is dominated by the $N = 0$ (time-independent) components ($\bar{\beta}$ and $\bar{\psi}$, with $\bar{\gamma} = 0$). Thus, the effective Hamiltonian for the stellar spin axis is (see Eq. [53] of SL15)

$$H = -\frac{1}{2}p^2 + \epsilon \bar{\psi} p - \epsilon \sqrt{1-p^2} \bar{\beta} \cos \phi, \quad (2.55)$$

where $p = \cos \theta_{\text{sl}}$ and ϕ (the phase of precession of $\hat{\mathbf{S}}_*$ around $\hat{\mathbf{L}}$) are the conjugate canonical variables.

Since H is time-independent, the range of variation of p can be derived from

energy conservation. Suppose $p = p_F$ at $\phi = \pi/2$. For $\epsilon \ll 1$, we find

$$p \simeq p_F - \frac{\epsilon \bar{\beta} \sqrt{1 - p_F^2}}{p_F} \cos \phi. \quad (2.56)$$

Thus the spread (full width) of θ_{sl} as ϕ circulates between 0 and 2π is

$$\Delta\theta_{\text{sl}} \simeq \frac{2\epsilon \bar{\beta}}{|\cos \theta_{\text{sl},F}|} = \frac{2}{\mathcal{A}_F}, \quad (2.57)$$

where

$$\mathcal{A}_F \equiv \frac{\langle |\Omega_{\text{pl}}| \rangle}{\langle |\Omega_{\text{pl}} \sin \theta_{\text{lb}}| \rangle}. \quad (2.58)$$

The bracket $\langle \dots \rangle$ in Eq. (2.58) indicates time averaging over the small “residual” LK oscillations. If the eccentricity variation is “frozen” or has small amplitude, then the averaging is unnecessary and \mathcal{A}_F is the same as \mathcal{A} defined in Eq. (6.37). Thus, in order for the spin-orbit angle to freeze at $\theta_{\text{sl},F}$ to within $\Delta\theta_{\text{sl}}$ (e.g., 2°) requires

$$\mathcal{A} \gtrsim 60 \left(\frac{\Delta\theta_{\text{sl}}}{2^\circ} \right)^{-1}. \quad (2.59)$$

2.4 Paths Toward Misalignment

In this section we present a series of numerical experiments to illustrate various paths of spin-orbit evolution during LK migration. These will be useful for understanding our population synthesis results of the final spin-orbit angles for HJs in Section 2.5. The theoretical basis for these different evolutionary paths is presented in Storch et al. (2017).

2.4.1 Effects of Varying Stellar Spin Rate

To isolate the effects of the stellar spin dynamics, and highlight the importance of the stellar spin properties on the final spin-orbit angle, we first ignore the feedback of the stellar spin on the planetary orbit (thus ignoring the mutual precession of \mathbf{S}_* and \mathbf{L}). Possible types of evolution are illustrated in Figs. 2.7 and 2.8. In both figures, we vary the stellar spin period while keeping all other system parameters constant. Figure 2.7 presents an example of chaotic spin evolution: three closely spaced values of the stellar spin period result in very different spin evolutions and final spin-orbit misalignments. Figure 2.8 presents three different types of non-chaotic spin evolution, only two of which are able to generate spin-orbit misalignment.

The leftmost panel (with $P_* = 30$ days) of Fig. 2.8 (with θ_{sl} in the middle row) shows an example of non-adiabatic spin behavior. Here, the spin-orbit misalignment angle θ_{sl} evolves slowly, with step-like changes corresponding to LK eccentricity maxima, during which the spin evolves the most rapidly. Since the planet orbit changes much faster than the spin can respond, the spin axis effectively precesses about the time average of the planet orbital angular momentum vector.

On the opposite end of the spectrum, the middle panel of Fig. 2.8 (with $P_* = 7.07$ days) is an example of adiabatic spin behavior. Here, the stellar spin axis evolves quickly enough that it easily “keeps up” with the planet angular momentum vector, and hence θ_{sl} is approximately conserved, making it difficult to generate misalignment.

The rightmost panel of Fig. 2.8 (with $P_* = 1.67$ days) shows a more compli-

cated variation of the adiabatic evolution, which we term “adiabatic advection”. As discussed in detail in SL15, the adiabatic regime of stellar spin evolution is governed by a set of resonances between the time-averaged spin precession rate and the mean LK oscillation rate. Under certain conditions, it is possible for a trajectory to become trapped inside one of the resonances. As tidal dissipation acts to make the system even more adiabatic, the resonance moves in phase space, dragging the trajectory with it and thus generating misalignment. We discuss and clarify the mechanism of this phenomenon in Storch et al. (2017).

Fig. 2.9 presents final spin-orbit angles $\theta_{\text{sl},f}$ for many different values of the stellar spin period, for three different orbital evolutions (characterized by different initial inclinations $\theta_{\text{lb},0}$). This illustrates the role of the adiabaticity parameter \mathcal{A}_0 (see Eq. [2.11]) in determining which of the four types of evolution the spin-orbit angle undergoes. For low values of \mathcal{A}_0 , chaotic and regular non-adiabatic behaviors are prevalent. For intermediate values, e.g. $10 \lesssim \mathcal{A}_0 \lesssim 100$ in the rightmost panel, adiabatic advection dominates, with each of the striated lines corresponding to adiabatic advection by resonances of different orders (see Storch et al., 2017). For $\mathcal{A}_0 \gtrsim 100$, stationary adiabatic behavior prevails. Thus, \mathcal{A}_0 can be used as an indicator for the behavior of a system with a particular set of initial conditions.

2.4.2 Effects of Varying Inclination

In this subsection we take a different tack and examine the effect of varying the initial planet orbit inclination θ_{lb} , for different values of the stellar spin period and the planet mass. As before, we continue to ignore the back-reaction torque

the star exerts on the planet orbit. Fig. 2.10 demonstrates that changing the initial inclination effectively changes \mathcal{A}_0 , and thus systems with different initial inclinations can also exhibit the different behaviors shown in Figs. 2.7 and 2.8 of Section 2.4.1. In particular, the three columns of Fig. 2.10 correspond to chaotic evolution (left panels), adiabatic advection (middle panels), and an extreme case of stationary adiabatic evolution (right panels).

In Fig. 2.11 we show the dependence of the final spin-orbit misalignment angle on the initial inclination, for several combinations of planet mass and stellar spin period. As expected, chaotic behavior occurs mainly at lower initial inclinations (less adiabatic – see the right two panels of Fig. 2.11). We note, however, that despite spanning approximately the same range of \mathcal{A}_0 , heavier planets are much more likely to produce chaotic behavior than lower-mass planets - this implies that \mathcal{A}_0 is not the only parameter governing the evolution of θ_{sl} (Storch et al., 2017). Stationary adiabatic behavior manifests here as the “tail” of the distributions at higher initial inclinations, e.g. between 88.5° and 90° in the top left panel, and near 90° in the bottom right panel. The long stretches of nearly-constant $\theta_{\text{sl},f}$ present in the higher-mass (more adiabatic) panels are due to adiabatic advection.

The non-adiabatic behavior regime shown in Fig. 2.8 (left panels) manifests here as a bimodal split in $\theta_{\text{sl},f}$ (see the left two panels of Fig. 2.11). This bimodality is the result of a bifurcation phenomenon that occurs at the moment the system transitions from being non-adiabatic to being adiabatic (due to the orbital decay from tidal dissipation). Before the transition, the system undergoes wide $0 - 180^\circ$ degree oscillations in θ_{sl} ; after the transition, the system must evolve adiabatically and be confined either above or below $\theta_{\text{sl}} = 90^\circ$. The tran-

sition between these two states is akin to a bifurcation. We illustrate this in Fig. 2.12 by showing the time evolution of two trajectories with nearly identical initial conditions. Unlike the previous chaotic examples shown (with positive Lyapunov exponents) the trajectories in Fig. 2.12 do not quickly diverge, but rather remain qualitatively similar while accumulating some phase difference. This phase difference, if pronounced enough, leads to a bifurcation in the final spin-orbit angle. We discuss this phenomenon in detail in Storch et al. (2017).

In summary, the evolution of the spin-orbit misalignment angle can proceed in four distinct ways. (i) *Chaotic*. Neighboring spin trajectories diverge exponentially and $\theta_{\text{sl},f}$ is very sensitive to initial conditions. (ii) *Regular non-adiabatic*. θ_{sl} initially undergoes wide, regular $0 - 180^\circ$ oscillations. After significant semi-major axis decay has occurred, the evolution of θ_{sl} undergoes a bifurcation and becomes confined either above or below 90° degrees. This leads to the bimodality seen in Fig. 2.11 (left panels). (iii) *Stationary adiabatic*. θ_{sl} is approximately conserved and no misalignment can be generated. (iv) *Adiabatic advection*. The phase space trajectory becomes trapped in a resonance and advected to higher misalignments. $\theta_{\text{sl},f}$ depends sensitively on the stellar spin period (Fig. 2.9, right panel), but only weakly on the initial inclination (Fig. 2.11, right panels).

2.4.3 Effects of the Backreaction Torque from the Stellar Quadrupole on the Orbit

All examples in Sections 2.4.1 and 2.4.2 have neglected the backreaction torque from the stellar quadrupole on the planet’s orbit, in order to simplify the analysis of the spin-orbit dynamics. However, under some conditions, the backre-

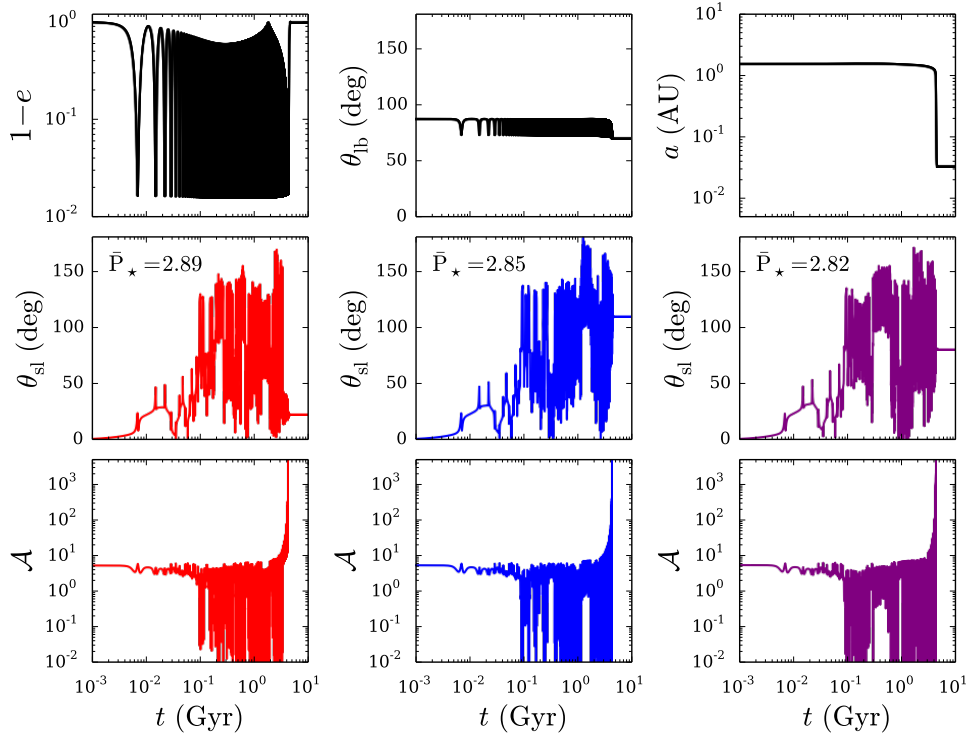


Figure 2.7: Examples of chaotic evolution for three values of the stellar spin period (in days) as labeled, neglecting the feedback torque from the stellar quadrupole on the orbit. Without feedback, the orbital evolution for each system is identical (shown in the top panels), while the spin-orbit angle settles to a final value that is highly sensitive to the initial conditions. The adiabaticity parameter \mathcal{A} is defined in Eq. (6.37). Parameters are $M_p = 5M_J$, $a_0 = 1.5$ AU, $a_b = 300$ AU, $e_b = 0$, $\theta_{lb,0} = 87^\circ$.

action torque can significantly affect the evolution of the spin-orbit misalignment. In the following discussion, we show how including this torque affects (and complicates) the dynamics, and delineate the parameter space where this torque can compete with the torque from the binary companion in changing the orbital axis.

The stellar quadrupole has two effects on the planetary orbit. First, it

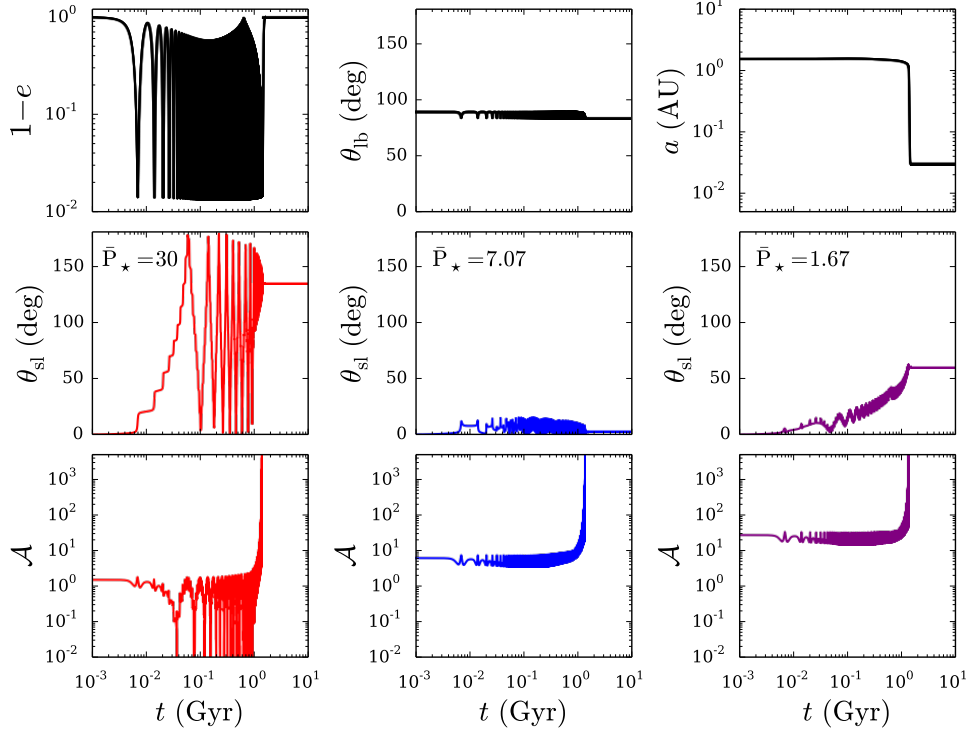


Figure 2.8: Examples of possible non-chaotic evolution of the spin-orbit angle, depending on the stellar spin rate. As in Fig. 2.7, feedback has been neglected, so that the orbital evolution, shown in the top row, is identical for all three examples: Non-adiabatic with $P_\star = 30$ days (left), stationary adiabatic with $P_\star = 7.07$ days (middle), and adiabatic advection with $P_\star = 1.67$ days (right). Parameters are $M_p = 5M_J$, $a_0 = 1.5$, $a_b = 300$ AU, $e_b = 0$, $\theta_{lb,0} = 89^\circ$.

changes the direction of the angular momentum axis $\hat{\mathbf{L}}$ at the rate given by

$$\frac{d\hat{\mathbf{L}}}{dt} \Bigg|_{SL} = \Omega_{ps} \frac{S_\star}{L} \hat{\mathbf{S}}_\star \times \hat{\mathbf{L}} \propto M_\star^{-1/2} R_\star^5 \Omega_\star^2. \quad (2.60)$$

Second, it causes the eccentricity vector \mathbf{e} to precess around $\hat{\mathbf{L}}$,

$$\frac{d\mathbf{e}}{dt} \Bigg|_{SL,rot} = \frac{\dot{\omega}_\star}{2} (5 \cos^2 \theta_{sl} - 1) \hat{\mathbf{L}} \times \mathbf{e} \quad (2.61)$$

where

$$\dot{\omega}_\star = - \frac{S_\star}{L} \frac{\Omega_{ps}}{\cos \theta_{sl}}. \quad (2.62)$$

The subscript ‘‘rot’’ in Eq. (2.61) implies that the time derivative is done in the frame rotating with the nodal precession of the orbit (at the rate $\Omega_{ps} S_\star / L$), so that

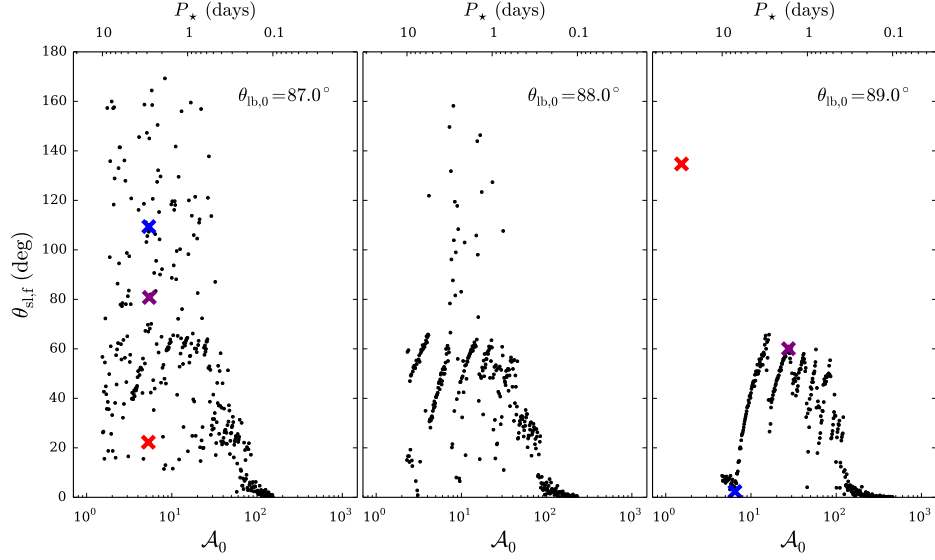


Figure 2.9: The final spin-orbit angle $\theta_{\text{sl},f}$ (for systems with planets that undergo inward migration to produce hot Jupiters) as a function of the adiabaticity parameter A_0 . Here, we vary A_0 by varying $P_\star = 0.1 - 10$ days (as depicted on the upper x-axis). Results are shown for initial inclinations $\theta_{\text{lb},0} = 87^\circ$ (left), 88° (middle), and 89° (right). The colored marks correspond to the time evolution presented in Fig. 2.7 and 2.8. As the initial inclination increases, the adiabaticity parameter A_0 increases, leading to systems with a smaller spread in $\theta_{\text{sl},f}$. Parameters are $M_p = 5M_J$, $a_0 = 1.5$, $a_b = 300$ AU, $e_b = 0$, no feedback.

$\hat{\mathbf{L}}$ is fixed in space (compare Eq. [2.61] with Eq. [A.7]). The effect of the stellar quadrupole on the eccentricity vector does not introduce any new features in the orbital evolution, but simply contributes to the rate of pericenter precession due to other SRFs (GR, tidal and rotational distortions of the planet). By contrast, the effect on the orbital axis $\hat{\mathbf{L}}$ does directly change θ_{lb} , thereby influencing the evolution of the spin-orbit angle.

Consider now the change in θ_{lb} due to the backreaction torque of the stellar quadrupole (Eq. [2.60]). The maximum possible change is

$$\begin{aligned} (\Delta\theta_{\text{lb}})_{\text{max}} &\sim \left(\frac{S_\star}{L} \right)_{e_{\text{max}}} \\ &\simeq 0.12 \frac{\bar{k}_\star \bar{M}_{\text{tot}}^{1/2} \bar{R}_\star^2}{\bar{M}_p} \left(\frac{\bar{a}_F}{0.05} \right)^{-1/2} \left(\frac{P_\star}{30 \text{ days}} \right)^{-1}, \end{aligned} \quad (2.63)$$

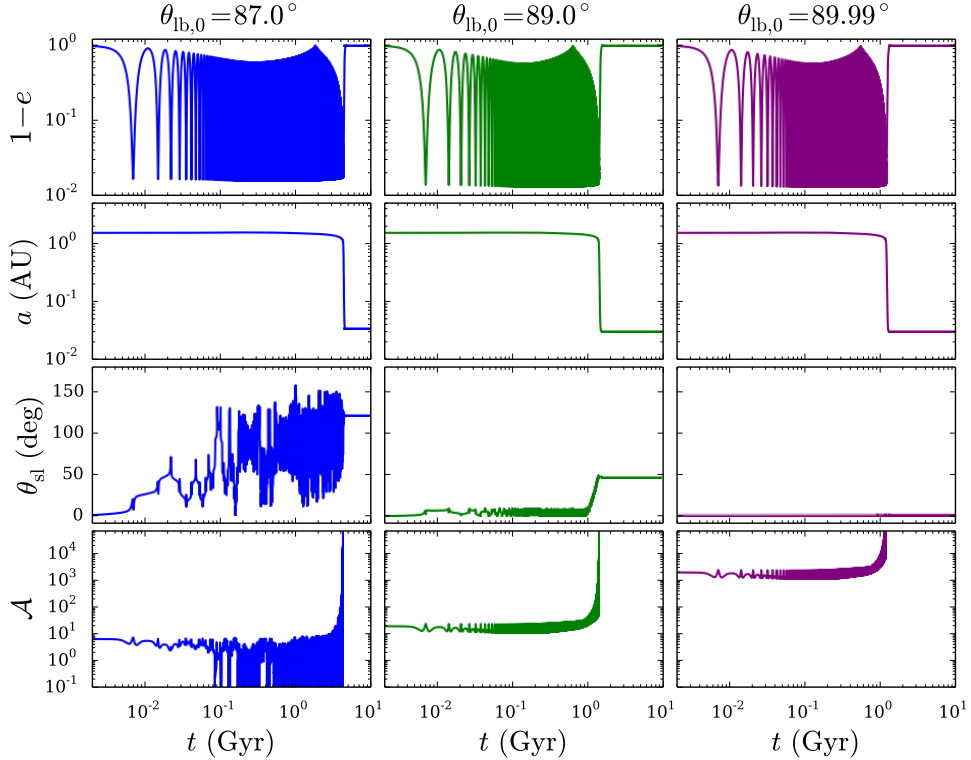


Figure 2.10: Examples of possible evolution of the spin-orbit angle, depending on the initial inclination. All examples have $M_p = 5M_J$, $a_0 = 1.5$ AU, $a_b = 300$ AU, $P_\star = 2.3$ days, and the feedback torque from the stellar quadrupole has been neglected. The system with $\theta_{lb,0} = 87^\circ$ (left panels) has $\mathcal{A}_0 \lesssim 10$, sufficiently low to generate large spin-orbit misalignments. The system with $\theta_{lb,0} = 89^\circ$ (middle panels) has $\mathcal{A}_0 \gtrsim 10$, sufficiently high to preserve the initially low misalignment, but eventually undergoes adiabatic advection (see text). The extreme example shown on the right with $\theta_{lb,0} = 89.99^\circ$ has $\mathcal{A}_0 \gtrsim 10^3$, so that θ_{sl} is very nearly constant for all time.

assuming $L \gtrsim S_\star$. The actual change of θ_{lb} in an LK cycle can be obtained by integrating Eq. (2.60) through time t_k around the eccentricity maximum, yielding

$$\begin{aligned}
(\Delta\theta_{lb})_{\text{actual}} &\sim \left(\left| \frac{d\hat{\mathbf{L}}}{dt} \right| \Delta t \right)_{e_{\max}} \\
&\sim \left(|\Omega_{ps}| \frac{S_\star}{L} \right)_{e_{\max}} t_k \sqrt{1 - e_{\max}^2} \\
&\simeq 0.1 \frac{\bar{k}_q \bar{R}_\star^5 \bar{M}_{\text{tot}} \bar{a}_{b,\text{eff}}^3}{\bar{M}_b \bar{M}_\star \bar{a}^{7/2}} \left(\frac{\bar{a}_F}{0.05} \right)^{-3/2} \left(\frac{P_\star}{6\text{days}} \right)^{-2}
\end{aligned} \tag{2.64}$$

where we have used Eq. (2.31) for $\Delta t(e_{\max})$. Note that $(\Delta\theta_{lb})_{\text{actual}}$ is also approx-

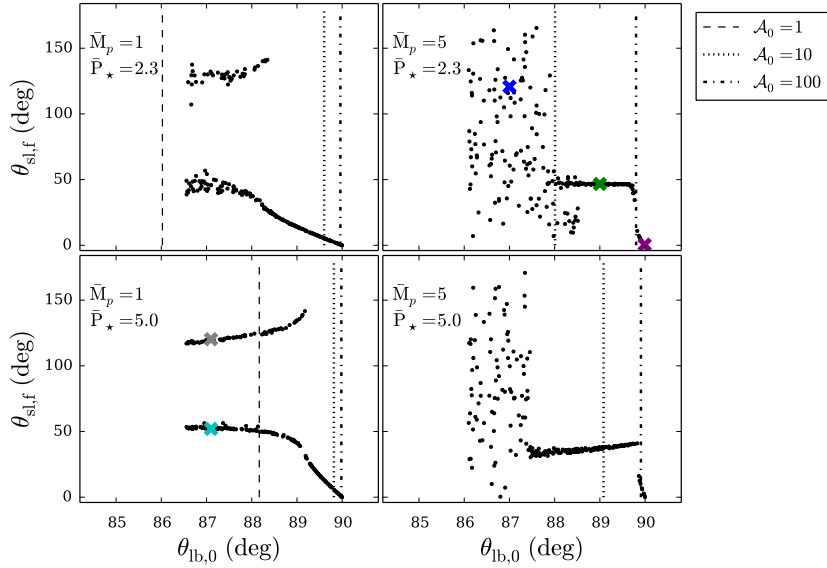


Figure 2.11: Final spin orbit misalignments as a function of the initial inclination, for various combinations of planet mass and (constant) stellar spin period, as labeled. In this example, we neglect the feedback torque from the stellar quadrupole on the planetary orbit. We indicate various benchmark values of \mathcal{A}_0 by the vertical lines. The colored crosses correspond to the time evolution presented in Fig. 2.10 (upper right panel), and Fig. 2.12 (lower left panel). Parameters are $a_0 = 1.5$ AU, $a_b = 300$ AU, $e_b = 0$.

imately equal to the ratio between $|d\hat{\mathbf{L}}/dt|_{\text{SL}}$ and $|d\hat{\mathbf{L}}/dt|_{\text{LK}}$. Eq. (2.64) assumes $\Delta\theta_{\text{lb,actual}} \lesssim \Delta\theta_{\text{lb,max}}$. That is, the actual change in θ_{lb} due to the backreaction torque is given by Eq. (2.63) or Eq. (2.64), whichever is smaller.

We have already seen from Fig. 2.11 that the final spin-orbit misalignment can depend strongly on $\theta_{\text{lb},0}$. We expect that the backreaction torque will significantly affect $\theta_{\text{sl,f}}$ when $(\Delta\theta_{\text{lb}})_{\text{actual}} \gtrsim 0.1$. Eqs. (2.63) and (2.64) indicate that this condition is satisfied for $P_★ \lesssim$ a few days, depending on various parameters (such as $a_{b,\text{eff}}$ and M_p). Fig. 2.13 shows $\theta_{\text{sl,f}}$ as a function of $\theta_{\text{lb},0}$ for several values of $P_★$ and M_p , with the backreaction torque included in the calculations (cf. Fig. 2.11, which neglects the backreaction torque).

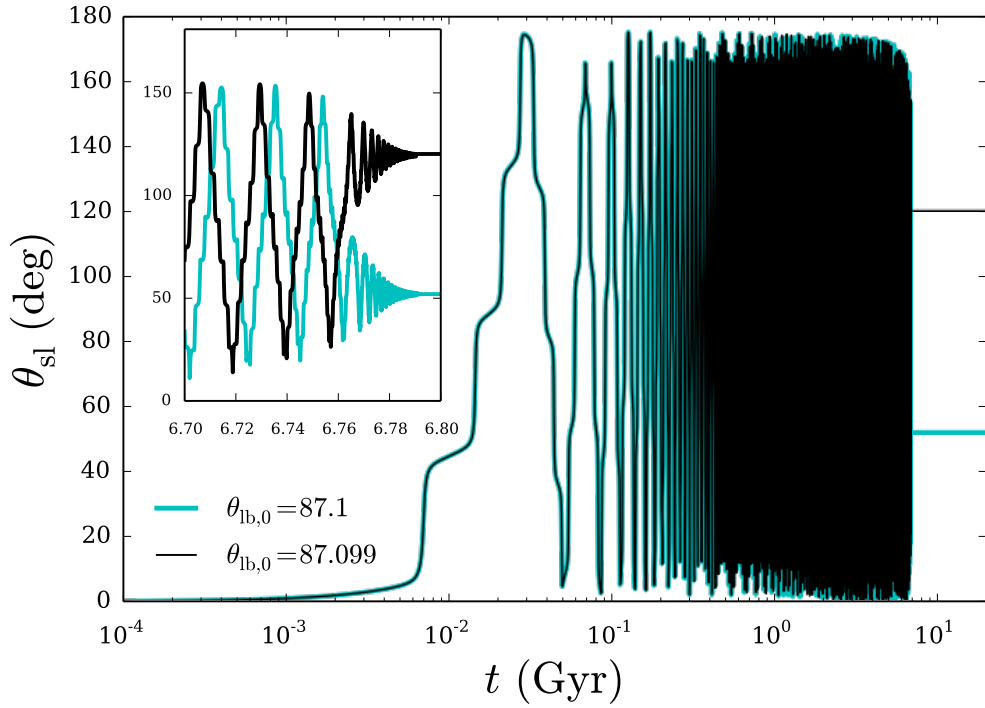


Figure 2.12: Time evolution for two systems with very similar initial inclinations, illustrating the bimodality in the final misalignment angle, as depicted in the lower left panel of Figure 2.11. Parameters are $M_p = 1M_J$, $P_\star = 5$ days, $a_b = 300$ AU, no feedback. Nearly identical initial inclinations accumulate some phase difference over the course of the evolution, which at the moment of transition to the adiabatic regime, give rise to different final angles, with $\theta_{lb,f} \approx 52^\circ$ and 120° .

Comparing Figs. 2.11 and 2.13 reveals the main effects of the backreaction torque on the final spin-orbit angle. Systems with the lowest planet mass and shortest spin period ($M_p = 1M_J$, $P_\star = 2.3$ days, top left) are most strongly affected by feedback, and the clean bimodality present in $\theta_{sl,f}$ in Fig. 2.11 is erased, and replaced by clustering near $\theta_{sl,f} \sim 90^\circ$. The results for the large planet mass and short spin period ($M_p = 5M_J$, $P_\star = 2.3$ days, top right) are also significantly affected, due to planets becoming tidally disrupted at high inclinations. The systems with longer stellar spin periods (bottom panels) are less affected by

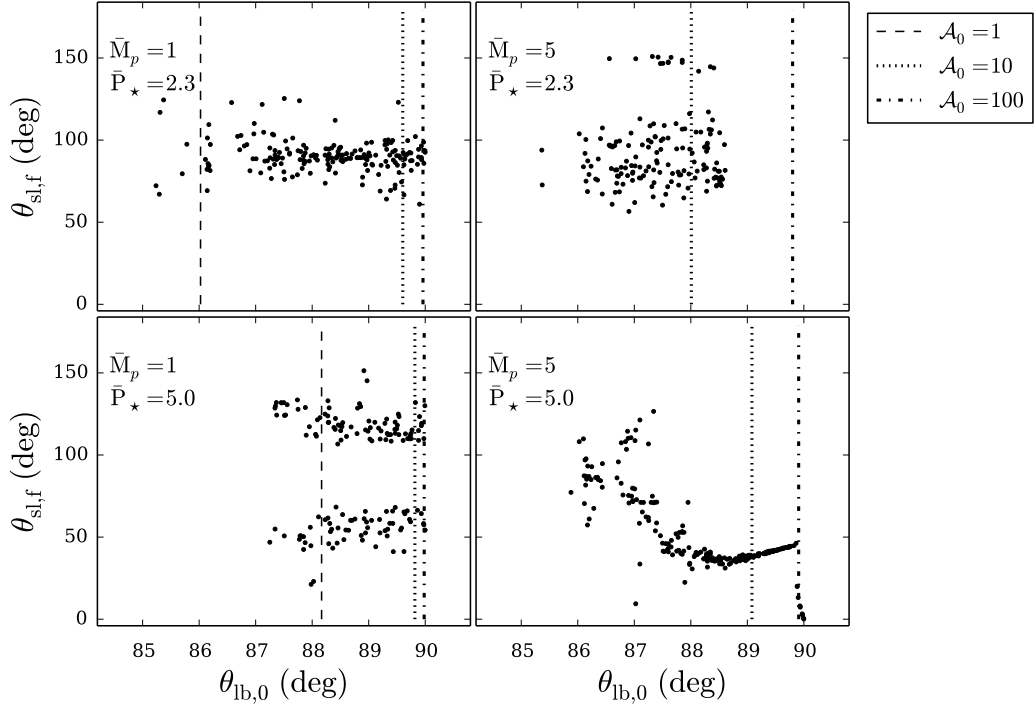


Figure 2.13: Same as Fig. 2.11, but including feedback from the stellar quadrupole on the orbit.

feedback, and the general structure found in Fig. 2.11 is partially preserved.

2.5 Population Synthesis

2.5.1 Setup and Computational Procedure

In this section we perform a detailed parameter space survey for giant planets undergoing LK migration, exploring the dependence of the final spin-orbit misalignment angle distribution on the planet mass and stellar spin properties. We focus on two types of host stars: a solar-mass ($M_\star = 1M_\odot$, spectral type G) star, and a massive ($M_\star = 1.4M_\odot$, spectral type F) star. The initial spin period of both

types of stars is set to $P_\star = 2.3$ days, corresponding to 5% of breakup for the G star; both stars subsequently spin-down according to the Skumanich law (see Section 2.2.1). The G (F) star is calibrated to reach a spin period of 28 (9) days after 5 Gyr, to account for the fact that massive stars are observed to rotate more rapidly at a given age (e.g. McQuillan et al., 2014). The stellar radius is set to $R_\star = 1R_\odot$ for G-type stars, and $R_\star = 1.26R_\odot$ for F-type stars. We consider four planet masses ($M_p = 0.3, 1, 3$, and $5M_J$), all having a radius $R_p = 1R_J$. Note that this is a simplification, as some observed close-in gas giant planets are found to be inflated in size, while others are more compact (e.g. Laughlin et al., 2011).

We integrate the full equations of motion for the planetary orbit, including the octupole terms from the stellar companion, feedback torque from the host stellar spin, and all short-range forces, together with evolution equations for the host stellar spin, and the planetary spin rate (due to tidal dissipation). As in previous population studies (Naoz et al., 2012; Petrovich, 2015b), systems that do not obey the stability condition (Mardling & Aarseth, 2001)

$$\frac{a_b}{a} > 2.8 \left(1 + \frac{M_b}{M_{\text{tot}}}\right)^{2/5} \frac{(1 + e_b)^{2/5}}{(1 - e_b)^{6/5}} \left[1 - 0.3 \frac{\theta_{lb,0}}{180^\circ}\right] \quad (2.65)$$

are discarded. To increase the efficiency of the parameter survey, for each integration we adopt the following stopping conditions:

1. If after 500 LK timescales (Eq. [2.3]) the pericenter distance has never reached $r_p = a(1 - e) < 0.07$ AU, we terminate the calculation to avoid unnecessary integrations, and classify the planet as non-migrating. The time needed for such planets to undergo significant orbital decay is greater than $\sim 10^{11}$ years (see Section 2.3.2, Eq. [2.32]). This is far too long to allow significant migration within the lifetime of the host star.³

³Note that with the octupole terms from the binary companion included, the planet can

2. If at any point the pericenter distance $r_p = a(1-e) < r_{\text{Tide}}$, where r_{Tide} is the tidal disruption radius, given in Eq. (2.48), we terminate the integration, and classify the planet as tidally disrupted.
3. If the semi-major axis has decayed to $a < 0.1$ AU, we terminate the integration and classify the planet as a hot Jupiter. In such cases, the spin-orbit angle has always safely reached the adiabatic regime (so that the adiabaticity parameter \mathcal{A} has become sufficiently large), with $\hat{\mathbf{S}}_*$ and $\hat{\mathbf{L}}$ undergoing mutual precession, and θ_{sl} is nearly constant, varying by less than 1° . At this point, LK oscillations from the binary companion are completely suppressed (see Section 2.3.1), and the planet will continue to undergo pure tidal evolution at nearly constant angular momentum, with final semimajor axis $a_f \simeq a(1 - e^2)$, where a and e are evaluated at the point at which the integration is stopped.
4. If none of these conditions are satisfied during the integration, we terminate the integration at $t = 5$ Gyr and classify the planet as non-migrating.

For each set of system parameters, we begin by integrating the full equations of motion. However, in situations where the planet experiences sufficient orbital decay, the LK oscillations become suppressed so that the range of eccentricity variation narrows, and the stellar spin axis enters the adiabatic regime where $\theta_{\text{sl}} \approx \text{constant}$ (see Sections 2.3.1 and 2.3.5). In such cases, the eccentricity vector \mathbf{e} precesses much more rapidly compared to the tidal decay rate. Resolving this

achieve extreme values of eccentricity e_{lim} when $\theta_{\text{lb},0}$ is sufficiently large (see Section 2.3.4). Although these octupole extreme eccentricities are nearly always achieved sooner than $500t_k$ (depending on ε_{oct} , see Liu et al. 2015), the possibility of the planet achieving such a high eccentricity cannot be ruled out for $t > 500t_k$. We therefore run the risk of terminating systems that might later undergo orbital decay. However, note that in such cases, the eccentricity usually becomes so high that the planet would be tidally disrupted, and removed from the sample of HJs. We have tested this stopping criterion and found that the approximation causes a very small fraction of tidally disrupted planets to be misclassified as non-migrating, but the fraction of HJs is unaffected.

rapid precession is computationally expensive, but does not influence the final result. Therefore, once the LK eccentricity oscillations and spin-orbit angle have both “frozen” we stop following the eccentricity precession (i.e. by neglecting the SRF and LK terms in the planet’s equations of motion), and allow the orbit to evolve purely under tidal dissipation.⁴

We assume that the initial planet orbital axis $\hat{\mathbf{L}}$ is isotropically distributed with respect to $\hat{\mathbf{L}}_b$. In principle, the initial inclination should be sampled over the entire range ($\theta_{lb,0} = [0^\circ, 90^\circ]$).⁵ In practice however, we explore a limited range of $\theta_{lb,0}$ to avoid unnecessary computation for planets that have no chance of migrating. Note that systems with inclinations $\theta_{lb,0} \lesssim 40^\circ$ (the critical “Kozai angle”) can be safely excluded, because they do not undergo large excursions in eccentricity. We find empirically that systems with $\theta_{lb,0} \lesssim 65^\circ$ rarely reach sufficiently high eccentricities to induce tidal migration. In the rare cases where migration occurs, the system always results in tidal disruption, rather than HJ formation. We therefore restrict the inclination to lie in the range $65^\circ \leq \theta_{lb,0} \leq 90^\circ$.

Of primary interest in this paper is the fraction of total systems that result in the production of an HJ or tidal disruption, for fixed planet mass and stellar type, and considering the full possible ranges of $(\theta_{lb,0}, a, a_b, e_b)$. For a given combination of host star properties and planet mass, we run N_{run} trials (typically ~ 9000) by repeatedly sampling the inclination randomly from the restricted

⁴In practice, we consider the e -oscillations to have frozen when $\varepsilon_{\text{GR}} > 30$, and θ_{sl} to have settled to its final value when the adiabaticity parameter satisfies $\mathcal{A}_0 \sin 2\theta_{lb} > 5$ (see Sections 2.3.1 and 2.3.5). We have tested both conditions extensively and find they are extremely conservative estimates, so that the LK oscillations and variation in θ_{sl} are always safely quenched at the point when the SRF and LK terms are neglected in the equations of motion.

⁵Since $M_p \ll M_\star, M_b$, the triple systems considered here exhibit symmetry around $\theta_{lb,0} = 90^\circ$, so that $90^\circ \leq \theta_{lb,0} \leq 180^\circ$ need not be considered (e.g. Liu et al., 2015).

range ($65^\circ \leq \theta_{lb,0} \leq 90^\circ$)⁶. The fractions of HJ formation and tidal disruption can be obtained from $f_{HJ} = \cos 65^\circ N_{HJ}/N_{\text{run}}$ and $f_{\text{dis}} = \cos 65^\circ N_{\text{dis}}/N_{\text{run}}$, where N_{HJ} and N_{dis} are the number of systems among N_{run} runs that resulted in HJs and tidal disruptions.

The ultimate goals of this section are to present distributions of final stellar spin-orbit angles, and obtain the fractions of total systems that result in HJs and disruptions for a given planet mass and stellar type, sampling over the entire possible ranges of a, a_b, e_b . However, we begin by fixing $e_b = 0$, thereby eliminating complications introduced by octupole terms. Section 2.5.2 shows results for fixed binary separation a_b and planet semimajor axis a , in order to isolate and highlight the effects of changing the planet mass and stellar mass/spin properties. Next, Section 2.5.3 presents results for non-zero binary eccentricity (with fixed a_b and a), thus showing how the octupole term in the disturbing potential of the binary companion can affect the results. Finally, in Section 2.5.4, we randomly sample over a wide range in (a, a_b, e_b) parameter space, and present results appropriate for comparison with the observational sample of close-in giant planets.

2.5.2 Quadrupole Results

To start, we fix the initial planet semimajor axis $a_0 = 1.5$ AU, binary separation $a_b = 200$ AU, and binary eccentricity $e_b = 0$ (so that the octupole contributions vanish). We consider planet masses $M_p = 0.3, 1.0, 3.0$ and $5.0 M_J$, and run a fine grid of initial inclinations, selected randomly from an isotropic distribution

⁶The only exception is in Section 2.5.2, where we explore initial inclinations in the range $80^\circ \leq \theta_{lb,0} \leq 90^\circ$, since the parameters considered there never produce migrating planets when $\theta_{lb,0} \lesssim 80^\circ$

(uniform in $\cos \theta_{lb,0}$). The argument of pericenter ω and orbital node Ω are randomly sampled uniformly in $[0, 2\pi]$. The results are shown in Figs. 2.14 (G star) and 2.15 (F star), where we plot the final spin-orbit angle $\theta_{sl,f}$ and semimajor axis a_f versus the initial inclination $\theta_{lb,0}$, as well as the distributions of $\theta_{sl,f}$ for the systems that resulted in HJs (with final semimajor axis $a_f < 0.1$ AU).

G Star

The dynamics considered in this section are considerably more complicated than the idealized analysis presented in Section 2.4, since the effects of stellar spin-down ($S_* \neq \text{constant}$) and the backreaction torque from the oblate host star on the planetary orbit are now included. Nonetheless, many of the general features remain for the G star (Fig. 2.14). The distribution of $\theta_{sl,f}$ for planets with mass $M_p = 1M_J$ is distinctly bimodal with peaks at $\theta_{sl,f} \sim 40^\circ$ and 120° (compare with Figs. 2.11 and 2.13 in Section 2.4). As M_p increases, the systems with larger initial inclinations ($\theta_{lb,0}$) show a preference for alignment due to their higher adiabaticity parameters, with $\mathcal{A}_0 \propto M_p / \cos \theta_{lb,0}$ (see Eq. [2.11]). The largest mass planets ($M_p = 5M_J$) tend to settle into low obliquity states ($\theta_{sl,f} \lesssim 10^\circ$), although high misalignments still remain possible. Note that the cases with $M_p = 5M_J$ and $\theta_{lb,0} \sim 88^\circ$ (in the top, rightmost plot in Fig. 2.14) have undergone adiabatic advection (see Section 2.4).

For the lowest mass planets ($M_p = 0.3M_J$), most systems result either in non-migrating planets or tidal disruptions, with very few “hot Saturns” produced. Tidal disruptions for low mass planets are more common because of the larger tidal disruption radius (see Eq. [2.48]). When $M_p = 0.3M_J$, $r_{\text{Tide}} \approx 4R_\odot$, whereas when $M_p = 5M_J$, $r_{\text{Tide}} \approx 1.6R_\odot$. As a result, with $M_p = 0.3M_J$ and

the fixed values of (a, a_b, e_b) that we consider in this subsection, there is only a very narrow range of initial inclinations that lead to pericenter distances that are small enough to induce orbital decay, but large enough to prevent tidal disruption (see Fig. 2.14, left panels). For $a_0 = 1.5$ AU, $a_b = 200$ AU, and $e_b = 0$, systems with $M_p \geq 1M_J$ never result in tidal disruptions, because the condition for disruption to be possible, derived in Section 2.3.4 (see Fig. 2.6 and Eq. [2.49]) is never satisfied. However, note that these results depend on the assumed tidal disruption radius (Eq. 2.48). The exact tidal radius is somewhat uncertain, and depends on the assumed planetary mass-radius relation, which can vary for close-in giant planets.

F Star

The results of identical calculations for the F star are shown in Fig. 2.15. The HJ fractions are consistently lower compared to the G star, for all planet masses, but most noticeably for $M_p = 0.3M_J$, with only a single HJ produced in ~ 5000 trials. For planet mass $M_p = 1M_J$, the distribution of $\theta_{\text{sl,f}}$ remains bimodal, but with larger spread. For $M_p = 5M_J$, the distributions of $\theta_{\text{sl,f}}$ are strikingly different between the F and G stars. The peak of the distribution occurs at $\theta_{\text{sl,f}} \approx 70^\circ - 80^\circ$, i.e. producing many HJs in near polar orbits with respect to the stellar spin axis. This contrasts strongly with results for the G star, where the peak occurs at $\theta_{\text{sl,f}} = 0^\circ - 10^\circ$. These differences between the G star (Fig. 2.14) and F star (Fig. 2.15) arise for two reasons. First, the larger stellar mass and radius affect the net rate of pericenter precession from SRFs, $\dot{\omega}$. The contributions to $\dot{\omega}$ from general relativity and the planetary tidal deformation are higher for more massive stars, which lead to a lower maximum achievable eccentricity and tend to reduce HJ

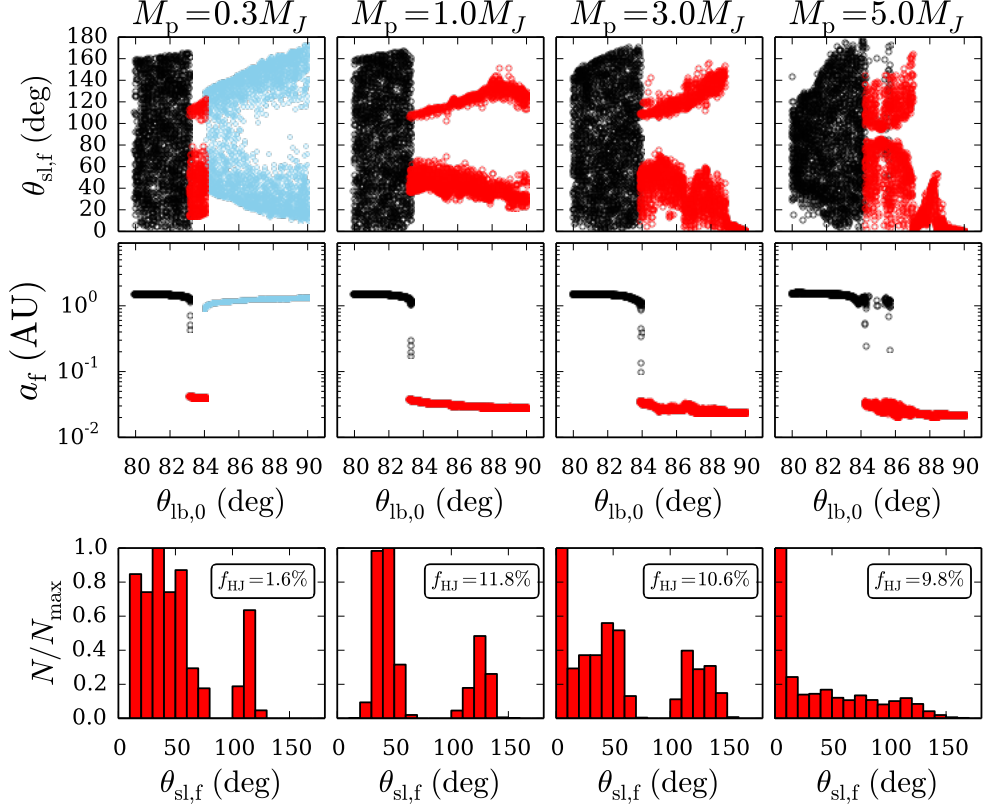


Figure 2.14: Final spin-orbit angle $\theta_{sl,f}$ (top panels) and semi-major axis a_f (middle panels) as a function of $\theta_{lb,0}$, for planet masses $M_p = 0.3, 1, 3$ and $5 M_J$ (from left to right, as labeled). Bottom panels show distributions of the final spin-orbit misalignments for the systems that circularized (HJs). All systems have $M_\star = 1M_\odot$, $a = 1.5$ AU, $a_b = 200$ AU, $e_b = 0$. Black points: non-migrating planets. Blue points: tidally disrupted planets. Red points: HJs. Note that the values of $\theta_{sl,f}$ and a_f for the disrupted planets are simply the values at the time-step before tidal disruption is achieved, and thus have no particular observational significance. Tidal disruptions only occur here when $M_p = 0.3M_J$, because the condition for disruption (Section 2.3.4, Eq. [2.49]) is not satisfied for the other planet masses. See Table 2.2 for further information on the outcomes of the simulations. The distribution of $\theta_{sl,f}$ is distinctly bimodal for $M_p = 1M_J$, with a preference for prograde orbits. As the planet mass increases, the adiabaticity parameter \mathcal{A}_0 increases (see Section 3), and for $M_p = 5M_J$, the peak of the distribution occurs at low obliquities $\theta_{sl,f} = 0^\circ - 10^\circ$.

production fractions (however, note that the contribution to $\dot{\omega}$ from the oblate host star has the opposite sign, and can, under some circumstances, cancel the increases in $\dot{\omega}$ from GR and tidal distortion). Second, the larger stellar radius and spin frequency (compared to the G star) both lead to a more pronounced torque on the planetary orbit from the stellar quadrupole, since $(d\mathbf{L}/dt)_{\text{SL}} \propto R_*^5 \Omega_*^2$; see Section 2.4.3, Eq. [2.60]). The increased stellar radius alone leads to an increase in the backreaction torque of the stellar quadrupole on the orbit by a factor of ~ 3 , with a further increase due to higher Ω_* .

Both the wider spread in the bimodal distributions (when $M_p = 1M_J$), and peak near $\theta_{\text{sl,f}} \sim 90^\circ$ (when $M_p = 5M_J$) can be understood from the results of Section 2.4, where we presented final spin-orbit angles for varying initial inclinations, both with and without feedback included. Comparing the lower left panels of Figs. 2.11 and 2.13 shows that in some cases, including feedback causes the bimodality to be partially preserved, but with significant broadening. Similarly, comparing the upper left panels of Figures 2.11 and 2.13 shows that in other cases, including feedback completely erases the bimodality, causing $\theta_{\text{sl,f}}$ to instead cluster around $\sim 90^\circ$. Thus, we attribute the qualitative differences in $\theta_{\text{sl,f}}$ between the G and F star to enhanced feedback from the oblate F star on the orbit.

2.5.3 Octupole Results: Fixed Binary Eccentricity and Separation

Having demonstrated results for binary companions with zero eccentricity, we now consider binaries with non-zero eccentricity, so that the octupole terms

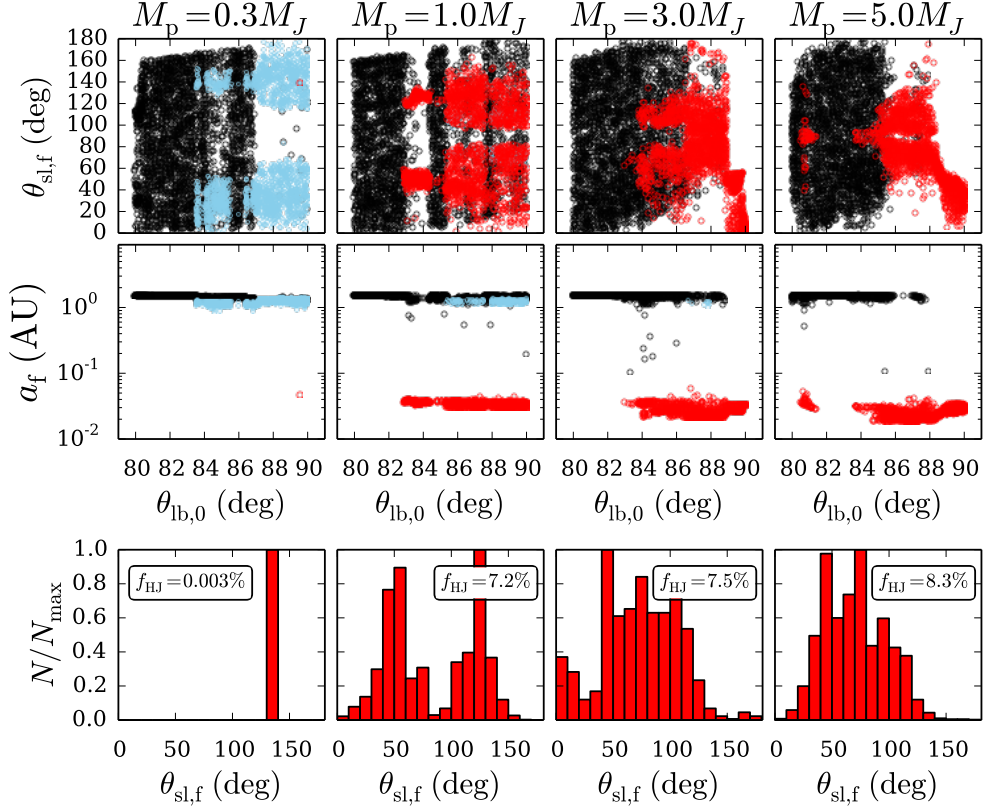


Figure 2.15: Same as Fig. 2.14, except for an F-type host star, with $M_\star = 1.4M_\odot$, $R_\star = 1.26R_\odot$ and corresponding spin properties (see text). Note that the histogram for $M_p = 0.3M_J$ has only one data point. When $M_p = 1M_J$, the distributions of $\theta_{\text{sl},f}$ are similar to those for the G star, but are broadened. When $M_p = 5M_J$, however, the strong peak near low obliquities ($\theta_{\text{sl},f} = 0 - 10^\circ$) observed for planets around G stars has vanished. We attribute these differences to the increased torque from the stellar quadrupole on the planetary orbit, as well as stronger periastron precession from SRFs.

can contribute to the dynamics. We limit the discussion in this section to the solar-type (G) star, and present one example of fixed non-zero binary eccentricity (see Section 2.5.4 for general combinations of a_b and e_b). For a straightforward comparison with the results from Section 2.5.2, and to illustrate the role of the octupole, we choose the parameters so that the quadrupole LK timescale t_k (Eq. [2.3]) is unchanged (since t_k depends only on the combination $a_{b,\text{eff}} = a_b \sqrt{1 - e_b^2}$). We thus specify the binary eccentricity e_b and choose the

separation a_b such that the quantity $a_{b,\text{eff}} = 200$ AU. Figure 2.16 shows results for $e_b = 0.8$, $a_b = 333$ AU, corresponding to $\varepsilon_{\text{oct}} \approx 0.01$. Additional results with $e_b = 0.4$, $a_b = 218$ AU, so that $\varepsilon_{\text{oct}} \approx 0.003$ are included in Table 2.2. Recall that ε_{oct} quantifies the “strength” of the octupole potential; see Eq. (2.4).

Without the octupole terms, the limiting eccentricity e_{lim} during an LK cycle is achieved at $\theta_{\text{lb},0} = 90^\circ$. One effect of the octupole term is to allow this limiting eccentricity to be realized at $\theta_{\text{lb},0} < 90^\circ$ (Liu et al., 2015), so that migration becomes possible for a wider range of inclinations, thereby increasing the production efficiency (Naoz et al., 2012).

Comparing Figs. 2.14 and 2.16 allows the role of the octupole terms to be identified, since they would produce identical results to quadrupole order. Low mass planets are affected by the octupole potential less than high mass planets, because the rate of pericenter precession due to tidal distortion of the planet has the dependence $\dot{\omega}_{\text{Tide}} \propto M_p^{-1}$ (see Eq. [A.11]). This precession can act to suppress the extreme octupole dynamics, such as increased eccentricities and orbit flipping. Thus for the lowest mass planets ($0.3M_J$) the results do not differ significantly from the pure quadrupole case. More massive planets ($M_p = 1 - 5M_J$) are affected more strongly, with the production fraction of HJs increasing with the octupole strength ε_{oct} (see Section 2.5.4 for further discussion of HJ and disruption fractions).

In terms of the final obliquity $\theta_{\text{sl,f}}$, one effect of the octupole is to increase the number of significantly misaligned $5M_J$ planets, as demonstrated in Fig. 2.17. There are two possible reasons for this. First, the octupole allows close-in planets to be produced at lower inclinations, with lower adiabaticity parameters ($\mathcal{A}_0 \propto 1/\cos \theta_{\text{lb},0}$). Since the degree of misalignment depends on \mathcal{A}_0 , systems

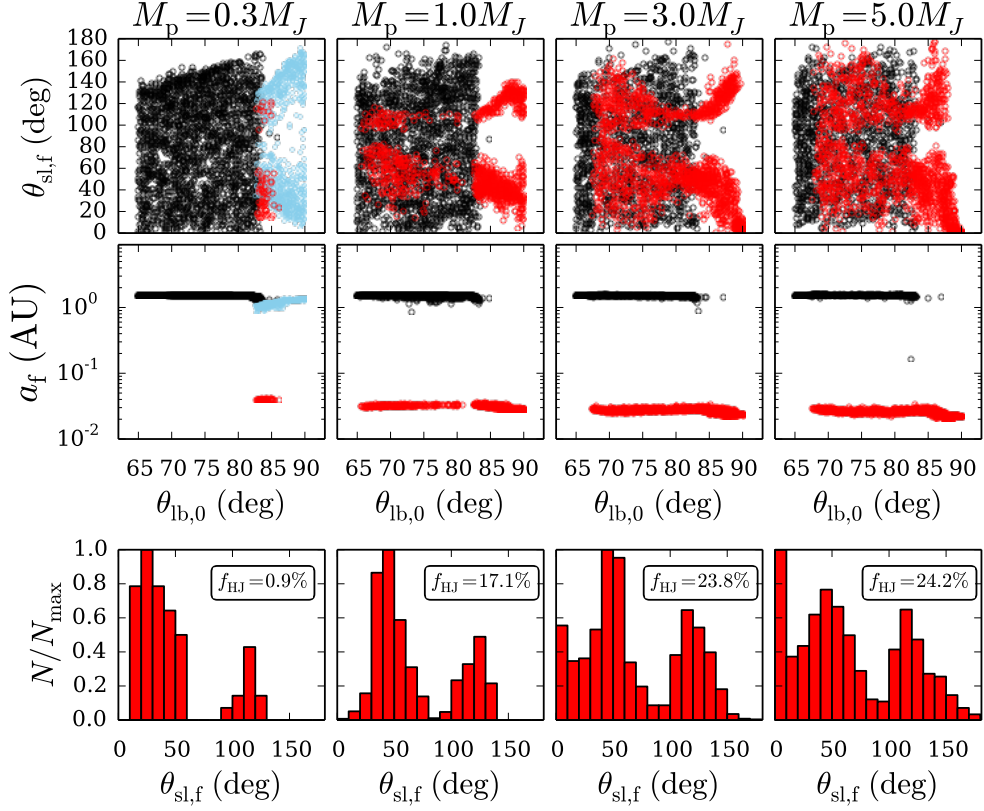


Figure 2.16: Same as Fig. 2.14, except that $e_b = 0.8$, and $a_b = 333.33$ AU (so that $a_{b,\text{eff}} = 200$, AU, and $\varepsilon_{\text{oct}} \approx 0.01$). For $M_p = 0.3M_J$, the results are nearly unchanged (compared to Fig. 2.14), because pericenter precession from SRFs is higher for low-mass planets (see text), and the effects of the octupole (e.g. extreme high eccentricities) are more easily suppressed. For $M_p \geq 1M_J$, the HJ production fraction is increased. In terms of $\theta_{sl,f}$, the main effect of the octupole is to add HJs with a primarily bimodal distribution, thereby increasing the fraction of significantly misaligned planets.

with low inclinations have a tendency to settle to larger obliquities, and exhibit bimodality. Second, the chaos induced in the orbit due to the octupole terms may act to disrupt the tendency for alignment found for the pure quadrupole calculations. Despite these effects, for $5M_J$ planets with the octupole included, the strong peak near zero obliquity observed for the pure quadrupole results ($e_b = 0$, Fig. 2.14) is partially preserved.

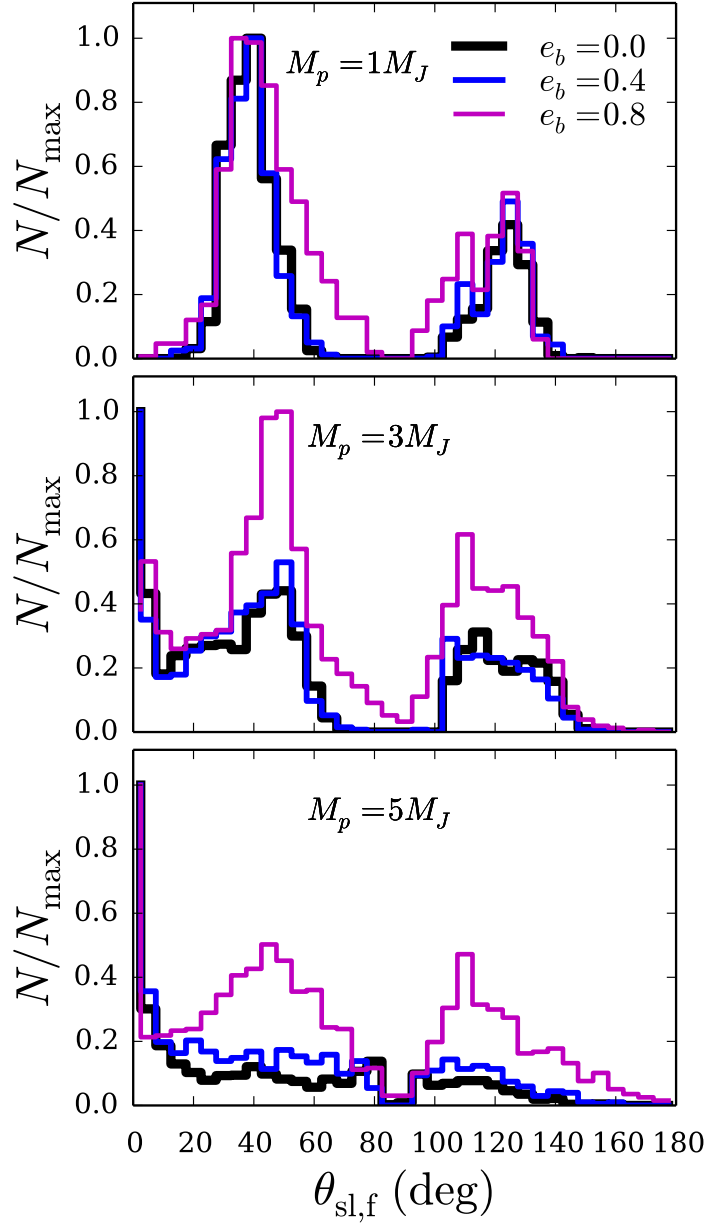


Figure 2.17: Distributions of $\theta_{\text{sl,f}}$ for various binary eccentricities, $e_b = 0, 0.4, 0.8$, as labeled, and showing planet masses $M_p = 1, 3, 5M_J$ (from top to bottom). Binary separations have been chosen such that $a_{b,\text{eff}} = a_b \sqrt{1 - e_b^2} = 200$ AU. As a result, the quadrupole LK timescale t_k is identical, so that the results depicted in each panel would be identical to quadrupole order. This illustrates the role of the octupole in generating spin-orbit misalignment.

Table 2.2: Input parameters and results of the calculations presented in Sections 2.5.2 and 2.5.3. Each line is the result of N_{run} trials with initial inclination $\theta_{\text{lb},0}$ randomly sampled from an isotropic distribution in the range $65^\circ - 90^\circ$ (the only exception are the first eight rows, with $e_b = 0$, where $\theta_{\text{lb},0}$ is sampled in $80^\circ - 90^\circ$). Each set of trials has a fixed a_b and e_b , as indicated, and $a_0 = 1.5$ AU, and tidal enhancement factor $\chi = 10$. The initial spin-orbit angle is set to $\theta_{\text{lb},0} = 0^\circ$. We display the “migration fraction” $f_{\text{mig}} \equiv f_{\text{HJ}} + f_{\text{dis}}$, as well as the “prograde fraction” f_{prog} i.e. the fraction of HJ systems with final obliquities $\theta_{\text{sl,f}} < 90^\circ$. We also include relevant figure numbers in the rightmost column. Note that the stellar radius is set to $R_\star = 1 R_\odot$ when $M_\star = 1 M_\odot$, and $R_\star = 1.26 R_\odot$ when $M_\star = 1.4 M_\odot$.

$M_\star (M_\odot)$	$M_p (M_J)$	a_b (AU)	e_b	N_{run}	$f_{\text{HJ}} (\%)$	$f_{\text{dis}} (\%)$	$f_{\text{mig}} (\%)$	$f_{\text{prog}} \%$	Figure
Section 2.5.2									
1.0	0.3	200.0	0.0	5000	1.6	10.3	12.0	84.3	2.14, 2.17
1.0	1.0	200.0	0.0	5000	11.8	0.0	11.8	71.2	2.14, 2.17
1.0	3.0	200.0	0.0	5000	10.6	0.0	10.6	72.0	2.14, 2.17
1.0	5.0	200.0	0.0	5000	9.8	0.0	9.8	82.6	2.14
1.4	0.3	200.0	0.0	5000	0.003	7.8	7.8	0.0	2.15
1.4	1.0	200.0	0.0	5000	7.2	0.9	8.2	54.5	2.15
1.4	3.0	200.0	0.0	5000	7.5	0.0	7.5	66.8	2.15
1.4	5.0	200.0	0.0	5000	8.3	0.0	8.3	74.0	2.15
Section 2.5.3									
1.0	0.3	218.22	0.4	3000	1.3	10.8	12.2	89.5	2.17
1.0	1.0	218.22	0.4	3000	12.2	0.0	12.2	68.1	2.17
1.0	3.0	218.22	0.4	3000	12.4	0.0	12.4	73.4	2.17
1.0	5.0	218.22	0.4	3000	12.9	0.0	12.9	78.6	2.17
1.0	0.3	333.33	0.8	3000	0.9	11.4	12.3	82.5	2.16, 2.17
1.0	1.0	333.33	0.8	3000	17.1	0.0	17.1	70.4	2.16, 2.17
1.0	3.0	333.33	0.8	3000	23.8	0.0	23.8	65.7	2.16, 2.17
1.0	5.0	333.33	0.8	3000	24.2	0.0	24.2	66.3	2.16, 2.17

2.5.4 General Results for a Range of Binary Separations, Eccentricities, and Planet Semi-major Axes

We now survey the parameter space in (a_0, a_b, e_b) , sampling the initial planet semi-major axis a_0 uniformly in the range $a_0 = 1 - 5$ AU, the binary separation $a_b = 100 - 1000$ AU (uniform in $\log a_b$), and the binary eccentricity uniformly in $e_b = 0 - 0.8$. This choice of eccentricity distribution is highly approximate, as the actual eccentricity distribution of wide binaries is uncertain (Tokovinin

Table 2.3: Same format as Table 2.2, but showing results for the full population synthesis calculations in Sections 2.5.4, 2.5.5, and 2.5.6. We vary a_0 , a_b , and e_b uniformly in the ranges $a_0 = (1 - 5)$ AU, $a_b = (100 - 1000)$ AU (note that a_b is sampled uniformly in $\log a_b$), and $e_b = (0 - 0.8)$. $\theta_{\text{lb},0}$ is sampled isotropically in the range $65^\circ - 90^\circ$. The other parameters and notation are the same as in Table 2.2.

M_* (M_\odot)	M_p (M_J)	$\theta_{\text{sl},0}$ (\circ)	χ	N_{run}	f_{HJ} (%)	f_{dis} (%)	f_{mig} (%)	f_{prog} %	Figure
Section 2.5.4									
1.0	0.3	0.0	10.0	8988	0.5	12.3	12.8	70.4	2.18,2.20
1.0	1.0	0.0	10.0	8991	2.4	11.0	13.4	78.3	2.18,2.20
1.0	3.0	0.0	10.0	8996	3.8	9.3	13.1	72.0	2.18,2.20
1.0	5.0	0.0	10.0	8994	4.7	8.4	13.0	74.1	2.18,2.20
1.4	0.3	0.0	10.0	8993	0.0	12.3	12.3	100.0	2.21
1.4	1.0	0.0	10.0	8994	1.4	10.9	12.3	64.9	2.21
1.4	3.0	0.0	10.0	8998	3.0	9.8	12.8	67.7	2.21
1.4	5.0	0.0	10.0	8997	3.6	9.1	12.6	69.4	2.21
Section 2.5.5									
1.0	0.3	0.0	1.0	8998	0.0	11.8	11.8	0.0	2.23, 2.24
1.0	1.0	0.0	1.0	8991	0.7	11.1	11.8	75.6	2.23, 2.24
1.0	3.0	0.0	1.0	8997	2.3	9.6	11.9	69.6	2.23, 2.24
1.0	5.0	0.0	1.0	8993	3.1	9.5	12.5	70.9	2.23, 2.24
1.4	0.3	0.0	1.0	8997	0.0	10.9	10.9	0.0	2.25
1.4	1.0	0.0	1.0	8995	0.4	10.6	10.9	52.0	2.25
1.4	3.0	0.0	1.0	8996	1.5	10.4	11.8	58.1	2.25
1.4	5.0	0.0	1.0	8998	1.9	9.9	11.8	61.9	2.25
1.0	0.3	0.0	100.0	8995	2.4	11.6	14.0	61.6	2.23, 2.24
1.0	1.0	0.0	100.0	8997	4.1	9.7	13.8	68.7	2.23, 2.24
1.0	3.0	0.0	100.0	8994	6.4	5.9	12.4	71.8	2.23, 2.24
1.0	5.0	0.0	100.0	8994	7.8	4.1	12.0	71.0	2.23, 2.24
1.4	0.3	0.0	100.0	8997	1.5	11.7	13.2	65.5	2.25
1.4	1.0	0.0	100.0	8996	3.3	9.9	13.2	65.0	2.25
1.4	3.0	0.0	100.0	8994	6.3	6.2	12.5	66.3	2.25
1.4	5.0	0.0	100.0	8999	7.6	4.1	11.6	66.7	2.25
Section 2.5.6									
1.0	0.3	30.0	10.0	8995	0.3	12.8	13.1	67.2	2.26
1.0	1.0	30.0	10.0	8996	2.6	10.6	13.1	62.1	2.26
1.0	3.0	30.0	10.0	8986	4.0	9.5	13.5	61.1	2.26
1.0	5.0	30.0	10.0	8995	4.8	8.8	13.6	70.6	2.26
1.0	0.3	60.0	10.0	8993	0.4	12.8	13.2	52.4	2.26
1.0	1.0	60.0	10.0	8995	2.6	11.2	13.8	47.5	2.26
1.0	3.0	60.0	10.0	8993	4.4	10.0	14.5	49.3	2.26
1.0	5.0	60.0	10.0	8993	4.9	9.4	14.3	54.5	2.26

& Kiyaeva, 2015). Moreover, planet formation at a few AU may be quenched by the presence of a highly eccentric binary companion (when $a_b[1 - e_b]$ is not sufficiently larger than a_0). As in previous subsections, the initial inclination $\theta_{lb,0}$ is sampled isotropically in the range $65^\circ - 90^\circ$. We fix the tidal enhancement factor at $\chi = 10$ in this section; we explore the effects of varying χ in Section 2.5.5.

Hot Jupiter and Disruption Fractions

Figure 2.18 depicts the outcomes of our simulations for planets around G stars, where we plot the initial semi-major axis ratio a_b/a_0 and binary eccentricity e_b versus the initial inclination $\theta_{lb,0}$. The final outcome of each integration is indicated by the color (HJ, disrupted planet, or non-migrating). Results for planets around F stars are qualitatively similar, and are omitted. See Table 2.3 for further information, including the HJ and disruption fractions.

Figure 2.18 shows that HJs are produced for a relatively narrow range of the ratio a_b/a_0 . Planets with $a_b/a_0 \lesssim 60$ are always either tidally disrupted or non-migrating, while those with $a_b/a_0 \gtrsim 300$ never undergo migration. This result places constraints on the requirements for stellar companions to induce migration without destroying the planet (see also Section 2.3.4 for a discussion of the conditions that must be satisfied for migration and tidal disruption). In the bottom panels of Fig. 2.18, we plot the values of ε_{oct} versus $\theta_{lb,0}$. We find that systems with $\varepsilon_{oct} \gtrsim 0.03$ always lead to tidal disruptions, and that no HJs are produced for $\varepsilon_{oct} \gtrsim 0.01 - 0.02$. This finding can be understood by examining Fig. 2.19, where we plot the initial conditions in terms of $(a_{b,eff}, a_0)$ for the $1M_J$ planets that resulted in tidal disruptions and HJs, along with the criteria for mi-

gration (disruption) to occur, shown as solid red (blue) curves (see also Fig. 2.6). We see that the migration/disruption conditions derived in Section 2.3.4 are in good agreement with our numerical calculations.

Also plotted in Fig. 2.19 are curves of constant $\varepsilon_{\text{oct}} = 0.015$ (dashed black curves, with $e_b = 0.4, 0.6, 0.8$, from bottom to top). The uppermost dashed line, with $e_b = 0.8$, nearly coincides with the tidal disruption boundary, so that $\varepsilon_{\text{oct}} \gtrsim 0.015$ can only be achieved for combinations of $(a_{b,\text{eff}}, a_0)$ that are located in the “disruption zone” i.e. below the solid blue curve, where systems are likely to result in tidal disruption, rather than HJs. Since we consider a range of binary eccentricities uniform in $e_b = [0, 0.8]$, all of our systems with $\varepsilon_{\text{oct}} \gtrsim 0.015$ reside in the disruption zone, thereby explaining the lack of circularized planets in our calculations with $\varepsilon_{\text{oct}} \gtrsim 0.015$.

Planets with mass $M_p = 1-3M_J$ around G stars have HJ production fractions f_{HJ} in the range 2.4–3.8%, and f_{HJ} for planets around F stars is somewhat lower (1.4 – 3%). For both stellar types, the fraction of HJs produced increases with planet mass (see also Table 2.3, and the discussion in Section 2.5.3). This arises from our tidal disruption criterion (Eq. [2.48]), with $r_{\text{Tide}} \approx 4R_\odot$ for the sub-Jupiter mass planet ($M_p = 0.3M_J$), and $r_{\text{Tide}} \approx 1.6R_\odot$ for $M_p = 5M_J$. Low mass planets are therefore much more susceptible to tidal disruption, and are more readily removed from the sample of surviving planets. We find that the fraction of “hot Saturns” ($M_p = 0.3M_J$) produced is especially low, with $f_{\text{HJ}}(0.3M_J) \approx 0.5\%$ and 0.02% for the G and F stars respectively.

Comparing the results of Sections 2.5.2 and 2.5.3 (see Table 2.2), and this subsection (Table 2.3), we see that although certain combinations of (a_0, a_b, e_b) can lead to HJ fractions of $f_{\text{HJ}} \sim 24\%$ (specifically when the octupole effect is

included; see also Naoz et al. 2012), when ranges of (a_0, a_b, e_b) are considered, the overall HJ fraction is always less than a few percent for planets with mass $M_p = 1M_J$.

Inspection of Table 2.3 reveals that the “migration fraction” $f_{\text{mig}} \equiv f_{\text{HJ}} + f_{\text{dis}} \approx 12 - 13\%$ is nearly constant for all planet masses and stellar types, varying by only $\sim 1\%$. Given the complicated interplay between the various ingredients in our system (SRFs, octupole-level dynamics, tidal dissipation), and the dependence of these physical processes on planet and stellar mass, this result is not necessarily expected, but can be qualitatively understood from the discussion in Section 2.3.4. To achieve planet migration (either HJ formation or tidal disruption) within the lifetime of the host star, two conditions must be satisfied: (i) The planet must attain a sufficiently large eccentricity ($\sim e_{\text{lim}}$) so that the corresponding periastron distance $a(1 - e_{\text{lim}})$ is less than a critical value ($\simeq 0.025$ AU). This translates into a necessary condition for migration as given by Eq. (2.47). (ii) For systems that satisfy this condition, whether or not migration actually occurs depends on the initial inclination $\theta_{\text{lb},0}$. As discussed in Section 2.3.4, without the octupole effect, e_{lim} is achieved very close to $\theta_{\text{lb},0} = 90^\circ$. With octupole, e_{lim} can be achieved for initial inclinations $\theta_{\text{lb},0}$ in the range $\theta_{\text{lb,crit}} \leq \theta_{\text{lb},0} \leq 90^\circ$, where $\theta_{\text{lb,crit}}$ (the minimum inclination that can lead to $e_{\text{max}} = e_{\text{lim}}$) is determined by $\varepsilon_{\text{oct}} \simeq ae_b/a_b(1 - e_b^2)$, with no dependence on planet or stellar mass (see Liu et al., 2015). The fact that the “window of extreme eccentricity” ($\theta_{\text{lb,crit}} \leq \theta_{\text{lb},0} \leq 90^\circ$) is independent of M_p and M_\star , combined with the weak dependence of Eq. (2.47) on M_p and M_\star explains the nearly constant migration fraction observed in our calculations. Note however that the migration fraction does depend on the assumed distributions of the planetary and binary orbital properties $(a_0, a_b, e_b, \theta_{\text{lb},0})$, and alternate choices for these distributions

would yield different migration fractions. A semi-analytic calculation of the migration/disruption fractions, based on the idea discussed here, is presented in Muñoz et al. (2016, submitted).

Regardless of the reason, the fact that $f_{\text{mig}} \approx \text{constant}$ is a useful finding. Recall that the disruption fractions quoted herein depend on the disruption condition, which depends on the planetary mass-radius relation, and is somewhat uncertain. However, noting that $f_{\text{mig}} \approx \text{constant}$ allows us to estimate an upper limit on the possible HJ fraction for any giant planet mass, by setting $f_{\text{dis}} \rightarrow 0$, so that $f_{\text{mig}} \rightarrow f_{\text{HJ,max}} \sim 13\%$.

Final HJ Orbital Periods and Spin-Orbit Misalignments

Figures 2.20 and 2.21 show the final orbital periods and spin-orbit misalignments versus the initial inclination $\theta_{\text{lb},0}$ for the HJs produced in our calculations. Note that we have removed the systems that resulted in tidal disruptions and non-migrating planets for clarity.

We see that the distribution of the final stellar obliquities are distinctly bimodal for $M_p = 1 - 3M_J$ around both G and F host stars, with peaks around $30^\circ - 40^\circ$, and $120^\circ - 130^\circ$. As planet mass increases, greater differences emerge between the results for G and F stars. For the G-type host star, massive planets tend to settle to lower obliquities. When $M_p = 5M_J$, the peak of the histogram occurs in the first bin ($\theta_{\text{sl,f}} = 0^\circ - 10^\circ$), with an underlying bimodal distribution of larger misalignments (Fig. 2.20). Thus, the tendency for spin-orbit alignment for massive planets presented in Section 2.5.3 and in Storch et al. (2014) is partially preserved when sampling over arbitrary binary eccentricities and sep-

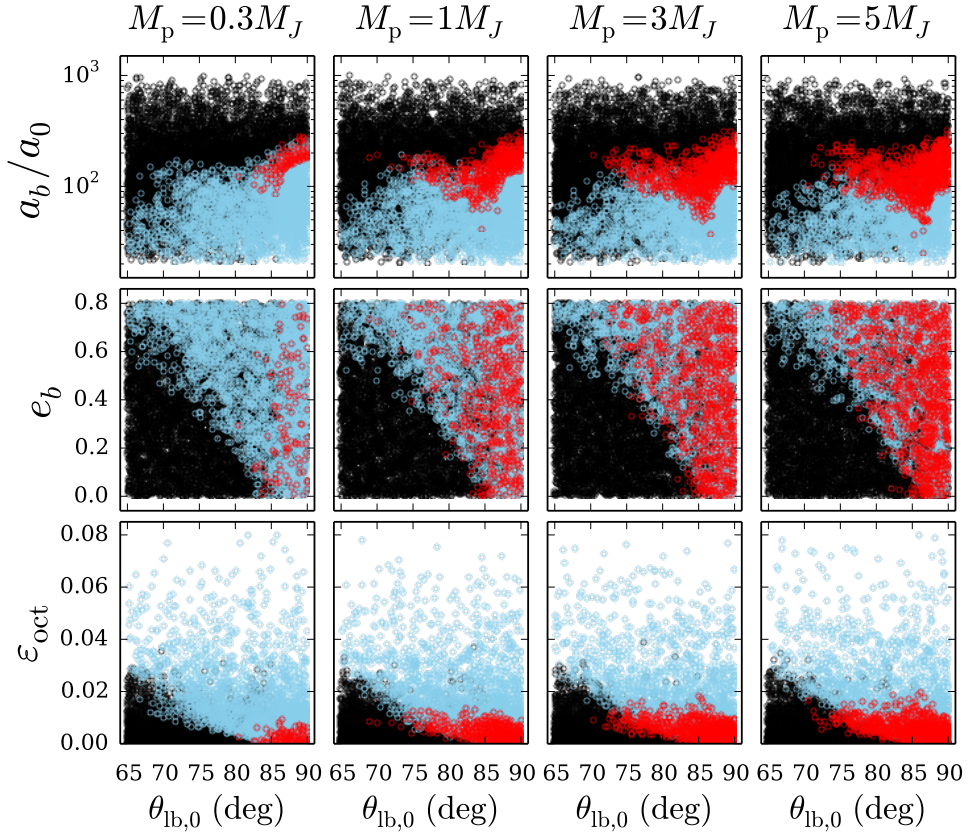


Figure 2.18: Parameter space producing HJs (red), tidally disrupted planets (blue), and non-migrating planets (black), around G stars. Top panels: initial binary separation ratio (a_b/a_0) versus the initial inclination $\theta_{lb,0}$. Middle panels: Binary eccentricity e_b . Bottom panels: “Octupole strength” ε_{oct} . Results are separated into columns by planet mass, as labeled. HJs are able to be produced over the full range of $e_b = [0, 0.8]$, but only in a relatively narrow range of a_b/a_0 . As a result, the range of ε_{oct} capable of producing HJs is limited, with $\varepsilon_{oct} \lesssim 0.01 - 0.02$.

arations. By contrast, the results for massive planets ($5M_J$) around the F-type host star (Fig. 2.21) show a greater degree of misalignment, with the peak of the distribution at $\theta_{sl,f} \sim 45^\circ$. This is in qualitative agreement with the pure quadrupole calculations in Section 2.5.2 (see Fig. 2.15).

We find that all combinations of stellar type and planet mass lead to a greater

fraction of prograde ($\theta_{\text{sl,f}} \leq 90^\circ$), rather than retrograde ($\theta_{\text{sl,f}} \geq 90^\circ$) configurations (see Table 2.3). However, the percentage of prograde planets around F stars is consistently lower than around G stars. For example, we find that for $M_p = 1M_J$, the prograde percentage is $\approx 78\%$ for the G star, and $\approx 65\%$ for the F star.

The bimodal $\theta_{\text{sl,f}}$ distributions for Jupiter-mass planets around G stars shown in Fig. 2.20 is quite different from those obtained by Naoz et al. (2012) and Petrovich (2015b). These authors find much broader $\theta_{\text{sl,f}}$ distributions, with no apparent “gap” at $\theta_{\text{sl,f}} \sim 90^\circ$. A key reason for this difference is that the previous works considered slowly-rotating host stars (and non-evolving spin rates), which have weak spin-orbit couplings.

Also depicted in Figs. 2.20 and 2.21 are the final orbital periods $P_{\text{orb,f}}$ as a function of initial inclination. After the LK oscillations are suppressed, the tidal evolution occurs at nearly constant angular momentum, so that all planets settle to a final semi-major axis $a_f \gtrsim 2r_{\text{Tide}}$. Since r_{Tide} depends inversely on planet mass, high mass planets are able to achieve shorter final orbital periods than low mass planets. As a result, the lowest mass planets ($M_p = 0.3M_J$) reside farthest from their host stars, and exhibit the smallest spread in $P_{\text{orb,f}}$. All calculations result in extremely close-in planets, with $P_{\text{orb,f}} \lesssim 3$ days. This lack of longer period HJs produced by the LK mechanism is in agreement with calculations by Petrovich (2015b).

Migration Time

For the subset of planets that undergo migration (resulting in either HJ formation or tidal disruption), it is useful to examine the migration time t_{mig} . For systems that result in HJs, we define t_{mig} as the moment when the semi-major axis has decayed to $a < 0.1$ AU, so that the planet is classified as an HJ (this is also the time at which we stop our integrations). For disrupted planets, t_{mig} is the point at which the planet crosses the tidal radius.

Figure 2.22 shows cumulative distributions of the migration time t_{mig} for HJs and disrupted planets obtained from our simulation with G-type host stars (as in Figures 2.18 and 2.20). Two trends are apparent: First, most tidal disruptions occur early, with more than 75% occurring within 0.1 Gyr. Second, the range of the HJ formation time varies with planet mass. For $5M_J$ planets, $2\text{Myr} \lesssim t_{\text{mig}} \leq 5\text{Gyr}$. In contrast, the HJ formation time for $0.3M_J$ planets lies in the much more restricted range $2\text{Gyr} \lesssim t_{\text{mig}} \leq 5\text{Gyr}$. The minimum migration time for low mass planets thus differs significantly for low mass planets.

The cause behind the lengthier HJ formation times for low mass ($M_p = 0.3M_J$) planets is as follows. Recall that the orbital decay rate for planets undergoing LK migration (Eq. [2.32]) has the dependence

$$\left| \frac{1}{a} \frac{da}{dt} \right|_{\text{Tide,LK}} \propto M_p^{-1} a_F^{-7} \quad \text{where} \quad a_F = a(1 - e_{\text{max}}^2), \quad (2.66)$$

so that the tidal decay timescale $t_{\text{Tide}} \propto M_p a_F^7$. Since systems that produce surviving planets must satisfy $a_F/2 \geq r_{\text{Tide}}$, for each planet mass there is a minimum tidal decay timescale

$$t_{\text{Tide,min}} \propto M_p r_{\text{Tide}}^7 \propto M_p^{-4/3}. \quad (2.67)$$

The minimum decay time needed to produce a surviving HJ thus increases for lower mass planets, as we find in our numerical calculations.

Finally, we note that LK migration is often attributed to need a long time to operate, usually $\sim 0.1\text{--}1$ Gyr timescales, in contrast with disk-driven migration, which must occur before the gas dispersal time of a few Myr. While we confirm that this is indeed the case for Jupiter and sub-Jupiter mass planets, we find that massive planets ($M_p \sim 3 - 5M_J$) can migrate more quickly, within tens or occasionally even a few Myr, much more comparable to the timescale for disk-driven migration.

2.5.5 Dependence on Tidal Dissipation Strength

All results presented thus far adopt the tidal dissipation strength $\chi = 10$, corresponding to tidal lag time $\Delta t_L = 1$ second. We now examine the effect of varying dissipation rate, by considering tidal enhancement factors $\chi = 1$ and $\chi = 100$, so that $\Delta t_L = 0.1$ and 10 seconds respectively. All simulations presented in Section 2.5.4 were repeated with these values of χ ; see Table 2.3.

Figure 2.23 shows distributions of the HJ final orbital periods $P_{\text{orb,f}}$ around the G star for each tidal dissipation strength (note that the corresponding results for the F star are nearly identical, and are not shown). The distributions for $\chi = 1$ are narrow, and concentrated toward low orbital periods, with $P_{\text{orb,f}} \lesssim 2$ days across all planet masses. As χ increases, the distributions widen, since the enhanced tidal dissipation strength allows planets with larger pericenters to migrate inward within 5 Gyr (see Eq. [2.32]). However, note that regardless of the tidal dissipation strength, no HJs with final orbital periods $P_{\text{orb,f}} \gtrsim 4.6$

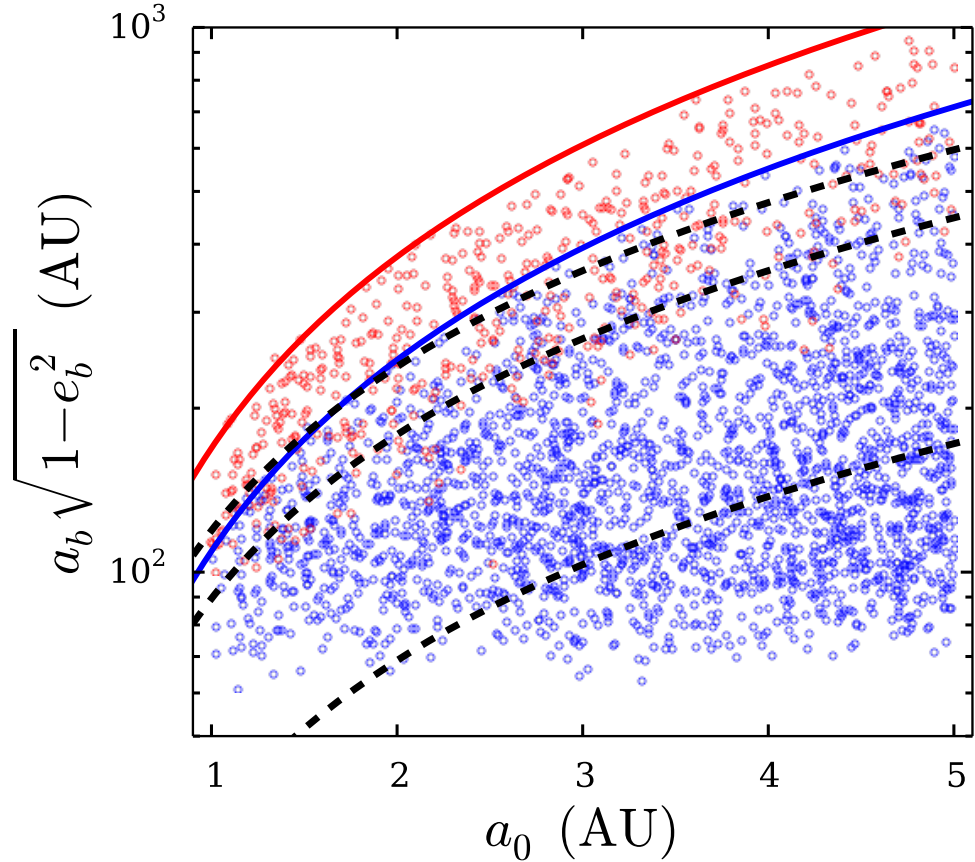


Figure 2.19: Parameter space producing tidally disrupted planets (blue points) and HJs (red points) for the calculations presented in Fig. 2.18 with $M_p = 1M_J$. The red solid curve shows the maximum value of $a_{b,\text{eff}} = a_b \sqrt{1 - e_b^2}$ for migration to be possible, as a function of a_0 (Eq. [2.47] with $a_{p,\text{crit}} = 0.025$ AU), and the blue solid curve shows the maximum value of $a_{b,\text{eff}}$ for tidal disruption to be possible (Eq. [2.49], with $f = 1$). If a given combination of $(a_0, a_{b,\text{eff}})$ is located below the red (blue) curve, migration (disruption) is possible, but not guaranteed. See also Fig. 2.6. The dashed lines depict curves of constant $\varepsilon_{\text{oct}} = 0.015$ in $(a_{b,\text{eff}}, a_0)$ space, with $e_b = 0.8, 0.6$ and 0.4 (from top to bottom). The region above the top black dashed curve cannot have $\varepsilon_{\text{oct}} > 0.015$, unless $e_b > 0.8$. Since the location of this black curve coincides with the tidal disruption limit (blue curve), there is very little parameter space with $\varepsilon_{\text{oct}} > 0.015$ capable of inducing planet migration, without tidal disruption.

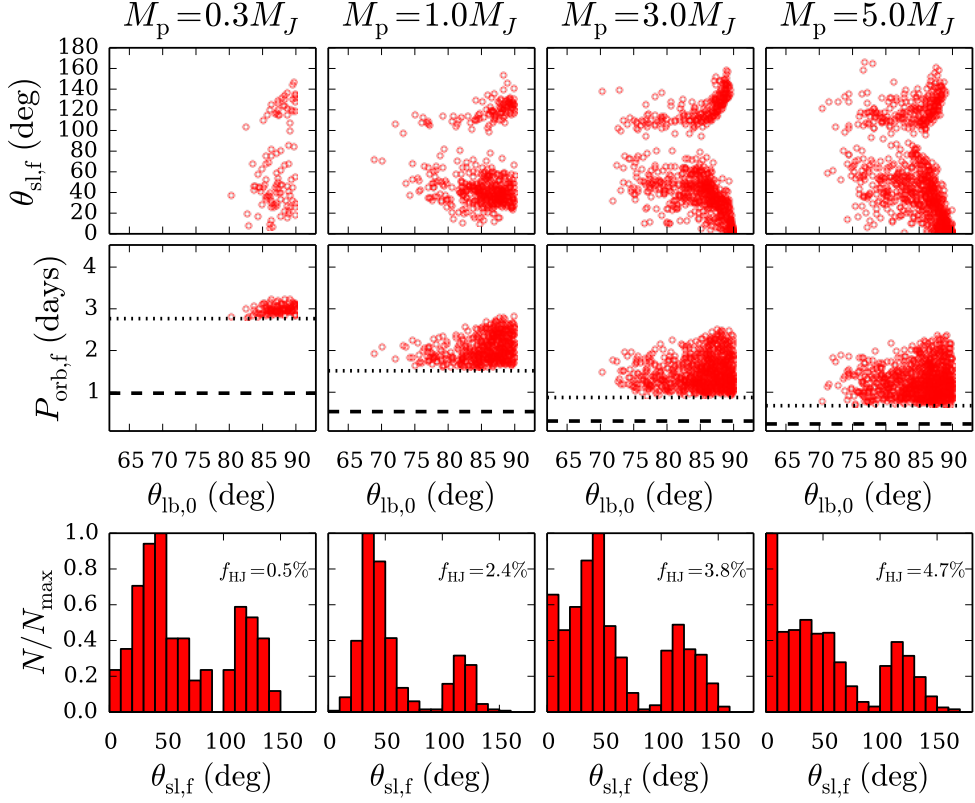


Figure 2.20: Final stellar obliquities $\theta_{\text{sl,f}}$ and orbital periods $P_{\text{orb,f}}$ for the systems shown in Figure 2.18 that resulted in HJs. Parameters are $M_\star = 1.0M_\odot$ (the G-type star), and $a_0, a_b, e_b, \theta_{\text{lb},0}$ randomly sampled over wide ranges, as described in the text, and indicated in Table 2.3. Top and middle panels depict the final spin-orbit angle $\theta_{\text{sl,f}}$ and orbital period $P_{\text{orb,f}}$ versus $\theta_{\text{lb},0}$. The dashed lines, included for reference, indicate the orbital period at the tidal disruption radius, and the dotted lines indicate the minimum achievable orbital period, defined by $a_f \geq 2R_{\text{tide}}$. Bottom panels show histograms of $\theta_{\text{sl,f}}$, with a bin width $\Delta\theta_{\text{sl,f}} = 10^\circ$.

days were produced. This lack of longer period HJs is consistent with previous calculations of HJ formation via the LK mechanism (Petrovich, 2015b).

Not surprisingly, the HJ fraction f_{HJ} increases as χ increases. However, the migration fraction $f_{\text{mig}} = f_{\text{HJ}} + f_{\text{dis}}$ remains roughly constant, varying by only a few percent across all combinations of planet mass, stellar type, and dissipation strength, between $\sim 11 - 14\%$. This is consistent with the discussion in Section

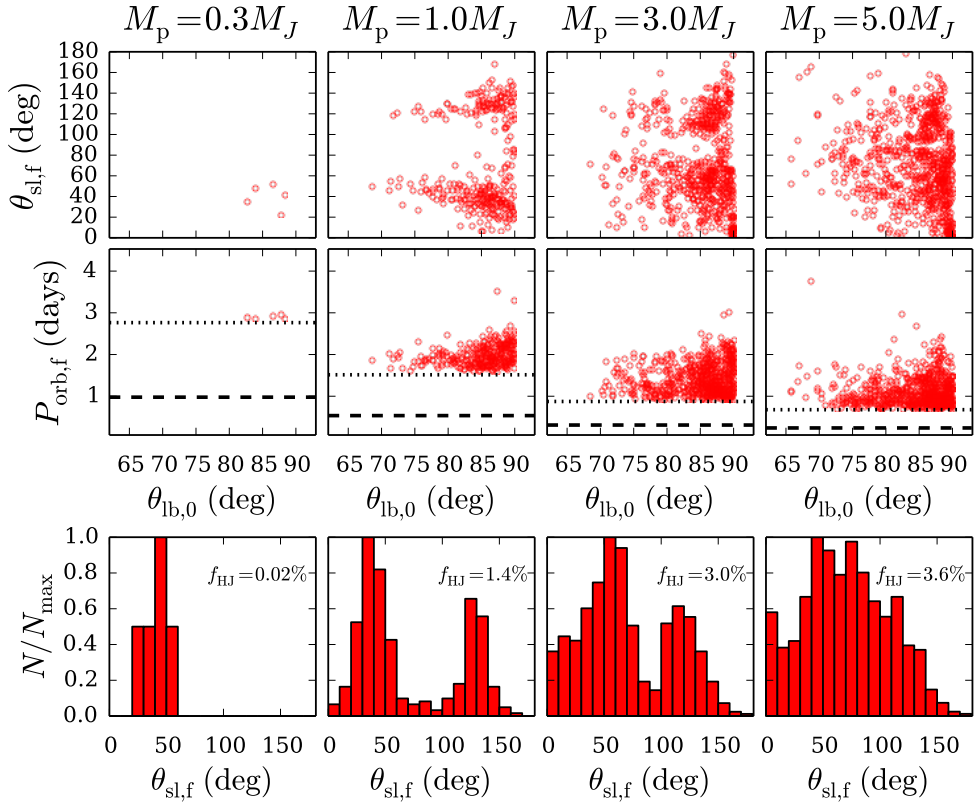


Figure 2.21: Same as Fig. 2.20, but showing results for planets around F stars.

2.5.4 (see last two paragraphs of that subsection). Most of the migrating planets originate from systems where the octupole effect plays an important role, and the “window of extreme eccentricity” (needed for achieving migration) is independent of M_p , M_* , and χ . On the other hand, most HJs originate from systems with low ε_{oct} and high $\theta_{lb,0}$ (see Figs. 2.18 and 2.19), where the octupole effect is not essential for migration. For these systems, enhanced tidal dissipation allows planets with larger periastron distances to migrate (see Eq. [2.32]), leading to a larger f_{HJ} .

Figures 2.24 and 2.25 compare the effects of varying χ on the distribution of $\theta_{sl,f}$ for planets around G and F stars. Increasing χ generally leads to broader distributions, with a greater fraction of planets at relatively low obliquities

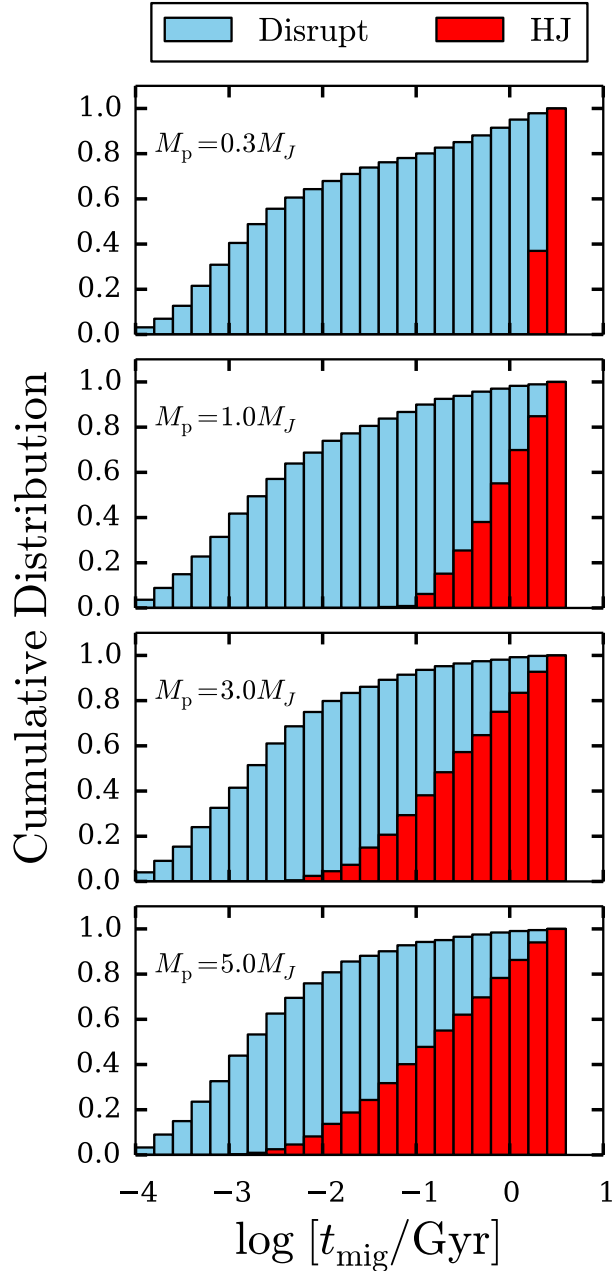


Figure 2.22: Cumulative distributions of migration times t_{mig} , defined as the time at which the planet crosses the tidal radius (for the disrupted planets), or the time at which the semi-major axis decreases below 0.1 AU (for the HJs). The results shown are the same set of simulations as depicted in Figs. 2.18 and 2.20. Most tidal disruptions occur relatively early, with $\gtrsim 75\%$ occurring within 0.1 Gyr. The minimum time needed to produce an HJ depends on planet mass, and is ~ 2 Gyr for $0.3M_J$ planets, but ~ 2 Myr for $5M_J$ planets.

($\theta_{\text{sl,f}} \lesssim 30^\circ$), but has little effect on the overall shape. In particular, the bimodality observed previously for $(1 - 3)M_J$ planets is preserved.

2.5.6 Primordial Misalignment

Finally, we present HJ stellar obliquity distributions for systems in which the initial stellar spin-orbit angle is misaligned, i.e. $\theta_{\text{sl},0} \neq 0$. Such initially misaligned configurations are relevant because various works (e.g. Bate et al., 2010; Lai et al., 2011; Batygin, 2012; Batygin & Adams, 2013; Lai, 2014) have suggested the possibility of “primordial misalignments” in which the protoplanetary disk becomes tilted relative to the stellar spin axis. We limit the discussion to planets around G stars, and the canonical tidal dissipation strength $\chi = 10$. We fix $\theta_{\text{sl},0}$, and integrate a series of systems with the initial phase of $\hat{\mathbf{S}}_*$ around $\hat{\mathbf{L}}$ (i.e. $\phi_{\text{sl},0}$, where $\phi_{\text{sl},0}$ is the azimuthal angular coordinate in the frame where $\hat{\mathbf{L}}$ is along the z -axis) randomly sampled uniformly in $[0, 2\pi]$.

Figure 2.26 shows results for $\theta_{\text{sl},0} = 30^\circ$ and 60° , along with the canonical $\theta_{\text{sl},0} = 0^\circ$ case shown previously in Fig. 2.20. When $\theta_{\text{sl},0} = 30^\circ$, the distributions of $\theta_{\text{sl,f}}$ are bimodal for all planet masses, including planets with $M_p = 5M_J$. For $\theta_{\text{sl},0} = 60^\circ$, the bimodality has vanished, and the distributions are roughly symmetric around 90° . We conclude that non-zero initial obliquities can affect the final spin-orbit misalignment, such that the bimodal peaks present for $\theta_{\text{sl},0} = 0^\circ$ tend to merge as $\theta_{\text{sl},0}$ increases.

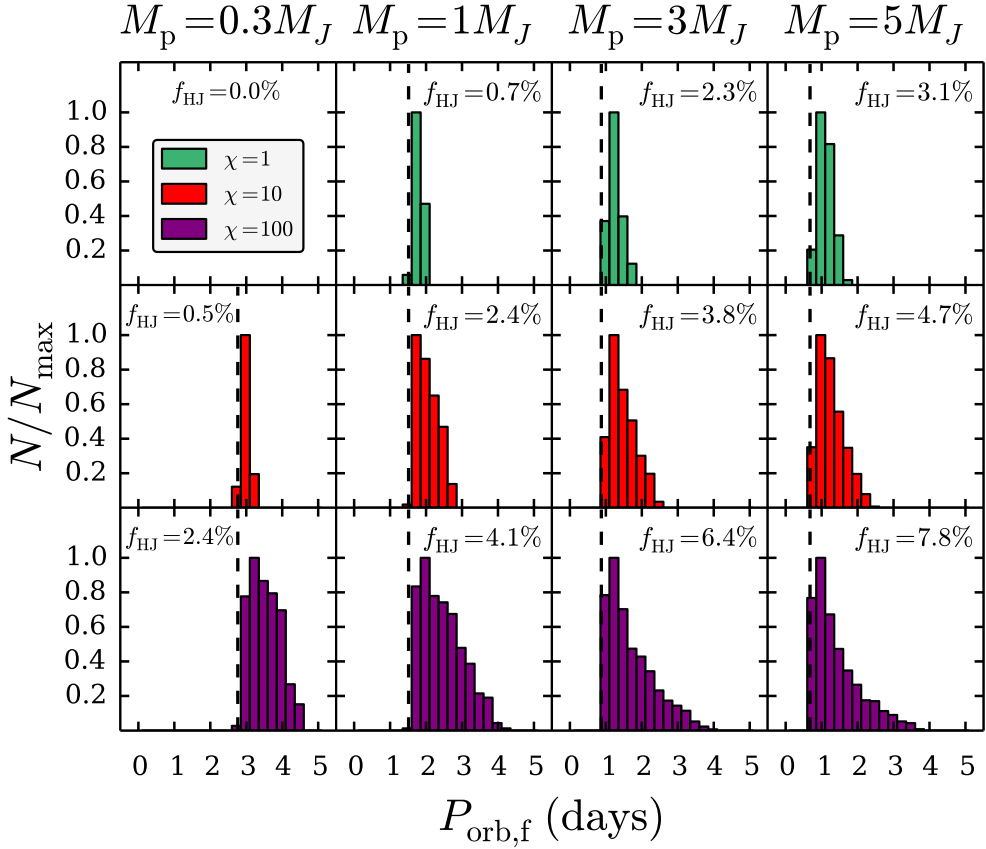


Figure 2.23: Effects of varying tidal dissipation strength χ on the distribution of final HJ orbital periods $P_{\text{orb},f}$ for planets around G stars. We show $\chi = 1$ (green, top row), $\chi = 100$ (purple, bottom row), along with our canonical value $\chi = 10$ (red, middle row). The distributions shown are the result of $N_{\text{run}} \sim 9000$ total trials, out of which a fraction f_{HJ} resulted in HJ formation (see also Table 2.3). Each column shows a different planet mass, as labeled. The vertical dashed lines, included for reference, indicate the minimum achievable orbital period, at $a_f = 2R_{\text{Tide}}$. For $M_p = 0.3, 1, 3, 5M_J$ respectively, the number of data points N_{HJ} in each histogram are as follows: top row, $\chi = 1$, $N_{\text{HJ}} = 0, 156, 490, 650$; middle row, $\chi = 10$, $N_{\text{HJ}} = 108, 502, 811, 990$; bottom row, $\chi = 100$, $N_{\text{HJ}} = 513, 875, 1370, 1670$. Note that no close-in planets were produced for the combination $M_p = 0.3M_J$, $\chi = 1$.

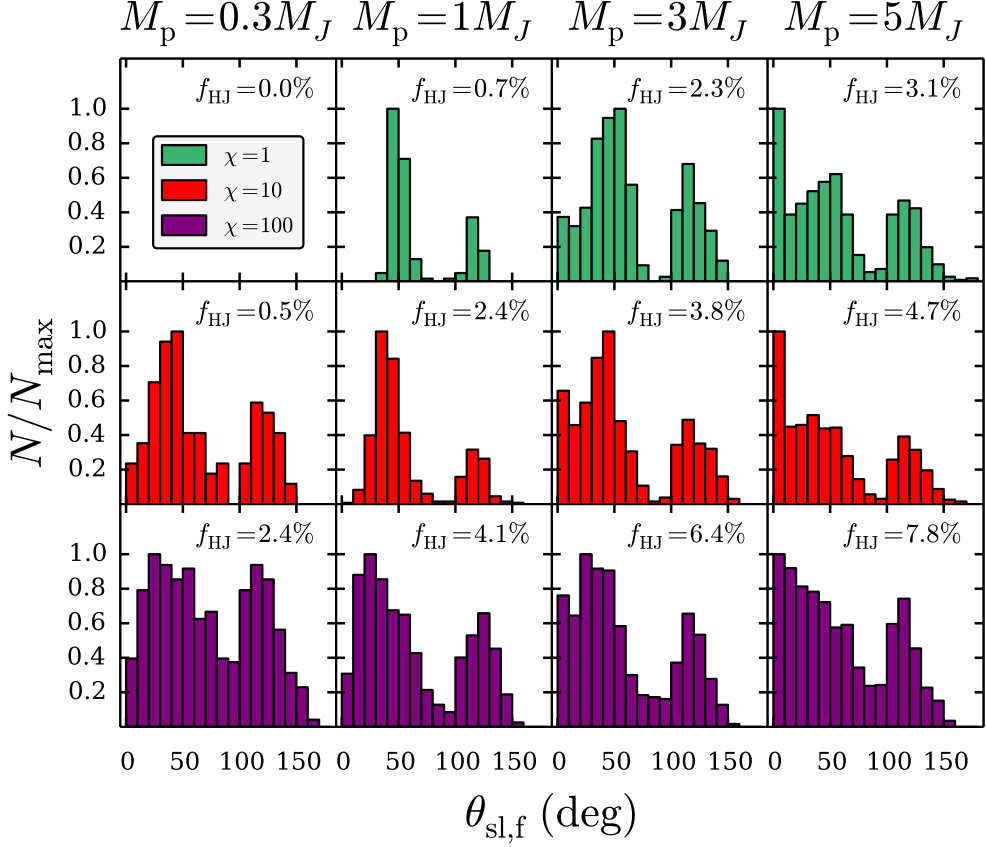


Figure 2.24: Effects of varying tidal dissipation strength χ on the distributions of $\theta_{\text{sl,f}}$ for HJs around G stars (the same sample as in Fig. 2.23). We show $\chi = 1$ (green, top row), $\chi = 100$ (purple, bottom row), along with our canonical value $\chi = 10$ shown previously in Fig. 2.20 (red, middle row). For $M_p = 0.3, 1, 3, 5M_J$ respectively, the number of data points N_{HJ} in each histogram are as follows: top row (from left to right), $\chi = 1$, $N_{\text{HJ}} = 0, 156, 490, 650$; middle row, $\chi = 10$, $N_{\text{HJ}} = 108, 502, 811, 990$; bottom row, $\chi = 100$, $N_{\text{HJ}} = 513, 875, 1370, 1670$. Note that no close-in planets were produced for $M_p = 0.3M_J$, $\chi = 1$. For most planet masses, increasing χ broadens the distribution of $\theta_{\text{sl,f}}$, but the overall shape (usually bimodal) remains unchanged. Increasing χ leads to more planets with low obliquities ($\theta_{\text{sl,f}} \lesssim 20^\circ$)

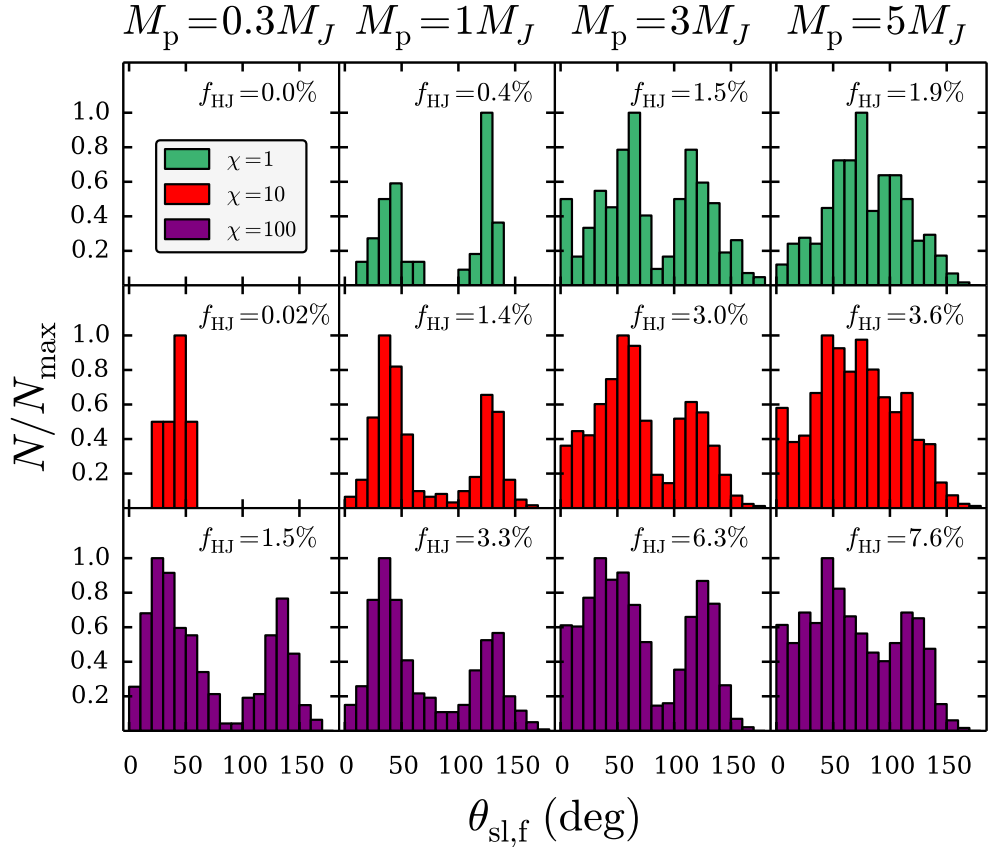


Figure 2.25: Same as Figure 2.24, but showing results for planets around F stars. The distributions shown are the result of $N_{\text{run}} \sim 9000$ total trials, out of which a fraction f_{HJ} resulted in HJ formation (see also Table 2.3). For $M_p = 0.3, 1, 3, 5M_J$ respectively, the number of data points N_{HJ} in each histogram are as follows: top row, $\chi = 1$, $N_{\text{HJ}} = 0, 75, 310, 394$; middle row, $\chi = 10$, $N_{\text{HJ}} = 5, 305, 640, 764$; bottom row, $\chi = 100$, $N_{\text{HJ}} = 330, 711, 1339, 1609$.

2.6 Conclusion

2.6.1 Summary of Results

The main goal of this paper is to conduct a thorough population synthesis of the production of misaligned close-in giant planets (Hot Jupiters, HJs) in stellar bi-

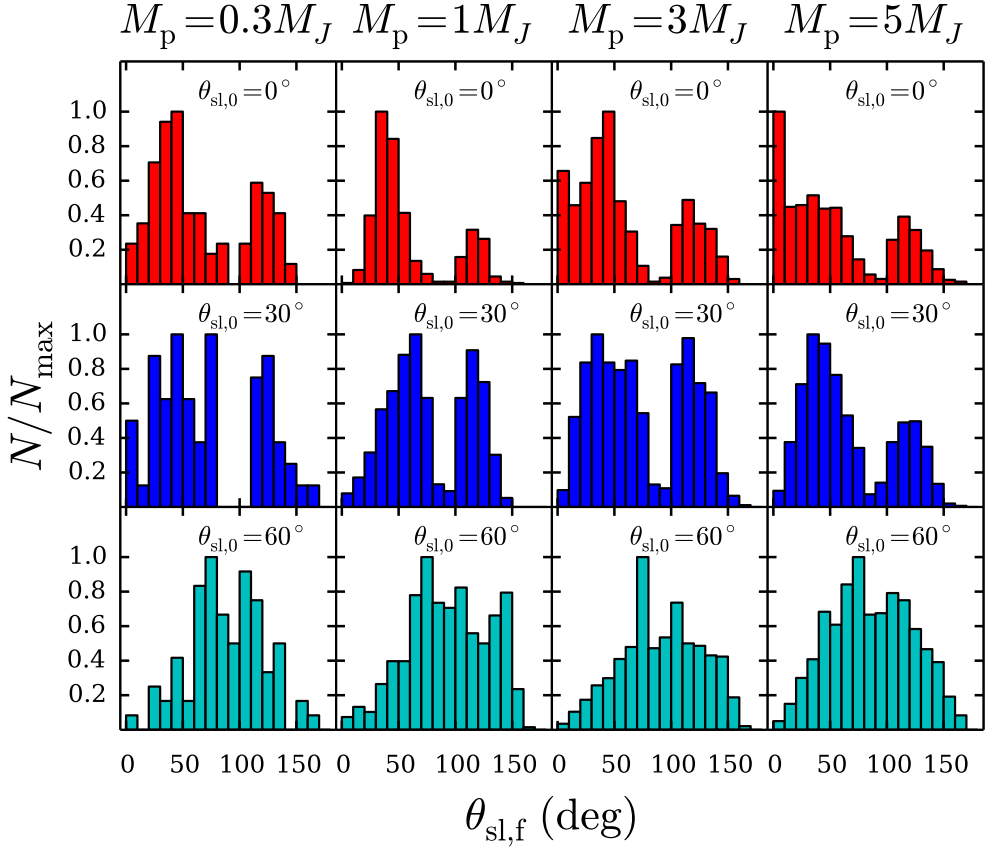


Figure 2.26: The effect of primordial misalignment ($\theta_{\text{sl},0} \neq 0$) on distributions of $\theta_{\text{sl},f}$. We show results for planets around G stars, with the canonical dissipation strength $\chi = 10$. Top row (red): $\theta_{\text{sl},0} = 0^\circ$, as shown previously in Fig. 2.20. Middle row (blue): $\theta_{\text{sl},0} = 30^\circ$. Bottom row (cyan): $\theta_{\text{sl},0} = 60^\circ$. For $M_p = 0.3, 1, 3, 5M_J$ respectively, the number of data points N_{HJ} in each histogram are as follows: top row (from left to right), $\theta_{\text{sl},0} = 0^\circ$, $N_{\text{HJ}} = 108, 502, 811, 990$. Middle row, $\theta_{\text{sl},0} = 30^\circ$, $N_{\text{HJ}} = 61, 544, 844, 1021$. Bottom row, $\theta_{\text{sl},0} = 60^\circ$, $N_{\text{HJ}} = 82, 556, 943, 1037$. See Table 2.3 for further information.

naries by the mechanism of Lidov-Kozai (LK) oscillations with tidal dissipation, examining the previously unexplored dependence on planet mass, and stellar type and spin properties. The complex evolution of the stellar spin axis in systems with planets undergoing LK oscillations poses a rich dynamical problem (see also Storch et al., 2014; Storch & Lai, 2015), and can affect the final distributions of spin-orbit misalignments. We have calculated the HJ production fractions and planet tidal disruption fractions for a wide variety of systems, exploring their dependence on planet mass, stellar properties and tidal dissipation rate. We have also presented a number of semi-analytical calculations, which are useful in understanding the results of our population synthesis. Our main results can be summarized as follows.

- Planet mass is important in determining the HJ formation and tidal disruption fractions (see Table 2.3). The fraction of systems resulting in HJs (f_{HJ}) increases with planet mass, due to fewer tidal disruptions. For Jupiter-mass planets, we find that $f_{\text{HJ}} \approx 0.5\% - 4\%$ depending on the assumed tidal dissipation rate and host star mass. In general f_{HJ} increases with the tidal dissipation rate and decreases with stellar mass. For more massive ($5M_J$) planets, we find a higher fraction, with $f_{\text{HJ}} \approx 3\% - 7.5\%$. The fraction of systems resulting in “hot Saturns” ($M_p \sim 0.3M_J$) are low, especially around massive ($M_\star = 1.4M_\odot$, spectral type F) stars. As a result, hot Saturns around massive stars are unlikely to be produced by LK migration in binaries, unless the tidal dissipation strength in the planet is high (with $\chi \gtrsim 100$, corresponding to $\Delta t_L \gtrsim 10$ sec).
- We find that the “migration fraction,” defined as the sum of the HJ and disruption fractions, $f_{\text{mig}} = f_{\text{HJ}} + f_{\text{dis}}$, has a rather weak dependence on planet mass, stellar type and tidal dissipation rate, and is always in the

range of 11 – 14% (see Table 3). This behavior can be qualitatively understood from analytical migration criteria (see Section 3.4 and Section 5.4.1, particularly Eq. (2.47)). Since the tidal disruption fraction for lower mass planets is higher (due to the increased tidal radius), a constant migration fraction implies that f_{HJ} should decrease with planet mass, as described above.

- HJs are produced only in systems when the ratio of the binary semi-major axis a_b and the initial planet semi-major axis a_0 lies in the range $60 \lesssim a_b/a_0 \lesssim 300$ (see Figs 18-19). In addition, no HJs are produced for systems with the dimensionless octupole parameter (see Eq. [2.4]) $\varepsilon_{\text{oct}} \gtrsim 0.01 - 0.02$, where the range depends on the planet mass (see Figs. 2.18-2.19). These place constraints on the types of binary properties and initial planet semi-major axes that are able to induce migration without causing tidal disruption.
- The distribution of final spin-orbit misalignment angles depends on planet mass and the spin history of host stars (see Figs. 24-25). For $M_p = (1-3)M_J$, the distributions are always bimodal, with peaks near $\theta_{\text{sl,f}} \approx 40^\circ$ and 130° . This bimodality is independent of stellar type. For solar-type stars, higher-mass planets ($M_p = 5M_J$) exhibit a preference for low final obliquities, with $\theta_{\text{sl,f}} < 10^\circ$ (see Fig. 2.20 and Fig. 2.24), although misalignment still remains possible. By contrast, for F-stars, the $\theta_{\text{sl,f}}$ distributions for massive planets are broad, with no clear bimodality (see Fig. 2.25). We attribute the higher degree of misalignment around F stars to the stronger torque from the (more rapidly rotating) host star acting on the orbit, thereby erasing the tendency towards alignment observed for $5M_J$ planets around G stars. In general, the backreaction torques from the stel-

lar quadrupole on the planet’s orbit, as well as the octupole effect from the binary companion, give rise to a variety of evolutionary paths toward spin-orbit misalignments during LK migration (Section 4), and result in a complicated dependence of the $\theta_{\text{sl},f}$ -distribution on planet mass and stellar type.

- The final stellar obliquity distribution does not depend significantly on tidal dissipation rate within the planet, although higher rates of dissipation do tend to broaden the distributions.
- While most of the calculations in this paper assume initial alignment between the stellar spin and planet’s orbit axis ($\theta_{\text{sl},0} = 0^\circ$), we also explore the effect of an initial (“primordial”) misalignment. We find that the bimodality present when $\theta_{\text{sl},0} = 0^\circ$ begins to merge as $\theta_{\text{sl},0}$ increases (see Fig. 2.26). For modest initial misalignments ($\theta_{\text{sl},0} = 30^\circ$), the final $\theta_{\text{sl},f}$ distribution remains bimodal across all planet masses, with the peaks slightly shifted towards 90° . For higher initial misalignment ($\theta_{\text{sl},0} = 60^\circ$) the bimodality has nearly vanished, and the distribution is broadly distributed and centered near $\theta_{\text{sl},f} \sim 70^\circ - 80^\circ$.

2.6.2 Discussion

Previous studies of HJ production in stellar binaries that include the octupole potential (Naoz et al., 2012; Petrovich, 2015b) focused on a single planet mass and initial planet semi-major axis ($M_p = 1M_J$, $a_0 = 5$ AU), and a single host star type ($M_\star = 1M_\odot$, with constant spin rate). This paper has expanded upon these previous works by exploring a range of giant planet masses and orbital separations ($M_p = 0.3 - 5M_J$, $a_0 = 1 - 5$ AU) and two host stellar types ($M_\star = 1, 1.4M_\odot$),

with each stellar type governed by differing magnetic braking laws. We also consider systems with “primordial misalignment” where the initial stellar obliquity $\theta_{\text{sl},0} \neq 0$.

In terms of HJ production fractions (f_{HJ}), our results are in good agreement with Petrovich (2015b). We find $f_{\text{HJ}} \sim$ a few percent typically, except for sub-Jupiter mass planets which can have much lower fractions ($f_{\text{HJ}} \lesssim 1\%$). In terms of tidal disruptions, Petrovich (2015b) finds a much higher disruption fraction, with $f_{\text{dis}} \sim 25\%$, in part because he places all planets initially at $a_0 = 5$ AU from the host star, whereas we vary the initial semi-major axis uniformly in the range $a_0 = 1 - 5$ AU. Planets that begin at larger orbital separations experience stronger forcing from the binary and less pericenter precession due to SRFs, and thus can achieve sufficiently high eccentricities such that the pericenter distance $a_p = a(1 - e_{\max})$ is smaller, resulting in more disruptions (see Fig. 6). Another reason for the higher disruption fractions quoted in Petrovich (2015b) lies in the choice of binary eccentricity range (he chooses a maximum $e_b = 0.9 - 0.95$, in contrast with 0.8 assumed in this work). As noted before (see the beginning of Section 5.4), the actual eccentricity distribution of stellar binaries (especially those that allow planet formation) is very uncertain. Also, including binaries with $e_b \gtrsim 0.9$ may result in over-populating systems close to the stability limit (with small $a_b(1 - e_b)/a_0$). Our HJ fractions (for $M_p = 1 M_J$ around solar-type stars) are lower than those found in Naoz et al. (2012), who give $f_{\text{HJ}} \sim 15\%$. One major reason for the difference is that Naoz et al. (2012) use the tidal radius Eq. (2.48), but set $f \simeq 0.6$, whereas we use $f = 1$. Note that since the migration fraction $f_{\text{mig}} = f_{\text{HJ}} + f_{\text{dis}}$ is always in range of 11-14% regardless of planet mass and stellar type (see Section 5.4.1 and Table 3), in the extremely unlikely event that all of our tidally disrupted planets actually survived as HJs, the maximum

possible HJ production fraction from our simulations is $f_{\text{HJ,max}} = f_{\text{mig}} \sim 13\%$.

Observations constrain the HJ occurrence rate around solar-type stars to be $\sim 1\%$ (e.g. Wright et al., 2012). Since the observed stellar companion fraction in HJ systems is $\lesssim 50\%$ (Ngo et al., 2015), our calculations imply that LK migration from stellar companions can probably explain around $\sim 15\%$ of observed HJs (using $f_{\text{HJ}} = 3\%$, and assuming a giant planet occurrence rate of 10%).

The calculations presented in this paper never produce HJs with final orbital periods $P_{\text{orb,f}} \gtrsim 4.5$ days, with typical periods in the range of 1 – 3 days, depending on planet mass and tidal dissipation strength (see Fig. 23). More massive planets tend to have shorter periods (sometimes $\lesssim 1$ day) because they can survive tidal disruption during the high-eccentricity periastron passage. Thus, it is clear that LK migration in stellar binaries cannot explain the observed population of HJs with periods greater than 4 days (see also Petrovich 2015b for an in-depth discussion of the tendency for LK migration to produce an excess of “Very Hot Jupiters” compared to observations.) In addition, for both types of stars, our calculations yield very few planets in the process of migration. In particular, very few “warm Jupiters” are produced with $0.1 \lesssim a \lesssim 0.5$ AU after evolving the system for 5 Gyr (see also Petrovich 2015b).

In the absence of primordial misalignment (so that $\theta_{\text{sl},0} = 0^\circ$), our calculations always predict, for planet masses $M_p = 1 - 3M_J$, a bimodal distribution of final stellar spin-orbit misalignments, with peaks at $\theta_{\text{sl,f}} \approx 40^\circ$ and 130° , and a dearth around 90° . This result is independent of host stellar type and tidal dissipation strength (see Figs. 24-25). Such bimodality results from the stellar spin evolution transitioning from the non-adiabatic to fully adiabatic regime (Storch et al., 2017), and thus may be interpreted as a clear signature of HJ formation

from LK oscillations with tidal dissipation. However, for $M_p = 5M_J$ planets, the shape of the distribution of $\theta_{\text{sl},f}$ differs substantially, and for planets around F stars, nearly polar orbits ($\theta_{\text{sl},f} \sim 90^\circ$) are commonly produced (see Fig. 2.25, right panels).

On the other hand, when significant primordial misalignments are present, with $\theta_{\text{sl},0} \gtrsim 60^\circ$ (see Section 5.6), the bimodality of the final misalignment distribution disappears, and planets on polar orbits are easily produced (see Fig. 2.26, bottom row). Observationally, the distribution of HJ spin-orbit misalignments does not exhibit a clear bimodal structure (e.g. Albrecht et al., 2012a) and a handful of observed systems have nearly polar orbits, such as WASP-1b (Simpson et al., 2011), WASP-7b (Albrecht et al., 2012b), and WASP-79b (Addison et al., 2013) (these systems mostly have $M_p \sim 1M_J$ and host star mass $M_\star \approx 1.2 - 1.5M_\odot$). Thus, without substantial primordial misalignments, LK migration in stellar binaries cannot explain the observed $\theta_{\text{sl},f}$ distribution of HJs. This again suggests that the majority ($\sim 85\%$) of HJs are probably formed by other mechanisms (e.g., disk-driven migration).

One physical effect not included in this paper is tidal dissipation in the host stars. This can in principle affect the semi-major axis of very close-in giant planets, and change the spin-orbit misalignment angle, as studied in numerous papers (e.g., Barker & Ogilvie, 2009; Jackson et al., 2009; Winn et al., 2010; Matsumura et al., 2010; Lai, 2012; Rogers & Lin, 2013; Xue et al., 2014; Valsecchi et al., 2014). We neglect stellar tidal dissipation on purpose in this paper because, compared to tidal dissipation in planets, stellar tides play a negligible role in circularizing high-eccentricity planets undergoing LK oscillations. Moreover, the stellar tidal dissipation rate is highly uncertain, and likely depends on the stel-

lar type and planet mass (see Ogilvie 2014 for a review); it is also possible that the tidal process and timescale for spin-orbit alignment are different from those for orbital decay (Lai 2012). Once an HJ has formed through high-eccentricity migration, it is straightforward to examine the effect of stellar tides (using parameterized tidal models) on the subsequent evolution of the system.

CHAPTER 3

**TEETERING STARS: RESONANT EXCITATION OF STELLAR
OBLIQUITIES BY HOT AND WARM JUPITERS WITH EXTERNAL
COMPANIONS**

3.1 Introduction

Stellar spin-orbit misalignments (obliquities) in exoplanetary systems with a close-in planet have received significant attention in recent years. The majority of detailed obliquity measurements have been conducted in hot Jupiter (HJ, giant planets with orbital periods less than ten days) systems via Rossiter-McLaughlin observations (e.g. Winn et al., 2005; Hébrard et al., 2008; Narita et al., 2009; Winn et al., 2009; Triaud et al., 2010; Albrecht et al., 2012a), yielding a wide range of sky-projected obliquities, and even some retrograde systems (Winn & Fabrycky, 2015). Stellar obliquities provide a clue to the system's dynamical history, and may shed insight into planetary migration mechanisms. Since there is still no consensus on how HJs arrived at their short-period orbits, with several different proposed migration theories, and even in-situ formation (e.g. Dawson, & Johnson, 2018), understanding the origins of stellar obliquities will further our understanding of HJ formation/migration. In recent years, warm Jupiters (WJs, giant planets with orbital periods between 10 and 300 days) have gained considerable attention alongside HJs, and raise similar questions regarding their formation/migration. Whether HJs and WJs arise from a single

This chapter is adapted from Anderson, & Lai (2018).

or multiple formation channels is still an open question.

Low stellar obliquities are frequently attributed to either in-situ formation or disk-driven migration, in which the planetary orbit shrinks due to gravitational torques from the protoplanetary disk. In contrast, high obliquities may be attributed to high-eccentricity migration, in which gravitational interactions with other planets or a distant stellar companion raise the orbital eccentricity of a “cold Jupiter” to a large value, so that tidal dissipation at pericenter passages leads to orbital decay (e.g. Rasio & Ford, 1996; Wu & Murray, 2003; Fabrycky & Tremaine, 2007; Nagasawa et al., 2008; Wu & Lithwick, 2011; Beaugé & Nesvorný, 2012; Naoz et al., 2012; Petrovich, 2015a,b; Anderson et al., 2016; Muñoz et al., 2016; Hamers et al., 2017). High-eccentricity migration often results in large changes in orbital inclination, and even more extreme changes in the orientation of stellar spin axis itself (Storch et al., 2014; Storch & Lai, 2015; Anderson et al., 2016; Storch et al., 2017), and is thus a natural way of producing large stellar spin-orbit misalignments. However, as an alternative explanation for high obliquities, various works have investigated the possibility of tilting the protoplanetary disk itself relative to the stellar spin axis. Such primordial misalignments may allow for in-situ formation or disk-migration to result in high obliquities, albeit with varying degrees of success (Bate et al., 2010; Foucart & Lai, 2011; Lai et al., 2011; Batygin, 2012; Batygin & Adams, 2013; Lai, 2014; Spalding & Batygin, 2014; Fielding et al., 2015; Zanazzi & Lai, 2018). Given these results, exactly what obliquities inform us about planetary migration history remains far from obvious.

Thus far, primordial disk misalignment has been the main competitor to high-eccentricity migration in generating high stellar obliquities. In this pa-

per, we consider another mechanism in which a HJ/WJ that formed in-situ or through disk migration may attain in a high stellar obliquity. This mechanism requires that the system host an external, inclined planetary or stellar companion. The companion induces nodal precession of the inner planet, causing its orbital axis to change direction; meanwhile, the oblate host star and the inner planet (a HJ/WJ) experience a mutual torque, causing precession of both the stellar spin and orbital axes. A secular resonance occurs when the spin axis precession frequency (driven by the inner planet) is comparable to the orbital nodal precession frequency driven by the companion, potentially leading to large stellar obliquities, even for nearly aligned initial configurations (Lai, Anderson, & Pu, 2018). In this paper, we show that a system consisting of a host star, a HJ or WJ, and an outer companion may naturally pass through this secular resonance due to the spin-down of the star (by magnetic braking), and we examine to what extent large obliquities can be generated through this process. We focus exclusively on planetary companions, but note that the results of this paper may also be applied to stellar companions. In some scenarios, such companions may have previously induced high-eccentricity migration, leading to the formation of a HJ/WJ with a high obliquity. However in this paper, we assume a formation process that resulted in a low initial obliquity (e.g. in-situ formation or migration within a protoplanetary disk aligned with the stellar equator), and identify the prospects for the companion to secularly raise the obliquity following the formation/migration. The assumption of an initially low obliquity may be particularly appropriate for WJs, given that a high-eccentricity migration origin for such planets suffers from a number of difficulties (e.g. see Huang et al. 2016, Antonini et al. 2016, Anderson & Lai 2017).

The role of external companions in affecting stellar obliquities has been stud-

ied before. Some papers considered a spherical host star (e.g. Kaib et al., 2011; Becker et al., 2017) or a slowly rotating star (e.g. Mardling, 2010), so that the direction of the spin axis remains fixed or experiences little variation. Boué & Fabrycky (2014) and Lai, Anderson, & Pu (2018) examined the whole range of spin-orbit behaviors for oblate stars with a constant spin period, taking account of the spin axis changes due to gravitational torques from the inner planet. Our paper builds upon these works by exploring the dynamical evolution on Gyr timescales, so that the stellar spin-down (by magnetic braking) plays an important role in the evolution of the stellar obliquity. In addition, we show that the resulting spin-orbit dynamics and obliquity excitation act to decrease the mutual inclination between the two planets.

The resonant obliquity excitation mechanism studied in this paper requires that the HJ/WJ have external companions with certain ranges of masses and orbital separations, as well as modest inclinations. Distant planetary companions to HJs and WJs are common, with estimated occurrence rates 50% for WJs and up to 80% for HJs (Bryan et al., 2016). There is a growing number of systems with well-characterized orbits for the companion, especially for WJs (see Antonini et al., 2016, for a recent compilation of WJs with external companions). Mutual inclinations in giant planet systems remain far less constrained, although recent observations are beginning to probe individual systems, with several in high-inclination configurations (Mills & Fabrycky, 2017; Masuda, 2017). Upcoming *Gaia* results may provide further constraints on mutual inclinations of giant planet systems (e.g. Perryman et al., 2014).

We note that the present sample of stellar obliquity measurements is limited mostly to HJs. The results of this paper show that high obliquities may be com-

mon for WJs with external companions, regardless of their formation history.

This paper is organized as follows. In Section 6.2.1 we outline the problem setup and review the relevant spin-orbit dynamics. In Section 3.3 we explore in detail the process of resonant obliquity excitation using a somewhat idealized model, where the stellar spin angular momentum is much less than the inner planet orbital angular momentum. Such a model serves as a starting point in understanding the dynamics of more realistic systems, with comparable spin and orbital angular momenta. In Section 6.4 we relax the assumption of small spin angular momentum, and numerically explore the parameter space for HJs/WJs with various types of external companions. We summarize and conclude in Section 5.4.

3.2 Setup & Classification of Dynamical Behavior

We consider an oblate star of mass M_* , radius R_* , and spin period P_* , hosting a close-in giant planet m_1 (either a HJ or WJ) in a circular orbit with semi-major axis a_1 , and a distant perturber m_p , with semi-major axis a_p , eccentricity e_p , and inclination I relative to the orbit of the inner planet. Both planets are considered as point masses. The star has spin angular momentum S_* , and the inner planet and the perturber have orbital angular momenta L_1 and L_p respectively. The quadrupole-order secular equations of motion for the spin unit vector $\hat{s}_* = S_*/S_*$ and the orbital angular momentum unit vectors $\hat{l}_1 = L_1/L_1$ and

$\hat{\mathbf{l}}_p = \mathbf{L}_p/L_p$ are

$$\frac{d\hat{\mathbf{s}}_\star}{dt} = \omega_{\star 1}(\hat{\mathbf{s}}_\star \cdot \hat{\mathbf{l}}_1)(\hat{\mathbf{s}}_\star \times \hat{\mathbf{l}}_1) \quad (3.1)$$

$$\frac{d\hat{\mathbf{l}}_1}{dt} = \omega_{1p}(\hat{\mathbf{l}}_1 \cdot \hat{\mathbf{l}}_p)(\hat{\mathbf{l}}_1 \times \hat{\mathbf{l}}_p) + \frac{S_\star}{L_1}\omega_{\star 1}(\hat{\mathbf{l}}_1 \cdot \hat{\mathbf{s}}_\star)(\hat{\mathbf{l}}_1 \times \hat{\mathbf{s}}_\star) \quad (3.2)$$

$$\frac{d\hat{\mathbf{l}}_p}{dt} = \frac{L_1}{L_p}\omega_{1p}(\hat{\mathbf{l}}_p \cdot \hat{\mathbf{l}}_1)(\hat{\mathbf{l}}_p \times \hat{\mathbf{l}}_1), \quad (3.3)$$

where the relevant precession frequencies are

$$\omega_{\star 1} = \frac{3k_{q\star}}{2k_\star} \left(\frac{m_1}{M_\star} \right) \left(\frac{R_\star}{a_1} \right)^3 \Omega_\star, \quad (3.4)$$

and

$$\omega_{1p} = \frac{3m_p}{4M_\star} \left(\frac{a_1}{\tilde{a}_p} \right)^3 n. \quad (3.5)$$

In equation (3.4), $\Omega_\star = 2\pi/P_\star$ is the angular frequency of the star, and k_\star and $k_{q\star}$ are related to the stellar moment of inertia and quadrupole moment (see Lai, Anderson, & Pu 2018) for precise definitions. In equation (3.5), $n = \sqrt{GM_\star/a_1^3}$ is the orbital mean motion of the inner planet, and we have defined an effective semi-major axis of the perturber²,

$$\tilde{a}_p \equiv a_p \sqrt{1 - e_p^2}. \quad (3.6)$$

Note that in equations (3.1) - (3.3) we have neglected the coupling between the star and outer planet (see Lai, Anderson, & Pu, 2018), which induces precession of $\hat{\mathbf{s}}_\star$ at a rate $\omega_{\star p} \sim (m_p/M_\star)(R_\star^3/\tilde{a}_p^3)\Omega_\star$, and is completely negligible for this problem.

The dynamical behavior of the system can be described as follows: $\hat{\mathbf{s}}_\star$ and $\hat{\mathbf{l}}_1$ mutually precess around the axis defined by $\mathbf{S}_\star + \mathbf{L}_1$, while, $\hat{\mathbf{l}}_1$ and $\hat{\mathbf{l}}_p$ undergo mutual precession around the total orbital angular momentum axis defined by

²The perturber properties enter mainly in the combination $\tilde{a}_p/m_p^{1/3}$; however, we note that additional dependence is introduced through the ratio L_1/L_p .

$\mathbf{L}_1 + \mathbf{L}_p$. The evolution of $\hat{\mathbf{s}}_*$ due to the forcing of $\hat{\mathbf{l}}_1$ (which is itself being forced by $\hat{\mathbf{l}}_p$) is therefore complicated, depending crucially on the relative precession rates ω_{*1} and ω_{1p} , as well as the angular momentum ratio S_*/L_1 . For a rapidly rotating star, S_* can be comparable to L_1 , so that the back-reaction torque from the oblate star on the orbit is non-negligible.

Meanwhile, the rotation rate of the star Ω_* decreases due to magnetic braking. We adopt the Skumanich law ($\dot{\Omega}_* \propto -\Omega_*^3$; see Skumanich 1972, Bouvier 2013) for the stellar spin-down, so that the spin frequency as a function of time is given by

$$\Omega_* = \frac{\Omega_{*,0}}{\sqrt{1 + \alpha_{MB}\Omega_{*,0}^2 t}}, \quad (3.7)$$

where $\Omega_{*,0}$ is the initial spin rate and α_{MB} is a constant, calibrated such that the rotation period reaches ~ 30 days at an age ~ 5 Gyr. In this work we adopt $\alpha_{MB} = 1.5 \times 10^{-14}$ yr, appropriate for solar-mass stars (Barker & Ogilvie, 2009).

The qualitative spin-orbit dynamics depend on the relevant precession rates (Boué & Fabrycky, 2014; Lai, Anderson, & Pu, 2018). Lai, Anderson, & Pu (2018) describe the spin-orbit dynamics by introducing the dimensionless parameter ϵ_{*1} , which, for a giant planet on a short period orbit can be approximated as

$$\begin{aligned} \epsilon_{*1} &= \frac{\omega_{1p} - \omega_{*p}}{\omega_{*1}(1 + S_*/L_1)} \simeq \frac{\omega_{1p}}{\omega_{*1}} \left(\frac{1}{1 + S_*/L_1} \right) \\ &\simeq 1.25 \left(\frac{k_*}{6k_{q*}} \right) \left(\frac{m_p}{m_1} \right) \left(\frac{a_1}{0.04 \text{ AU}} \right)^{9/2} \left(\frac{\tilde{a}_p}{1 \text{ AU}} \right)^{-3} \\ &\quad \times \left(\frac{P_*}{30 \text{ d}} \right) \left(\frac{M_*}{M_\odot} \right)^{1/2} \left(\frac{R_*}{R_\odot} \right)^{-3} \left(\frac{1}{1 + S_*/L_1} \right). \end{aligned} \quad (3.8)$$

We summarize the key points from Lai, Anderson, & Pu (2018) here: (i) If $\epsilon_{*1} \ll 1$, $\hat{\mathbf{s}}_*$ and $\hat{\mathbf{l}}_1$ are strongly coupled and undergo rapid mutual precession, and the spin-orbit angle $\theta = \theta_{*1}$ (the angle between $\hat{\mathbf{s}}_*$ and $\hat{\mathbf{l}}_1$) satisfies $\theta \simeq \text{constant}$. If $\hat{\mathbf{s}}_*$ and $\hat{\mathbf{l}}_1$ are initially aligned, spin-orbit misalignment cannot be generated

when $\epsilon_{*1} \ll 1$. (ii) If $\epsilon_{*1} \gg 1$, \hat{s}_* and \hat{l}_1 are weakly coupled, and both precess around the total orbital angular momentum axis, but \hat{l}_1 precesses at a much faster rate than \hat{s}_* . As a result, the spin-orbit angle varies between a minimum and a maximum value. For an initially aligned system, and when $L_1 \ll L_p$, the spin-orbit angle varies in the range $0 \lesssim \theta \lesssim 2I$ over a precession cycle. (iii) If $\epsilon_{*1} \simeq 1$, a secular spin-orbit resonance occurs due to the commensurability between the precession frequencies ω_{*1} and ω_{1p} , and θ may grow to a large value. See also Lai & Pu (2017) (particularly Appendix A) and Pu & Lai (2018) (Section 2.2) for more theory on the details of this resonance.

Lai, Anderson, & Pu (2018) considered systems where the stellar spin-rate was held constant. In this case, resonant excitation of obliquity requires an outer perturber with somewhat fine-tuned properties, due to the strong dependence of ϵ_{*1} on \tilde{a}_p . However, over Gyr timescales, the stellar spin period is reduced by a factor of ~ 10 due to magnetic braking, so that ϵ_{*1} is a function of time. Systems that begin with spin-orbit alignment and $\epsilon_{*1} \ll 1$ (in the strong-coupling regime) may eventually cross $\epsilon_{*1} \simeq 1$ due to magnetic braking, so that θ resonantly grows. After the resonance is encountered, the system enters the weak-coupling regime, with θ varying between a minimum and a maximum. We will show in this paper that the “final” range of variation of the spin-orbit angle (following resonant excitation) depends on the spin history of the system.

Resonant excitation of stellar obliquities requires that the system initially satisfy $\epsilon_{*1} \lesssim 1$. In addition, in order for the resonance to be encountered within a reasonable time (within, say 5 Gyr), we require that $\epsilon_{*1}(t = 5\text{Gyr}) \gtrsim 1$. For an inner planet with $m_1 = M_J$ and various values of a_1 , and an initial stellar spin period of 1 day (roughly the lower limit obtained from observations of T-Tauri

stars), the range of perturber “strength” ($\tilde{a}_p/m_p^{1/3}$) allowing resonant obliquity excitation may be identified, shown as the shaded grey region in Fig. 3.1. Note that this region allowing resonant growth narrows slightly with increasing initial stellar spin period (the lower boundary, solid blue line). The upper boundary (dashed blue line) is independent of initial spin period, because solar-type stars “forget” their initial spin periods after several hundred Myr. The boundaries of parameter space allowing resonant obliquity excitation in Fig. 3.1 are approximate. In Section 6.4 we perform a thorough numerical exploration of the parameter space and numerically confirm that the shaded region in Fig. 3.1 does indeed identify the parameter space available for resonant obliquity growth.

Since a sufficiently inclined perturber can also excite the inner planet eccentricity, we plot the necessary condition for quadrupole-level Lidov-Kozai eccentricity oscillations in Fig. 3.1. This arises from requiring that the rate of apsidal precession due to general relativity is sufficiently slow compared to that induced by the perturber (see, e.g. equation 29 of Anderson et al., 2017). For a given value of a_1 , perturbers below the black dotted line may induce Lidov-Kozai oscillations. Note that this condition is necessary for Lidov-Kozai cycles to develop, but not sufficient, because a minimum mutual inclination ($I_{LK,min}$) is also required.³ In the idealized scenario where apsidal precession from general relativity and other “short-range-forces” are neglected, $I_{LK,min} \simeq 40^\circ$. Inclusion of short-range forces causes $I_{LK,min}$ to exceed 40° , often by a considerable amount. Inspection of Fig. 3.1 reveals that there is some parameter space for HJs that may allow both resonant obliquity excitation and Lidov-Kozai cycles (although note that the required perturber must be quite close/strong, and of-

³An upper boundary $I_{LK,max}$ also exists, so that Lidov-Kozai cycles also require $I_0 < I_{LK,max}$ (with $I_{LK,max}$ retrograde). However, this upper boundary is probably irrelevant for planetary companions, as such retrograde inclinations are not easily produced.

ten in conflict with observational constraints of companions to HJs; Huang et al. 2016). Since this paper assumes circular orbits for HJs/WJs, for simplicity we will always restrict our attention to initial inclinations less than 40° to ensure that Lidov-Kozai oscillations do not arise. However, we note that the qualitative spin-orbit dynamics discussed in this paper will often hold for higher inclinations, as long as $I_0 < I_{\text{LK},\min}$. If Lidov-Kozai oscillations do occur, then the evolution of the stellar spin axis becomes chaotic (Storch et al., 2014; Storch & Lai, 2015), which may allow the full range of obliquities ($0^\circ - 180^\circ$) to be explored. This issue is beyond the scope of this paper.

In this paper we neglect tides raised by the planet on the host star, which may lead to orbital decay and damping of obliquities. The timescale for tides to reduce the semi-major axis of a planet around a solar-type star is

$$t_a \simeq 1.3 \times 10^{11} \text{ yr} \left(\frac{Q'_*}{10^7} \right) \left(\frac{m_1}{M_J} \right)^{-1} \left(\frac{a_1}{0.04 \text{ AU}} \right)^{13/2}, \quad (3.9)$$

where $Q'_* = 3Q_*/(2k_2)$ is the reduced tidal quality factor. The timescale for obliquity decay is $t_\theta \sim (S_*/L_1)t_a$ (see Lai, 2012, for a discussion on the relation between t_a and t_θ). Although stellar tides can be important for HJs that are massive and/or in sufficiently short-period orbits, tides are unimportant for HJs that may experience changes in stellar obliquity from external companions. For example, using the canonical values of Q'_* and m_1 in equation (3.9), a HJ with $a_1 \simeq 0.02$ AU has a tidal decay timescale $t_a \simeq 1.4$ Gyr, so that tides may indeed sculpt the semi-major axis and stellar obliquity over the \sim Gyr timescales of interest in this paper. However, such a system will always be in the strong-coupling regime ($\epsilon_{*1} \ll 1$) throughout the main-sequence lifetime of the star, unless the system hosts an extremely strong external perturber, with $\tilde{a}_p/m_p^{1/3} \lesssim 0.4 \text{ AU}/M_J^{1/3}$. Since HJs have been shown to lack such companions (Huang et al., 2016), we expect tides (for $Q'_* \sim 10^6 - 10^7$) to be completely negligible for the

systems of interest in this paper.

The above estimate of the tidal timescales (with $Q'_* \sim 10^7$) assumes equilibrium tides (Zahn, 1977), where the source of dissipation is damping by turbulent viscosity in the convective region. Mathis (2015) and Bolmont & Mathis (2016) have recently suggested that Q'_* may briefly attain a much lower value ($Q'_* \sim 10^{3.5}$) for rapidly rotating pre-main-sequence stars, due to excitation and damping of inertial waves in the convective shell (see Ogilvie 2013 for the original calculation based on idealized two-zone stellar models). The ensuing orbital evolution of HJs in this scenario was recently explored by Heller (2018). While intriguing, such a tidal treatment is beyond the scope of this present paper.

3.3 Spin-Orbit Dynamics when $S_* \ll L_1$

In this section we review and develop some analytic results in order to gain insight into the spin-orbit dynamics. We consider a limiting case where $S_*/L_1 \ll 1$, and defer the discussion of comparable S_* and L_1 to Section 3.4. Since realistic HJs and WJs often satisfy $S_* \sim L_1$, especially when the host star is young, the following discussions are somewhat idealized, but shed insight into the dynamical evolution of more complicated systems. Readers interested in the quantitative results and conclusions for more typical HJ and WJ systems (with $S_* \sim L_1$) are referred to Sections 3.4 and 5.4.

The spin-axis dynamics in the limit $S_*/L_1 \ll 1$ has been studied in a variety of contexts, and is related to the well-known Cassini state problem (e.g. Colombo, 1966; Peale, 1969, 1974; Ward et al., 1979; Henrard & Murigande, 1987; Ward & Hamilton, 2004; Fabrycky et al., 2007). In the following we review the

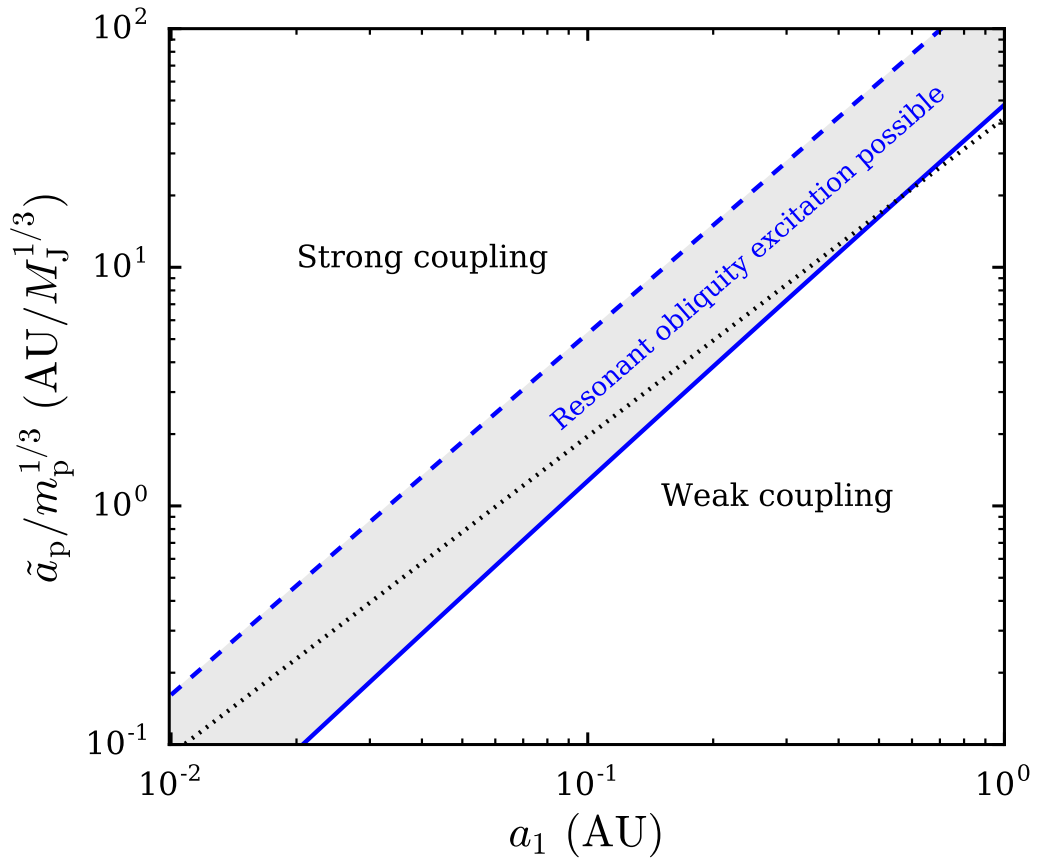


Figure 3.1: Parameter space for resonant excitation of the stellar obliquity to be possible (grey region) for an inner planet with mass $m_1 = M_J$, in terms of its semi-major axis a_1 , and the perturber “strength” $\tilde{a}_p/m_p^{1/3}$, where \tilde{a}_p is given by equation (3.6). The blue solid (dashed) lines indicate constant $\epsilon_{*1} = 1$, with $P_* = 1$ (30) days. The black dotted line indicates the maximum value of $\tilde{a}_p/m_p^{1/3}$ for Lidov-Kozai eccentricity oscillations to be possible, given a sufficiently high inclination.

relevant spin-axis dynamics and Cassini state theory.

3.3.1 Cassini States & Phase Space Structure

When $S_\star \ll L_1$, the back-reaction torque of the spin on the orbit vanishes, so that the orbital axis \hat{l}_1 is unaffected by \hat{s}_\star , and simply undergoes nodal precession due to m_p . The invariable plane is thus defined by the unit vector \hat{j} , in the direction of the total orbital angular momentum $\mathbf{J} = \mathbf{L}_1 + \mathbf{L}_p$, and \hat{l}_1 precesses around \hat{j} , with constant inclination I' according to

$$\frac{d\hat{l}_1}{dt} = g(\hat{j} \times \hat{l}_1), \quad (3.10)$$

where the precession frequency g is

$$g = -\frac{J}{L_p} \omega_{1p} \cos I, \quad (3.11)$$

and where I is the angle between \hat{l}_1 and \hat{l}_p . For ease of notation, we will work in the limit $L_1 \ll L_p$ for the remainder of Section 3, so that $I' \rightarrow I$ and $g \rightarrow -\omega_{1p} \cos I$, but the following results are valid for comparable L_1 and L_p , with \hat{j} replacing \hat{l}_p and I' replacing I .

Following standard procedures, we transform to the frame rotating with frequency g , where \hat{l}_1 is fixed and directed along the z -axis. In this rotating frame, \hat{l}_p is fixed, and \hat{s}_\star evolves according to

$$\left(\frac{d\hat{s}_\star}{dt} \right)_{\text{rot}} = \alpha(\hat{s}_\star \cdot \hat{l}_1)(\hat{s}_\star \times \hat{l}_1) + g(\hat{s}_\star \times \hat{l}_p). \quad (3.12)$$

In equation (3.12), we have adopted standard notation, where the spin precession constant $\alpha = \omega_{\star 1}$. We may rescale time such that $\tau = \alpha t$; thus the spin dynamics only depend on the ratio g/α and I .

The dynamical evolution of \hat{s}_\star can be specified by the obliquity θ (the angle between \hat{s}_\star and \hat{l}_1), and the phase angle ϕ (the longitude of ascending node of

the stellar equator in the rotating frame). Note that $\cos \theta$ and ϕ are canonical variables for the Hamiltonian governing this system, which is given by

$$\mathcal{H} = -\frac{\alpha}{2}(\hat{s}_* \cdot \hat{l}_1)^2 - g(\hat{s}_* \cdot \hat{l}_p). \quad (3.13)$$

The equilibrium, or Cassini states, are obtained by setting equation (3.12) to zero. This requires that \hat{s}_* , \hat{l}_1 , and \hat{l}_p are coplanar (with $\phi = 0$ or π), implying that \hat{s}_* and \hat{l}_1 precess at the same rate in inertial space around \hat{l}_p . The Cassini state obliquities satisfy

$$\frac{g}{\alpha} \sin(\theta - I) + \sin \theta \cos \theta = 0. \quad (3.14)$$

Equation (3.14) has either two or four solutions, depending on the values of g/α and I . Following standard convention and nomenclature (See Figs. 3.2 and 3.3), Cassini states 1, 3 and 4 ($\theta_{1,3,4} < 0$) occur when \hat{s}_* and \hat{l}_p are on opposite sides of \hat{l}_1 ($\phi = 0$), while Cassini state 2 ($\theta_2 > 0$) occurs when \hat{s}_* and \hat{l}_p are on the same side of \hat{l}_1 ($\phi = \pi$).

For convenience, we define $\eta \equiv |g|/\alpha$. Note that η is related to the parameter ϵ_{*1} introduced in Section 2 (see equation 3.8), by $\eta = \epsilon_{*1} |\cos I|$ (for $S_*/L_1 \ll 1$). Thus, $\eta \ll$ corresponds to strong coupling between \hat{s}_* and \hat{l}_1 , while $\eta \gg 1$ corresponds to weak coupling. When $\eta < \eta_{\text{crit}}$, with

$$\eta_{\text{crit}} = (\sin^{2/3} I + \cos^{2/3} I)^{-3/2}, \quad (3.15)$$

all four Cassini states exist, whereas when $\eta > \eta_{\text{crit}}$, only θ_2 and θ_3 exist (see Fig. 3.3).

The Cassini states $\theta_1, \theta_2, \theta_3$ are stable, while θ_4 is unstable and lies along a separatrix in the underlying phase space $(\cos \theta, \phi)$. In Fig. (3.3a) the Cassini states are depicted as a function of η with fixed $I = 20^\circ$. When $\eta = \eta_{\text{crit}}$, θ_1 and θ_4 merge and destroy each other.

The phase space structure (contours of constant \mathcal{H} , see equation [3.13]) is shown in Fig. (3.3b - 3.3e) for increasing values of η . For values of $\eta \ll 1$ (Fig. 3.3b), the separatrix (which passes through θ_4 and encloses θ_2) is relatively narrow, and most of the trajectories circulate (over ϕ) with little variation of $\cos \theta$, although librating trajectories exist close to θ_1 , θ_2 and θ_3 . As η increases, the separatrix widens, and eventually when η is close to, but less than η_{crit} , the “top” of the separatrix touches $\cos \theta = 1$. As η increases further, the shape of the separatrix changes, and encloses θ_1 (see Fig. 3.3c). The phase space just before θ_1 and θ_4 merge is shown in Fig. 3.3d, and just after merging in Fig. 3.3e. When $\eta > \eta_{\text{crit}}$, the only prograde Cassini state is θ_2 .

3.3.2 Spin-Orbit Resonance and Separatrix Crossing

We next consider the scenario where η slowly increases with time. The exact form of $\eta(t)$ is unimportant, as long as η increases slowly compared to all the precession timescales.

When η changes slowly, the area of the phase-space trajectory is constant, so that

$$A \equiv \oint \cos \theta d\phi = \text{constant}. \quad (3.16)$$

Equation (3.16) only holds as long as there are no abrupt changes in the phase space structure (e.g. if η crosses η_{crit} , A is not conserved).

A numerical integration of equation (3.12) with slowly increasing η is shown in Fig. 3.4, where initially $\theta \simeq 0$ and $\eta \ll 1$. At early times, the spin axis is strongly coupled to the orbital axis, so that θ remains nearly constant, and the system librates around Cassini state 1 (θ_1), and the area of the trajectory (A) is

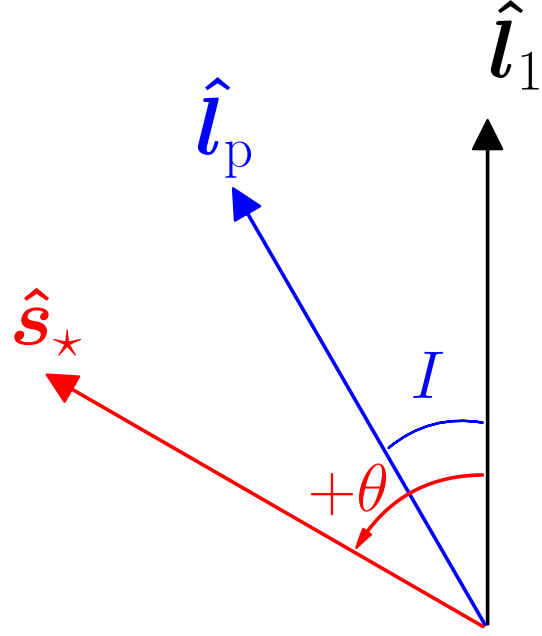


Figure 3.2: Cartoon illustration of the Cassini state configuration (with \hat{s}_* , \hat{l}_1 , and \hat{l}_p located in the same plane) and the adopted sign convention for θ . When $\theta > 0$, \hat{s}_* and \hat{l}_p are located on the same side of \hat{l}_1 (as shown, corresponding to θ_2). When $\theta < 0$, \hat{s}_* and \hat{l}_p are on opposite sides of \hat{l}_1 (corresponding to $\theta_{1,3,4}$).

small. As η increases, θ_1 increases in magnitude, and the spin axis continues to librate around θ_1 while preserving phase-space area. Eventually, when $\eta = \eta_{\text{crit}}$, θ_1 merges with θ_4 , and the system is forced to cross the separatrix. At the separatrix crossing, the obliquity undergoes a rapid increase and the phase-space area increases by a factor of ~ 100 . After the separatrix crossing, ϕ circulates, and θ varies between a maximum and minimum value, determined by the area of the separatrix when $\eta = \eta_{\text{crit}}$. The system continues to evolve, while preserving the new, much larger phase space area. We refer to the process of rapid obliquity growth during the separatrix crossing as resonant excitation of the obliquity.

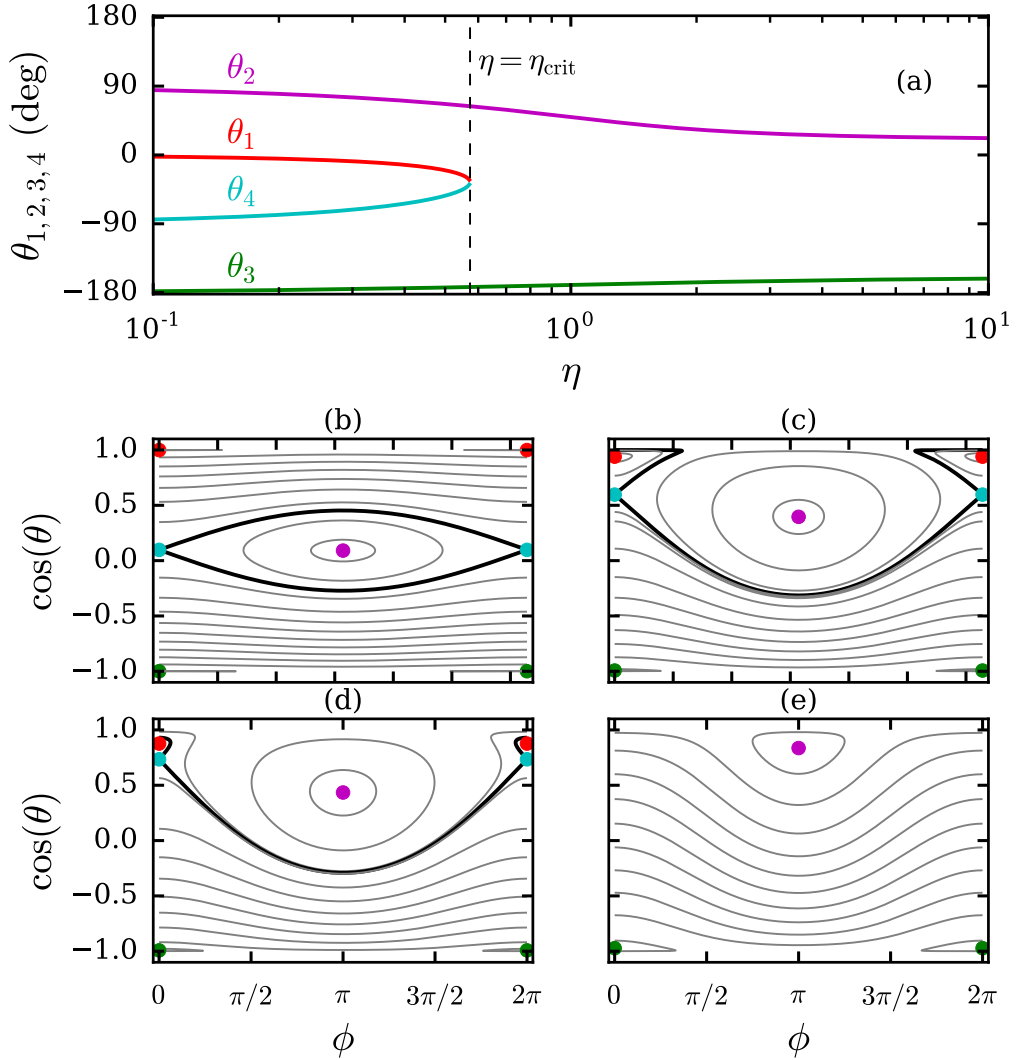


Figure 3.3: Panel (a): Cassini states $\theta_{1,2,3,4}$ versus $\eta = |g|/\alpha$, with fixed $I = 20^\circ$. Panels (b) - (e): Phase-space portraits for various values of η . Panel (b): $\eta = 0.1$. For such a small η , the separatrix (thick black curve passing through θ_4) is narrow, and almost all trajectories outside of the separatrix circulate, except for small librations very close to θ_1 and θ_3 . Panel (c): $\eta = 0.5$. As η increases, the separatrix expands until it touches $\cos \theta = 1$ (not shown here), after which the shape of the separatrix abruptly changes, now enclosing θ_1 . Panel (d): $\eta = 0.561$. Phase space just before θ_1 and θ_4 merge. Panel (e): $\eta = 2$. Phase space after θ_1 and θ_4 have merged, so that the only remaining Cassini states are θ_2 and θ_3 .

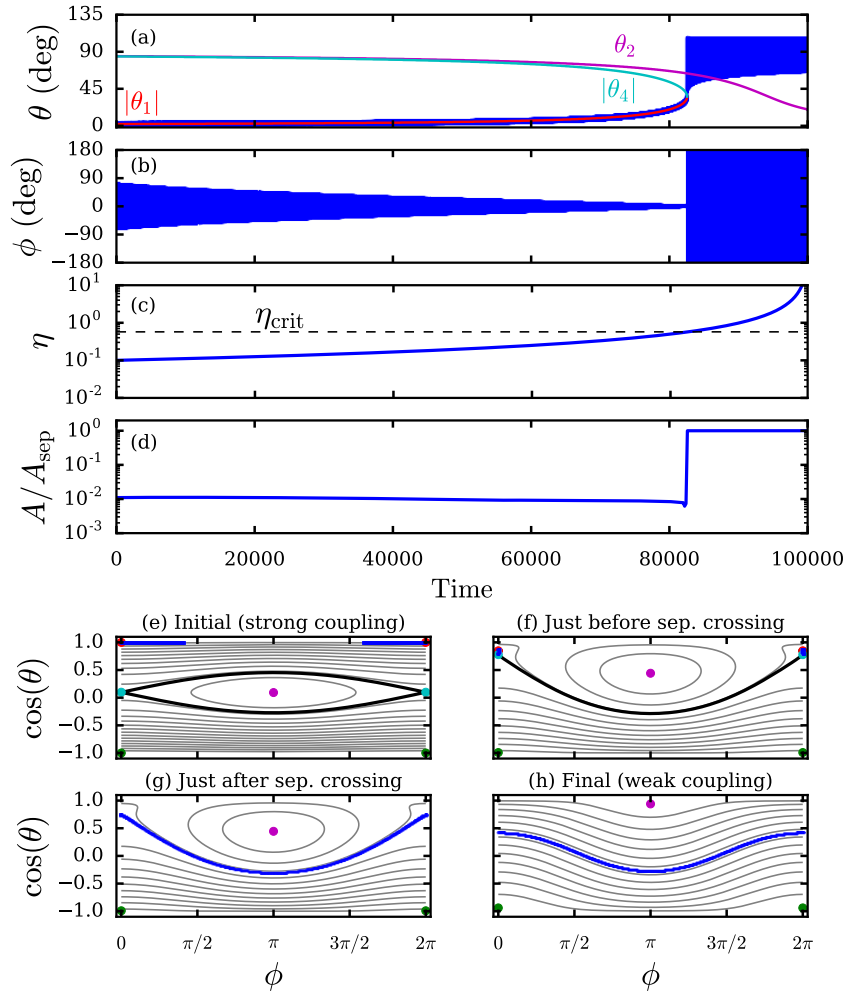


Figure 3.4: Spin evolution with slowly increasing η , for a system with $S_*/L_1 \ll 1$, so that $I = \text{constant}$ (as discussed in Section 3). All blue curves show the result of a numerical integration of equation (3.12), where $\eta = |g|/\alpha$ slowly increases with time according to $\eta \propto (1-ct)^{-1}$, where c is a constant. Panels (a)-(d) show the obliquity (θ), the precessional phase of \hat{s}_* in the rotating frame (ϕ), the coupling parameter η , and phase space area A (normalized by the area of separatrix when $\eta = \eta_{\text{crit}}$). Panels (e)-(h) show the phase space trajectory obtained from the numerical integration (blue curves), along with the underlying phase space (grey contours), fixed points, and separatrix (thick black curve). Panel (e): Initial phase space, when $\eta = 0.1$ and the spin axis librates around θ_1 . Panel (f): Phase space just before θ_1 and θ_4 merge, with the spin axis tightly enclosed by the separatrix and librating around θ_1 (compare with Fig. 3.3c). Panel (g): Phase space just after θ_1 and θ_4 merge. The spin axis now circulates around the only remaining prograde Cassini state, θ_2 . Panel (h): Phase space when $\eta \gg 1$, showing the final degree of obliquity variation, which varies in the range $2I$.

Since the phase-space area following the separatrix crossing is simply the area enclosed by the separatrix itself when $\eta = \eta_{\text{crit}}$ (denoted as A_{sep}), the final (when $\eta \gg 1$), average value of θ can be estimate from

$$(\cos \theta)_{\text{ave}} \simeq \frac{A_{\text{sep}}}{2\pi}. \quad (3.17)$$

Since the spin and orbit are weakly coupled when $\eta \gg 1$, the range of obliquity variation (centered around θ_{ave}) is simply $2I$. Fig. 3.5 shows θ_{ave} as a function of inclination, as determined by equation (3.17), along with the range of obliquity variation when $\eta \gg 1$, obtained from numerical integrations. Equation (3.17) well captures the “average” value of obliquity following resonant excitation.

In the example shown in Fig. 3.4, \hat{s}_* and \hat{l}_1 were initially aligned and librating around θ_1 . When \hat{s}_* and \hat{l}_1 are initially slightly misaligned and circulating around θ_1 (with small initial obliquity, $\theta_0 \lesssim 10^\circ$), the spin axis is eventually be captured into libration around θ_1 , after which the evolution proceeds very similarly to the case with zero initial obliquity. Thus, the post-resonant obliquity variation does not depend sensitively on the initial obliquity, as long as the initial obliquity is not very large.

3.4 Spin-Orbit Dynamics for Comparable S_* and L_1

The previous section considered the idealized case where $S_* \ll L_1$, so that the torque from \hat{s}_* on \hat{l}_1 vanishes. This simplified problem serves as a useful reference point in understanding the dynamics of systems with comparable S_* and L_1 . For the HJ/WJ systems of interest in this paper S_* and L_1 may be comparable for rapidly rotating stars, although nearly always satisfying $S_* \lesssim L_1$. For the remainder of the paper we undertake numerical integrations of the “real”

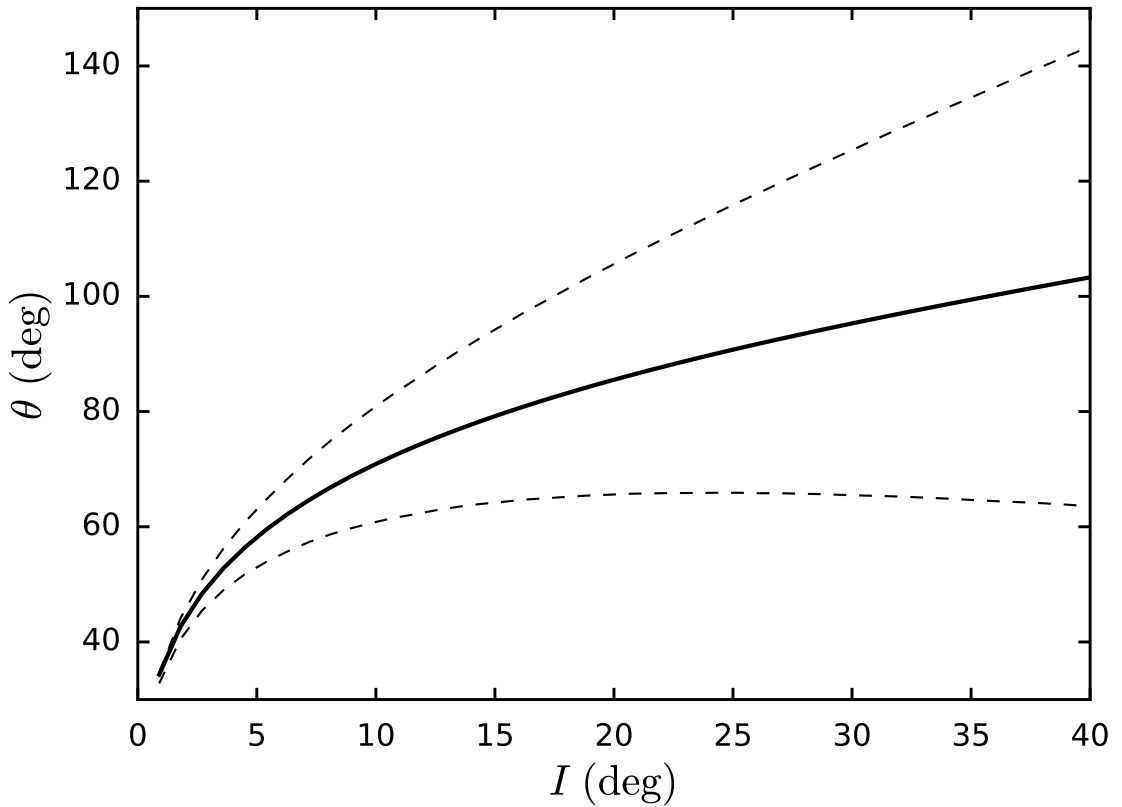


Figure 3.5: Solid curve: Average value of θ following resonant excitation, as calculated from the area of the separatrix when θ_1 and θ_4 merge (equation [3.17]). Dashed curves: variation of θ obtained from numerical integrations. Since the system is in the weak-coupling regime after resonant excitation, the final obliquity variation is simply $2I$.

system, accounting for the torque on \hat{l}_1 due to \hat{s}_* (see equations [3.1] - [3.3]), while allowing the stellar spin to decrease via magnetic braking according to equation (3.7). In Section 3.4.1 we extend the previous Cassini state analysis and derive results for generalized Cassini states, accounting for the effect of the spin on the orbit of the inner planet. We show that this “real” system behaves qualitatively similar to the idealized problem, with a similar Cassini state transition coinciding with resonant obliquity growth. In Section 6.4 we undertake numerical integrations and obtain quantitative results for generating spin-orbit

misalignment for HJs and WJs with external companions of varying properties.

3.4.1 Cassini States for Finite S_*/L_1 and an Evolution Example

Generalized Cassini states when S_* and L_1 are comparable were studied before by Boué & Laskar (2006) and Correia (2015). In equilibrium, \hat{s}_* , \hat{l}_1 , and \hat{l}_p are coplanar, as in the case when $S_* \ll L_1$. This coplanar configuration must be maintained through time (\hat{s}_* , \hat{l}_1 , and \hat{l}_p simply precess as a fixed plane in inertial space). We therefore require

$$\frac{d}{dt} \left[\hat{s}_* \cdot (\hat{l}_1 \times \hat{l}_p) \right] = 0. \quad (3.18)$$

After some algebra and substituting in the equations of motion (see equations [3.1] - [3.3]), the equilibrium condition in equation (3.18) can be written as

$$\begin{aligned} & \frac{\omega_{1p}}{\omega_{*1}} \cos I \left[\cos I \cos(\theta - I) - \cos \theta \right] \\ & + \frac{S_*}{L_1} \cos \theta \left[\cos I - \cos(\theta - I) \cos \theta \right] \\ & - \sin I \sin \theta \left[\cos \theta - \frac{L_1}{L_p} \frac{\omega_{1p}}{\omega_{*1}} \cos I \right] = 0. \end{aligned} \quad (3.19)$$

Equation (3.19) specifies the Cassini state obliquities, valid for general S_*/L_1 , and L_1/L_p . In the limits $S_*/L_1 \ll 1$ and $L_1/L_p \ll 1$, equation (3.19) reduces to equation (3.14). Fig. 3.6 shows the generalized Cassini states as a function of $\omega_{1p}/\omega_{*1} \propto \epsilon_{*1}$, for a fixed $I = 20^\circ$, $L_1/L_p = 0.3$, and various values of S_*/L_1 . Fixing the ratio S_*/L_1 while varying ω_{1p}/ω_{*1} is admittedly somewhat artificial, but allows for a straightforward comparison with the case of $S_*/L_1 = 0$ explored previously in Section 3. The number of Cassini states as a function of coupling strength, as well as the obliquity values are qualitatively similar for different

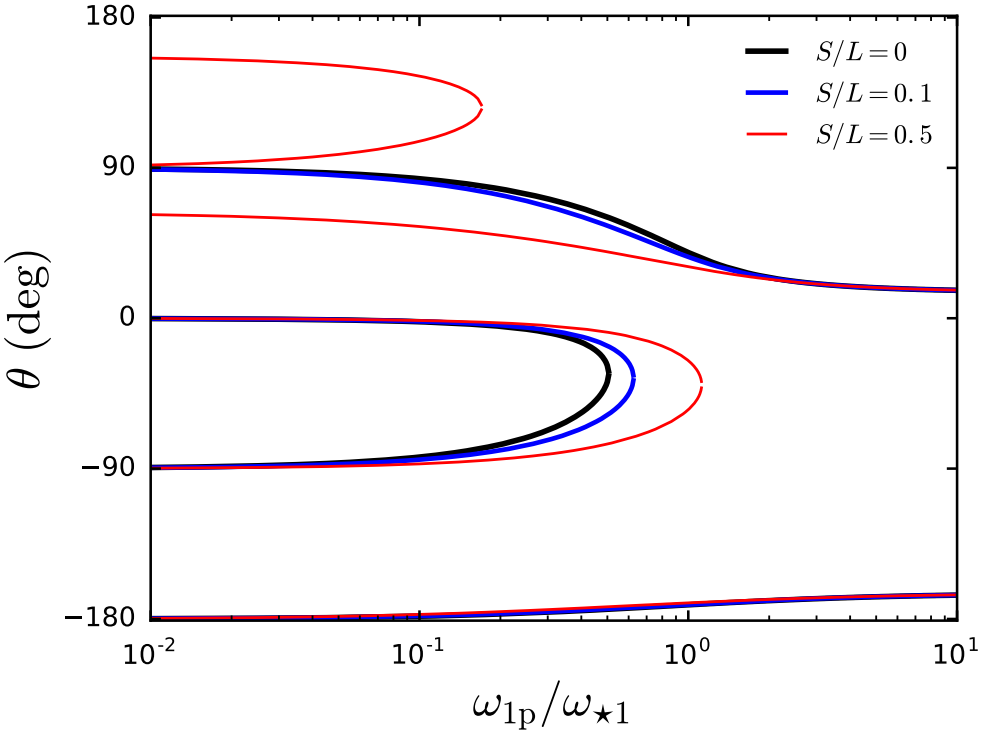


Figure 3.6: Generalized Cassini state obliquities as a function of the coupling parameter ω_{1p}/ω_{*1} , obtained from equation (3.19). We have fixed $I = 20^\circ$ and $L_1/L_p = 0.3$. The number of Cassini states as a function of coupling strength, as well as the obliquity values themselves are qualitatively similar for different values of S_*/L_1 . For $S_*/L_1 = 0.5$, additional retrograde equilibrium states exist for $\omega_{1p}/\omega_{*1} \lesssim 0.2$.

values of S_*/L_1 . When S_*/L_1 is of order unity, additional retrograde equilibrium states emerge, but they are not expected to strongly affect the obliquity evolution for systems that start out with spin-orbit alignment, as considered in this paper.

Figure 7.3 shows an example of resonant obliquity excitation for an inner planet with $m_1 = M_J$, $a_1 = 0.2$ AU, and an external perturber with $m_p = M_J$, $a_p = 10$ AU, and $e_p = 0$. The mutual inclination between the two planets is initially $I_0 = 30^\circ$, and the stellar spin period is initially $P_{*,0} = 3$ days, so

that $\epsilon_{*1} \simeq 0.1$ at the start of the integration. Inspection of Fig. 7.3 reveals that the obliquity evolution is quite similar to the idealized example presented in Fig. 3.4: At early times, the spin and orbit are strongly coupled, and the spin axis librates closely around the instantaneous Cassini state 1 (θ_1 , as determined by equation [3.19]). Eventually, when the coupling parameter ϵ_{*1} becomes of order unity, the Cassini states θ_1 and θ_4 merge. At this point, the obliquity jumps to a large value. Following this resonant excitation, when the spin and orbit become more weakly coupled, the obliquity oscillates between a minimum and maximum value.

One new feature in the dynamical evolution that emerges when $S_* \sim L_1$ (and not captured in the idealized problem discussed in Section 3), is damping of the mutual inclination. As is evident from the bottom panel of Fig. 7.3, the mutual inclination decreases with time, with a sharp decline at $t \simeq 0.8$ Gyr, coinciding with the resonant obliquity growth. This decrease in inclination can be understood as follows: The system initially librates around the Cassini state θ_1 , with $\theta_1 < 0$, so that \hat{s}_* , \hat{l}_1 , and \hat{l}_p are (in an average sense) coplanar, with \hat{s}_* and \hat{l}_p located on the opposite sides of \hat{l}_1 ; see Fig. 3.2. As ϵ_{*1} increases (due to stellar spin-down), $|\theta_1|$ increases, so that \hat{s}_* and \hat{l}_1 are pushed apart. This then implies that \hat{l}_1 is pushed closer to \hat{l}_p , and I must decrease. By manipulating equations (3.1)-(3.3), we can derive expressions for $d(\hat{s}_* \cdot \hat{l}_1)/dt = d \cos \theta/dt$ and $d(\hat{l}_1 \cdot \hat{l}_p)/dt = d \cos I/dt$, yielding the change in I compared to the change in θ :

$$\frac{dI}{d\theta} = -\frac{S_* \omega_{*1}}{L_1 \omega_{1p}} \left(\frac{\cos \theta \sin \theta}{\cos I \sin I} \right). \quad (3.20)$$

At late times, once the star has spun down, the quantity $S_* \omega_{*1}/L_1 \omega_{1p}$ becomes small, and the decrease in inclination ceases, although the inclination may still undergo oscillations. Resonant excitation of stellar obliquities thus tends to erase the mutual inclination between the inner planet and outer perturber.

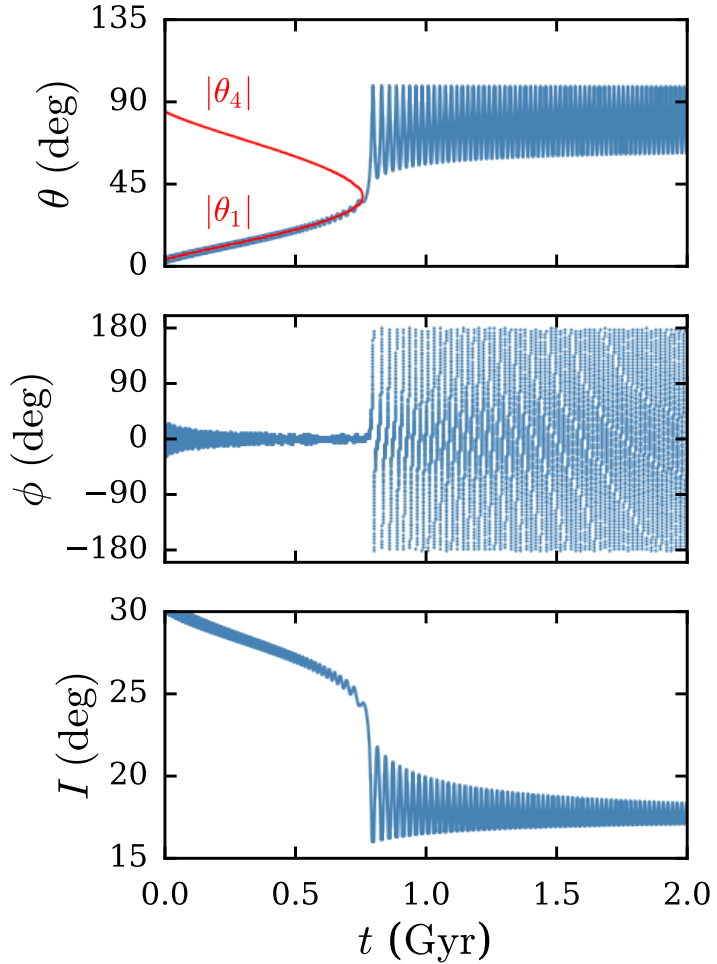


Figure 3.7: Example of resonant obliquity excitation for a system with finite S_\star and L_1 . The top panel shows the obliquity θ , the middle panel shows the phase of \hat{s}_\star relative to \hat{l}_1 (ϕ), and the bottom panel shows the mutual inclination between m_1 and m_p (I). The inner planet is a WJ, with $m_1 = M_J$, $a_1 = 0.2$ AU, and the external perturber has $m_p = M_J$, $a_p = 10$ AU, and $e_p = 0$, with an initial inclination (with respect to the orbit of m_1) $I_0 = 30^\circ$. The initial stellar spin period is $P_{\star,0} = 3$ days. As the stellar spin decreases due to magnetic braking, θ evolves in a manner qualitatively similar to the idealized example shown in Fig. 3.4, with the spin axis librating around the instantaneous Cassini state 1 (θ_1). Eventually θ_1 merges with θ_4 , and the obliquity is excited to a large value. The increase in obliquity is accompanied by a decrease in mutual inclination.

3.4.2 Results for HJs and WJs with External Companions

Having demonstrated in Fig. 7.3 a typical example of resonant obliquity excitation (accompanied by a decrease in mutual orbital inclination), we next explore the parameter space for HJs/WJs with external companions of varying properties. All results in this section have been initialized with aligned stellar spin and orbital axes ($\theta = 0$).

To start, we set both the planet and perturber masses to $1M_J$, and consider first an inner planet with $a_1 = 0.05$ AU (a canonical HJ) and next an inner planet with $a_1 = 0.2$ AU (a canonical WJ). We set the initial stellar spin period to $P_{*,0} = 3$ days, and explore various initial inclinations ($I_0 = 10^\circ - 40^\circ$) and perturber semi-major axes. In all cases, we integrate the equations of motion for a timespan of 5 Gyr⁴, and record the “final” (between 4.5 - 5 Gyr) range of variation of the spin-orbit angle, $\min(\theta)$, $\max(\theta)$, and the final variation of the mutual orbital inclination, $\min(I)$, $\max(I)$.

Results for the canonical HJ case (with $a_1 = 0.05$ AU) are depicted in the left panels of Figure 3.8. For a close perturber with $a_p \lesssim 0.5$ AU, the spin and orbit are relatively weakly-coupled ($\epsilon_{*1} \gtrsim 1$) throughout the integration span. After 5 Gyr, the obliquity oscillates, with the final degree of variation depending on the initial mutual inclination, roughly in the range $0 - 2I$. A more distant perturber, at $a_p \simeq 0.75 - 1.75$ AU, induces resonant obliquity excitation, with the final variation of θ exhibiting a complicated dependence on a_p and I_0 . The obliquity excitation is often accompanied by a dramatic decrease in mutual inclination. For example, when $I_0 = 30^\circ$ and $a_p \simeq 1 - 1.3$ AU, the final mutual inclination

⁴Since the spin-down rate is quite slow after ~ 1 Gyr due to the $P_* \propto t^{1/2}$ dependence, these results are not particular sensitive to the chosen integration timespan of 5 Gyr.

is less than 5° . For perturbers beyond $a_p \simeq 1.75$ AU, the spin and orbit are always strongly coupled, so that the perturber is ineffective in exciting spin-orbit misalignment.

The results for the canonical WJ case (with $a_1 = 0.2$ AU), shown in the right panels of Fig. 3.8, are qualitatively similar to those for the HJ case. Given the larger value of a_1 for the WJ and the sensitive dependence of the spin precession on semi-major axis, resonant obliquity excitation may occur for much more distant (weaker) perturbers, with a_p in the range $\sim 5 - 13$ AU. For both the canonical HJ and WJ, a sufficient initial inclination is needed to generate a substantial obliquity. For example, a perturber inclined by 10° generates only a modest obliquity ($\lesssim 30^\circ$). To produce a retrograde obliquity ($\gtrsim 90^\circ$) requires an initial inclination of at least $20^\circ - 30^\circ$.

Both the HJ and the WJ cases exhibit an abrupt decrease in obliquity excitation for perturbers beyond a maximum distance. The maximum effective perturber semi-major axis $\tilde{a}_{p,\max}$ may be estimated by requiring that $\epsilon_{\star 1}(5\text{Gyr}) \gtrsim 1$, so that (see equation [3.8])

$$\tilde{a}_{p,\max} \simeq 1.5 \text{ AU} \left(\frac{a_1}{0.05 \text{ AU}} \right)^{3/2} \left(\frac{m_p}{m_1} \right)^{1/3}. \quad (3.21)$$

For $\tilde{a}_p \gtrsim \tilde{a}_{p,\max}$, the perturber is unable to excite spin-orbit misalignment due to the strong coupling between \hat{s}_\star and \hat{l}_1 throughout the stellar spin evolution.

Finally, we conduct a larger parameter survey, and examine the steady-state distribution of stellar obliquities and mutual orbital inclinations by plotting the values of θ and I at a random time between $[0 - 5]$ Gyr. We sample the parameters in the following ranges: $a_1 = [0.05 - 0.5]$ AU, $a_p = [10 - 100]a_1$, $e_p = 0$, $m_p = [0.1 - 10]M_J$, $I_0 = 10^\circ - 40^\circ$, and the initial stellar spin period in the observationally-motivated range $P_{\star,0} = 1 - 10$ days (see, e.g. Fig. 1 of Gal-

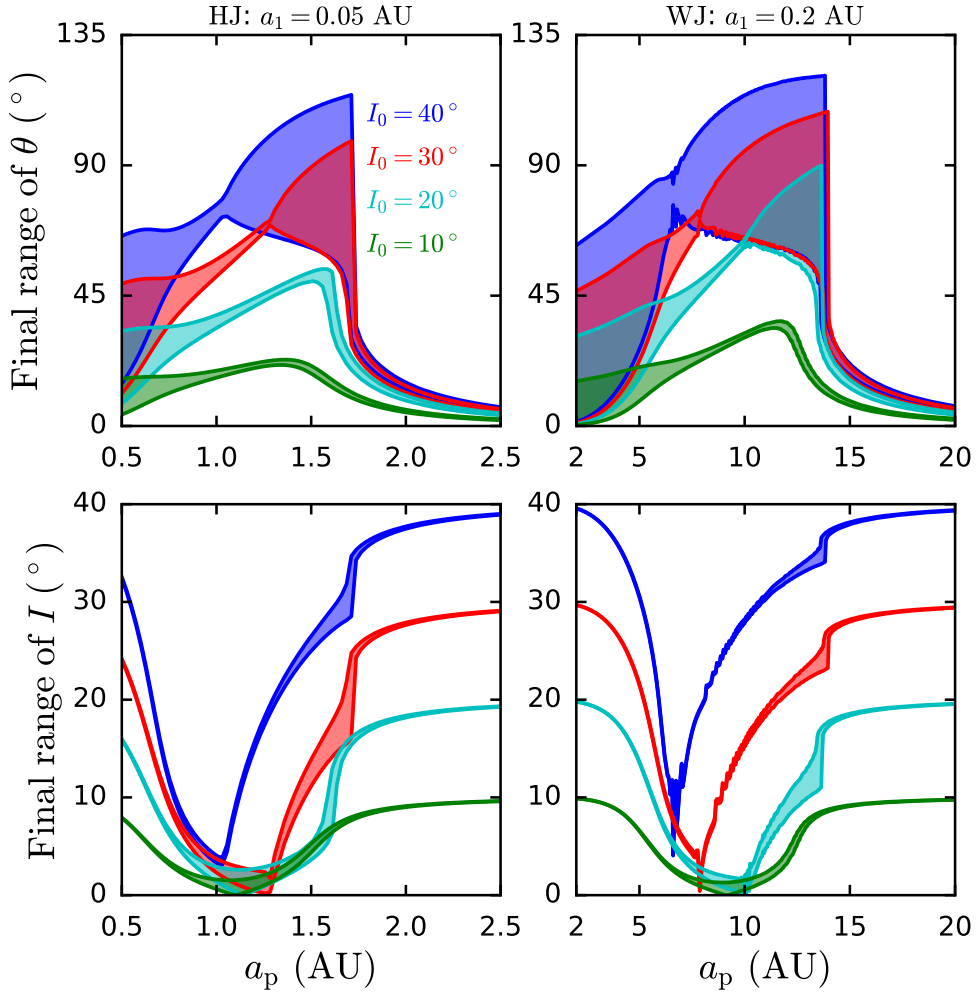


Figure 3.8: Obliquity excitation as a function of perturber semi-major axis, showing various initial inclinations, as labeled. The planet and perturber masses are $m_1 = m_p = 1M_J$, and the initial stellar spin period is $P_{*,0} = 3$ days. The left panels show results for an inner planet with $a_1 = 0.05$ AU (a canonical HJ), and the right panels show an inner planet with $a_1 = 0.2$ AU (a canonical WJ). The top panels show the final range of obliquities (between θ_{\min} and θ_{\max}) at 4.5-5 Gyr, and the bottom panels show the final mutual inclination variation at 4.5-5 Gyr. To excite substantial spin-orbit misalignment, an initial inclination $I_0 \gtrsim 20^{\circ}$ is needed, and the perturber must be located sufficiently close (see equation [3.21]). Obliquity excitation (top panels) is accompanied by a decrease in mutual inclination (bottom panels). In some instances, the initial inclination is almost completely erased.

let & Bouvier, 2013). Given the large uncertainties in the statistical properties of long-period giant planets, this experiment is not meant to serve as a precise quantitative prediction for HJ/WJ obliquities, but rather to identify the orbital geometries that may lead to high obliquities. We discard any systems that do not satisfy the stability condition given by Petrovich (2015c). To avoid integrating systems that clearly will maintain spin-orbit alignment for the entire integration span, we also discard systems that satisfy $\epsilon_{*1}(P_{*} = 30\text{d}) < 0.01$.

Figure 3.9 shows the results of this parameter survey. The top left panel depicts the main result, with the perturber “strength” $a_p/m_p^{1/3}$ versus the inner planet semi-major axis a_1 , and the color indicating the value of the obliquity at a random time. The grey line shows the analytic estimate for the maximum perturber strength that may induce changes in the obliquity (see equation [3.21]). The analytic estimate is in good agreement with the numerical results: Perturbers beyond $a_{p,\max}$ are unable to generate high obliquities. The bottom left panel shows the steady-state distribution of obliquities (at a random time). Recall that the initial distribution of obliquities is a δ -function at $\theta = 0$. Due to the presence of the perturber, a wide range of obliquities is generated, with a maximum obliquity of $\sim 113^\circ$. For systems that undergo resonant excitation, the degree of obliquity excitation is highest for the weaker perturbers (near the grey line of the top left panel of Fig. 3.9). This occurs because the amount of obliquity growth increases with decreasing S_{*}/L_1 . Since the systems with weaker perturbers encounter the resonance at a later time (when S_{*}/L_1 is smaller), such systems tend to result in higher obliquities.

The results for the steady state inclinations are depicted in the upper and lower right panels of Fig. 3.9. Recall that the distribution of initial inclinations

(I_0) is chosen to be uniform in $10^\circ - 40^\circ$. Examining the distribution of inclinations (lower right panel), obliquity excitation leads to decreased inclinations, with a removal of points from the highest inclination bins ($\sim 30^\circ - 40^\circ$), and addition of points at the lowest inclination bins ($0 - 10^\circ$). In some cases, the initial inclination is completely erased, as indicated in the upper right panel.

Recall that in this paper the range of initial inclinations is restricted to $I_0 < 40^\circ$, so that Lidov-Kozai eccentricity oscillations have no chance of developing. However, the minimum inclination allowing Lidov-Kozai oscillations is often significantly larger than 40° , depending on the rate of apsidal precession due to GR compared to the apsidal precession due to the perturber (e.g. Liu et al., 2015). As a result, qualitatively similar results to those shown in this paper may often occur for $I_0 > 40^\circ$, but with even larger excitement of obliquity. Furthermore, if Lidov-Kozai cycles *do* arise, the evolution of the spin axis becomes chaotic (Storch et al., 2014; Storch & Lai, 2015), so that the full possible range of obliquities ($0^\circ - 180^\circ$) may in some circumstances be reached.

3.5 Summary & Discussion

In this paper we have studied a new mechanism for generating spin-orbit misalignments in HJ and WJ systems with external planetary companions via resonant excitation. Starting from initial spin-orbit alignment, we evolve the stellar spin axis and the orbital angular momentum axes of both planets (the HJ/WJ and outer perturber), accounting for the gravitational torques between the inner and outer planets and the oblate host star, as well as stellar spin-down due to magnetic braking. For appropriate companion semi-major axis and mass (see

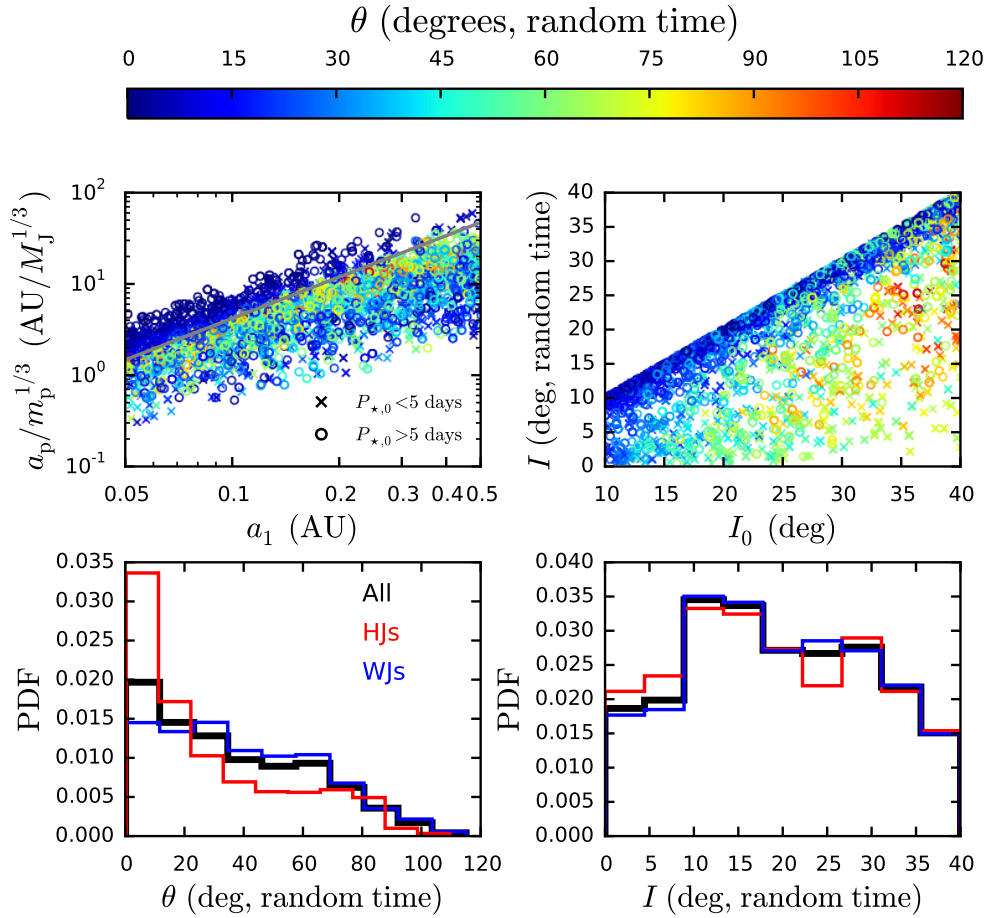


Figure 3.9: Parameter survey of obliquity excitation and inclination decay in systems consisting of a host star, a HJ or WJ, and an external perturber. We integrate the full secular equations of motion for a duration of time randomly chosen between 0 – 5 Gyr and record the value of the obliquity θ (the angle between \hat{s}_* and \hat{l}_1) and inclination I (the angle between \hat{l}_1 and \hat{l}_p). We fix the inner planet mass $m_1 = 1M_J$ and vary the initial spin period uniformly in the range $P_{*,0} = 1 - 10$ days, the initial mutual inclination uniformly in $I_0 = 10^\circ - 40^\circ$, and the inner planetary semi-major axis in $a_1 = 0.05 - 0.5$ AU (where HJs are defined to have $a_1 < 0.1$ AU and WJs have $a_1 > 0.1$ AU). We vary the perturber mass in the range $m_p = 0.1 - 10M_J$ and the semi-major axis in the range $a_p = (10 - 100)a_1$. *Top left:* Perturber “strength” $a_p/m_p^{1/3}$ vs inner planet semi-major axis a_1 . The color of the points indicates the obliquity θ at a random time. The dashed grey line indicates the analytic estimate for the perturber strength in order to affect the obliquity (see equation [3.21]). *Top right:* Steady-state inclination I versus initial inclination I_0 , illustrating how resonant obliquity excitation can erase mutual inclinations. *Bottom panels:* Distributions of steady-state stellar obliquities (left), and mutual inclinations (right). The thick black histograms show all systems, while the red (blue) histograms show results for HJs (WJs).

Fig. 3.1), the inner system transitions from strong spin-orbit coupling ($\epsilon_{*1} \ll 1$; see equation [3.8] for the definition of this “coupling parameter”) at earlier times to weak coupling ($\epsilon_{*1} \gtrsim 1$) at later times as the star spins down. Appreciable stellar obliquity may be excited during resonance crossing ($\epsilon_{*1} \sim 1$), when the stellar spin precession rate (around the inner planet) is comparable to the orbital precession rate of the inner planet (due to the outer perturber). Following the resonant obliquity growth, the spin and orbit are weakly coupled, and the stellar obliquity oscillates between a minimum and a maximum, whose values depend on the details of the prior (pre-resonant) spin history.

Insight into the resonant growth of obliquity can be gained by considering the idealized case where the stellar spin angular momentum S_* is much less than the angular momentum of the inner planet (HJ or WJ) L_1 (Section 3). In this case, the stellar spin axis closely follows one of the Cassini (equilibrium) states, as stellar spin-down gradually reduces the spin-orbit coupling strength, until a separatrix crossing (at the resonance $\epsilon_{*1} \sim 1$) leading to rapid obliquity excitation (see Fig. 3.4). The final average value of spin-orbit misalignment can be computed analytically (see Fig. 3.5).

For realistic HJ/WJ systems, S_* can be comparable to L_1 , but the spin-orbit dynamics remain qualitatively similar to the $S_* \ll L_1$ case. In particular, an initially aligned system follows a generalized Cassini state (valid for arbitrary S_*/L_1 ; see Fig. 3.6) until the resonance crossing, leading to rapid obliquity excitation (see Fig. 7.3). An important new feature for systems with $S_* \sim L_1$ is that the inclination angle between the inner planet and the outer companion tends to decrease as a result of obliquity growth (see Figs. 7.3 - 3.8).

Concerning spin-orbit misalignments of HJ and WJ systems, our main find-

ings are as follows:

- Due to their close proximity to the host star, HJs have orbital axes that are strongly coupled to the host star spin axis (note the strong semi-major axis dependence in the coupling parameter $\epsilon_{\star 1}$ in equation [3.8]). As a result, for any kind of obliquity growth to be possible, a strong perturber is required (see equation [3.21] and Figs. 3.1 and 3.8 - 3.9). For example, a $1M_J$ HJ with semi-major axis 0.05 AU requires that a $1M_J$ perturber be located within ~ 1.75 AU.
- In contrast, the spin-orbit coupling in WJ systems is weaker, so that distant or low-mass perturbers may excite obliquities. For example, a $1M_J$ WJ with semi-major axis 0.2 AU requires that a $1M_J$ perturber be located within ~ 13 AU (see Figs. 3.1 and 3.8 - 3.9).
- For both HJ and WJ systems, external perturbers must have modest inclinations ($I_0 \gtrsim 20^\circ$) in order to produce substantial obliquity growth (see Figs. 3.8 and 3.9).
- Obliquity growth is generally accompanied by a decrease in mutual orbital inclination between the inner planet and outer perturber (see Figs. 7.3 - 3.9). Resonant obliquity growth may thus erase high initial mutual inclinations in such systems.

This paper has focused on planetary companions to HJs/WJs, but stellar companions may also resonantly excite obliquities. For HJs, a stellar-mass companion must be very close (within $\sim 10 - 20$ AU, due to the dependence on perturber properties as $\tilde{a}_p/m_p^{1/3}$). Since such close stellar companions may inhibit planet formation in the first place (Wang et al., 2014), it is unclear to what

extent they contribute to HJ obliquities. In contrast, more distant (\sim hundred AU) stellar-mass companions to WJs may easily lead to resonant obliquity excitation. Such stellar companions may be especially effective because they are expected to follow an isotropic distribution in inclination, so that a substantial fraction of binary perturbers may have high inclinations.

Throughout this paper, we have fixed the mass of the host star to $M_\star = 1M_\odot$. Hot Jupiter obliquities exhibit a well-known dependence on stellar effective temperature (Winn et al., 2010), with HJs around cool stars ($T_{\text{eff}} \lesssim 6200$ K) having low obliquities, and HJs around hot stars having high obliquities (see Winn et al. 2017 and Muñoz, & Perets 2018 for recent discussions and statistics of this trend). Hot stars do not experience strong magnetic braking (likely due to the absence of a surface convective zone), and remain rapidly rotating throughout their lifetimes. As a result, resonant obliquity excitation is unlikely to occur around hot stars, because it requires that the perturber properties be somewhat fine-tuned. Thus, the dependence of resonant excitation on stellar effective temperature appears to yield the opposite trend compared to observations. This fact, together with the requirement that HJs need quite strong perturbers to have their obliquities raised at all, implies that resonant obliquity excitation is certainly not the entire story in HJ obliquities. However, it may nonetheless be at work in individual misaligned systems. Indeed, exceptions to the observed obliquity-effective temperature correlation do exist (e.g. WASP-8b, Queloz et al. 2010, WASP-2b, Triaud et al. 2010).

The story for WJs may be very different. As noted previously in Section 1, a large fraction of WJs are observed to have external giant planet companions (Bryan et al., 2016), many of which have the appropriate combinations of

semi-major axis ($\sim 5 - 20$ AU) and mass to cause resonant obliquity excitation. Provided that such companions are sufficiently inclined, we predict that many WJs around cold stars have significant stellar spin-orbit misalignments due to resonant excitation, whereas hot stars would not have their obliquities resonantly excited, and tend to have low obliquities. So far, WJ stellar obliquities are largely un-probed. In the near future, NASA’s TESS mission (Ricker et al., 2014) will discover a large number of WJs/HJs around bright stars. These systems will be amenable to Rossiter-McLaughlin measurements of spin-orbit misalignments, in addition to providing better statistics on the orbital parameters. These new observations will help determine whether resonant obliquity excitation by external companions play an important role in WJ systems.

Regardless of the extent to which WJ obliquities are probed in the near future, resonant obliquity excitation has interesting implications for exoplanetary systems, due to the possibility that high initial inclinations can be erased. The mutual inclinations ($\gtrsim 20^\circ$) needed for resonant excitation must be generated either via a scattering event of three or more giant planets or perturbations from a stellar companion. As observations continue to constrain mutual inclinations in multi-planet systems, it is useful to keep in mind that such inclinations may not reflect the “initial” (i.e. previously higher inclinations following a scattering event or excitation from a nearby star), if resonant obliquity excitation has occurred.

CHAPTER 4

MODERATELY ECCENTRIC WARM JUPITERS FROM SECULAR INTERACTIONS WITH EXTERIOR COMPANIONS

4.1 Introduction

Despite over twenty years of observations, the origins and dynamical histories of close-in ($\lesssim 1$ AU) giant planets remain elusive. Hot Jupiter (HJ, giant planets with semi-majors axes $\lesssim 0.1$ AU) formation continues to be a major topic in exoplanet research. The general consensus is that HJs cannot form in their present locations, and must instead have migrated from farther out (although see Boley et al. 2016; Batygin et al. 2016), but whether there exists a dominant migration mechanism is unclear. Proposed mechanisms include disk-migration, and various forms of “high-eccentricity migration” in which the planet’s eccentricity is excited to a large value, leading to tidal dissipation during pericenter passages and orbital decay. Warm Jupiters (WJs, with semi-major axes in the range $\sim 0.1 - 1$ AU) raise the same formation questions as HJs. Proposed channels of WJ formation include disk migration, high-eccentricity migration, scatterings, and in-situ formation. If multiple channels of WJ formation exist, whether one channel produces most of the observed WJs is of great interest but remains unknown.

Many WJs are moderately eccentric, with $e \sim 0.2 - 0.7$. These eccentricities are difficult to explain with both in-situ formation and disk-driven migration.

This chapter is adapted from Anderson & Lai (2017)

High-eccentricity migration has therefore been proposed as a major formation mechanism for WJs. If WJs are undergoing high-eccentricity migration, they must reach sufficiently small pericenter distances ($\lesssim 0.05$ AU) to experience tidal dissipation and orbital decay. Most WJs are not sufficiently eccentric to achieve such small pericenter distances, but this issue can be circumvented if the planets are undergoing secular eccentricity oscillations induced by exterior companions, and are currently observed in a lower eccentricity phase. The requirement that the minimum pericenter distance be small enough such that tidal decay may occur within the lifetime of the host star constrains the properties of the perturbers, requiring them to be sufficiently close and/or massive (Dong et al., 2014).

However, the proposal that most WJs reach their current orbits through high-eccentricity migration suffers from some problems. Antonini et al. (2016) find that most observed WJs with exterior planetary companions would not be stable if the WJ originated beyond ~ 1 AU and subsequently underwent high-eccentricity migration. Furthermore, population synthesis studies of HJ formation by various high-eccentricity migration mechanisms typically yield very low fractions of planets at WJ distances (Petrovich 2015b, Petrovich 2015a, Anderson et al. 2016, Hamers et al. 2017, Hamers 2017; although see Dawson & Chiang 2014, Petrovich & Tremaine 2016). For example, studies of high-eccentricity migration due to Lidov-Kozai oscillations from stellar perturbers (Petrovich, 2015b; Anderson et al., 2016) produce HJs at rates of a few percent, but essentially no WJs. This arises because, for a stellar perturber at a distance of \sim few hundred AU, once the planetary orbit shrinks to WJ distances, eccentricity oscillations have ceased due to general relativistic precession, and the eccentricity has frozen to very high value (~ 0.99), after which the migration to

HJ distances proceeds rapidly (see, e.g. Fig. 1 of Anderson et al. 2016). Hamers et al. (2017) find a similarly negligible amount of WJs compared to HJs for high-eccentricity migration due to secular chaos in systems of multiple giant planets. Observations of giant planets paint a very different picture. Despite the existence of a “period valley” of giant planets with orbital periods of 10 – 20 days (e.g. Udry et al., 2003; Jones et al., 2003; Santerne et al., 2016), the total occurrence rate of WJs (with semi-major axes in the range 0.1AU-1AU) exceeds that of HJs ($a < 0.1$ AU see Santerne et al., 2016, Fig. 8). We note that the ratio of WJs to HJs does depend somewhat on the definition of a WJ. Taking the RV planets listed on exoplanets.org² with $m \sin i > 0.5M_J$, we find that the WJ/HJ ratio is ~ 3.9 . If we adopt a more conservative definition of a WJ, with $0.1\text{AU} < a < 0.5\text{AU}$, the WJ/HJ ratio is ~ 1.6 . Accounting for selection effects would further increase the WJ/HJ ratio.

The observed WJ/HJ ratio is thus in contradiction with most population synthesis results. Considering migration due to Lidov-Kozai oscillations from a planetary companion, Petrovich & Tremaine (2016) produce roughly twice as many HJs as WJs. This WJ/HJ ratio is the highest found in a population synthesis thus far, but may result in part from the rather specific semi-major axes selected for both planets, chosen so that eccentricity oscillations are not frozen by general relativity at WJ distances. The semi-major axis of the outer planet in particular may strongly affect the migration rate at WJ distances, because it helps determine the orbital distance at which eccentricity oscillations freeze to a large value (see Anderson et al., 2016, Section 3.1), after which the planet migrates inward to HJ territory quickly, and spends a negligibly small amount of time at WJ distances.

²accessed on August 22, 2017.

The above difficulties in forming WJs by high-eccentricity migration leads us to consider the possibility that most WJs form in-situ, by disk migration, or some combination of these two processes. At typical WJ semi-major axes (~ 0.3 AU), theoretical work shows that sufficiently massive rocky cores can accrete gas and undergo runaway accretion (Lee et al., 2014), although growing the core quickly enough before the gas disperses may be challenging (Lee & Chiang, 2016). In-situ formation of WJs was also recently argued by Huang et al. (2016), who found that close, rocky neighbors are common in observed WJ systems. However, both in-situ formation and disk-driven migration have difficulty in explaining eccentric WJs. Distinct populations of WJs have previously been proposed, with the eccentric WJs forming via some form of high-eccentricity migration, and the circular WJs forming by a different channel (Dawson & Murray-Clay, 2013; Petrovich & Tremaine, 2016).

This paper considers the scenario in which most WJs reach their current sub-AU orbits either by in-situ formation or disk migration, after which a subset of WJs undergo secular eccentricity oscillations driven by an exterior companion – many such companions have been detected through radial velocity studies (see Section 4.3). We examine the possibility of raising the eccentricities of WJs by secular interactions with distant planetary companions, so that the eccentricity varies between $e \simeq 0$ and a maximum value $e = e_{\max}$. In order for a WJ with observed eccentricity e_{obs} to have its eccentricity raised by an external (and possibly undetected) companion, the maximum eccentricity must satisfy $e_{\max} \geq e_{\text{obs}}$. This places constraints on the properties of the planetary perturber, in terms of its mass, separation, inclination, and eccentricity. We focus exclusively on secular perturbations, because in-situ scatterings have been shown to be ineffective in raising the eccentricities of close-in planets (Petrovich et al., 2014).

The role of external companions in raising the eccentricities of WJs has been studied before. However, most previous works (e.g. Dong et al., 2014; Dawson & Chiang, 2014; Antonini et al., 2016; Petrovich & Tremaine, 2016) have focused on the situation where WJs achieve very small pericenter distances such that the orbit decays via tidal dissipation (and are thus in the process of becoming HJs). If we do not require the WJs to attain such small pericenter distances, and instead focus on generating more modest eccentricities ($e \simeq 0.2 - 0.5$), the requirements on the external companion are less stringent. Note that recent work has considered generating eccentric WJs in systems with three or more giant planets through relatively violent scattering events (Mustill et al., 2017). In contrast, in this paper we focus on systems of two widely-spaced planets where scattering does not occur, and we identify the necessary properties of external planets in generating modest eccentricities in WJs through secular processes. This scenario requires that the outer planet have a non-zero eccentricity or inclination; such eccentricities/inclinations may result from either an initial scattering event with three or more giant planets, or perturbations from a tertiary stellar companion. Note that in order for a tertiary stellar companion to increase the eccentricity/inclination of an outer giant planet via secular interactions, it must be sufficiently close/massive so that the stellar companion induces pericenter precession in the outer planet that overcomes the precession induced by the WJ.

This paper is organized as follows. In Section 4.2 we summarize our method and relevant analytic expressions for identifying the requirements for an external companion to increase the eccentricity of a WJ. We first consider coplanar systems (Section 6.2.5), so that eccentricity oscillations (including the effect of an apsidal precession resonance) can be studied analytically. We then consider

inclined systems, for which octupole-level Lidov-Kozai oscillations may arise, requiring numerical integrations. Section 4.3 considers the sample of observed and eccentric WJs with detected outer companions, and identifies the mutual inclinations necessary to raise the eccentricity of the WJ to the observed value. In Section 4.4 we consider small neighboring planets to WJs, and their role in suppressing eccentricity oscillations. We conclude in Section 4.5.

4.2 Secular Interactions of Warm Jupiters With Distant Planet Companions

4.2.1 Setup and Method

We consider a system of two well-separated giant planets m_1 (the WJ) and m_2 (the exterior perturber), orbiting a star of mass M_\star . We denote the semi-major axis and eccentricity of m_1 and m_2 as $a_{\text{in}}, e_{\text{in}}$ and $a_{\text{out}}, e_{\text{out}}$ respectively. The planets may have a mutual inclination I , defined through $\cos I = \hat{\mathbf{L}}_{\text{in}} \cdot \hat{\mathbf{L}}_{\text{out}}$, where $\hat{\mathbf{L}}_{\text{in}}$ and $\hat{\mathbf{L}}_{\text{out}}$ are unit vectors along the angular momenta \mathbf{L}_{in} and \mathbf{L}_{out} . The orbits are also specified by the eccentricity vectors \mathbf{e}_{in} and \mathbf{e}_{out} . For ease of notation, we frequently omit the subscript “in”, so that $e = e_{\text{in}}$, $a = a_{\text{in}}$, etc.

In general, we follow the evolution of $(\mathbf{L}_{\text{in}}, \mathbf{e}_{\text{in}})$ and $(\mathbf{L}_{\text{out}}, \mathbf{e}_{\text{out}})$ due to the mutual interaction between m_1 and m_2 up to octupole order, using the vector equations derived in Liu et al. (2015) (see also Petrovich, 2015b). The eccentricities of both planets may undergo periodic oscillations, with maximum eccentricity of the inner orbit denoted by e_{\max} . The eccentricity oscillations occur on

a characteristic timescale t_k (the quadrupole “Kozai timescale”), given by

$$\frac{1}{t_k} = \frac{m_2}{M_\star} \frac{a^3}{a_{\text{out,eff}}^3} n_{\text{in}}, \quad (4.1)$$

where we have introduced an “effective” outer semi-major axis,

$$a_{\text{out,eff}} \equiv a_{\text{out}} \sqrt{1 - e_{\text{out}}^2}, \quad (4.2)$$

and where $n_{\text{in}} = \sqrt{GM_\star/a^3}$ is the orbital mean motion of the inner planet.

Octupole effects are manifested by terms of order ε_{oct} , where

$$\varepsilon_{\text{oct}} = \frac{M_\star - m_1}{M_\star + m_1} \frac{a}{a_{\text{out}}} \frac{e_{\text{out}}}{1 - e_{\text{out}}^2} \simeq \frac{a}{a_{\text{out}}} \frac{e_{\text{out}}}{1 - e_{\text{out}}^2}. \quad (4.3)$$

We also include the short-range-forces (SRFs) introduced by general relativity and tidal distortion³ of m_1 . These non-Keplerian potentials lead to pericenter precession and introduce two additional parameters in the equations of motion:

$$\varepsilon_{\text{GR}} \simeq 0.1 \left(\frac{M_\star}{M_\odot} \right)^2 \left(\frac{m_2}{M_J} \right)^{-1} \left(\frac{a}{0.3 \text{ AU}} \right)^{-4} \left(\frac{a_{\text{out,eff}}}{3 \text{ AU}} \right)^3, \quad (4.4)$$

and

$$\begin{aligned} \varepsilon_{\text{Tide}} \simeq & 6.4 \times 10^{-5} \frac{k_2}{0.37} \left(\frac{R_1}{R_J} \right)^5 \left(\frac{M_\star}{M_\odot} \right)^2 \left(\frac{m_2}{M_J} \right)^{-1} \\ & \times \left(\frac{a}{0.3 \text{ AU}} \right)^{-8} \left(\frac{a_{\text{out,eff}}}{3 \text{ AU}} \right)^3, \end{aligned} \quad (4.5)$$

where R_1 and k_2 are the radius and tidal Love number of m_1 . See Anderson et al. (2016) and Liu et al. (2015) for further details and the secular equations of motion. Since we focus on generating modest eccentricities in the inner planet via secular interactions, we neglect dissipative tides, which act over much longer timescales than the timescale for eccentricity growth, and only modify the WJ orbit for pericenter distances much smaller than those of interest here.

³We do not consider the additional precession due to rotational distortion of either M_\star or m_1 , because they are both smaller than the GR term (dominant at low eccentricities) and the tidal term (dominant at high eccentricities).

This paper aims to explain eccentric WJs by secular perturbations from exterior giant planet companions. For an observed WJ with eccentricity $e = e_{\text{obs}}$, the constraint on an undetected outer companion can be obtained by calculating e_{max} for outer perturbers with varying properties, and requiring $e_{\text{max}} \geq e_{\text{obs}}$. In a similar vein, if a WJ with e_{obs} does have a detected companion, we can identify whether such a companion is capable of producing e_{obs} , by checking whether $e_{\text{max}} \geq e_{\text{obs}}$. This latter idea is considered in Section 4.3 for observed WJs with exterior companions.

In the following we consider a “canonical” WJ, with $m_1 = 1M_J$ and $a = 0.3$ AU, and explore various properties for the outer companion. Sections 6.2.5 and 5.3.1 consider coplanar systems, while Sections 4.2.4 and 4.2.5 consider inclined systems. See Section 4.2.5 for the main results of Section 4.2.

4.2.2 Coplanar Systems

We begin with coplanar systems ($I = 0$). The maximum eccentricity of m_1 (to octupole order) is completely specified by energy and angular momentum conservation (Lee & Peale, 2003), without the need for numerical integrations of the equations of motion. The total energy per unit mass, including the octupole-order interaction potential between m_1 and m_2 and SRF effects for m_1 is

$$\Phi = \Phi_{\text{Int}} + \Phi_{\text{SRF}}, \quad (4.6)$$

where

$$\begin{aligned} \Phi_{\text{Int}} &= \Phi_{\text{Quad}} + \Phi_{\text{Oct}} \\ &= \frac{\Phi_0}{8} \left[-2 - 3e^2 + \frac{15}{8}e(3e^2 + 4)\varepsilon_{\text{oct}} \cos \Delta\varpi \right], \end{aligned} \quad (4.7)$$

and

$$\begin{aligned}\Phi_{\text{SRF}} &= \Phi_{\text{GR}} + \Phi_{\text{Tide}} \\ &= -\frac{\varepsilon_{\text{GR}}\Phi_0}{j} - \frac{\varepsilon_{\text{Tide}}\Phi_0}{15j^9} \left(1 + 3e^2 + \frac{3}{8}e^4\right).\end{aligned}\tag{4.8}$$

Note that in Eqs. (6.33) and (4.8), we have defined

$$\Phi_0 = \frac{Gm_2a^2}{a_{\text{out,eff}}^3},\tag{4.9}$$

as well as $j = \sqrt{1 - e^2}$, and $\Delta\varpi \equiv \varpi_{\text{in}} - \varpi_{\text{out}}$ (difference in longitude of pericenter of the inner and outer orbits). Unless the eccentricity reaches extreme values ($e \gtrsim 0.9$), the SRFs are dominated by the GR contribution, and to simplify the remainder of the analytic discussion we ignore the tidal contribution (note however that we always include it in the numerical integrations presented in this paper).

Figure 4.1 shows the maximum eccentricity (e_{max}) of the canonical WJ (with $m_1 = 1M_J$, $a = 0.3$ AU, and initial eccentricity $e_0 \simeq 0$) as a function a_{out} for various outer planet masses and eccentricities. In general, e_{max} increases with decreasing a_{out} , except for significant peaks at certain values of a_{out} . These peaks arise from the “apsidal precession resonance” (Liu et al., 2015b), which occurs when the total apsidal precession rate of the inner orbit (which consists of the precession driven by m_2 and the GR contribution, $\dot{\varpi}_{\text{in}} = \dot{\varpi}_{12} + \dot{\varpi}_{\text{GR}}$) matches the apsidal precession rate of the outer orbit ($\dot{\varpi}_{\text{out}} = \dot{\varpi}_{21}$). To quadrupole order, the precession frequencies due to the secular interactions between m_1 and m_2 are

$$\dot{\varpi}_{12} = \frac{3}{4}\alpha^3 n_{\text{in}} \frac{m_2}{M_*} \frac{j}{(1 - e_{\text{out}}^2)^{3/2}}\tag{4.10}$$

and

$$\dot{\varpi}_{21} = \frac{3}{8}\alpha^2 n_{\text{out}} \frac{m_1}{M_*} \frac{2 + 3e^2}{(1 - e_{\text{out}}^2)^2},\tag{4.11}$$

where $\alpha \equiv a/a_{\text{out}}$, and n_{in} (n_{out}) is the orbital mean motion of m_1 (m_2). The precession of m_1 due to GR is

$$\dot{\varpi}_{\text{GR}} = \frac{3n_{\text{in}}}{j^2} \frac{GM_{\star}}{ac^2}. \quad (4.12)$$

The resonance condition $\dot{\varpi}_{\text{in}} \simeq \dot{\varpi}_{\text{out}}$ yields

$$\begin{aligned} & \frac{3}{4}\alpha^3 n_{\text{in}} \frac{m_2}{M_{\star}} \frac{j}{(1 - e_{\text{out}}^2)^{3/2}} + \frac{3n_{\text{in}}}{j^2} \frac{GM_{\star}}{ac^2} \\ & \simeq \frac{3}{8}\alpha^2 n_{\text{out}} \frac{m_1}{M_{\star}} \frac{2 + 3e^2}{(1 - e_{\text{out}}^2)^2}. \end{aligned} \quad (4.13)$$

This resonance is only precisely defined in the limit $e_{\text{in}}, e_{\text{out}} \ll 1$, for which Eq. (4.13) reduces to

$$\frac{m_2}{M_{\star}} \simeq \alpha^{1/2} \frac{m_1}{M_{\star}} - 4\alpha^{-3} \frac{GM_{\star}}{ac^2}. \quad (4.14)$$

In this limit, the peak eccentricity of m_1 is [see Eq. (33) of (Liu et al., 2015b)]

$$e_{\text{peak}} = e_{\text{out},0} \left(\frac{m_2}{m_1} \right)^{1/2} \alpha^{-1/4}. \quad (4.15)$$

For moderate values of e and e_{out} , the resonance becomes “fuzzy” because of the variations of e and e_{out} during the secular evolution. Nevertheless, the condition $\dot{\varpi}_{\text{in}} \simeq \dot{\varpi}_{\text{out}}$, with $e_{\text{out}} \simeq e_{\text{out},0}$ and $e \sim 0$ provides a good indicator for the resonance, as long as the eccentricity of the WJ remains moderate ($e_{\text{max}} \lesssim 0.5$).

For increasingly massive perturbers, the resonance cannot be achieved, unless the perturber semi-major axis is small. For the $5M_{\text{J}}$ perturber in Fig. 4.1, the resonance can only occur when a_{out} is comparable to a , where non-secular effects clearly will be emerge and the stability of the system compromised.

To illustrate what kind of outer planet may be capable of increasing the eccentricity of the WJ through the apsidal precession resonance, Fig. 4.2 shows

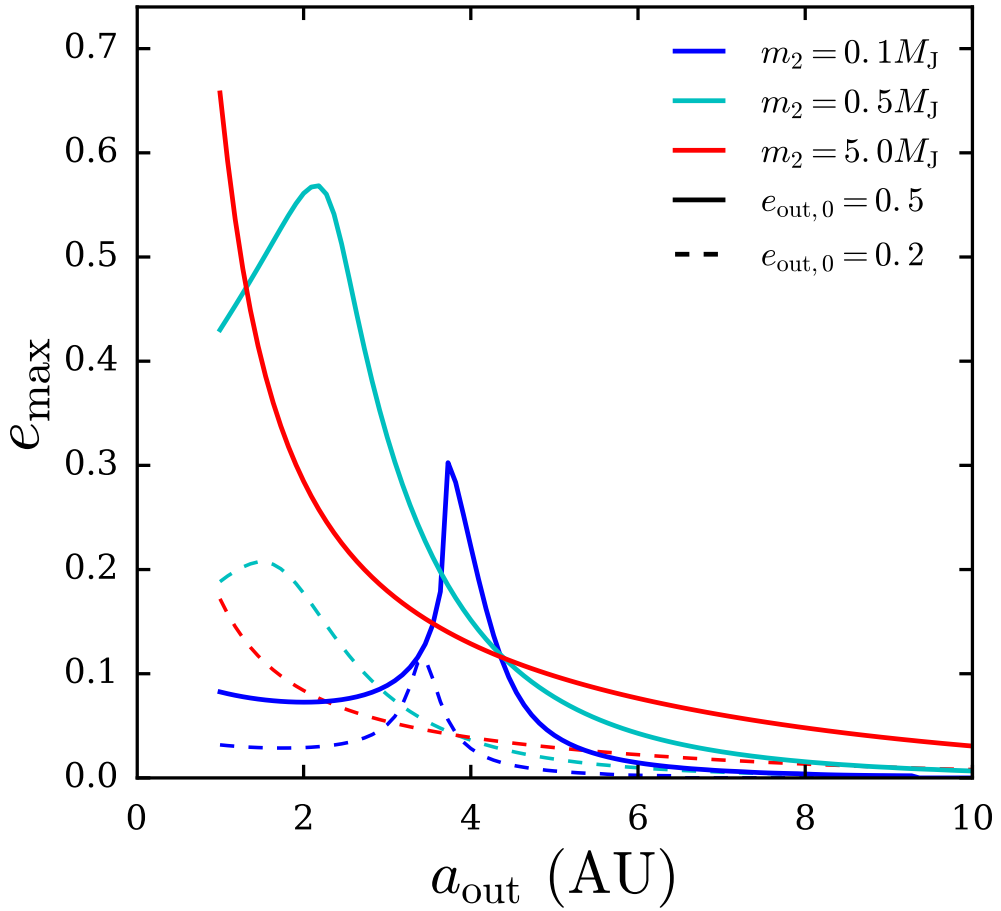


Figure 4.1: Maximum eccentricity of the WJ as a function of a_{out} , for various masses and eccentricities of the outer planet m_2 . The two planets are coplanar, with the WJ ($m_1 = 1M_J$) placed at $a = 0.3$ AU. The initial eccentricity of m_2 is $e_{\text{out},0} = 0.5$ (solid), and $e_{\text{out},0} = 0.2$ (dashed). The curves for the low mass perturbers ($m_2 = 0.1, 0.5M_J$) have a distinctive spike, corresponding to an apsidal precession resonance, where $\dot{\varpi}_{\text{in}}/\dot{\varpi}_{\text{out}} \simeq 1$. For the $5M_J$ perturber, the resonance can only be achieved at small separations, where the secular approximation is no longer valid.

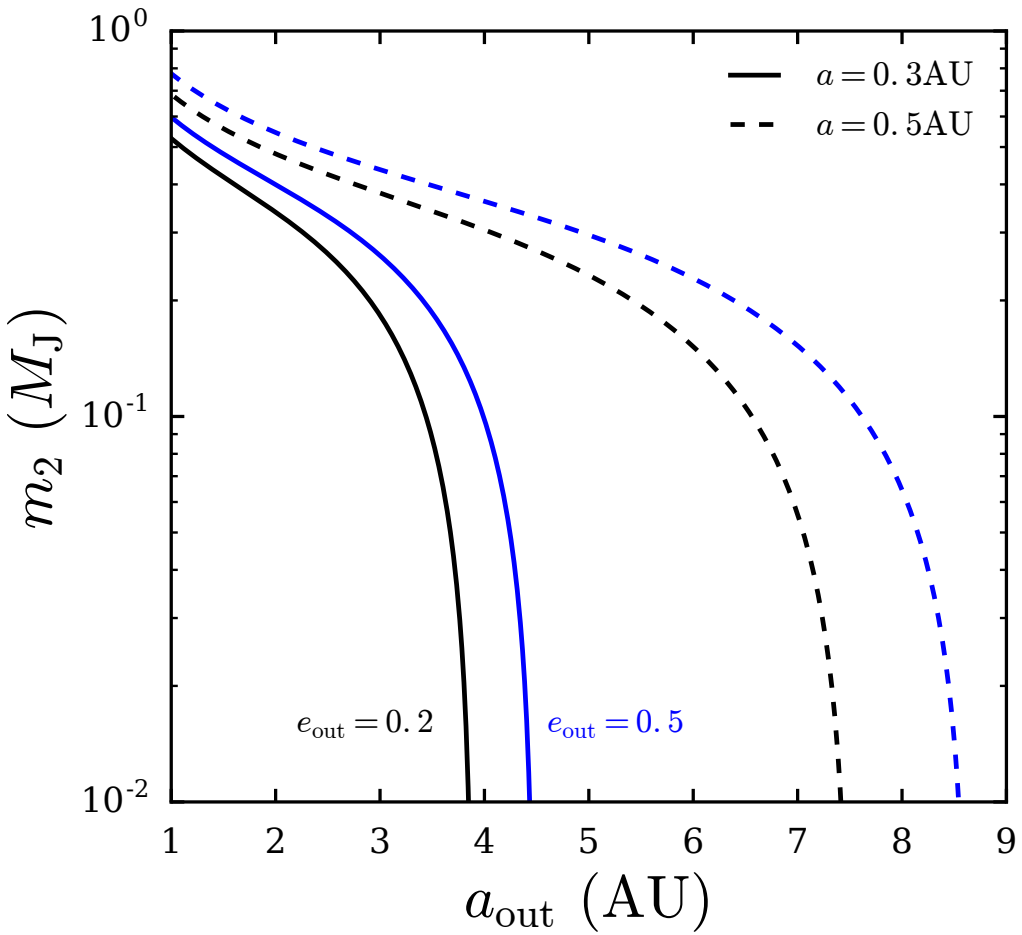


Figure 4.2: Contours of $\dot{\varpi}_{in}/\dot{\varpi}_{out} = 1$, indicating the combinations of outer planet mass m_2 and separation a_{out} that may lead to an apsidal precession resonance and increased e_{max} . In evaluating $\dot{\varpi}_{in} = \dot{\varpi}_{12} + \dot{\varpi}_{GR}$ and $\dot{\varpi}_{out} = \dot{\varpi}_{21}$ (see Eqs. [4.10] - [4.12]), we have set $e_{in} = 0$ and $e_{out} = e_{out,0} = 0.2$ (black), and 0.5 (blue). The WJ has mass $m_1 = 1M_J$ and semi-major axis $a = 0.3$ AU (solid curves), and $a = 0.5$ AU (dashed curves).

the approximate “resonance” condition (curves of $\dot{\varpi}_{in}/\dot{\varpi}_{out} = 1$, evaluated at $e = 0, e_{out} = 0.2, 0.5$). Combinations of (m_2, a_{out}) close to the lines may result in eccentricity increases in the inner orbit. However, note that the resonance does not guarantee large e_{max} : If $e_{out,0}$ is too small, e_{peak} will necessarily be small (see Eq. [4.15]).

4.2.3 Coplanar Systems With Modest Initial Eccentricity

Here we examine how eccentricity growth in coplanar systems depend on the initial eccentricity of the inner orbit. Li et al. (2014) have previously shown that the inner planet can achieve extreme eccentricity without SRFs (the so-called “coplanar-Kozai mechanism”). To obtain a simple criterion for large eccentricity excitation, we approximate the outer planet eccentricity as constant. This is justified since the change in $j_{\text{out}} = \sqrt{1 - e_{\text{out}}^2}$ is related to the change in $j_{\text{in}} = \sqrt{1 - e^2}$ through

$$\Delta j_{\text{out}} = -\frac{m_1}{m_2} \alpha^{1/2} \Delta j_{\text{in}}, \quad (4.16)$$

and thus, the change in e_{out} is often small compared to the change in e .

Suppose the inner planet starts with an initial e_0 and $\Delta\varpi_0$, and attains the maximum eccentricity e_{max} at $\Delta\varpi = 0$.⁴ Energy conservation ($\Phi = \text{constant}$; see Eq. [4.6]) gives

$$\varepsilon_{\text{oct}} = \frac{8}{15} \left[\frac{3(e_{\text{max}}^2 - e_0^2) - 8\varepsilon_{\text{GR}}(j_0^{-1} - j_{\text{max}}^{-1})}{e_{\text{max}}(3e_{\text{max}}^2 + 4) - e_0(3e_0^2 + 4) \cos \Delta\varpi_0} \right], \quad (4.17)$$

where $j_{\text{max}} \equiv \sqrt{1 - e_{\text{max}}^2}$ (note that j_{max} corresponds to the minimum value of j). Therefore, to attain a certain value of e_{max} , we require $\varepsilon_{\text{oct}} \geq \varepsilon_{\text{oct,min}}$, with

$$\varepsilon_{\text{oct,min}} = \frac{8}{15} \left[\frac{3(e_{\text{max}}^2 - e_0^2) - 8\varepsilon_{\text{GR}}(j_0^{-1} - j_{\text{max}}^{-1})}{e_{\text{max}}(3e_{\text{max}}^2 + 4) + e_0(3e_0^2 + 4)} \right]. \quad (4.18)$$

Figure 4.3 shows $\varepsilon_{\text{oct,min}}$ as a function of e_0 for several values of ε_{GR} . Since this paper considers the scenario where WJs form either in-situ or by disk migration, we expect low initial eccentricities, with $e_0 \lesssim 0.1$. As a result, we see from Fig. 4.3 that the outer planet must have a strong octupole (with $\varepsilon_{\text{oct}} \gtrsim 0.1$) to produce a moderate eccentricity ($e_{\text{max}} \sim 0.5$) in the WJ.

⁴By applying $de/d\Delta\varpi = 0$ in the energy conservation equation, it is easy to see that the eccentricity extremum occurs at $\Delta\varpi = 0$ or π .

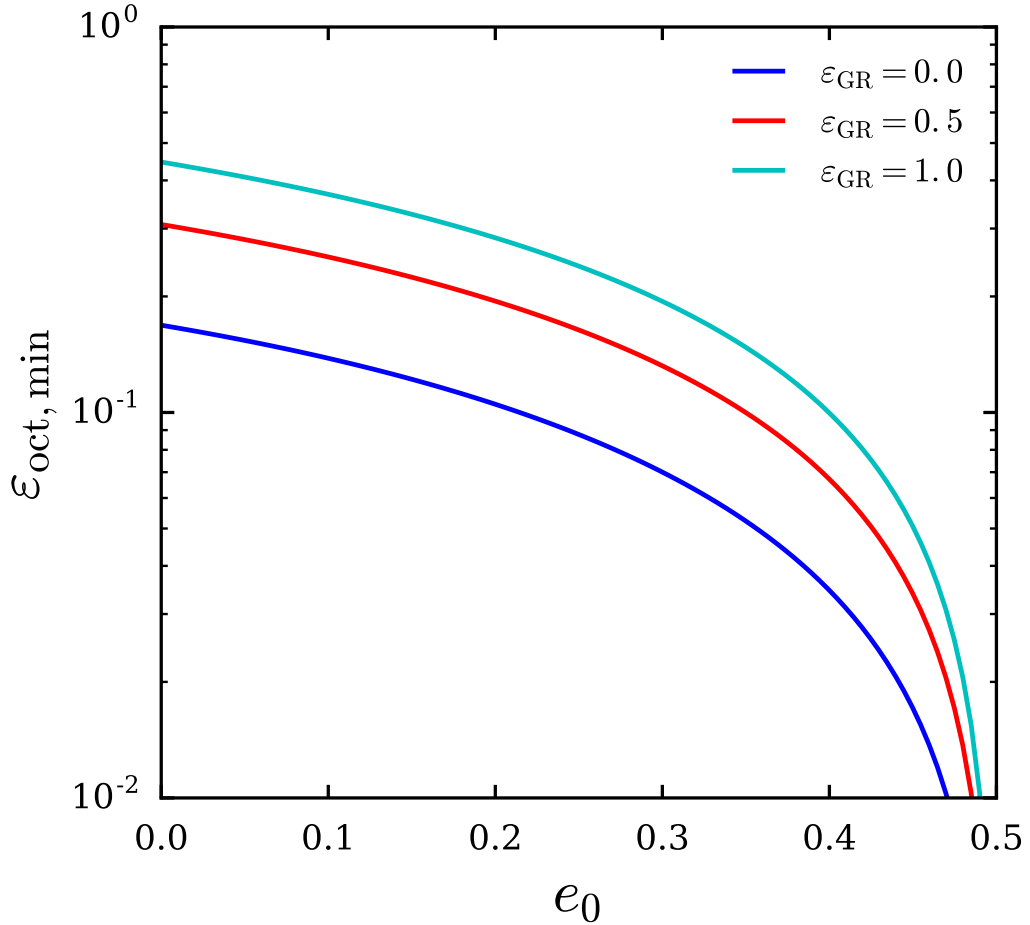


Figure 4.3: Minimum value of ε_{oct} (see Eq. [4.3]) required to raise the eccentricity of the WJ from e_0 to $e_{\max} = 0.5$; see Eq. (4.18).

We briefly comment on the possibility of extreme eccentricity excitation (and the associated orbit flip) first discussed in Li et al. (2014). To achieve $e_{\max} \rightarrow 1$, Eq. (4.18) implies

$$\varepsilon_{\text{oct}} \geq \frac{8}{15} \left[\frac{3(1 - e_0^2) + 8\varepsilon_{\text{GR}}(j_{\max}^{-1} - j_0^{-1})}{7 + e_0(3e_0^2 + 4)} \right]. \quad (4.19)$$

Setting $\varepsilon_{\text{GR}} = 0$ recovers the flip condition in Li et al. (2014) [see their Eq. (14)]. Since extreme eccentricities imply $j_{\max} \ll 1$, the large value of ε_{oct} required by Eq. (4.19) cannot be achieved by most dynamically stable systems. For example,

the dynamical stability condition of Petrovich (2015c) is

$$\frac{a_{\text{out}}(1 - e_{\text{out}})}{a(1 + e)} \gtrsim 2.4 \left[\max\left(\frac{m_1}{M_*}, \frac{m_2}{M_*}\right) \right]^{1/3} \left(\frac{a_{\text{out}}}{a} \right)^{1/2} + 1.15. \quad (4.20)$$

Considering a system with $e_0 = e_{\text{out},0} = 0.5$ and $m_1/M_* = m_2/M_* = 10^{-3}$, and using $\varepsilon_{\text{GR}} \simeq 10^{-2}$ and $j_{\text{max}} = 0.1$ (note that these values lead to an extremely conservative estimate of the ratio $\varepsilon_{\text{GR}}/j_{\text{max}}$), Eq. (4.19) implies $a_{\text{out}}/a \lesssim 1.2$ AU, whereas stability [Eq. (6.38)] requires $a_{\text{out}}/a \gtrsim 5$ AU. We conclude that SRFs make extreme eccentricity excitation and orbit flipping highly unlikely for realistic systems.

4.2.4 Moderately Inclined Companions

Next we allow the outer companion to be inclined. When $I_0 \neq 0$, e_{max} must be determined numerically. The remaining results in this paper are obtained by integrating the octupole-level vector equations of motion, evolving the eccentricity and angular momentum vectors of both m_1 and m_2 (e.g. Liu et al., 2015). For the inner orbit we also include apsidal precession introduced by GR and tidal distortion of m_1 .

In order to capture the octupole-order effects, the equations of motion must be integrated sufficiently long. In all of our calculations we integrate for a timespan $10t_k/\varepsilon_{\text{oct}}$ (multiple “octupole timescales”) and record the maximum value of e . If the inner planet achieves a pericenter distance $a(1 - e) < R_{\text{Tide}} \lesssim 2.7R_J(M_*/m_1)^{1/3}$ (e.g. Guillot et al., 2011), we terminate the integration and consider the planet tidally disrupted.

We integrate a grid of inclined systems in the range $I_0 \simeq 10^\circ - 60^\circ$, and vary the separation a_{out} of the outer planet. Figure 4.4 shows our numerical result

for e_{\max} versus a_{out} for the various inclinations, where the inner planet properties have been set to the canonical WJ values ($m_1 = 1M_J$, $a = 0.3$ AU), and the perturber has initial eccentricity $e_{\text{out},0} = 0.5$, and mass $m_2 = 0.1M_J$ (top panel) and $m_2 = 1M_J$ (bottom panel). For the $0.1M_J$ perturber and modest inclinations ($I_0 \lesssim 30^\circ$), the behavior is similar to the coplanar systems discussed in Section 6.2.5. The sharp peaks in e_{\max} exhibited in Fig. 4.4 occur when $\dot{\varpi}_{\text{in}} \simeq \dot{\varpi}_{\text{out}}$ (cf. Fig. 4.1). For this set of parameters, the location of the peak eccentricity shifts to smaller a_{out} with increasing I_0 , until the inclination becomes large enough so that Lidov-Kozai oscillations begin. This result, along with previous work (Liu et al., 2015b) shows that the apsidal precession resonance remains effective for moderately inclined systems, with $I_0 \lesssim 30^\circ$.⁵

Of course, as in the coplanar case (Section 2.2), when the external companion is too massive, the resonance peak disappears (see Fig. 4.1 and Eq. [4.14]).

4.2.5 General Inclinations: Lidov-Kozai Cycles

If the initial inclination I_0 is sufficiently high, Lidov-Kozai (LK) eccentricity/inclination oscillations may be induced (Lidov, 1962; Kozai, 1962), even when the interaction between m_1 and m_2 is truncated to the quadrupole order. (By contrast, eccentricity excitation in coplanar or low-inclination systems operates only when the octupole effect is included.)

To quadrupole order, LK oscillations of general hierarchical triple systems, including SRFs, can be determined analytically (Fabrycky & Tremaine, 2007;

⁵Similar peaks in eccentricity were seen in previous numerical calculations by Ford et al. (2000) and (Naoz et al., 2013b). The physical explanation of these peaks in terms of “apsidal precession resonance” was first discussed in Liu et al. (2015b) in the context of merging compact binaries with tertiary companions.

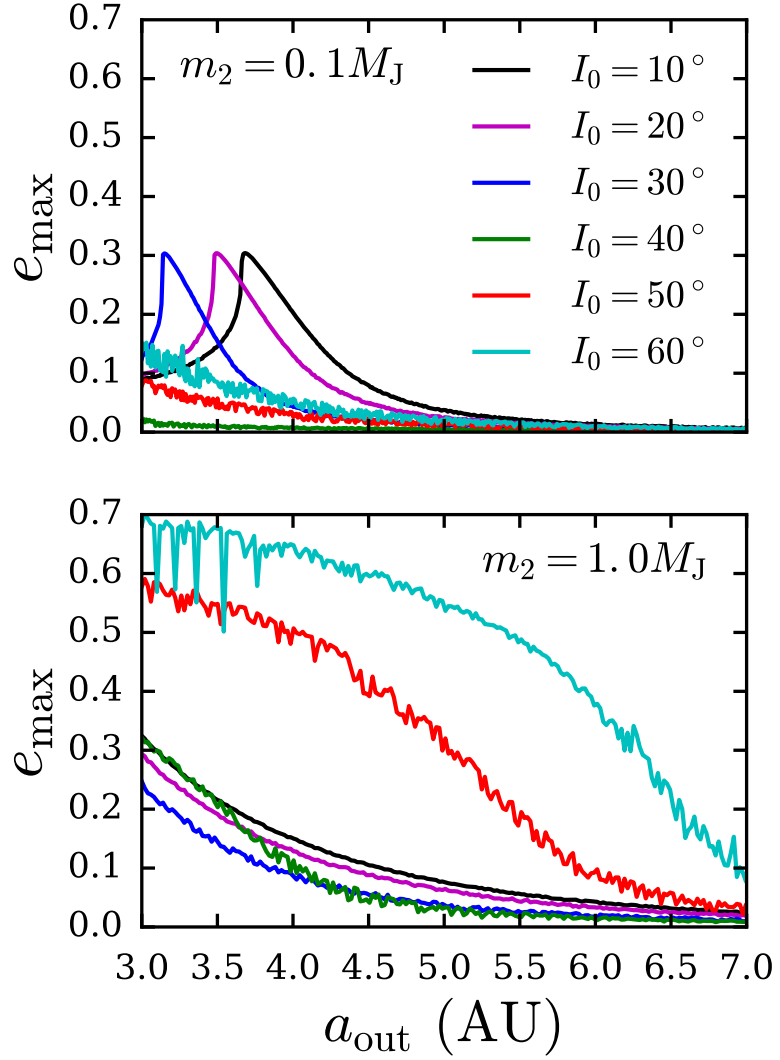


Figure 4.4: e_{\max} versus a_{out} for various initial inclinations, as labeled, obtained by integrating the octupole equations of motion. We have set $e_0 = 10^{-3}$, $e_{\text{out},0} = 0.5$, $a = 0.3$ AU, $m_1 = 1M_J$, $m_2 = 0.1M_J$ (top panel), and $m_2 = 1M_J$ (bottom panel). Each case is initialized with ω_{in} and Ω_{in} randomly chosen in the range $[0, 2\pi]$ (where ω_{in} and Ω_{in} are the argument of pericenter and longitude of ascending node of the inner orbit, with the invariant plane defined by the initial orbital plane of the companion). For $m_2 = 0.1M_J$ and inclinations $I_0 \lesssim 30^\circ$, the behavior is qualitatively similar to the coplanar systems (see Section 6.2.5), with a peak eccentricity (maximum value of e_{\max}) corresponding to values of a_{out} satisfying $\dot{\varpi}_{\text{in}}/\dot{\varpi}_{\text{out}} \simeq 1$.

Liu et al., 2015; Anderson et al., 2017). The behavior of e_{\max} as a function of I_0 depends on two dimensionless parameters: the angular momentum ratio of the inner and outer orbits,

$$\eta = \left(\frac{L_{\text{in}}}{L_{\text{out}}} \right)_{e=0} = \frac{m_1}{m_2} \sqrt{\frac{a}{a_{\text{out}}(1 - e_{\text{out}}^2)}}, \quad (4.21)$$

and the strength of the SRFs (e.g. ε_{GR} , $\varepsilon_{\text{Tide}}$; see Eqs. [4.4] and [4.5]). The most general expression for $e_{\max}(I_0)$ can be found in Anderson et al. 2017 (see their Eqs. [20] and [23]). In particular, eccentricity excitation of the inner planet occurs when I_0 lies in the “LK window”, given by

$$(\cos I_0)_- \leq \cos I_0 \leq (\cos I_0)_+, \quad (4.22)$$

where

$$(\cos I_0)_+ = \frac{1}{10} \left(-\eta + \sqrt{60 + \eta^2 - \frac{80}{3}\varepsilon_{\text{GR}}} \right), \quad (4.23)$$

and

$$(\cos I_0)_- = \begin{cases} \frac{1}{10} \left(-\eta - \sqrt{60 + \eta^2 - \frac{80}{3}\varepsilon_{\text{GR}}} \right), & \text{if } \eta \leq 2(1 + \frac{2}{3}\varepsilon_{\text{GR}}) \\ -\frac{2}{\eta} \left(1 + \frac{2}{3}\varepsilon_{\text{GR}} \right), & \text{otherwise.} \end{cases} \quad (4.24)$$

In the above expressions, we have included only the SRF associated with GR.

When the octupole effect is included, the properties of the eccentricity-inclination oscillations cannot be determined analytically, and the relation $e_{\max}(I_0)$ and the associated “LK window” can be significantly modified. Nevertheless, one analytical quadrupole result survives: The “limiting eccentricity” e_{\lim} , which is the peak of the $e_{\max}(I_0)$ relation, remains valid even when the octupole terms are included (Liu et al., 2015; Anderson et al., 2017). This e_{\lim} (assuming $e_0 = 0$) is given by

$$\frac{3}{8}(j_{\lim}^2 - 1) \left[-3 + \frac{\eta^2}{4} \left(\frac{4j_{\lim}^2}{5} - 1 \right) \right] + \left(\frac{\Phi_{\text{SRF}}}{\Phi_0} \right)_{e=0}^{e=e_{\lim}} = 0, \quad (4.25)$$

where $j_{\lim} = \sqrt{1 - e_{\lim}^2}$, and occurs at the inclination $I_{0,\lim}$, given by

$$\cos I_{0,\lim} = \frac{\eta}{2} \left(\frac{4}{5} j_{\lim}^2 - 1 \right). \quad (4.26)$$

(see Anderson et al., 2017). Note that e_{\lim} is not achievable if Eq. (4.26) yields unphysical values of $\cos I_{0,\lim}$.

To examine how the quadrupole “LK window” (Eqs. [4.23] - [4.24]) may be modified by octupole, we conduct a large set of numerical integrations for the canonical WJ ($m_1 = 1M_J$, $a = 0.3$ AU), for perturber masses $m_2 = 0.1, 1, 10M_J$. For each perturber mass, we explore several values of the initial eccentricity $e_{\text{out},0}$, and sample over the full range of initial inclinations I_0 and a wide range of separations a_{out} . Figure 4.5 shows the results in the (I_0, a_{out}) parameter space, where we plot the value of e_{\max} achieved over the integration span $(10t_k/\varepsilon_{\text{oct}})$. For reference, the quadrupole “LK window” is also depicted, as calculated from Eqs.(4.23) - (4.24). Non-zero e_{\max} outside these inclination limits arises from octupole effects, either from the apsidal precession resonance (see Section 6.2.5) for low inclination systems, or from octupole-level LK oscillations. For the lowest value of $e_{\text{out},0}$ considered ($e_{\text{out},0} = 0.25$), the systems are well-described by the quadrupole limit. As $e_{\text{out},0}$ increases, deviations from the quadrupole predictions begin to emerge, and non-zero e_{\max} may be generated well outside of the quadrupole LK window, especially when $e_{\text{out},0} = 0.75$. Notice that the results are approximately symmetric around $I_0 = 90^\circ$ when $m_2 = 1, 10M_J$, but exhibit considerable asymmetry when $m_2 = 0.1M_J$. This arises because in the test-particle limit ($\eta \ll 1$) the equations of motion are symmetric around 90° , but this symmetry disappears when $\eta \sim 1$ (e.g. Liu et al. 2015).

Inspection of Fig. 4.5 allows us to identify the types of outer planetary perturbers necessary to raise the eccentricity of a canonical WJ. To generate

$e_{\max} \simeq 0.5$, relatively high ($I_0 \gtrsim 50^\circ$) mutual inclinations are needed. A Jupiter-mass outer planet must be located within ~ 10 AU, unless it is extremely eccentric, with $e_{\text{out}} = 0.75$. A sub-Jovian mass planet ($m_2 = 0.1M_J$) must be located within ~ 3 AU, most likely in a retrograde orbit. Such a sub-Jovian mass perturber is therefore ineffective in generating many eccentric WJs, because only narrow ranges of separations and inclinations lead to substantial eccentricity increases. In contrast, a massive ($\sim 10M_J$) perturber can generate high eccentricities at $a_{\text{out}} \sim 15$ AU and beyond.

Figure 4.6 depicts the same numerical experiments as in Fig. 4.5, but shows the fraction of the total integration time that the WJ spends above a specified eccentricity. Figure 4.6a shows the fraction of time spent above $e = 0.2$ [$f(e > 0.2)$], and Fig. 4.6b shows the fraction of time spent above $e = 0.5$ [$f(e > 0.5)$]. The fraction of time spent above $e = 0.2$ is relatively high ($\gtrsim 0.5$) for many separations and inclinations, as long as the perturber mass is $1M_J$ or greater. The fraction of time spent above $e = 0.5$ is much lower, usually not exceeding ~ 0.2 .

We conclude that external giant planet perturbers are often effective in generating mild (~ 0.2) eccentricities in WJs at low mutual inclination, but in order to produce moderate (~ 0.5) eccentricities in WJs requires a relatively high inclination. Furthermore, even with a high inclination, generating a moderate eccentricity in the WJ orbit may be difficult, because of the small fraction of time the WJ spends at or above such an eccentricity.

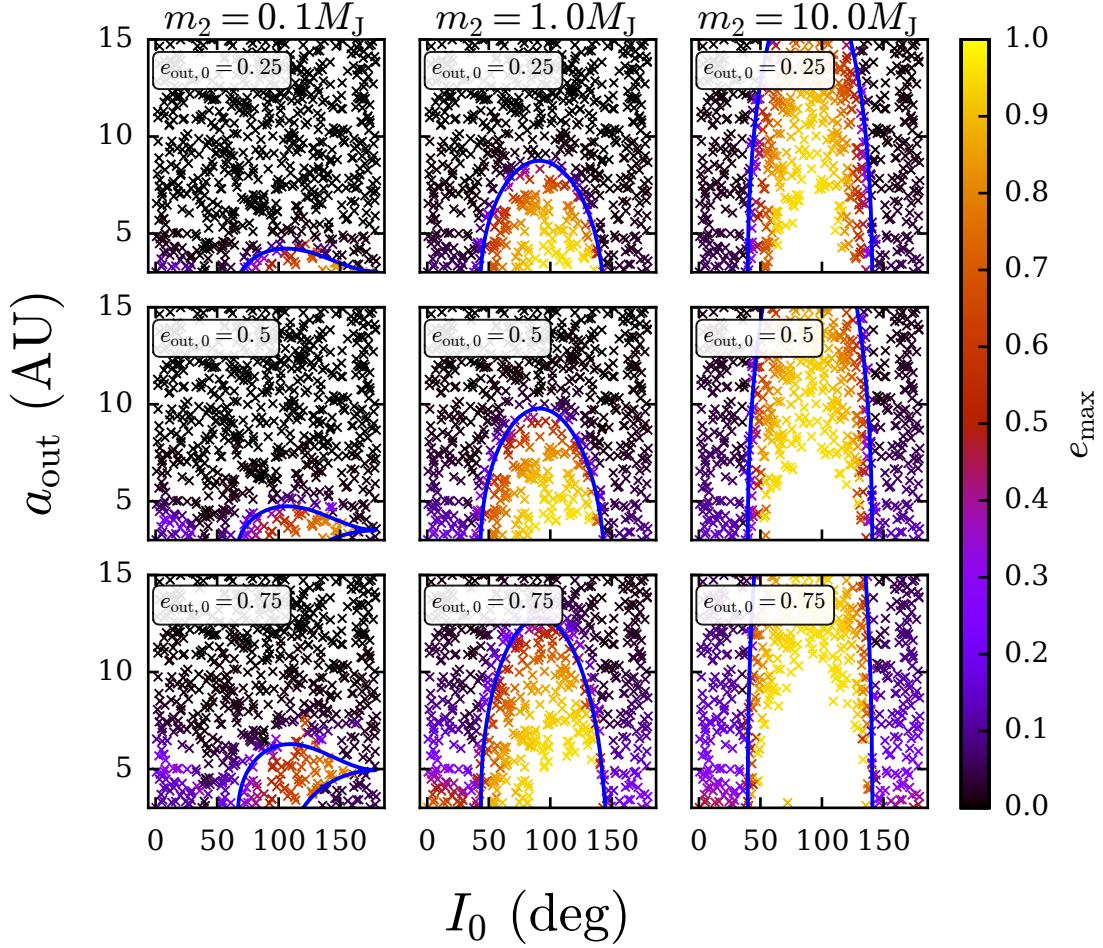


Figure 4.5: Maximum eccentricity e_{\max} , in terms of (I_0, a_{out}) parameter space, for various outer planet masses and eccentricities, as labeled. Each point represents a system that survives tidal disruption of the WJ (which occurs when e_{\max} is too large). The maximum eccentricity is obtained by integrating the octupole equations of motion for a number of octupole timescales, and recording the maximum value of e achieved. The blue curves depict the quadrupole “LK window” for eccentricity excitation (see Eqs.[6.19] - [4.24]). The quadrupole prediction for the LK window is reasonably accurate for $e_{\text{out},0} = 0.25, 0.5$, but fails for $e_{\text{out},0} = 0.75$.

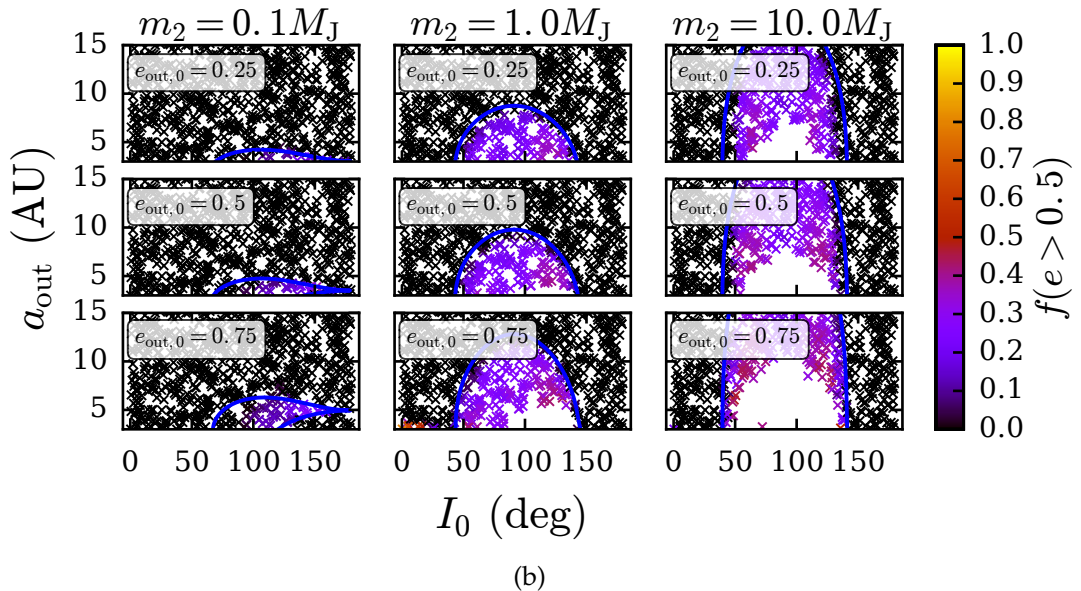
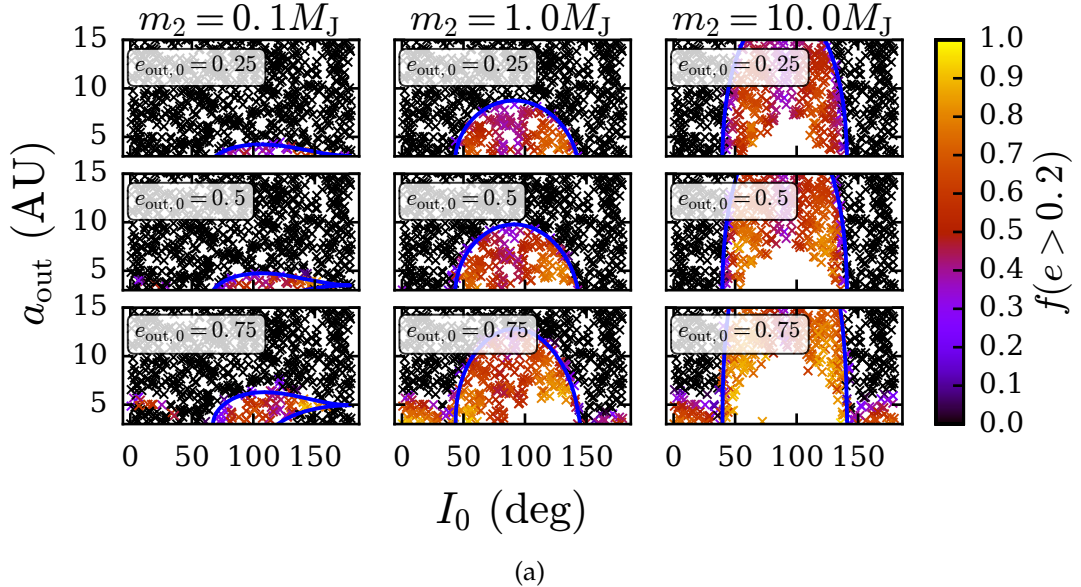


Figure 4.6: (a): Same numerical experiments as depicted in Fig. 4.5, but showing the fraction of the total integration time that the WJ spends with e above 0.2. Note that $f(e > 0.2)$ is relatively high, often $\gtrsim 0.5$. (b): Same as (a), but showing the fraction of time spent above $e = 0.5$. Note that $f(e > 0.5)$ is typically less than ~ 0.2 .

4.3 Observed WJ Systems with Exterior Companions

4.3.1 Sample Description and Method

The results of Section 4.2 demonstrate the types of perturber necessary in generating eccentricity in a WJ with canonical properties ($m_1 = 1M_J$, $a_{\text{in}} = 0.3$ AU). We now consider the observed radial velocity sample of WJs with giant planet companions, and evaluate the prospects for the exterior planet to raise the eccentricity of the WJ to the observed value e_{obs} . This sample consists of 21 systems, and is given in Antonini et al. 2016 (see their Table 1). These systems have measured minimum masses, semi-major axes, and eccentricities for both the inner and outer planets, but lack information on the mutual inclination between m_1 and m_2 .

Several of the two-planet systems in the Antonini et al. (2016) sample are sufficiently non-hierarchical (with $a_{\text{out}}/a_{\text{in}} < 10$) such that the (purely secular) results described in this paper may not apply. We immediately exclude systems satisfying $a_{\text{out}}/a_{\text{in}} < 3$, as non-secular effects will likely dominate. This reduces the sample from 21 to 15 systems. We conduct an additional (albeit less extensive) set of N-body integrations for the remaining systems, and look for changes in semi-major axis of either orbit (indicative of non-secular effects). We use the N-body code REBOUND (Rein & Liu, 2012), and include the apsidal precession from GR and tidal distortion of m_1 using the REBOUNDX library⁶.

In all numerical experiments we set a and a_{out} equal to the observed values, uniformly sample the argument of pericenter and orbital node of each planet

⁶<https://github.com/dtamayo/reboundx>

in the range $[0, 2\pi]$, and sample the initial inclination between m_1 and m_2 in the range $I_0 = [0, \pi]$. We explore various possibilities for the planet masses m_1 and m_2 and initial values of e and e_{out} , as described below. The integration times are the same as described in Section 4.2.4, and we record the maximum value of e , as well as the fraction of time the system spent with $e \geq e_{\text{obs}}$ [denoted as $f(e \geq e_{\text{obs}})$].

4.3.2 Fiducial Experiment

First we conduct a fiducial set of experiments assuming that the inner planet orbit is initially circular, while the outer planet has the initial $e_{\text{out},0}$ given by the observed value, and the observed minimum masses for m_1 and m_2 are equal to the true masses. Figure 4.7 depicts results for a grid of inclinations. We split the results into three possible outcomes: $e_{\text{max}} \leq e_{\text{obs}}$, $e_{\text{max}} \geq e_{\text{obs}}$, and tidal disruption. The color scale indicates the fraction of the total integration time spent with eccentricity exceeding the observed value [$f(e \geq e_{\text{obs}})$]. In all but two systems (HD159243 and HD207832), high mutual inclinations ($I_0 \gtrsim 40^\circ - 50^\circ$) are needed to produce the observed eccentricity.

Although Fig. 4.7 presents a qualitative picture of the necessary initial inclinations, it is incomplete because each inclination corresponds to a particular set of initial orbital phases. Thus, we present a large set (1000 trials) of numerical integrations, sampling the full range of precession phases (ω_{in} , Ω_{in} , ω_{out}) and mutual inclinations. For each observed system, the trials that led to $e_{\text{max}} \geq e_{\text{obs}}$ (without resulting in tidally disruption) are plotted in Fig. 4.8, showing $f(e \geq e_{\text{obs}})$ versus I_0 . In nearly all cases with $e_{\text{obs}} \gtrsim 0.2$, a mutual inclination

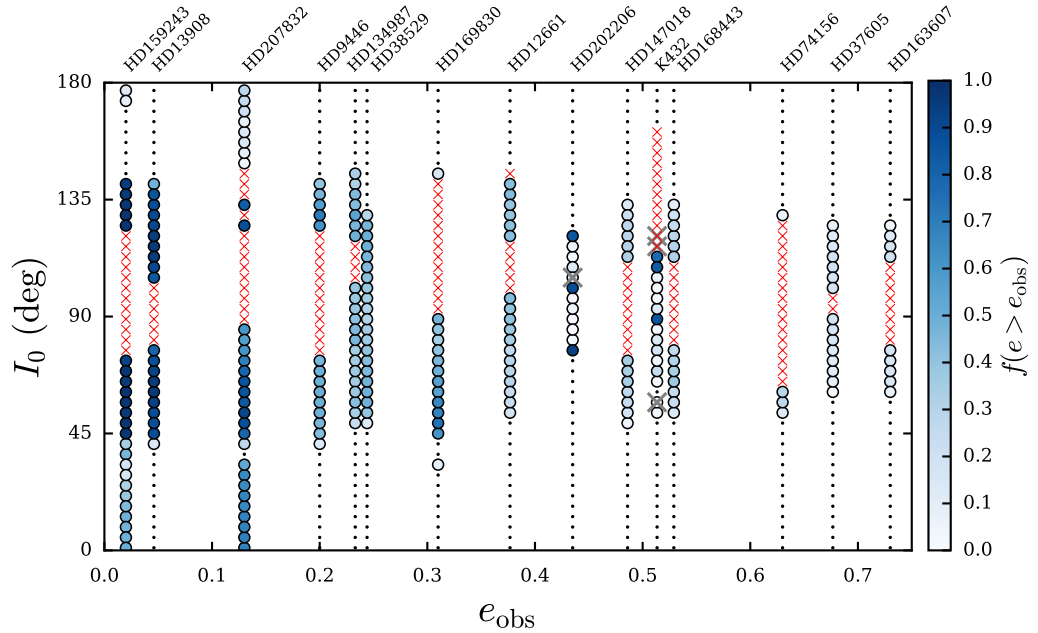


Figure 4.7: Constraints on the required mutual orbital inclination of observed WJs with external companions (see Antonini et al. 2016, Table 1 for the system parameters). The results are obtained through numerical integrations, including apsidal precession from GR and tides. If $a_{\text{out}}/a_{\text{in}} < 10$ we conduct N-body integrations, while if $a_{\text{out}}/\text{in} > 10$ we conduct secular integrations. The outcome of the integration is indicated by the symbol type. Small red crosses: tidally disrupted (i.e. forbidden inclinations). Black dots: $e_{\text{max}} < e_{\text{obs}}$. Blue circles: $e_{\text{max}} > e_{\text{obs}}$ (i.e. the inclinations needed to generate the observed eccentricity). The color scale indicates the fraction of time the system spent with eccentricity $e \geq e_{\text{obs}}$. The large grey crosses depicted in the results for HD202206 and Kepler-432 indicate N-body integrations where either a_{in} or a_{out} changed by more than 10 percent, indicative of non-secular effects. In most cases, mutual inclinations $I_0 \gtrsim 40^\circ - 50^\circ$ are needed to generate the observed WJ eccentricity. This is in agreement with the results for the canonical WJ system considered in Section 4.2.5.

greater than about $40^\circ - 50^\circ$ is required to generate the observed eccentricity. The exterior companions simply do not have sufficient octupole strengths for a coplanar configuration to drive eccentricity oscillations of sufficient amplitude in the WJ, and instead require high inclinations so that LK oscillations are induced. Two exceptions are HD159243 and HD207832. The observed eccentricities of both of these WJs are readily explained with coplanar configurations because of the relatively low values ($e_{\text{obs}} \simeq 0.02$ and 0.1 respectively).

As discussed in Section 4.2.5, in order for secular eccentricity oscillations from exterior companions to be a plausible explanation for eccentric WJs, we also require that the system spend a sufficiently large fraction of time with $e \geq e_{\text{obs}}$. The quantity $f(e \geq e_{\text{obs}})$ has a complicated dependence on inclination and system parameters, and must be examined on a case-by-case basis (see Fig. 4.8). As expected, systems with higher e_{obs} usually have lower values of $f(e \geq e_{\text{obs}})$. The two systems with the highest eccentricities (HD37605 and HD163607) have $f(e \geq e_{\text{obs}}) \lesssim 0.2$ for all inclinations.

We note that unlike in Fig. 4.7, all the results in Fig. 4.8 were obtained by integrating the secular equations of motion, without accompanying N-body calculations for the less hierarchical systems. These results thus may not completely capture the full physical behavior for some of the less hierarchical systems, especially Kepler-432 (the system that exhibits occasional non-secular behavior in our N-body integrations shown in Fig. 4.7). However, note that Kepler-432 is a WJ orbiting an evolved star (Ciceri et al., 2015; Ortiz et al., 2015; Quinn et al., 2015), and the large stellar radius may lead to enhanced tidal interactions and possibly dissipation in the star and orbital decay. The results for Kepler-432 should therefore be taken with caution, since the treatment in this paper does

not include these additional physical ingredients.

4.3.3 Additional Numerical Experiments

Next we investigate how the results of the fiducial experiments (Section 4.3.2) may change when several of the assumptions are modified. We repeat the experiments depicted in Fig. 4.8, but vary the following:

- We allow the initial eccentricity of the WJ to be non-zero. A WJ that formed either in-situ or underwent disk migration is expected to begin with low eccentricity, but here we allow for an initial value $e_0 = 0.1$. Such an eccentricity may conceivably be induced by planet-disk interactions (e.g. Goldreich & Sari, 2003; Tsang et al., 2014; Duffell & Chiang, 2015), or perhaps from a scattering event with another body early in the system’s history. We denote this set of experiments as Eccentric-in (with all other parameters identical to the fiducial set).
- We consider the possibility that the outer planet initially had a higher eccentricity than the observed value. If both planets are observed at a random point in a mutual eccentricity oscillation cycle, then the initial eccentricity of the outer planet may have been higher. For a coplanar system, the change in $j_{\text{out}} = \sqrt{1 - e_{\text{out}}^2}$ is related to the change in $j_{\text{in}} = \sqrt{1 - e_{\text{in}}^2}$ via Eq. (4.16). Since some of the observed systems are not exceedingly hierarchical, there may be a moderate change in e_{out} over the eccentricity oscillation cycle. To explore this possibility, we repeat the fiducial experiments but increase the outer eccentricity by 0.1 relative to the observed value. Thus, the initial outer eccentricity is $e_{\text{out},0} = e_{\text{out,obs}} + 0.1$ (keeping

Table 4.1: Various sets of numerical experiments involving observed WJs with outer planetary companions (see Sections 4.3.2, 4.3.3, and Fig. 4.9). The data set is given in Antonini et al. 2016 (see their Table 1). For each observed system, both planets have measured eccentricities, semi-major axes, and minimum masses. For all experiments we set a_{in} , a_{out} to the observed values, and randomly sample the argument of pericenter and node (ω, Ω) of both planets in the range $[0 - 2\pi]$, and the mutual inclination of the planets in $I_0 = [0, \pi]$. For each experiment we conducted 1000 numerical integrations, out which a small subset (less than 20%) resulted in tidal disruption of the inner planet.

Name	m_1	m_2	$e_{\text{in},0}$	$e_{\text{out},0}$
Fiducial	$(m_1 \sin i_1)_{\text{obs}}$	$(m_2 \sin i_1)_{\text{obs}}$	0.001	$e_{\text{out,obs}}$
Eccentric-in	$(m_1 \sin i_1)_{\text{obs}}$	$(m_2 \sin i_1)_{\text{obs}}$	0.1	$e_{\text{out,obs}}$
Eccentric-out	$(m_1 \sin i_1)_{\text{obs}}$	$(m_2 \sin i_1)_{\text{obs}}$	0.001	$e_{\text{out,obs}} + 0.1$
Increase-mass-in	$2(m_1 \sin i_1)_{\text{obs}}$	$(m_2 \sin i_1)_{\text{obs}}$	0.001	$e_{\text{out,obs}}$
Increase-mass-out	$(m_1 \sin i_1)_{\text{obs}}$	$2(m_2 \sin i_1)_{\text{obs}}$	0.001	$e_{\text{out,obs}}$

the other parameters identical to the fiducial set). We denote this set of experiments as Eccentric-out.

- We note that the observed masses are only lower limits. A higher value for the outer planet mass may lead to a higher eccentricity for the inner planet. To examine this possibility in a simple manner, we increase the outer planet mass by a factor of two: thus $m_2 = 2(m_2 \sin i_2)_{\text{obs}}$. We denote this set of experiments as Increase-mass-out.
- We increase the observed inner planet mass by a factor of two: thus $m_1 = 2(m_1 \sin i_1)_{\text{obs}}$. We denote this set of experiments as Increase-mass-in.

The parameters adopted for these experiments are summarized in Table 4.1. Note that all these experiments except Increase-mass-in provide a more optimistic scenario in producing eccentric WJs compared to the fiducial case.

For each experiment, we proceed exactly as in the fiducial experiment (Sec-

tion 4.3.2), generating 1000 initial conditions with initial inclinations and precession phases randomly sampled over the full ranges. In the interest of space, we omit figures analogous to Fig. 4.8, and instead show the minimum initial inclination needed to generate $e_{\max} \geq e_{\text{obs}}$ (denoted as $I_{0,\min}$) in Fig. 4.9.

In most cases, $I_{0,\min}$ does not differ substantially from the fiducial case: inclinations greater than about 40° are usually needed to achieve $e_{\max} \geq e_{\text{obs}}$. Two exceptions are HD169830 and Kepler-432: although the fiducial experiments imply minimum inclinations of $\sim 30^\circ$ and $\sim 50^\circ$, these additional experiments show that coplanar configurations may lead to the observed WJ eccentricity (however, see the discussion at the end of Section 4.3.2 about Kepler-432.).

In summary, we find that in order for the eccentricities of the observed WJs with external companions to have arisen from secular perturbations from the outer planet, the two planets must have a mutual inclination of at least $40^\circ - 50^\circ$ in most cases. This result is robust across various numerical experiments involving different assumptions on the initial eccentricities and masses of both planets. The exceptions are HD159243, HD207832, and (depending on the assumptions for the initial eccentricities and masses) possibly HD169830 and Kepler-432 – these systems can be explained with coplanar or low inclination configurations. There is a difficulty in explaining the most eccentric WJs in the sample, because the fraction of time spent at or above e_{obs} is low (less than ~ 0.2).

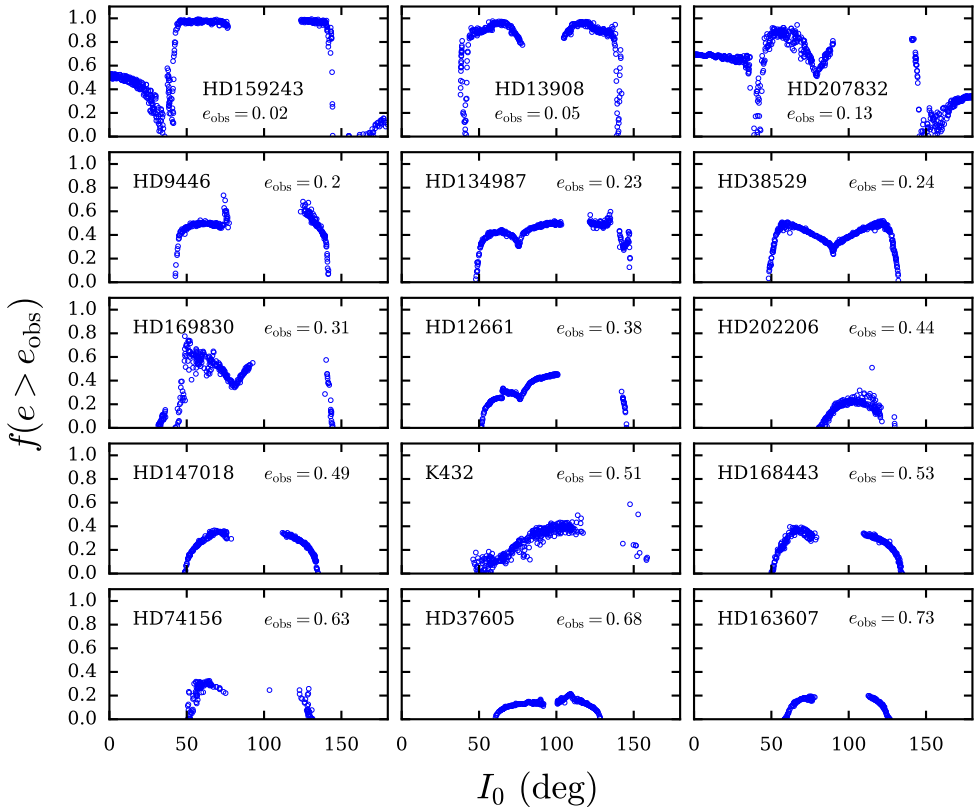


Figure 4.8: *Fiducial experiment* (Section 4.3.2): Large set (~ 1000 trials) of numerical integrations of observed WJ systems with external companions, with inclinations and orbital angles randomly sampled (see Table 4.1 for further information). For each set of initial conditions, we integrate the secular equations of motion, and calculate the fraction of time that the WJ spends at an eccentricity greater than the observed value [$f(e > e_{\text{obs}})$]. The dependence of f with initial inclination varies from system-to-system, and is often complex. High mutual inclinations are usually needed to generate the observed eccentricity, in agreement with Fig. 4.7.

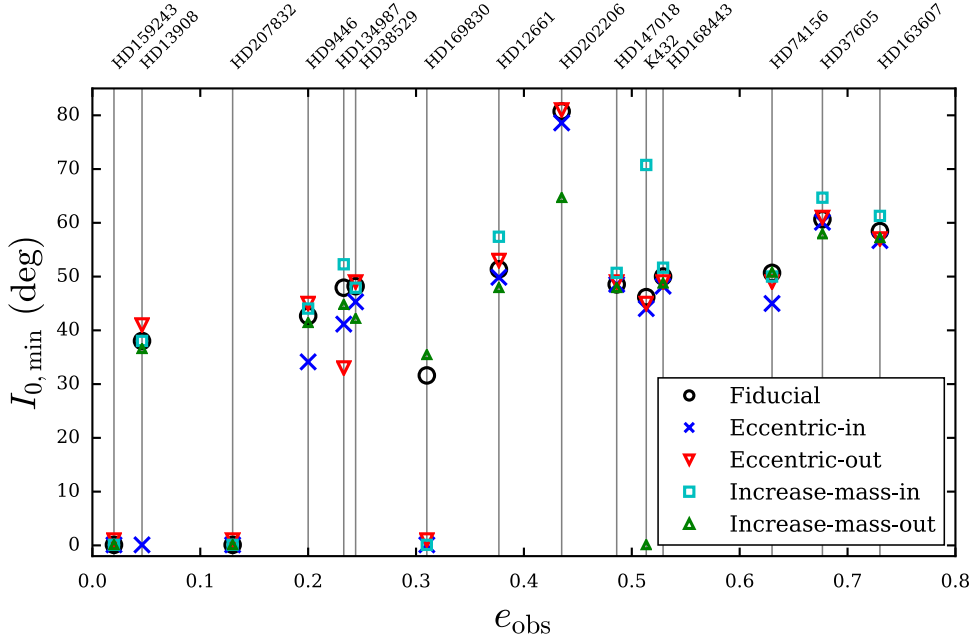


Figure 4.9: *All numerical experiments:* Comparison of the various experiments (see Table 4.1) involving observed WJs with external companions. Each experiment adopts different assumptions on the starting eccentricities and masses of both planets, to address the uncertainties in the initial conditions and sky-projected orientations of the orbits. For each system and experiment, we plot the minimum inclination $I_{0,\min}$ that led to $e_{\max} > e_{\text{obs}}$, determined from integrating 1000 systems (with initial precession angles and mutual inclinations sampled randomly). For most systems, $I_{0,\min}$ is not strongly affected by the experiment assumptions. See the text for further discussion.

4.4 Suppression of Eccentricity Oscillations by Close Rocky Neighbors

Here we consider WJs with close, rocky “neighbors,” in addition to a distant external giant planet. Huang et al. (2016) recently found that $\sim 50\%$ of WJs have nearby low-mass neighbors; such neighbors may lead to orbital precession of the WJ that is faster than that due to the distant giant planet, thereby suppressing eccentricity growth.

We denote the neighboring planet mass as m' , and the WJ and external giant planet companion haves masses m_1 and m_2 , as before⁷. The planet m' has semi-major axis a' , and may orbit interior or exterior to m_1 , but is always interior to m_2 . For simplicity, we assume that m' is circular and coplanar with m_1 . This yields a rouch estimate on the ability of m' to suppress eccentricity oscillations in m_1 . Identifying the precise influence of m' on the eccentricity of m_1 requires N-body integrations of three-planet systems and is beyond the scope of this paper.

In order for m_2 to raise the eccentricity of m_1 , the orbital precession of m_1 due to m' (denoted here as $\dot{\omega}$) must be smaller than the orbital precession of m_1 due to m_2 (of order t_k^{-1}). We thus require

$$\epsilon \equiv \frac{\dot{\omega}}{t_k^{-1}} \lesssim 1, \quad (4.27)$$

with ϵ given by

$$\epsilon = \begin{cases} \frac{m'}{m_2} \frac{a_{\text{out,eff}}^3}{a'^2 a} b_{3/2}^{(1)}(a/a'), & \text{if } a' > a \\ \frac{m'}{m_2} \frac{a' a_{\text{out,eff}}^3}{a^4} b_{3/2}^{(1)}(a'/a), & \text{if } a' < a, \end{cases} \quad (4.28)$$

where $b_{3/2}^{(1)}(\alpha)$ is a Laplace coefficient. As a result, for specified properties of a WJ and giant planet perturber, there is a maximum value of m' allowing eccentricity oscillations of m_1 (m'_{crit} , obtained from setting $\epsilon = 1$).

Figure 4.10a considers a canonical WJ ($m_1 = M_J$, $a = 0.3$ AU) and fixed giant planet perturber ($m_2 = M_J$, $a_{\text{out,eff}} = 3, 6$ AU) and shows m'_{crit} versus a'/a . A super-earth neighbor ($m' \sim 10M_\oplus$) is extremely effective in suppressing eccentricity oscillations in the WJ, and an Earth-mass neighbor may also prohibit eccentricity oscillations for close separations.

⁷We will refer to m' as the “neighbor” and m_2 as the “perturber.”

Figure 4.10b depicts the sample of WJs with close neighbors from Huang et al. (2016) (with the exception of KOI-191.01, since this WJ may actually be solitary [Law et al. 2014]). For the neighboring planets in each system, we calculate the value of ϵ , assuming a hypothetical giant perturber $m_2 = 1M_J$ and $a_{\text{out,eff}} = 5a$, with a the observed WJ semi-major axis. Since this sample consists entirely of Kepler objects, many planets lack mass constraints. WJs without mass estimates have been assigned $m_1 = M_J$, and the close neighbors have been assigned $m'/M_\oplus = 2.69(R'/R_\oplus)^{0.93}$ (Weiss & Marcy, 2014). Given these assumptions on planetary masses, the results in Fig. 4.10b should be interpreted with large uncertainties. Nonetheless, we see that nearly all systems have at least one neighboring planet satisfying $\epsilon \gtrsim 1$, so that eccentricity growth due to the external giant perturber is most likely prohibited, or at the very least, reduced. Given the strong giant planet perturber considered, the values of ϵ in 4.10b represent an optimistic scenario: weaker perturbers will lead to even larger values of ϵ .

We conclude that close (within $\sim [0.1 - 10]a$), low mass ($1 - 10M_\oplus$) neighbors to WJs are frequently capable of suppressing eccentricity oscillations in WJs. If eccentric WJs arise primarily due to secular perturbations from distant giant planet perturbers, they should generally lack nearby companions.

4.5 Summary & Discussion

Many warm Jupiters (WJs) are observed to have exterior giant planet companions. This paper considers the scenario where WJs form initially with low eccentricities, having reached their observed orbits either through in-situ formation, or disk migration. In order to produce the modest eccentricities observed in

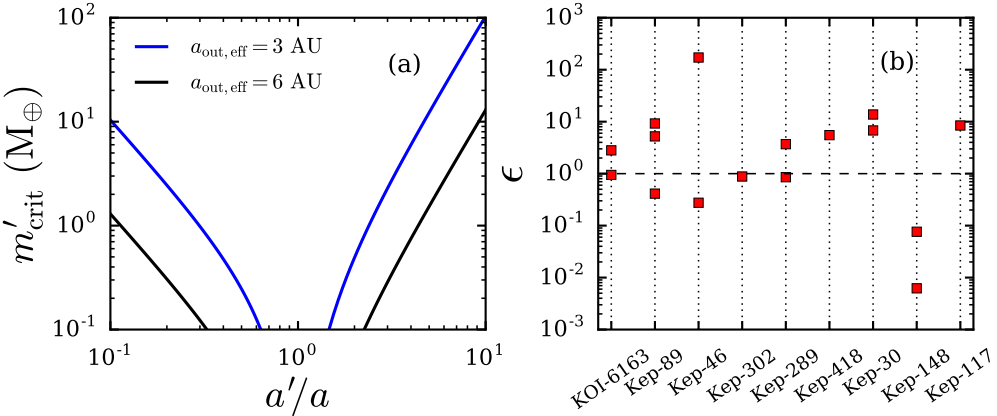


Figure 4.10: (a): Maximum mass of m' that allows eccentricity oscillations of m_1 (due to m_2), as a function of a'/a . m'_{crit} is determined by setting $\epsilon = 1$; see Eq. (4.28). The WJ has $m_1 = M_J$, $a = 0.3$ AU, and the perturber has $m_2 = M_J$, $a_{\text{out,eff}} = 3, 6$ AU, as labeled. (b): ϵ for the sample of WJs with close companions, from Huang et al. (2016). We have set the mass and separation of a giant planet perturber to $m_2 = M_J$ and $a_{\text{out,eff}} = 5a$, where a is the measured WJ semi-major axis. Nearly all systems have at least one neighboring planet that satisfies $\epsilon \gtrsim 1$, indicating that eccentricity-oscillations from an undetected giant planet perturber are likely to be suppressed.

many WJs, we invoke the presence of an exterior giant planet companion that raises the eccentricity of the WJ through secular perturbations. The eccentricity of the WJ thus oscillates between $e \simeq 0$ and a maximum value $e = e_{\text{max}}$. In order for the companion to generate the observed WJ eccentricity e_{obs} through eccentricity oscillations, we require $e_{\text{max}} \geq e_{\text{obs}}$. Furthermore, the fraction of time spent at eccentricities equal to or greater than the observed value [denoted as $f(e \geq e_{\text{obs}})$] should be relatively high. For a WJ with specified properties, these requirements place constraints on the properties of an external companion in terms of its mass, semi-major axis, eccentricity, and inclination.

In Section 4.2, we examine the different mechanisms/regimes of eccentricity excitation of a “canonical” WJ (with $m_1 = 1M_J$, $a = 0.3$ AU) by an outer planetary companion of various masses and orbital properties. Coplanar and

inclined systems are discussed separately, because coplanar systems allow an octupole-level analytic treatment, whereas octupole-level inclined systems require full numerical integrations. In addition to the secular interactions between the two planets, we also consider apsidal precession of the inner planet due to general relativity and tidal distortion. For coplanar and moderately inclined systems ($I_0 \lesssim 30^\circ$), the apsidal precession resonance, which occurs when the net precession rates of the two planets (driven by mutual interaction and the GR effect) become equal (see Eqs.[4.13]-[4.14]). This leads to efficient eccentricity excitation (see Figs. 4.1 and 4.4). We also show that the extreme eccentricity excitation and orbital flip discussed in previous work (Li et al., 2014) are unlikely to operate for realistic systems (Section 2.3). For higher mutual inclinations, the Lidov-Kozai eccentricity effect leads to eccentricity excitation.

The main results of Section 4.2 are summarized in Figs. 4.5 and 4.6. Figure 4.5 reveals that coplanar and low-inclination ($I_0 \lesssim 30^\circ$) perturbers may lead to substantial eccentricity increases, with $e_{\max} \simeq 0.2 - 0.6$, where the range in e_{\max} depends on the perturber mass, separation, and eccentricity. Massive perturbers with high eccentricities are especially effective in producing large e_{\max} over a wide range of separations. However, despite these large values of e_{\max} , the fraction of time the WJ spends in such eccentric states is often small (see Fig. 4.6). We conclude that a coplanar or low inclination companion may easily lead to a mildly eccentric WJ (with $e \simeq 0.2$), provided that the perturber is massive and highly eccentric (with $m_2 \gtrsim M_J$ and $e_{\text{out}} \simeq 0.75$). On the other hand, such a companion is unlikely to produce a moderately eccentric WJ (with $e \simeq 0.5$), because the fraction of time the WJ spends at or above $e = 0.5$ is very low.

Higher mutual inclinations are generally much more effective in producing

eccentric WJs, due to Lidov-Kozai cycles. Inspecting the high-inclination results (with $I_0 \gtrsim 40^\circ$) in Figs. 4.5 and 4.6, we find that such inclinations may easily produce a mildly eccentric WJ (with $e \simeq 0.2$), since $f(e \geq 0.2) \gtrsim 0.5$ in most cases. Producing a moderately eccentric WJ (with $e \simeq 0.5$) is also possible, with $f(e \geq 0.5) \simeq 0.3$ for some inclinations.

In Section 4.3 we apply our method and analysis to observed WJs with exterior giant planet companions. These systems have measured minimum masses, semi-major axes, and eccentricities for both the WJ and outer planet, but lack information on the mutual orbital inclination (see Table 1 in Antonini et al., 2016, for measured system parameters). For each system we have identified the necessary mutual inclinations to produce the observed WJ eccentricity (see Figs. 4.7, 4.8, and 4.9), for several different assumptions of the initial eccentricities and planetary masses of both planets. The majority of systems require mutual inclinations of at least $40^\circ - 50^\circ$, in agreement with the results of Section 4.2. Exceptions are HD159243, HD207832, and depending on the particular assumptions (see Section 4.3.3), possibly HD169830 and Kepler-432. The eccentricities of these four WJs may result from coplanar or low inclination configurations under some circumstances (but note the caveat concerning Kepler-432; see the discussion at the end of Section 4.3.2).

Explaining the three most eccentric WJs in the sample (HD74156, HD37605, and HD163607, with $e_{\text{obs}} \gtrsim 0.6$) is more difficult, because we find the fraction of time spent above the observed value is usually less than 20%. If the eccentricities of these planets are the result of secular eccentricity oscillations from the observed companion, then we are observing them at rather special moments during their oscillation cycles. On the other hand, such high eccentricities in

WJs are also less common, which may help alleviate this issue.

Since $\sim 50\%$ of WJs are estimated to have close rocky “neighbors” (Huang et al., 2016), we have also briefly explored the effects of a third, low-mass planet orbiting close to the WJ (see Section 4.4). The precession induced on the orbit of a WJ by such a neighbor may often overcome the precession induced by a more distant giant planet companion, thereby suppressing eccentricity oscillations. By comparing the precession rates induced by a low mass neighbor and a distant giant planet perturber, we find that $\sim (1 - 10)M_{\oplus}$ neighbors may frequently suppress eccentricity oscillations in a canonical WJ (see Fig. 4.10a). We also consider the observed close neighbors to WJs from Huang et al. (2016), and calculate the precession induced in the WJ by the neighbor(s), compared to that due to an undetected giant planet perturber. We show that even for a strong giant planet perturber, most systems contain at least one neighboring planet likely to suppress eccentricity oscillations (see Fig. 4.10b). In the Huang et al. (2016) sample, four WJs with close neighbors currently have constraints on the WJ eccentricity⁸, three of which (Kepler-46, Kepler-117, and Kepler-289) have low eccentricities, in the range $e_{\text{obs}} \simeq 0.003 - 0.03$, while the fourth (Kepler-418) has $e_{\text{obs}} \simeq 0.2$. The fact that WJs with close neighbors tend to have low or modest eccentricities is consistent with our finding that such neighbors probably do not allow the eccentricity of the WJ to grow from secular perturbations from a more distant giant planet. On the other hand, such lack of eccentric WJs with close neighbors may also simply result from dynamical stability requirements.

We conclude that the explanation for eccentric WJs proposed in this paper requires that eccentric WJs should generally lack close neighbors of masses

⁸Eccentricities were obtained from exoplanets.org and exoplanet.eu, accessed on July 17, 2017.

$\sim 10M_{\oplus}$. The consequence of a lower mass ($\sim 1M_{\oplus}$) neighbor is less certain, and should be explored in future work via N-body integrations of three planet systems.

Our results suggest that many observed WJs could have highly inclined ($\gtrsim 40^{\circ}$) external giant planet companions. This is intriguing, because it requires an initial scattering event to generate the mutual inclination, and therefore the existence of at least three giant planets. A recent measurement of a high mutual inclination for a WJ with an external companion, using transit-timing and transit duration variations, implies that high inclinations may be relatively common (Masuda, 2017). As observations continue to probe mutual inclinations in multiple planet systems (see McArthur et al. 2010 and Mills & Fabrycky (2017) for two examples of mutually inclined systems), a clearer picture of the role of external companions on the eccentricities of inner planets will emerge.

CHAPTER 5

IN-SITU SCATTERING OF WARM JUPITERS

5.1 Introduction

Warm Jupiters (WJs, giant planets with orbital periods in the range $\sim 10 - 300$ days) have been the focus of many studies, especially regarding their dynamical histories. Similar to hot Jupiters (HJs, with orbital periods less than ~ 10 days), whether WJs previously underwent migration from farther out, are currently in the process of migration, or formed in-situ, is uncertain. Planet migration comes two distinct flavors. One possibility is disk migration, in which planets are transported inwards due to torques from the protoplanetary disk (e.g. Lin et al., 1996; Tanaka et al., 2002; Kley, & Nelson, 2012; Baruteau et al., 2014). The second possibility is high-eccentricity migration, in which the planet's eccentricity is excited to an extreme value by a stellar or planetary companion(s), so that tides raised on the planet at pericenter distances shrink and eventually circularize the orbit. High-eccentricity migration itself comes in several distinct flavors, depending on the details of the eccentricity excitation, including excitation from an inclined companion due to Lidov-Kozai cycles (Lidov, 1962; Kozai, 1962) or other secular perturbations (Wu & Murray, 2003; Fabrycky & Tremaine, 2007; Naoz et al., 2012; Petrovich, 2015a,b; Anderson et al., 2016; Muñoz et al., 2016; Hamers et al., 2017; Vick et al., 2019), scatterings (possibly combined with secular interactions) (Rasio & Ford, 1996; Nagasawa et al., 2008; Nagasawa, &

This chapter is adapted from Anderson et al. (2019), to be submitted.

Ida, 2011; Beaugé & Nesvorný, 2012), and secular chaos (Lithwick, & Wu, 2011, 2014; Teyssandier et al., 2019). See also Dawson, & Johnson (2018) for a review.

WJs are observed to have a wide range of eccentricities. A large fraction have relatively low eccentricities (note the median eccentricity is ~ 0.17), but a substantial number have moderate to high eccentricities. Theories of planet formation/migration must be able to account for these observations, and many different mechanisms have been proposed in exciting WJ eccentricities.

One seemingly natural explanation for eccentric WJ is high-eccentricity migration. In this situation, WJs are caught in the act of inward migration, eventually to become HJs in circular orbits. In any high-eccentricity migration theory, a small pericenter distance is required, so that tidal dissipation may shrink the orbit within the lifetime of the host star. However, the majority of WJs have pericenter distances too large to allow for migration. As a result, the most promising flavor of high-eccentricity migration in producing WJs is secular perturbations from a perturber, so that WJs are currently undergoing eccentricity oscillations, and observed in a low-eccentricity phase (Dong et al., 2014; Dawson & Chiang, 2014; Petrovich & Tremaine, 2016). This scenario requires a relatively close or massive perturber, so that the secular perturbations that lead to eccentricity growth are not suppressed by general relativistic apsidal precession. Such a strong perturber is also required in order to produce any appreciable fraction of WJs in population synthesis studies. If the perturber is too weak to induce eccentricity oscillations at sub-AU distances, migration proceeds far too quickly, delivering the planet into HJ territory with little evidence of the time spent at WJ distances. As a result, although HJs may be formed for a relatively wide range of perturber properties (in terms of mass, semi-major axis, and eccentricity),

WJs require somewhat specific initial conditions. Observationally, the number of WJs exceeds the number of HJs. Population syntheses that choose a broad range of properties for the perturber do not produce any appreciable numbers of WJs (Petrovich, 2015b; Anderson et al., 2016; Hamers et al., 2017). Petrovich & Tremaine (2016) conducted the most successful study thus far in replicating the observed relative numbers of HJs and WJs by choosing as their initial conditions a population of WJs initially at 1 AU with strong perturbers in a narrow range of semi-major axis, at 5 – 6 AU. However, even these initial conditions still produce too few WJs compared to HJs by a factor of about 5. At this point, it remains unclear whether fine-tuning of the initial conditions is required to produce any substantial number of WJs via secular high-eccentricity migration.

Other difficulties of high-eccentricity migration in the context of WJ formation include the fact that unlike HJs, a large fraction of WJs are thought to have a close, low-mass neighbor (Huang et al., 2016). Such a configuration is difficult to envision in a violent high-eccentricity migration history. Furthermore, Antonini et al. (2016) examined the subset of observed WJs with characterized (in terms of mass, semi-major axis and eccentricity) external giant planet companions, and find most systems are inconsistent with a traditional secular high-eccentricity migration origin, where the WJ was originally located beyond 1 AU, due to the initial configurations being highly unstable.

These difficulties of high-eccentricity migration in reproducing properties of WJs indicate that in-situ formation or disk migration may be responsible for forming many, if not most WJs. However, both in-situ formation and disk migration generally predict low eccentricities, inconsistent with the mild to moderately eccentric component of the observed WJ population. As a result, mech-

anisms for generating eccentricity excitation are necessary. Some mechanisms utilize the presence of a protoplanetary disk. Planet-disk interactions are capable of exciting eccentricities (e.g. Goldreich & Sari, 2003; Tsang et al., 2014), but may be limited to modest eccentricities (Duffell & Chiang, 2015). Recently Petrovich et al. (2019) studied a mechanism for transferring eccentricity (more precisely, angular momentum deficit) from an outer planet to a WJ during dispersal of the protoplanetary disk.

Anderson et al. (2017) considered the possibility that eccentric WJs arise due to in-situ formation or disk migration (in an initially low-eccentricity orbit), followed by secular perturbations due to a distant companion, without requiring that the planet be undergoing high-eccentricity migration. Eccentricity may be excited due to a highly inclined perturber via Lidov-Kozai cycles, or by an eccentric coplanar perturber due to an apsidal precession resonance. Taking the sample of WJs with external planetary companions with characterized orbits, and assuming that the WJ formed in a circular orbit with subsequent secular eccentricity excitation from the companion, they found high mutual inclinations are needed ($\sim 50^\circ - 60^\circ$) to generate the observed eccentricity, so that Lidov-Kozai cycles are induced. The finding that high mutual inclinations are needed is intriguing, and consistent with previous evidence for high inclinations in many of the same systems found by Dawson & Chiang (2014). However, generating such inclinations is non-trivial, and clearly requires an early scattering event in the system's history.

Planet-planet scattering itself remains another possibility in producing eccentric WJs. Most studies of giant planet scattering have focused largely on “cold Jupiters,” giant planets located at several AU. A substantial literature

of planet scattering work exists, ranging from scattering of two planets to ten or more planets (e.g. Chambers et al., 1996; Lin, & Ida, 1997; Ford et al., 2001; Adams, & Laughlin, 2003; Chatterjee et al., 2008; Ford & Rasio, 2008; Jurić & Tremaine, 2008; Nagasawa, & Ida, 2011).

Previous scattering studies of “cold Jupiters,” giant planets located at several AU have been largely successful in reproducing the eccentricities of exoplanets. However, the scattering hypothesis suffers from some uncertainties at sub-AU distances from the host star, and the parameter space for scattering close to the host star is much less explored. Scattering outcomes depend on the “Safronov number”, roughly the ratio of the escape velocity from the planetary surface to the planet’s orbital velocity. When the Safronov number is much less than unity, close encounters between planets result in collisions, with the collision product having a low eccentricity. In contrast, when the Safronov number is much greater than unity, ejections are expected, efficiently raising the eccentricities of remaining planets. WJs have Safronov numbers of order unity and thus lie in a regime in which a combination of collisions and ejections may occur. Petrovich et al. (2014) undertook a scattering study of primarily HJs, within 0.15 AU and with close initial spacing, and found inefficient eccentricity excitation due to a preponderance of collisions. Whether this finding holds for WJs with a wider range of initial spacing has yet to be thoroughly explored.

This paper presents a systematic study of planet-planet scattering for systems of closely-spaced WJs starting with initially low eccentricities. This setup is consistent with either in-situ formation or arrival at a sub-AU orbit by disk migration. The goal of this paper is two-fold. (1) On observationally-motivated grounds, we aim to identify to what extent planet scattering may be contribut-

ing to eccentric WJs. (2) On the theoretical side, we aim to catalogue the outcomes of planet-planet scattering for planets in the range $0.1 - 1$ AU, where a rich variety of collisions and ejections are expected². We conduct N-body scattering experiments of (usually) three giant planets, with general relativistic apsidal precession included. We explore a variety of choices for planet masses and initial spacing, catalogue the scattering outcomes (branching ratios), and analyze the properties of the systems remaining after scattering. Radial velocity observations have yielded samples of solitary WJs and WJs with an external giant planet companion, with eccentricity measurements for both samples. We compare the results of the scattering experiments with observed system properties to evaluate the extent to which in-situ scattering may be contributing to the eccentric WJ population. We also briefly discuss how the results are affected by adding a fourth planet to the initial setup.

This paper is organized as follows. In Section 5.2, we describe the setup of our N-body scattering experiments, present scattering branching ratios, demonstrate how the scattering results depend on various parameters, and discuss the properties of the surviving planetary systems. In Section 5.3 we compare the results of Section 5.2 with observations. We conclude in Section 5.4.

²We note that a recent scattering study by Marzari, & Nagasawa (2019) explored a similar parameter regime

5.2 Scattering Experiments

5.2.1 Setup & Canonical Parameters

We begin with a system of three planets, with masses m_1, m_2, m_3 , orbiting a host star with mass $M_\star = 1M_\odot$ and radius $R_\star = 1R_\odot$. For each planet, we sample the initial eccentricities uniformly in the range $[0.01, 0.05]$, inclinations (relative to an arbitrary reference frame) uniformly in $[0, 2^\circ]$, and argument of pericenter, longitude of ascending node, and mean anomaly uniformly in $[0, 2\pi]$. The initial semi-major axes are specified in units of mutual hill radius K , so that $a_i - a_{i-1} = KR_{\text{H,mut}}$, with a_1 specified and $i = 2, 3$. We adopt a fiducial spacing of $K = 4$. The innermost semi-major axis is sampled uniformly in $a_1 = [0.1 - 1]\text{AU}$, and the planet masses are chosen to be $0.5, 1, 2M_J$, with randomly assigned ordering. We draw a sample of over 3000 systems with these parameters and evolve using N-body integrations. This set of simulations constitutes our fiducial sample, which we will refer to as `fiducial` (see also Table 5.1). Section 5.2.3 explores how the results depend on K, a_1 , and planet masses, and Section 5.2.4 considers scattering of four planets.

The N-body calculations are conducted using REBOUND (Rein & Liu, 2012). We include the effects of apsidal precession due to GR using the gr-potential option in REBOUNDX³. When the separation of any two bodies becomes less than the sum of their radii, we assume the bodies merge, conserving mass and momentum, as in the built-in REBOUND collision routine. Since we consider young giant planets, we set the radius of each planet to $R_p = 1.6R_J$. See also Appendix C. Planets are considered ejected if the distance from the host star

³<https://github.com/dtamayo/reboundx>

exceeds 1000 AU, and are subsequently removed from the simulation.

We integrate this system of three unstable planets using the IAS15 integrator in REBOUND(Rein, & Spiegel, 2015) for a timespan of $10^6 P_1$, with P_1 the initial orbital period of the innermost planet. We refer to this initial, highly unstable phase (with close encounters eventually resulting in collisions or ejections) as “Phase 1” of the integration. After this initial scattering has elapsed nearly 100% of the three-planet systems have become destabilized due to both collisions and ejections. We continue to integrate the remaining two-planet systems for a timespan of $10^8 P_{\text{in}}$ (or until another collision or ejection has occurred), where P_{in} is the orbital period of the inner planet at the end of “Phase 1”. We refer to this longer-term integration as “Phase 2,” and use the hybrid integrator Mercurius. Mercurius utilizes a symplectic Wisdom-Holman integrator WH-FAST for large separations between planets (Rein, & Tamayo, 2015), switching to IAS15 when the separation between any two bodies becomes less than a critical value. We choose this critical value to be 5 Hill radii. The timestep for the Wisdom-Holman integrator is chosen to be $0.02P_{\text{in}}$. Repeating a subset of the fiducial sample with a timestep $0.01P_{\text{in}}$ yielded statistically identical results.

5.2.2 Scattering Outcomes

Figure 5.1 shows the fractions of one, two, and three-planet systems as a function of time. The leftmost panel shows “Phase 1” of the integration using IAS15. Since the initial systems are highly unstable, the fraction of three-planet systems quickly decays, eventually reaching a negligible value after 10^6 initial orbital periods of the innermost planet. During the long-term follow-up integration of the

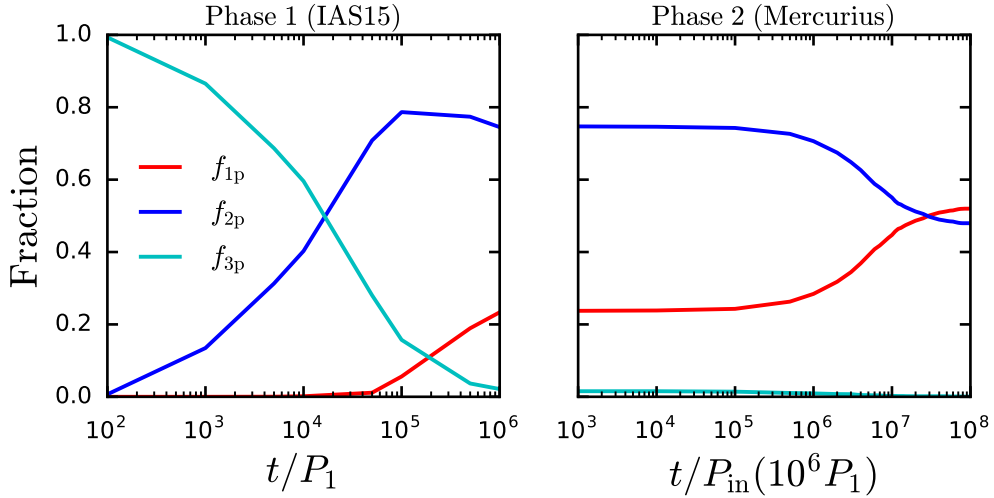


Figure 5.1: Fraction of one, two, and three-planet systems as a function of time for the fiducial set of simulations. *Left:* “Phase 1” of the integration, in which the initial (highly unstable) three-planet system was integrated using the IAS15 integrator in REBOUND. After 10^6 initial orbital periods of the innermost planet have elapsed, nearly all of the three-planet systems have become destabilized, due to a combination of planet collisions and ejections. *Right:* “Phase 2” of the integration, in which we integrate the two-planet systems using the hybrid Mercurius integrator, for a timespan of 10^8 orbital periods of the inner planet of the two-planet systems. At the end of the integration, the fractions of one and two-planet systems approach a constant value.

two-planet systems (“Phase 2”, right panel of Fig. 5.1), the fraction of two-planet systems declines, eventually approaching a constant value after 10^8 orbits. The vast majority of the two-planet systems are undergoing secular interactions at this point, with constant semi-major axes and oscillating eccentricities and inclinations. We thus conclude that the majority of the remaining 2-planet systems are stable at this time. Further instabilities may occur over much longer timescales, but such integrations are extremely costly to perform. We have randomly selected a subset of 30 closely-spaced systems (with $a_{\text{out}}/a_{\text{in}} < 3$), and integrated for an additional 10^9 orbits of the inner planet. Of these 30 systems, 3 became unstable.

A close encounter can result in a planet loss due to a planet-planet collision, planet-star collision, or planet ejection. Considering the first planet loss only (so that the total number of planets is reduced from three to two), the number of events for each particular outcome is denoted by N_{pp} (planet-planet collision), N_{ps} (planet-star collision), and N_{ej} (planet ejection), with total number of events $N_{\text{tot}} = N_{\text{pp}} + N_{\text{ps}} + N_{\text{ej}}$. The fractions of total systems resulting in a given outcome are thus

$$f_{\text{pp}} \equiv \frac{N_{\text{pp}}}{N_{\text{tot}}}, \quad f_{\text{ps}} \equiv \frac{N_{\text{ps}}}{N_{\text{tot}}}, \quad f_{\text{ej}} \equiv \frac{N_{\text{ej}}}{N_{\text{tot}}}. \quad (5.1)$$

Table 5.1 presents these fractions. For the fiducial sample, we see that the most common outcome is a planet-planet collision, with $f_{\text{pp}} \approx 65\%$. The second most common outcome is a planet ejection, with $f_{\text{ej}} \approx 29\%$. Planet-star collisions are least common, with $f_{\text{ps}} \approx 6\%$. Recall that here we only consider the first planet loss, occurring due to dynamical instability of the initial three-planet system. Some systems later lose a second planet, which we discuss separately below.

Next we separately analyze the scattering history of the one and two-planet systems that remain at the end of “Phase 2” of the integration. Considering first the two-planet systems, with number $N_{2\text{p}}$, we define $N_{\text{pp},2\text{p}}$ ($N_{\text{ps},2\text{p}}$, $N_{\text{ej},2\text{p}}$) as the number of two-planet systems that suffered a planet-planet collision (planet-star collision, planet ejection). Thus, the fractions of two planet systems that were formed by a particular outcome are

$$f_{\text{pp},2\text{p}} = \frac{N_{\text{pp},2\text{p}}}{N_{2\text{p}}} \quad f_{\text{ps},2\text{p}} = \frac{N_{\text{ps},2\text{p}}}{N_{2\text{p}}} \quad f_{\text{ej},2\text{p}} = \frac{N_{\text{ej},2\text{p}}}{N_{2\text{p}}}. \quad (5.2)$$

Inspecting Table 5.2, 100% of the two-planet systems were formed by planet-planet collisions.

The one-planet systems suffered two planet losses. Define the total number

of one-planet systems as N_{1p} . The number of one-planet systems where the first planet loss was a planet-planet collision (planet-star collision, planet ejection) is $N_{pp,1p}^{(1)}$ ($N_{ps,1p}^{(1)}$, $N_{ej,1p}^{(1)}$), where the superscript “(1)” indicates the first planet loss. Using similar notation as for the two-planet systems, we define the fractions

$$f_{pp,1p}^{(1)} \equiv \frac{N_{pp,1p}^{(1)}}{N_{1p}}, \quad f_{ps,1p}^{(1)} \equiv \frac{N_{ps,1p}^{(1)}}{N_{1p}}, \quad f_{ej,1p}^{(1)} \equiv \frac{N_{ej,1p}^{(1)}}{N_{1p}}. \quad (5.3)$$

Considering the second planet loss (so that the total number of planets is reduced from two to one) we use similar notation, $f_{pp,1p}^{(2)}$, $f_{ps,1p}^{(2)}$, and $f_{ej,1p}^{(2)}$, where the superscript “(2)” indicates the second planet loss. Table 5.3 shows that one-planet systems are formed through a combination of ejections and collisions. The first planet loss occurs due to an ejection $\sim 56\%$ of the time, and planet-planet and planet-star collisions 33% and 11% respectively. The second planet loss occurs almost entirely due to ejections, with $f_{ej,1p}^{(2)} \sim 92\%$.

In summary, scattering of a closely-spaced ($K = 4$) system of giant planets results in comparable numbers of one and two-planet systems. Two-planet systems are produced entirely due to planet-planet collisions, whereas one-planet systems form through a combination of ejections and collisions.

5.2.3 Properties of One and Two-Planet Systems and Parameter Exploration

Now we analyze the orbital characteristics of the one and two-planet systems, at the end of Phase 2 of the integration. In most figures we also show properties of observed WJ systems; however, we delay comparison with the observed systems until Section 5.3.

Table 5.1: Initial conditions, scattering outcomes, and final eccentricities for the different sets of simulations. We include here all surviving systems (see Tables 5.2 and 5.3 for the results separated into two and one-planet systems). The information is obtained at the end of “Phase 2” of the integration (see Fig. 5.1). In all sets of simulations, the initial innermost planet semi-major axis is sampled uniformly in $a_1 = [0.1 - 1]$ AU. The remaining two planets are then spaced in units of their mutual Hill radius K , as indicated. The simulation set `lognorm-mass` has all masses sampled from a log-normal distribution, with a mean of $\log(m_p/M_J) = 0$, width 0.5, and upper and lower limits of $m_p = 4M_J$ and $m_p = 0.25M_J$. The arguments of pericenter, longitude of ascending node and mean anomalies are sampled in $[0 - 2\pi]$ for all simulations. The initial inclinations are sampled uniformly in the range $[0.1^\circ - 2^\circ]$. For `fiducial`, `near-eq-mass`, `lognorm-mass`, and `fiducial-K-3`, the initial eccentricities are sampled in the range $[0.01 - 0.05]$. For `fiducial-K-5`, we increase the initial eccentricities so that instabilities occur within a practical amount of time, choosing the innermost eccentricity $e_1 = 0.08$ and the remaining two planets so that $a_3(1 - e_3) - a_2(1 + e_{i2}) = 3R_{H,\text{mut}}$, with $R_{H,\text{mut}}$ the mutual Hill radius. This leads to eccentricities at most ~ 0.11 for the outer two planets. The columns in the table are (from left to right), the simulation name, number of simulations (N_{run}), choice of planet masses, initial spacing in units of mutual Hill radii (K), fraction of one-planet systems produced (f_{1p}), fraction of two-planet systems produced (f_{2p}). The columns labeled f_{pp} , f_{ps} , and f_{ej} indicate the fraction of systems where the first planet loss (for one-planet systems), or only planet loss (for the two-planet systems) resulted from a planet-planet collision, planet-star collision, or planet ejection respectively. See also equation (5.1). The branching ratios for the second planet loss (resulting in one-planet systems) are included in Table 5.3. The average eccentricity is denoted as e_{ave} , and the 10th, 50th, and 90th percentile eccentricities as e_{10} , e_{50} , e_{90} . Note that for the two-planet systems in these samples, the eccentricities shown are for the inner planet only.

Name	N_{run}	Initial Masses (M_J)	K	f_{1p}	f_{2p}	f_{pp}	f_{ps}	f_{ej}	e_{ave}	e_{50}	e_{10}	e_{90}
<code>fiducial</code>	3313	0.5, 1.0, 2.0	4	0.52	0.48	0.65	0.06	0.29	0.23	0.19	0.05	0.48
<code>near-eq-mass</code>	973	0.9, 1.0, 1.1	4	0.34	0.66	0.78	0.10	0.12	0.28	0.23	0.05	0.59
<code>lognorm-mass</code>	965	See caption	4	0.50	0.49	0.69	0.00	0.31	0.22	0.17	0.05	0.47
<code>fiducial-K-3</code>	986	0.5, 1.0, 2.0	3	0.60	0.41	0.76	0.00	0.24	0.23	0.17	0.04	0.48
<code>fiducial-K-5</code>	949	0.5, 1.0, 2.0	5	0.50	0.48	0.63	0.00	0.37	0.23	0.18	0.05	0.48

Figure 5.2 shows the properties of the two-planet systems. The subscript “in” indicates the inner planet and “out” indicates the outer planet. We comment on the key features here, but see the caption and Table 5.2 for additional details. In Fig. 5.2a, we present the relative spacing, a_{out} versus a_{in} . The two-planet systems are quite closely-spaced, with 90% of systems satisfying $a_{\text{out}}/a_{\text{in}} < 3$. In Fig. 5.2c, we show semi-major axis versus eccentricity for the inner planet (a_{in} versus e_{in}). Smaller values of a_{in} lead to a wider range of eccentricities. The eccentricity distribution in Fig. 5.2e is peaked at small values, and has mean and 90th percentile values of $e_{\text{in}}^{\text{ave}} = 0.15$, $e_{\text{in}}^{90} = 0.34$. The mutual inclinations of the two-planet systems have mean and 90th percentiles $I_{\text{mut}}^{\text{ave}} = 5.25^\circ$ and $I_{\text{mut}}^{90} = 13.26^\circ$. The typically low eccentricities is consistent with the fact that the two-planet systems arose entirely due to planet-planet collisions.

Fig. 5.3 shows the properties of the one-planet systems. Most of these planets are WJs, but a small fraction have semi-major axes greater than 1 AU. In all eccentricity histograms in this paper, we have selected only the one-planet systems with $a < 1$ AU, in order to directly compare with observed WJ eccentricities (see Section 5.3). Compared to the two-planet systems, the degree of eccentricity excitation for the one-planet systems is higher, due to the fact that each one-planet system suffered at least one ejection. The distribution of eccentricities shown in Fig. 5.3b peaks near 0.25 with a long tail. The mean and 90th percentile eccentricities of the single-planet systems are $e_{\text{ave}} = 0.3$ and $e_{90} = 0.55$ respectively.

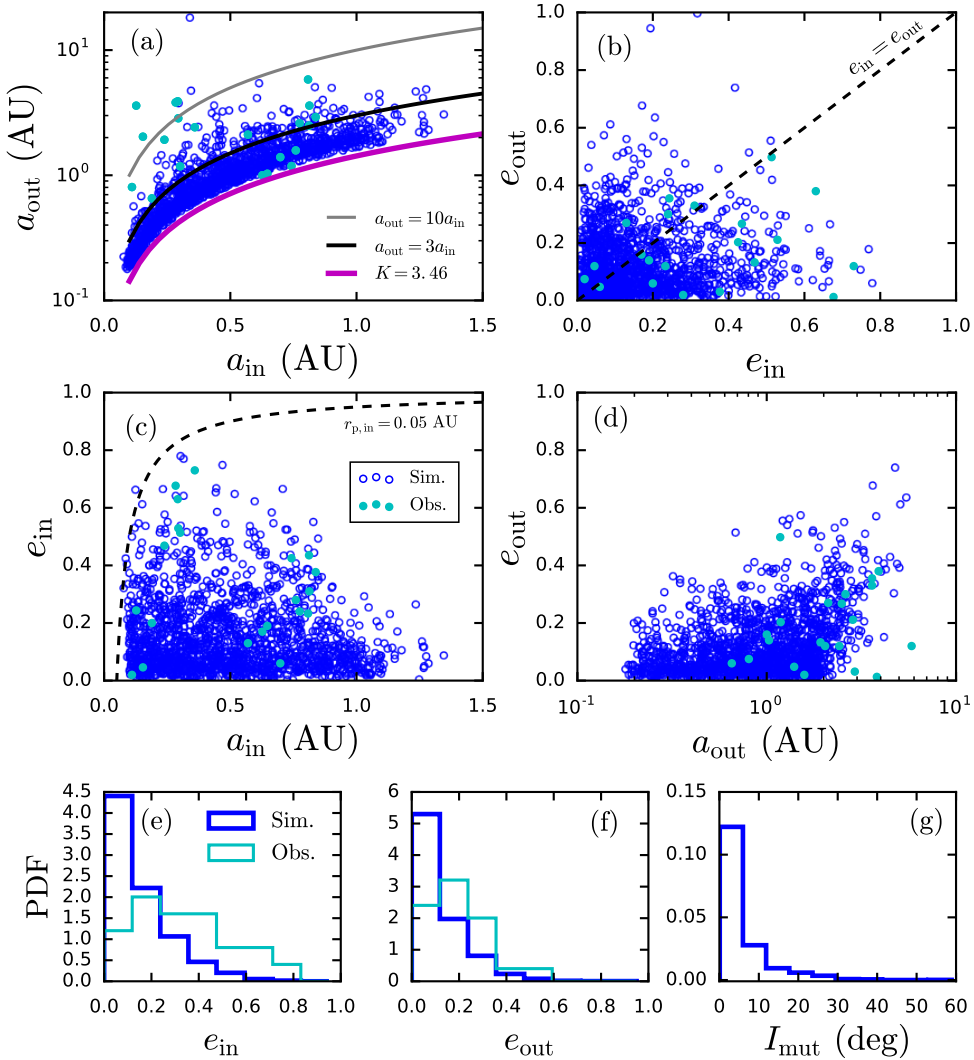


Figure 5.2: Two-planet systems (open blue circles), along with the observed WJ systems with external giant planet companions (solid cyan circles). *Panel a:* a_{in} versus a_{out} . Scattering tends to result in compact two-planet systems. Over 90% of systems satisfy $a_{\text{out}}/a_{\text{in}} \simeq 3$, although more hierarchical systems are also produced. *Panel b:* e_{in} versus e_{out} . Scattering results in a wide range of eccentricities for both planets, with a slight preference for a higher eccentricity of the inner planet. *Panel c* a_{in} versus e_{in} . Also plotted is a contour of constant pericenter distance $r_p = 0.05$ AU; systems below this curve are not expected to undergo inward migration due to tides raised on the planet. *Panel d:* a_{out} versus e_{out} . *Panels e-f:* Histograms of eccentricities of the inner and outer planets e_{in} , e_{out} . Note that the observational sample of WJs with characterized giant planet companions (cyan histograms) consists of only 24 systems at present. *Panel g:* Mutual inclination between the inner and outer planet I_{mut} . Scattering results in low inclinations, with 90% of systems satisfying $I_{\text{mut}} \lesssim 13^\circ$.

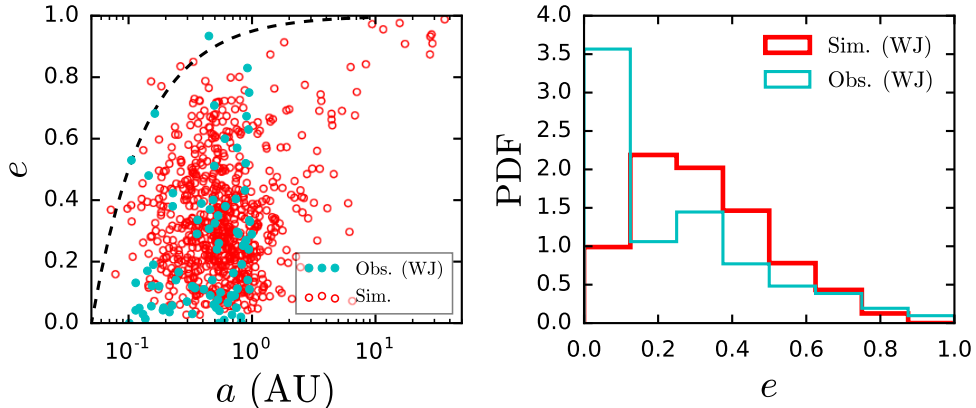


Figure 5.3: One-planet systems (open red circles), along with observed “solitary WJs” (without any identified giant planet companions), shown as cyan solid circles. This observed sample consists of 83 systems at present. *Left:* Eccentricity versus semi-major axis, along with a curve of constant pericenter $r_p = 0.05$ AU for reference. Systems below this dashed curve are not expected to undergo migration due to tides raised on the planet. *Right:* Histograms of WJ eccentricities. The scattered eccentricity distribution peaks near $e \simeq 0.2$ with a wide tail extending up to ~ 0.9 .

Dependence on initial spacing K

Next we discuss how the results depend on the initial spacing K . Previous work has shown that when planet collisions are infrequent, K primarily affects the time for instabilities (Chambers et al., 1996), rather than the degree of eccentricity excitation itself. However, when collisions are common, small values of K may lead to an artificially high number of collisions, resulting in low eccentricities.

The canonical initial spacing for the set of simulations previously discussed, titled `fiducial` is $K = 4$. To explore how the results depend on K , we perform additional sets of ~ 1000 simulations with $K = 3$ and $K = 5$, titled `fiducial-K-3` and `fiducial-K-5` respectively. Aside from the differences in the choice of K , both of these additional samples have most of the same pa-

rameters as fiducial. However, for fiducial-K-5 the timescale for instabilities to develop is sufficiently long to be impractical, so we slightly increase the initial eccentricities of the planets. We set the initial eccentricity of the inner planet to $e_1 = 0.08$ and assign the eccentricities of the outer two planets so that $a_3(1 - e_3) - a_2(1 + e_2) = 3R_{H,\text{mut}}$. Depending on the masses, the initial eccentricities of the outer planets are at most ~ 0.11 . Such eccentricities may conceivably develop due to planet-disk interactions.

Inspection of Tables 5.1 - 5.3 reveals that the value of K does not drastically affect the results. As expected, the fraction of planet-planet collisions is highest for the smallest K , with $f_{\text{pp}} = 0.76$ for $K = 3$, compared to $f_{\text{pp}} = 0.63$ for $K = 5$. The mean and 90th percentile eccentricities listed in Table 5.1 are identical to the second decimal place. The final spacing of the two-planet systems ($\alpha \equiv a_{\text{out}}/a_{\text{in}}$) is mildly dependent on K , with average $\alpha_{\text{ave}} = 1.93, 2.46, 2.63$ for $K = 3, 4, 5$, and 90th percentile spacing $\alpha_{90} = 2.5, 3.02, 3.42$.

Dependence on initial innermost semi-major axis

Next we discuss how the scattering results depend on the initial innermost planet semi-major axis, a_1 . Recall that in all sets of simulations we fix the value of a_1 and assign a_2 and a_3 according to the value of K . Taking the fiducial set of simulations, fid-mass (with $K = 4$) we split the set of simulations (~ 3300 total) into four bins of a_1 , each with width 0.225 AU and centers 0.21, 0.44, 0.66, and 0.89 AU.

Figure 5.4 shows how the results depend on a_1 . The top panel shows the frequencies of collisions and ejections. In the first bin, centered at 0.21 AU,

planet-planet collisions are very common, with $f_{\text{pp}} \simeq 82\%$ and $f_{\text{ej}} \simeq 15\%$. As a_1 increases, the frequency of ejections increases, so that in the last bin, centered at 0.89, $f_{\text{pp}} \simeq 50\%$. The fraction of planet-star collisions remains nearly constant at $f_{\text{ps}} \simeq 6\%$ across all bins.

The dependency of f_{pp} and f_{ej} on a_1 leads to a slight variation on the relative numbers of one and two-planet systems, as shown in the middle panel of Fig. 5.4. In the first a_1 bin, the fractions of one and two-planet systems are $f_{1\text{p}} = 37\%$ and $f_{2\text{p}} = 63\%$ respectively. The slightly larger value of $f_{2\text{p}}$ at small a_1 is a direct consequence of the fact that collisions are most common close to the host star, leading to collision products with lower eccentricities, and hence, more stable two-planet systems. As a_1 increases, $f_{2\text{p}}$ the number of ejections increases, so that the fraction of one-planet systems increases. In the largest a_1 bin, one-planet systems are somewhat favored, with $f_{1\text{p}} = 63\%$ and $f_{2\text{p}} = 37\%$. This dependency of collisions/ejections with a_1 leads to a slight increase in the average eccentricity with a_1 , as shown in the middle panel of Fig. 5.4.

Figure 5.5 illustrates how a_1 determines the properties of two-planet systems. The initial value of a_1 primarily determines the final semi-major axis (but not the relative spacing), since scattering typically limits changes in semi-major axis to factors of order unity. There is no significant dependence of a_1 on the final planet eccentricities, mutual inclination, or relative spacing. Examining the binned one-planet systems, a similar lack of dependence of a_1 on eccentricity is found.

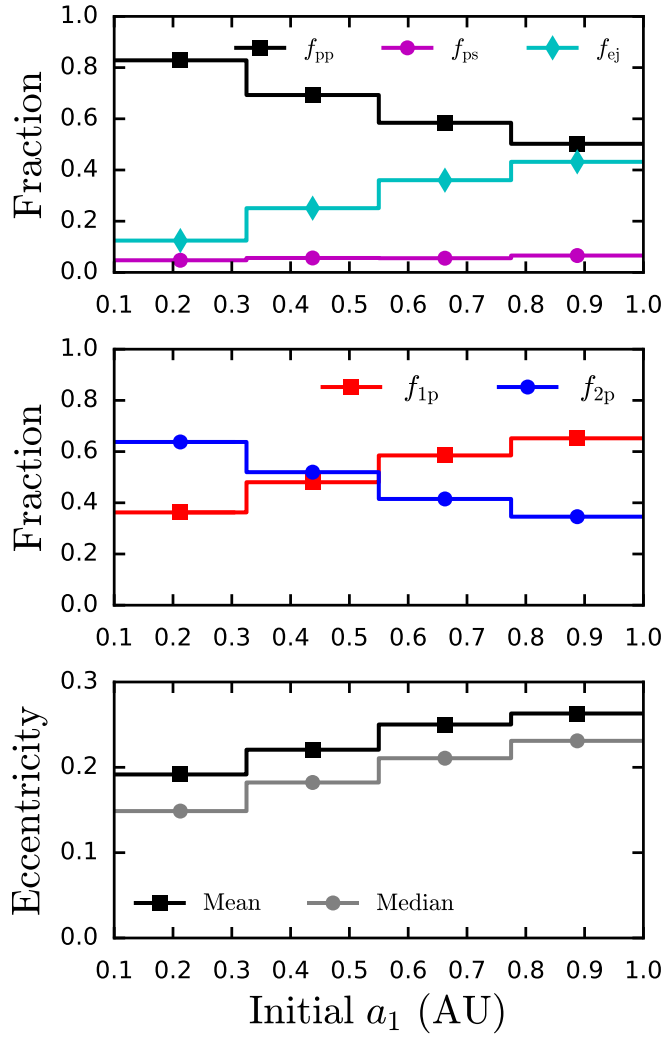


Figure 5.4: Scattering outcomes, fractions of one and two-planet systems, and average eccentricities for the fiducial set of calculations. Properties are taken at the end of “Phase 2” of the integration, and binned in terms of the initial inner planet semi-major axis a_1 (of the original three-planet system). *Top panel:* Fractions of systems resulting in planet-planet collisions (f_{pp}), planet-star collisions (f_{ps}), and planet ejections (f_{ej}) (see equation 5.1). Planet-planet collisions dominate at small values of a_1 , as expected. As a_1 increases, the frequency of planet ejections increases. Planet-star collisions remain constant across a_1 . *Middle panel:* Fractions of one-planet (f_{1p}) and two-planet (f_{2p}) systems produced via scattering. Due to the increasing frequency of ejections with a_1 , the fraction of one-planet systems increases with a_1 . *Bottom panel:* Median and mean eccentricities of both one and two-planet systems. Eccentricities increase with a_1 , due to the increasing fraction of one-planet systems, as a consequence of more planet ejections.

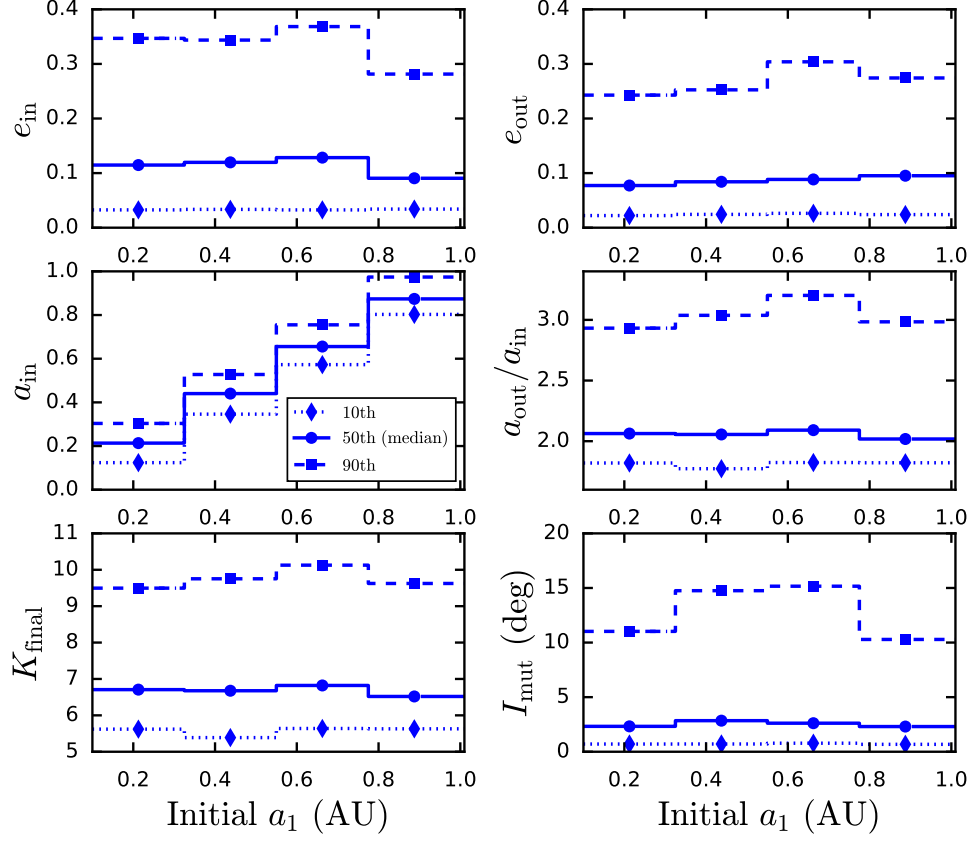


Figure 5.5: Dependence of two-planet system properties on the initial semi-major axis of the innermost planet of the initial three-planet system. The two-planet systems from the `fiducial` run have been separated into four bins of width 0.225AU. Bin centers are indicated by markers, showing 10th, 50th, and 90th percentiles of various quantities, as labeled. *Top left and right:* Inner and outer planet eccentricities. The initial value of a_1 does not strongly affect the distributions of e_{in} and e_{out} , with a median value ~ 0.1 for e_{in} across all bins, and slightly lower for e_{out} . *Middle left:* Inner planet semi-major axis a_{in} of the surviving two-planet systems following scattering. Scattering typically results in a_{in} within a factor of ~ 2 of the original inner semi-major axis. *Middle right:* $a_{\text{out}}/a_{\text{in}}$. In-situ scattering tends to produce closely-spaced two-planet systems ($a_{\text{out}}/a_{\text{in}} \simeq 2 - 3$), with more hierarchical systems ($a_{\text{out}}/a_{\text{in}} > 5$) quite rare. *Bottom left:* The spacing of the final two-planet systems in units of mutual Hill radii, with a median value $K_{\text{final}} \simeq 5$ across all bins. *Bottom right:* Mutual inclinations of the two-planet systems. Scattering typically results in low inclinations, with a median of $\sim 2^\circ$ across all bins.

Dependence on Planet Masses

Finally, we explore how the eccentricity distributions and relative spacing of two-planet systems depends on planet masses. When planet masses are unequal, scattering leads to fewer close encounters, due massive planets easily ejecting low-mass planets, whereas for equal-mass planets, ejection becomes more difficult and planets suffer a higher number of close encounters, thereby leading to efficient eccentricity excitation (Ford & Rasio, 2008). Besides `fiducial` (with masses $0.5, 1.2M_J$), we conduct two additional sets of simulations, with all parameters (except for masses) chosen/sampled identical to `fiducial`. We consider nearly equal mass planets, with masses $0.9, 1, 1.1M_J$, and refer to this set of simulations as `near-eq-mass`. We also consider masses sampled from a log-normal distribution, referred to as `lognorm-mass`, with mean $1M_J$, width $\log_{10}(m_p/M_J) = 0.5$, and upper and lower limits $0.25M_J$ and $4M_J$. These choices are somewhat arbitrary, but qualitatively mimic the observed distribution of giant planet masses. In all sets of simulations, the ordering of the three masses is randomly assigned.

Figure 5.6 compares the eccentricity distributions of `fiducial`, `fiducial-K-3`, and `fiducial-K-5`, showing both the combined distribution of one and two-planet systems (left panel), as well as eccentricities split into one-planet and two-planet systems (middle and right panels). Recall that we only show results for simulated one-planet systems with $a < 1\text{AU}$ in order to compare with observed WJ systems. The results for the two planet systems show the inner planet eccentricity only. As expected, `near-eq-mass` produces the highest eccentricities (see also Tables 5.1 - 5.3). No appreciable differences are observed between `fiducial` and `near-eq-mass`.

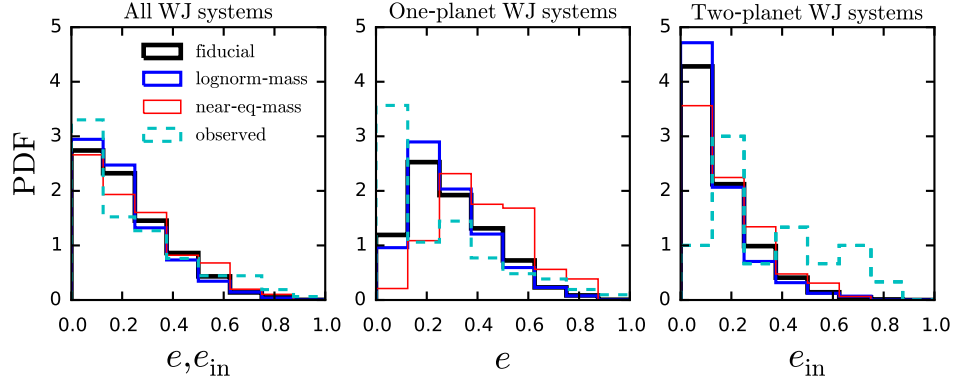


Figure 5.6: Eccentricities of WJ systems, illustrating the dependence on planet masses. The middle panel shows eccentricities of one-planet WJs and the right panel shows the inner planet eccentricity of the two-planet systems. The left panel combines the eccentricity distribution shown in the left in middle panels. Black histograms indicate the fiducial run, while blue and red indicate lognorm-mass and near-eq-mass respectively. Observed WJs are shown as the dashed cyan histograms.

The choice of planet masses affects the relative spacing of the two-planet systems, but only marginally. Inspecting Table 5.2, the average values of $a_{\text{out}}/a_{\text{in}}$ for fiducial, near-eq-mass, and lognorm-mass are 2.46, 2.62, and 2.3. As a result, the finding that in-situ scattering produces very compact, non-hierarchical two-planet systems is robust to the choice of planet mass.

5.2.4 In-Situ Scattering of Four Planets

All scattering experiments discussed thus far began with initially three unstable planets. In this section we briefly discuss scattering of four unstable planets. We construct a set of ~ 1000 systems, consisting of four planets with masses $0.5, 1, 1.25, 2M_J$ (placed in random order), and all other parameters identical to fiducial. We term this set of simulations 4-planets, integrate the systems through ‘‘Phase 1’’ and ‘‘Phase 2,’’ and analyze the properties of the remain-

ing planets following scattering. The effect of an additional planet allows more possibilities for ejections. As a result, while `fiducial` (with three planets) produces roughly equal numbers of one and two-planet systems, `4-planets` produces nearly four times more one-planet systems compared to two-planet systems. The average eccentricity for one-planet systems from `4-planets` is $e_{\text{ave}} = 0.35$ (see also Table 5.4), compared $e_{\text{ave}} = 0.3$ from `fiducial`.

Figure 5.7 shows the two-planet systems produced for `4-planets`, along with `fiducial` for reference. The top panel of Fig. 5.7 shows that `4-planets` produces more hierarchical systems, with mean value of $\alpha = a_{\text{out}}/a_{\text{in}} = 4.13$ (see also Table 5.4). The remaining panels of Fig. 5.7 show the inner and outer planet eccentricities. Unsurprisingly, the eccentricities of both planets tend to be higher, with an average inner planet eccentricity 0.2 for `4-planets` compared to 0.15 for `fiducial`.

5.3 Comparison with Observations

The Exoplanet Orbit Database (exoplanets.org, Han et al., 2014) lists 106 giant planets ($m_p \sin i > 0.3M_J$) with WJ semi-major axes ($0.1\text{AU} < a < 1\text{AU}$) and with eccentricity and mass measurements listed. Of these 106 systems, 83 lack detection of a giant planet companion, and 23 have an external giant companion with a characterized mass and orbit. The majority of these two-planet systems were previously discussed by Antonini et al. (2016), in the context of high-eccentricity migration, and by Anderson et al. (2017), in the context of secular perturbations. We augment this sample with the well-known Kepler-419 system (Dawson et al., 2014), which is not flagged by our search criteria due to

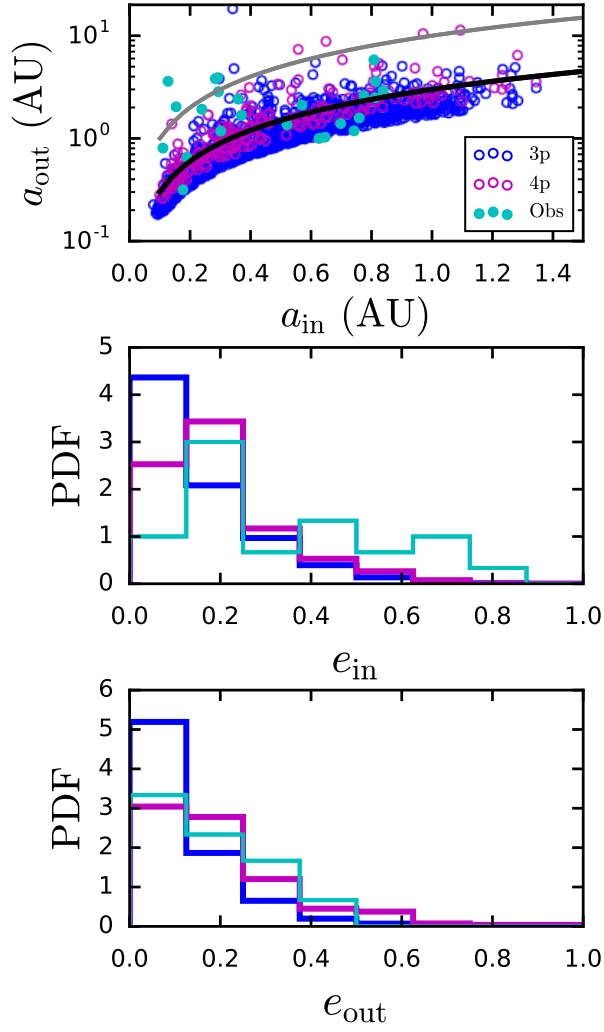


Figure 5.7: Properties of two-planet systems produced from 4-planets, along with those from fiducial for reference. 4-planets consists of systems of four initially unstable planets with masses $0.5, 1, 1.25, 2M_J$, and all other parameters identical to fiducial. *Top:* Inner versus outer planet semi-major axis. The blue open circles indicate fiducial (labeled as “3p” in the plot), and magenta open circles plotted above indicate 4-planets (labeled as “4p”). Observed two-planet systems are shown as solid cyan circles (see also Section 5.3). *Middle and bottom:* Eccentricities of the inner and outer planets, with the same color scheme as the top panel. 4-planets produces more eccentric planets and wider spacing compared to fiducial as expected.

lack of planet mass listings on exoplanets.org.

In the following we compare our scattering results to this observed sample of WJs. In all following discussions, if the initial number of planets (three versus four) under consideration is not explicitly stated, we are referring to three planet scattering; if the 4–planets simulations are under discussion, it will be explicitly noted.

5.3.1 Eccentricities

As discussed previously, in-situ scattering of three planets leads to a range of eccentricities in the final (post-scattering) planetary orbits(s). The left panel of Fig. 5.6 presents the combined eccentricity distributions of the one and two-planet systems produced by scattering and the observed distribution, consisting of e , the eccentricities of single WJs, and e_{in} , the inner planet eccentricity of the two-planet systems. Comparing the observed and simulated eccentricity distributions, we see that in-situ scattering of three planets with a variety of mass choices reproduces the observed distribution fairly well.

Next we separately discuss the eccentricities of the one and two-planet systems. Recall that the two-planet systems tend to have relatively low eccentricities due to the fact that they formed exclusively via planet–planet collisions (see Table 5.2). Comparing the observed and scattering model eccentricity distributions in Figs. 5.2e and 5.6, we see that although scattering is able to produce the full range of observed eccentricities, there is a clear discrepancy in the shapes of the distributions, with a fairly flat distribution of observed eccentricities. As a result, we conclude that in-situ scattering of three planets cannot

adequately account for the full sample of observed two-planet systems. Addition of a fourth planet alleviates, but does not completely resolve this problem. Inspecting Fig. 5.7, we see that the eccentricity distribution of 4-planets is in better agreement with observations compared to `fiducial`, but still produces too many low-eccentricity planets.

The single-planet systems, which previously suffered at least one ejection, tend to have much higher eccentricities. Figs. 5.3 and 5.6 reveal that the in-situ scattering of three planets can reproduce the substantial eccentricities of the observed solitary WJs. The observed peak at low eccentricities is not reproduced.

The tension between the observed and scattered eccentricity distributions of both the one and two planet systems may be relieved if some of the observed solitary WJs actually have an undetected external companion. Since scattering most commonly results in two-planet systems with relatively low eccentricities, misclassifying some two-planet systems as one-planet systems may decrease the excess observed one-planet systems that are circular, and increase the dearth of two-planet systems that are circular. To evaluate whether a significant fraction of solitary WJs may in fact have an undetected giant planet companion with properties consistent with in-situ scattering, we calculate the radial-velocity semi-amplitude and orbital periods of the outer planet in our simulated two-planet systems from `fiducial`, according to

$$K_{\text{RV}} = \frac{28.4 \text{ m/s}}{\sqrt{1 - e^2}} \left(\frac{m_p \sin i_{\text{sky}}}{M_J} \right) \left(\frac{P}{1 \text{ yr}} \right)^{-1/3} \left(\frac{M_\star}{M_\odot} \right)^{-2/3}, \quad (5.4)$$

(Cumming et al., 2008). In Fig. 5.8 we show the RV semi-amplitudes and orbital periods of the outer planet in the two-planet systems, where we have assumed an isotropic distribution of sky-projected inclinations i_{sky} (uniform in $\cos i_{\text{sky}}$). Scattering produces a population of outer planets with RV semi-

amplitudes mostly in the range $\sim 10 - 100$ m/s. Due to the compactness of the two-planet systems, many systems have large RV amplitudes and short-orbital periods (with $P_{\text{out}} \lesssim 1$ yr) which should be readily detected, but are typically not observed.

To test whether undetected companions to solitary WJs may reconcile the disparities in eccentricity distributions, we apply RVs cuts of 10 and 100 m/s to the two-planet simulations from `fiducial`, and classify any two-planet systems as one-planet systems if the outer planet has an RV semi-amplitude less than the specified cut. The results are shown in Fig. 5.9. A 10 m/s RV cut does not appreciably change the original eccentricity distributions from `fiducial`. A 100 m/s RV cut does provide a significantly better agreement with observations. However, since planets with tens of m/s RV amplitudes are readily discovered, we conclude that there is unlikely to be a large population of undetected companions to observed single WJs with the properties obtained from our scattering simulations. Thus, despite the apparent agreement in eccentricity distributions between observed and simulated for *all* WJs, we conclude that in-situ scattering is unable to separately reproduce the entire observed sample of one and two-planet systems.

Instead, the eccentricity distribution is consistent with in-situ scattering having occurred in a significant fraction of one-planet systems, along with a population of low-eccentricity planets that did not undergo scattering. Indeed, evidence for two populations of WJs has been previously argued based on stellar metallicities, consisting of a low-eccentricity population orbiting metal-poor stars, and an eccentric population orbiting metal-rich stars (Dawson & Murray-Clay, 2013). To help quantify the degree to which in-situ scattering may be

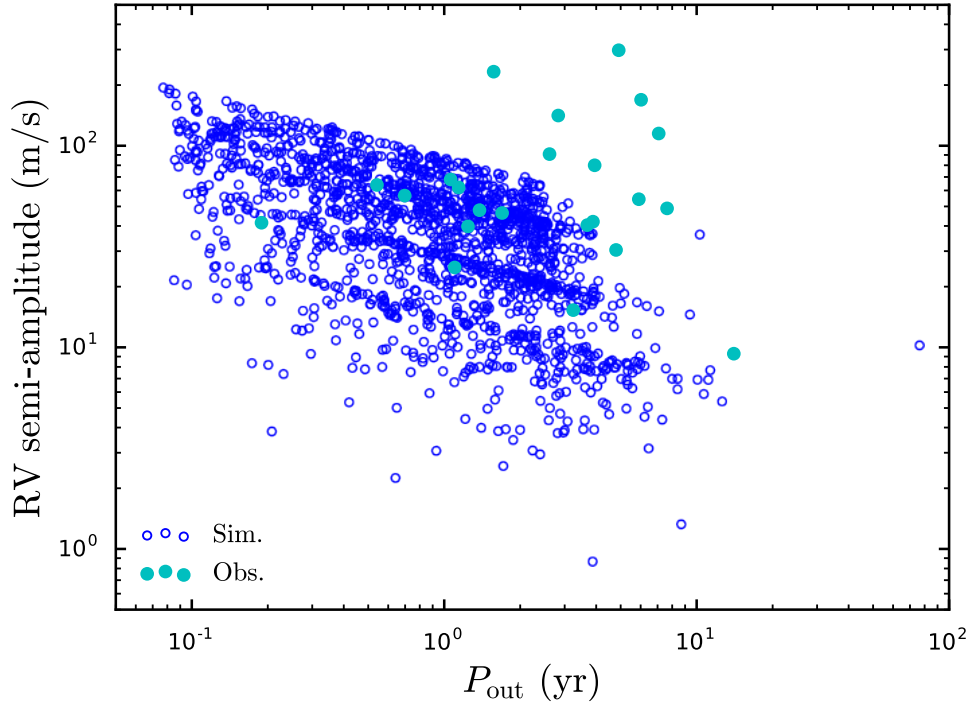


Figure 5.8: Radial velocity semi-amplitude versus orbital period for the outer planet. The fiducial simulations are shown as open blue circles, while observed systems are shown as filled cyan circles. An isotropic distribution of sky-projected inclinations has been assumed in calculating the expected radial velocity semi-amplitude.

contributing to eccentric solitary WJs, we inject a population of low-eccentricity planets to the one-planet systems from the fiducial scattering sample, assuming a half Gaussian peaked at $e = 0$ and with width σ (see Appendix D for more details). Performing a maximum likelihood estimation for the parameters of this mixture model, we find that the observed eccentricities of one-planet systems are consistent with an injected population of low-eccentricity planets (with spread $\sigma \approx 0.07$), constituting $\sim 35\%$ of the total population, and the remaining 65% from in-situ scattering. In other words, the eccentricity distribution of observed solitary WJs is consistent with over half of them having previously un-

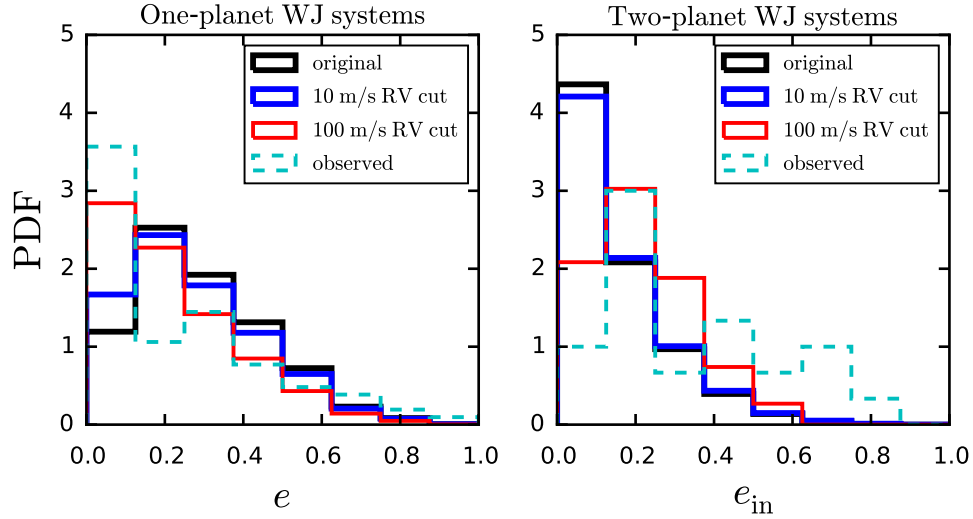


Figure 5.9: The effect of imposing an RV cut on the eccentricity distributions of one and two-planet systems from `fiducial` (shown as the thick black histogram). The left panel depicts eccentricities of one-planet systems and the right panel depicts inner planet eccentricities of two-planet systems. We have classified any two-planet systems as one-planet systems if the outer planet has an RV semi-amplitude less than the specified cut. Imposing a 10 m/s cut (blue histograms) barely affects the eccentricity distributions. A 100 m/s cut (red histograms) yields better agreement between simulations and observations for both the one and two-planet systems. However, since planets with RV amplitudes of tens of m/s are readily detectable, we conclude that missing companions to solitary WJs are unlikely to serve as a full solution to the disagreement in eccentricity distributions.

dergone in-situ scattering of three giant planets, and the rest having a relatively quiescent history.

5.3.2 Spacing and Mutual Inclinations of Two-Planet Systems

As previously discussed, scattering of three giant planets usually results in closely spaced systems, with 90% of the `fiducial` two-planet systems satisfying $a_{\text{out}}/a_{\text{in}} < 3$ (see Fig. 5.5). Some observed systems are also quite closely spaced (see Fig. 5.2a), but there exists many others that are much more hierar-

chical.

The mutual inclinations generated via scattering are generally quite low, with 90% of systems having inclinations less than $10 - 15^\circ$, and median inclinations of $\sim 2^\circ$. Except for a few special systems, observed giant exoplanet systems lack constraints on mutual inclinations at present.

5.3.3 Relative Numbers of One and Two-Planet Systems

As mentioned previously, there are 83 WJs with eccentricity and mass constraints without a detected companion and 24 WJs with a characterized external companion, giving relative numbers of one and two-planet systems $N_{1,\text{obs}}/N_{2,\text{obs}} \simeq 3.5$. However, note that 8 of the 83 solitary WJs have a linear trend in the RV curve, indicating the possibility of an external companion. If we assume the presence of a planetary companion in each of these 8 systems, then $N_{1,\text{obs}}/N_{2,\text{obs}} = 75/32 \simeq 2.3$.

The three-planet scattering experiments (i.e. fiducial, lognorm-mass, near-eq-mass, fiducial-K-3, fiducial-K-5) yield relative numbers of single WJs and WJs with external companions $N_{1,\text{sim}}/N_{2,\text{sim}} \simeq 0.5 - 1.5$, where the range arises from the choice of planet masses and initial spacing. As a result, in-situ scattering predicts an excess of WJs with a giant planet companion compared to observations. Four-planet scattering (4-planets) yields $N_{1,\text{sim}}/N_{2,\text{sim}} \simeq 3.3$, in good agreement with observations.

Clearly, agreement between the predicted and observed relative frequency of one and two-planet systems is not expected if in-situ-scattering occurred only

in a fraction of WJ systems. Indeed, given the difficulties in separately matching the eccentricity distributions of one and two-planet systems (See Section 5.3.1), we should not expect these ratios to agree precisely.

Nonetheless, it is useful to also consider the extreme hypothesis that the majority of WJs form in systems of three giant planets, which then undergo scatterings. In this scenario, there are two ways of reconciling the discrepancy between $N_{1,\text{obs}}/N_{2,\text{obs}}$ and $N_{1,\text{sim}}/N_{2,\text{sim}}$:

1. A fraction of the 2-planet systems generated through scattering are actually unstable, so that $N_{1,\text{sim}}/N_{2,\text{sim}}$ increases with time. Inspection of Fig. 5.1 shows the fraction of two-planet systems has settled to a constant value after $\sim 10^8$ orbits of the inner planet. However, a number of these two-planet could undergo instabilities over much longer timescales. Numerous empirical stability criteria for two-planets in eccentric/inclined orbits exist in the literature (e.g. Mardling & Aarseth, 2001; Petrovich, 2015c). However, such stability criteria are only reliable sufficiently far from the “fuzzy” stability boundary. Using the Petrovich (2015c) stability criterion, we find that over 90% of the fiducial two-planet systems are classified as unstable, but fall in the uncertain regime of parameter space near the boundary. Thus, the Petrovich (2015c) stability criterion is overly conservative in this application. In addition, his stability criterion does not consider the potentially stabilizing effects of GR apsidal precession, as well as the possibility of planet-planet collisions. As a result, full numerical integrations over long timescales are needed, which are prohibitively expensive. To evaluate how likely instabilities may be, we randomly choose 30 of the closely-spaced two-planet systems (with

$a_{\text{out}}/a_{\text{in}} < 3$) from the fiducial sample, and integrate the systems for an additional 10^9 orbits of the inner planet, i.e. an order of magnitude longer. Of these 30 systems, 3 became destabilized. We note that 10^9 orbits at many WJ distances is still short compared to the lifetimes of many observed systems. We thus conclude that at least $\sim 10\%$ of the two-planet systems are expected to go unstable, but the actual percentage over Gyr-timescales is likely higher. Under the assumption that all of the observed single WJs are indeed single, so that the observed relative number of one and two-planet systems ($N_{1,\text{obs}}/N_{2,\text{obs}}$) is equal to the true value, and using the ranges $N_{1,\text{obs}}/N_{2,\text{obs}} = 2.3 - 3.5$ and $N_{1,\text{sim}}/N_{2,\text{sim}} = 0.5 - 1.5$, the percentage of two-planet systems that would need to eventually go unstable is in the range $24\% - 67\%$.

2. The second way of matching the observed and predicted ratios of one and two-planet systems is if a fraction of the single WJs actually have an external companion, probably with $a_{\text{out}}/a_{\text{in}} < 3$. The possibility of undetected outer companions was already discussed in Section 5.3.1 and Fig. 5.8. Now we discuss what fraction of observed one-planet systems must actually have an external companion, in order to match the relative frequency of one and two-planet systems obtained from observations. In this estimate, we assume that all the two-planet systems obtained from N-body observations remain stable indefinitely, in order to obtain an upper bound on the undetected companion requirement. Again using $N_{1,\text{obs}}/N_{2,\text{obs}} = 2.3 - 3.5$ and $N_{1,\text{sim}}/N_{2,\text{sim}} = 0.5 - 1.5$ we find that $14\% - 57\%$ of single WJs must have an undetected companion. Given the large ($\sim 10 - 100$ m/s) RV semi-amplitudes predicted for the outer planet (see Fig. 5.8), we do not expect a major fraction of single WJs to have an undetected external companion

with properties predicted from our scattering experiments.

In summary: The relative numbers of observed of one and two-planet WJs is consistent with scattering of four planets (4-planets), but is inconsistent with scattering of only three planets (fiducial, etc). Under the extreme assumption that in-situ scattering of three giant planets occurred in all WJ systems, the relative numbers of one and two-planet WJ systems produced by in-situ scattering are consistent with observations, provided that a fraction of two-planet systems produced via scattering later undergo instabilities, or/and if some observed solitary WJs have an undetected companion. Alternatively, the discrepancy between the predicted and observed relative frequency of one and two-planet systems is resolved if in-situ-scattering occurred only in a fraction of WJ systems. Indeed, as discussed in Section 5.3.1, the large peak of low eccentricities in the observed distribution of one-planet systems (and not reproduced in the simulated one-planet systems) is consistent with two populations of WJs in similar proportions: one having undergone violent scattering, and the other having a quiescent dynamical history.

5.4 Summary of Results and Discussion

In this paper we have undertaken a comprehensive study of giant planet scattering at sub-AU distances from the host star, totaling ~ 8000 N-body integrations, and including the effects of general relativistic apsidal precession. Our setup of a system of giant planets in initially nearly circular orbits is consistent with a systems of WJs that formed either in-situ or by disk migration without substantial eccentricity excitation due to planet-disk interactions. The goal of this study

is two-fold: (1) On observational grounds we aim to identify to what extent planet scattering has contributed to the population of eccentric WJs. (2) On theoretical grounds, we systematically explore how in-situ scattering of WJs leads to a mixture of collisions and ejections, and catalogue our findings. Most of the paper focuses on systems of three initially unstable planets, but also briefly considers four planets. For the parameters we considered, scattering results in roughly equal proportions of one-planet and two-planet systems, the properties of which we analyze in some detail (see also Figs. 5.2 and 5.3).

Our main results are as follows:

- Scatterings result in a combination of collisions and ejections over our explored parameter range. For systems with initially three planets, the first (or only) scattering event results in planet-planet collisions 60% – 80% of the time. For systems that later undergo a second scattering, planet ejections occur over 90% of the time.
- We present a distribution of collision impact parameters (see Fig. C.1). Planet-planet collisions are usually grazing, rather than head-on.
- In-situ scattering tends to produce closely spaced two-planet systems. For systems of initially three unstable planets, over 90% of the surviving two-planet systems have a semi-major axis ratio $a_{\text{out}}/a_{\text{in}} \lesssim 3$. For systems of initially four unstable planets, over 90% of two-planet systems have $a_{\text{out}}/a_{\text{in}} \lesssim 5$.
- The combined eccentricity distribution of the one-planet WJ systems and inner planet of two-planet systems produced by scattering agrees well with the observed distribution (see the left panel of Fig. 5.6).

- Splitting the surviving WJs into one and two-planet systems (see the middle and right panels of Fig. 5.6), we find some discrepancies between the eccentricities produced by scattering and observations. Examining the surviving two-planet systems, we find that scattering produces too many low-eccentricity planets, due to the fact that all two-planet systems arose from planet-planet collisions. This is inconsistent with the observed, much flatter eccentricity distribution of WJs with a detected outer companion. This discrepancy is alleviated, but not fully resolved by addition of a fourth planet to the initial scattering setup (see Fig. 5.7).
- Examining the one-planet systems produced by scattering and comparing with observed WJs lacking a giant planet companion, we find scattering well reproduces the substantial tail of modest-to-high eccentricities, but does not reproduce the observed peak of low eccentricities.

At first glance, in-situ scattering provides a promising match to the entire WJ eccentricity distribution, as illustrated in the left panel of Fig. 5.6. However, splitting the results into one and two-planet systems yields an excess of circular two-planet systems, and a dearth of circular one-planet systems. A natural resolution to this puzzle is if observed solitary WJs have an undetected outer companion, thereby shifting the excess of circular planets from the two-planet systems to the one-planet systems. However, given the large RV amplitudes of the outer planets obtained from our scattering experiments (10 – 100 m/s, see Fig. 5.8), undetected outer companions probably cannot resolve the difference (Fig. 5.9).

The properties of the two-planet systems generated through in-situ scattering are also inconsistent with some of the observed two-planet systems. Be-

sides the disagreement in the shapes of the eccentricity distributions, the relative spacings of two-planet systems are more compact than many observed systems. The tendency for scattering to result in two-planet systems quite close to the stability limit was pointed out by Raymond et al. (2009). We note that the architectures of the compact observed systems HD73526 and HD82943, and are consistent with previously having undergone scattering, due to the close spacing and modest eccentricities (although the possibility of the planets simply forming in the observed configuration cannot be dismissed). The observed two-planet systems with $a_{\text{out}}/a_{\text{in}} \sim 10$ are more difficult to produce through in-situ scattering. However, such systems may be still have participated in a scattering event which originated at \sim AU distances, as explored by (Mustill et al., 2017). A thorough exploration of the parameter space for initial systems consisting of a single WJ and two or more unstable planets at \sim several AU is an important, but computationally expensive problem.

The two-planet systems also suffer from some uncertainties. Although these systems appear to be at least temporary stable (see Fig. 5.1), some may later become unstable. Follow-up long-term integrations of a small subset of the two-planet systems (spanning 10^9 orbits of the inner planet) indicate that $\sim 10\%$ will eventually go unstable, but the actual number may be higher over timescales comparable to observed \sim Gyr system ages. In addition, since the two-planet systems formed exclusively through planet-planet collisions, their properties are dependent upon the assumed treatment of planet collision (see also Appendix C). Since the majority of one-planet systems did not experience any planet-planet collisions, their properties are robust.

The results of this paper suggest that in-situ scattering is a promising mecha-

nism in accounting for the substantial eccentricities of many observed “solitary” WJs (those lacking an observed giant planet companion). In a given system, the occurrence of at least one planet ejection allows for efficient eccentricity excitation. As previously discussed in Section 5.3.1, the resulting eccentricity distribution (of one-planet systems) obtained through scattering does not reproduce the observed peak at low eccentricities. Constructing a mixture model consisting of our scattering results and an injected population of planets with a low-eccentricities (see Appendix D), we find that the eccentricity distribution of observed solitary WJs is consistent with half or more of systems having undergone in-situ scattering, and the rest having a quiescent history. Two populations of WJs have been previously proposed by Dawson & Murray-Clay (2013), consisting of a low-eccentricities around low-metallicity stars, and higher eccentricities around high-metallicity stars. Scattering is clearly consistent with such a metallicity trend, under the expectation that multiple closely spaced giant planets form more easily around higher metallicity stars.

Thus, we conclude that the observed eccentricity distribution of solitary WJs is consistent with roughly half having undergone in-situ scattering, and the other half having a more quiescent dynamical history. This is consistent with the fact that a substantial fraction ($\sim 50\%$) of WJs are thought to have low-mass companions (Huang et al., 2016), if we imagine a planet formation scenario in which the vast majority of WJs form with other planets nearby, either low-mass or giant planets. However, we acknowledge the substantial theoretical uncertainties of forming even one WJ in-situ, much less multiple planets.

CHAPTER 6

**ECCENTRICITY AND SPIN-ORBIT MISALIGNMENT IN
SHORT-PERIOD STELLAR BINARIES AS A SIGNPOST OF HIDDEN
TERTIARY COMPANIONS**

6.1 Introduction

Stellar binaries can exhibit a rich variety of dynamical behavior. In systems with sufficiently small separations, the orbit can precess due to non-Keplerian potentials (e.g. general relativistic corrections), and may also be sculpted by tidal dissipation. If the binary is a member of a higher multiplicity system, or previously experienced a close encounter with a neighboring star, the orbital properties can be further modified. In many observed binary systems, whether the orbital elements reflect the properties of the protostellar cloud, or result from post-formation dynamical evolution, remains an open question. Distinguishing between the two possibilities can shed light into star and binary formation processes.

A possible signature of post-formation dynamical evolution is stellar spin-orbit misalignment (obliquity). One method of probing stellar obliquities in binaries is by comparing the inclination of the stellar equator (estimated through measurements of $v \sin i$ and the rotational period) with the orbital inclination. Using this method, Hale (1994) found that solitary binaries tend to have low

This chapter is adapted from Anderson et al. (2017)

obliquities when the separation is less than $30 - 40$ AU, but for separations beyond $30 - 40$ AU, the obliquities are randomly distributed. However, for binaries residing in hierarchical multi-systems, even those with small separations can have substantial spin-orbit misalignments, as a result of post-formation dynamical evolution.

More recently, obliquities have been inferred from measurements of the Rossiter-McLaughlin effect (Rossiter, 1924; McLaughlin, 1924). A handful of eclipsing binaries have orbital axes that are misaligned (in projection) with respect to the spin axis of one or both members. In the ongoing BANANA Project, an effort to measure obliquities in comparable-mass eclipsing binaries, Albrecht et al. (2007, 2009, 2011, 2013, 2014) present Rossiter-McLaughlin measurements of several systems. Thus far, four systems exhibit spin-orbit alignment (Albrecht et al., 2007, 2011, 2013), while two systems contain misaligned components: in DI Herculis both the primary and secondary are misaligned, with $\lambda_{\text{pri}} \simeq 72^\circ$ and $\lambda_{\text{sec}} \simeq -84^\circ$ (Albrecht et al., 2009); in CV Velorum, the primary and secondary have $\lambda_{\text{pri}} \simeq -52^\circ$ and $\lambda_{\text{sec}} \simeq 3^\circ$ (Albrecht et al., 2014). A complementary study of spin-orbit misalignments in unequal mass eclipsing binaries (consisting of FGK-M members) is being undertaken via the EBLM project (Triaud et al., 2013). Although the current sample of binaries with Rossiter-McLaughlin measurements still consists of only a few members, these efforts, and others (e.g. eclipsing binaries observed by *Kepler*, see Dong et al. 2013), will increase the sample in the coming years.

In general, it is not clear whether large spin-orbit misalignments in eclipsing binaries are primordial (reflecting the initial state of the protostellar cloud), or have been driven to misalignment due to dynamical interactions with a per-

turber. In this paper, we consider the latter scenario, where the eclipsing binary is the inner component of a hierarchical triple stellar system, with a tertiary companion orbiting the center of mass of the inner binary. If the inclination between the inner and outer orbits is sufficiently high, the eccentricity of the inner binary can undergo periodic excursions to large values, known as Lidov-Kozai (LK) cycles (Lidov, 1962; Kozai, 1962), see also Harrington (1968). It is widely believed that binaries with $P_{\text{orb}} \lesssim 7$ days are not primordial, but have evolved from wider configurations via LK cycles with tidal friction (Mazeh & Shaham, 1979; Eggleton & Kiseleva-Eggleton, 2001; Fabrycky & Tremaine, 2007; Naoz & Fabrycky, 2014). Indeed, binaries with periods shorter than this threshold are known to have high tertiary companion fractions [of up to 96 % for periods < 3 days; see Tokovinin et al. (2006)], supporting the idea that three-body interactions have played a major role in their formation. There should also exist a population of longer-period, eccentric binaries that are undergoing LK-driven orbital decay (see Dong et al. 2013).

It is important to recognize that even a strong perturbation from a tertiary companion on the inner binary does not guarantee the production of spin-orbit misalignment in the inner binary. If the inner binary achieves a sufficiently small pericenter distance, a torque due to the stellar quadrupole (arising from stellar oblateness) may induce a change in the direction of the spin axis, but the degree of spin-orbit misalignment depends on several factors. In previous work (Storch et al., 2014; Anderson et al., 2016), we have investigated the spin dynamics of a planet-hosting star, as a result of the planet undergoing LK oscillations due to a distant stellar companion (see also Storch & Lai, 2015). The evolution of the stellar spin-axis can be complicated, with several qualitatively distinct types of possible behavior, depending on the combination of planet mass, stellar spin

period and the orbital geometries of the inner and outer binaries. In particular, for increasingly massive planets ($M_p \gtrsim 5 - 10M_J$), the coupling between the star and planet can be so strong that spin-orbit misalignment cannot be generated, despite drastic changes in the orbital inclination. As the mass of the secondary body increases from the planetary to the stellar regime, the ability to generate spin-orbit misalignment is even further hindered.

In light of these previous results, the main goal of this paper is to identify under what circumstances large spin-orbit misalignment can be generated in stellar binaries, due to secular interactions with a tertiary companion. Tertiary companions can also excite the binary eccentricity. Another goal of this paper is thus to identify the requirements for a tertiary companion to increase the eccentricity of the inner binary from $e \simeq 0$ to an observed eccentricity $e = e_{\text{obs}}$. The results of this paper will help interpret current observations of eclipsing binaries, and guide future efforts to detect tertiary companions in binaries exhibiting large spin-orbit misalignment and/or high eccentricities.

We do not consider the effects of tidal dissipation in this study. If tidal dissipation is sufficiently strong to circularize the orbit, it will almost certainly align the spin axis with the orbital axis on a shorter timescale, thereby erasing any obliquity excitation due to the outer companion. To avoid this complication, we focus here exclusively on the subset of systems that achieve minimum pericenter distances that are too large for dissipative tides to act. This is in similar spirit to the focus of the BANANA Project (Albrecht et al., 2011).

This paper is organized as follows. In Section 6.2, we review aspects of LK oscillations in hierarchical triples with comparable masses, and including the effects of short-range forces (due to general relativity and tidal and rotational

distortion). This section also contains new results concerning the “LK window” of inclinations for eccentricity excitation under general conditions. In Section 6.3 we discuss the spin-orbit dynamics of binaries undergoing LK cycles, and identify a requirement for generating spin-orbit misalignment. Section 6.4 presents numerical integrations of the octupole-order secular equations of motion for a large number of triple systems, and compares with the analytic results in Sections 6.2 and 6.3. In Section 5, we apply the results to the observed eclipsing binary system DI Herculis, and conclude in Section 6.

6.2 Lidov-Kozai Cycles in Triples with Comparable Angular Momentum and Short-Range Forces

6.2.1 Setup and Equations

We consider a hierarchical triple stellar system, composed of an inner binary with masses m_0 and m_1 , and outer companion with mass m_2 , orbiting the center of mass of m_0 and m_1 . In this notation, m_0 is the primary body of the inner binary, so that the secondary body always satisfies $m_1 \leq m_0$. The reduced mass for the inner binary is $\mu_{\text{in}} = m_0 m_1 / m_{01}$, with $m_{01} \equiv m_0 + m_1$. Similarly, the outer binary has reduced mass $\mu_{\text{out}} = m_{01} m_2 / m_{012}$ with $m_{012} \equiv m_0 + m_1 + m_2$. The orbital semi-major axis and eccentricity of the inner and outer binaries are $(a_{\text{in}}, e_{\text{in}})$ and $(a_{\text{out}}, e_{\text{out}})$ respectively. For convenience of notation, we will frequently omit the subscript “in,” and define $e = e_{\text{in}}$ and $j = \sqrt{1 - e_{\text{in}}^2}$. The orbital angular momenta of the inner and outer binaries are denoted by L_{in} and L_{out} respectively.

When the inclination between the inner and outer binaries is sufficiently high, the eccentricity and inclination of the inner binary can undergo large, cyclic excursions, known as Lidov-Kozai (LK) oscillations (Lidov, 1962; Kozai, 1962). See, for example, Fig. 1 of Holman et al. (1997). These oscillations are driven by the disturbing potential from the tertiary companion. To quadrupole order of the potential, the oscillations occur on a characteristic timescale t_k given by

$$\frac{1}{t_k} = \frac{m_2}{m_{01}} \frac{a_{\text{in}}^3}{a_{\text{out,eff}}^3} n, \quad (6.1)$$

where $n = \sqrt{Gm_{01}/a_{\text{in}}^3}$ is the orbital mean motion of the inner binary, and we have introduced an “effective outer binary separation” $a_{\text{out,eff}}$,

$$a_{\text{out,eff}} \equiv a_{\text{out}} \sqrt{1 - e_{\text{out}}^2}. \quad (6.2)$$

The octupole potential of the outer companion further contributes to the secular dynamics of the system, introducing under some conditions even higher maximum eccentricities and orbit flipping (Ford et al., 2000; Naoz et al., 2013a), as well as chaotic orbital evolution (Li et al., 2014). The “strength” of the octupole potential (relative to the quadrupole) is determined by

$$\varepsilon_{\text{oct}} = \frac{m_0 - m_1}{m_0 + m_1} \frac{a_{\text{in}}}{a_{\text{out}}} \frac{e_{\text{out}}}{1 - e_{\text{out}}^2}. \quad (6.3)$$

Thus, for equal-mass inner binaries ($m_0 = m_1$), or outer binaries with $e_{\text{out}} = 0$, the octupole contributions vanish.

Additional perturbations on the orbit of the inner binary occur due to short-range-forces (SRFs), including contributions from general relativity (GR), and tidal and rotational distortions of the inner bodies. These non-Keplerian potentials introduce additional pericenter precession of the inner orbit that acts to reduce the maximum achievable eccentricity (e.g. Wu & Murray, 2003; Fabrycky

& Tremaine, 2007), and can suppress the extreme orbital features introduced by octupole-level terms (Liu et al., 2015).

In Section 6.2, for simplicity, we treat the secondary body in the inner binary (m_1) as a point mass (although m_1 can be comparable to m_0). As a result, we do not consider the SRFs from tidal and rotational distortion of m_1 .² In order to attain analytical results, for the rest of this section we consider the gravitational potential of the tertiary companion only to quadrupole order (except in Section 6.2.5, where we briefly discuss coplanar hierarchical triples). These results are thus exact for equal-mass inner binaries ($m_0 = m_1$), or outer binaries with $e_{\text{out}} = 0$. In Section 4, we perform numerical integrations with octupole included, and including all SRFs (GR, and tidal and rotational distortion in both m_0 and m_1).

Here we present key results of LK oscillations with SRFs in systems where the angular momenta of the inner and outer binaries are comparable. The results of this section review and generalize several previous works. For example, Fabrycky & Tremaine (2007) derived the expression for the maximum eccentricity in LK oscillations (e_{max}) with the effects of GR included, in the limit where the angular momentum ratio satisfies $L_{\text{in}}/L_{\text{out}} \rightarrow 0$. Liu et al. (2015) presented results for general SRFs (GR, tides and rotational distortion) and general angular momentum ratios. For $L_{\text{in}}/L_{\text{out}} \ll 1$, they identified the existence of a “limiting eccentricity” (see Section 6.2.3), but for general $L_{\text{in}}/L_{\text{out}}$, Liu et al. (2015) did not fully explore the behavior of e_{max} and the boundaries of parameter space that allow LK oscillations (the “LK window,” see Section 6.2.2). When SRFs are neglected, the equations for general $L_{\text{in}}/L_{\text{out}}$ are first given by Lidov & Ziglin

²For example, the potential energy due to tidal distortion of m_1 is $W_{\text{Tide},1} \sim k_{2,1}Gm_0^2R_1^5/r^6$, while the energy due to tidal distortion of m_0 is $W_{\text{Tide},0} \sim k_{2,0}Gm_1^2R_0^5/r^6$, where $k_{2,0}$ and $k_{2,1}$ are the Love numbers of m_0 and m_1 . For the low mass main-sequence stars of interest in this paper, with $R \propto m^{0.8}$, we have $W_{\text{Tide},1}/W_{\text{Tide},0} \sim (m_1/m_0)^2 \lesssim 1$.

(1976) (and rederived by Naoz et al. 2013a), along with the analytical expression for the LK window. This is further studied by Martin & Triaud (2016) in the context of circumbinary planets.

The total orbital angular momentum of the system³ $\mathbf{L}_{\text{tot}} = \mathbf{L}_{\text{in}} + \mathbf{L}_{\text{out}}$ is constant, with magnitude

$$L_{\text{tot}}^2 = L_{\text{in}}^2 + L_{\text{out}}^2 + 2L_{\text{in}}L_{\text{out}} \cos I, \quad (6.4)$$

where I is the mutual inclination between the two orbits. To quadrupole order, e_{out} and L_{out} are constant. We can rewrite Eq. (6.4) in terms of the conserved quantity K , where

$$K \equiv j \cos I - \frac{\eta}{2} e^2 = \text{constant}, \quad (6.5)$$

and where we have defined

$$\eta \equiv \left(\frac{L_{\text{in}}}{L_{\text{out}}} \right)_{e_{\text{in}}=0} = \frac{\mu_{\text{in}}}{\mu_{\text{out}}} \left[\frac{m_{01}a_{\text{in}}}{m_{012}a_{\text{out}}(1-e_{\text{out}}^2)} \right]^{1/2}. \quad (6.6)$$

In the limit of $L_{\text{in}} \ll L_{\text{out}}$ ($\eta \rightarrow 0$), Eq. (6.5) reduces to the usual “Kozai constant,” $\sqrt{1-e^2} \cos I = \text{constant}$. We will set the initial eccentricity $e_0 \simeq 0$ for the remainder of this paper, so that $K \simeq \cos I_0$. See Appendix B for a brief consideration of the initial condition $e_0 \neq 0$.

The total energy per unit mass is conserved, and (to quadrupole order) given by

$$\Phi = \Phi_{\text{Quad}} + \Phi_{\text{SRF}}. \quad (6.7)$$

The first term in Eq. (6.7), Φ_{Quad} , is the interaction energy between the inner and

³We have neglected the contribution from the spins of m_0 and m_1 , since for stellar parameters of interest in this paper, the spin angular momentum S of each star satisfies $S/L_{\text{in}} \ll 1$.

outer binaries,

$$\begin{aligned}\Phi_{\text{Quad}} &= -\frac{\Phi_0}{8} [2 + 3e^2 - (3 + 12e^2 - 15e^2 \cos^2 \omega) \sin^2 I] \\ &= -\frac{\Phi_0}{8} \left\{ 2 + 3e^2 - (3 + 12e^2 - 15e^2 \cos^2 \omega) \right. \\ &\quad \times \left. \left[1 - \frac{1}{j^2} \left(K + \frac{\eta}{2} e^2 \right)^2 \right] \right\}. \end{aligned} \quad (6.8)$$

where ω is the argument of pericenter of the inner binary, and

$$\Phi_0 = \frac{Gm_2 a_{\text{in}}^2}{a_{\text{out,eff}}^3}. \quad (6.9)$$

The second term in Eq. (6.7), Φ_{SRF} , is an energy term due to short-range forces (SRFs) that lead to additional pericenter precession. The contributions to Φ_{SRF} consist of the general relativistic correction, as well as tidal and rotational distortion of m_0 , so that $\Phi_{\text{SRF}} = \Phi_{\text{GR}} + \Phi_{\text{Tide}} + \Phi_{\text{Rot}}$, with (e.g. Liu et al., 2015)

$$\begin{aligned}\Phi_{\text{GR}} &= -\varepsilon_{\text{GR}} \frac{\Phi_0}{j}, \\ \Phi_{\text{Tide}} &= -\varepsilon_{\text{Tide}} \frac{\Phi_0}{15} \frac{1 + 3e^2 + (3/8)e^4}{j^9}, \\ \Phi_{\text{Rot}} &= -\varepsilon_{\text{Rot}} \frac{\Phi_0}{2j^3}, \end{aligned} \quad (6.10)$$

where

$$\begin{aligned}\varepsilon_{\text{GR}} &\simeq 3 \times 10^{-2} \frac{\bar{m}_{01}^2 \bar{a}_{\text{out,eff}}^3}{\bar{m}_2 \bar{a}_{\text{in}}^4}, \\ \varepsilon_{\text{Tide}} &\simeq 9.1 \times 10^{-7} \frac{\bar{k}_{2,0} \bar{m}_1 \bar{m}_{01} \bar{R}_0^5 \bar{a}_{\text{out,eff}}^3}{\bar{m}_2 \bar{m}_0 \bar{a}_{\text{in}}^8}, \\ \varepsilon_{\text{Rot}} &\simeq 2.9 \times 10^{-5} \left(\frac{P_*}{10 \text{ d}} \right)^{-2} \frac{\bar{k}_{q,0} \bar{m}_{01} \bar{R}_0^5 \bar{a}_{\text{out,eff}}^3}{\bar{m}_0 \bar{m}_2 \bar{a}_{\text{in}}^5}. \end{aligned} \quad (6.11)$$

Here, P_* is the spin period of m_0 . The various dimensionless masses and radii, \bar{m}_i and \bar{R}_i are the physical quantities scaled by M_\odot and R_\odot . $\bar{a}_{\text{in}} = a_{\text{in}}/1 \text{ AU}$, and $\bar{a}_{\text{out,eff}} = a_{\text{out,eff}}/100 \text{ AU}$. $\bar{k}_{2,0}$ is the tidal Love number of m_0 scaled by its

canonical value $k_{2,0} = 0.03$. Similarly, $\bar{k}_{q,0}$ depends on the interior structure of m_0 and helps quantify the degree of rotational distortion, and is scaled by its canonical value $k_{q,0} = 0.01$ (Claret & Gimenez, 1992)⁴. Corresponding terms for the tidal and rotational distortions of m_1 are obtained by switching the indices 0 and 1 in Eqs. (6.11) (but are neglected in Section 2).

In the expression for Φ_{Rot} in Eq. (6.10), we have assumed alignment of the spin and orbital axes. When the spin and orbital axes are not aligned, Φ_{Rot} depends on the spin-orbit misalignment angle. In this situation, the problem is no longer integrable, and numerical integrations are required (however, see Correia 2015 for an analytic treatment). In order to attain analytic results, we will assume that the spin and orbital axes are aligned for the remainder of Section 2, and consider the spin-orbit dynamics separately, in Section 4 via numerical integrations.

For the system parameters of interest in this paper, the GR contribution to the SRFs usually dominates over the rotational contribution at low to moderate eccentricities, and the tidal contribution dominates at very high eccentricities ($e \gtrsim 0.9$). As a result, Φ_{Rot} can often be neglected. This approximation requires that $S \ll L_{\text{in}}$ (where S is the spin angular momentum of m_0), and is always satisfied for the systems considered in this paper. We also require $\varepsilon_{\text{Rot}}/2j^3 \lesssim 1$ (so that the rotational contribution does not suppress the LK cycles), and $\varepsilon_{\text{Rot}}/2j^3 \lesssim \varepsilon_{\text{GR}}/j$ (so that $\Phi_{\text{Rot}} \lesssim \Phi_{\text{GR}}$, i.e. rotational distortion is negligible compared to GR). Thus, ignoring the effects of rotational distortion is

⁴ $k_{q,0} = (I_3 - I_1)/m_0 R_0^2 \hat{\Omega}_0^2$, where I_1 and I_3 are the principal moments of inertia, and $\hat{\Omega}_0$ is the spin rate of m_0 in units of the breakup rate. $k_{q,0}$ is related to the apsidal motion constant κ by $k_{q,0} = 2\kappa/3$.

justified for eccentricities that satisfy

$$1 - e^2 \gtrsim 5.9 \times 10^{-4} \left(\frac{\bar{k}_{q,0} \bar{m}_{01} \bar{R}_0^5 \bar{a}_{\text{out,eff}}^3}{\bar{m}_0 \bar{m}_2 \bar{a}_{\text{in}}^5} \right)^{2/3} \left(\frac{P_\star}{10 \text{ d}} \right)^{-4/3}, \quad (6.12)$$

and

$$1 - e^2 \gtrsim 4.8 \times 10^{-4} \frac{\bar{k}_{q,0} \bar{R}_0^5}{\bar{m}_0 \bar{m}_{01} \bar{a}_{\text{in}}} \left(\frac{P_\star}{10 \text{ d}} \right)^{-2}. \quad (6.13)$$

Therefore, Φ_{Rot} is often negligible, unless the spin period is exceptionally rapid, or if the star has a large radius.

For a given initial condition (I_0 and $e_0 \simeq 0$), the conservation of Φ (Eq. [6.7]) and $K \simeq \cos I_0$ (Eq. [6.5]), yield e as a function of ω . The maximum eccentricity (where $de/d\omega = 0$), is achieved when $\omega = \pi/2$ and $3\pi/2$.

6.2.2 Range of Inclinations Allowing Eccentricity Excitation

The “window” of inclinations allowing LK oscillations (starting from an initial eccentricity $e_0 \simeq 0$) can be determined by enforcing $e_{\text{max}} > 0$. Expanding for $e^2 \ll 1$, the conservations of energy and $K = \cos I_0$ [valid to $\mathcal{O}(e^6)$] reduce to

$$ae^6 + be^4 + ce^2 = 0, \quad (6.14)$$

where

$$\begin{aligned} a &= \frac{\eta^2}{4} (4 - 5 \cos^2 \omega) - \frac{\varepsilon_{\text{GR}}}{6} + \frac{5\varepsilon_{\text{Rot}}}{12} + 7\varepsilon_{\text{Tide}} \\ b &= \frac{\eta^2}{4} + (4 - 5 \cos^2 \omega)(1 + \eta \cos I_0) - 1 \\ &\quad - \frac{\varepsilon_{\text{GR}}}{3} + \frac{\varepsilon_{\text{Rot}}}{2} + \frac{10\varepsilon_{\text{Tide}}}{3} \\ c &= 5 \cos^2 \omega \sin^2 I_0 + 5 \cos^2 I_0 + \eta \cos I_0 - 3 \\ &\quad + \frac{4\varepsilon_{\text{GR}}}{3} + 2\varepsilon_{\text{Rot}} + \frac{4\varepsilon_{\text{Tide}}}{3}. \end{aligned} \quad (6.15)$$

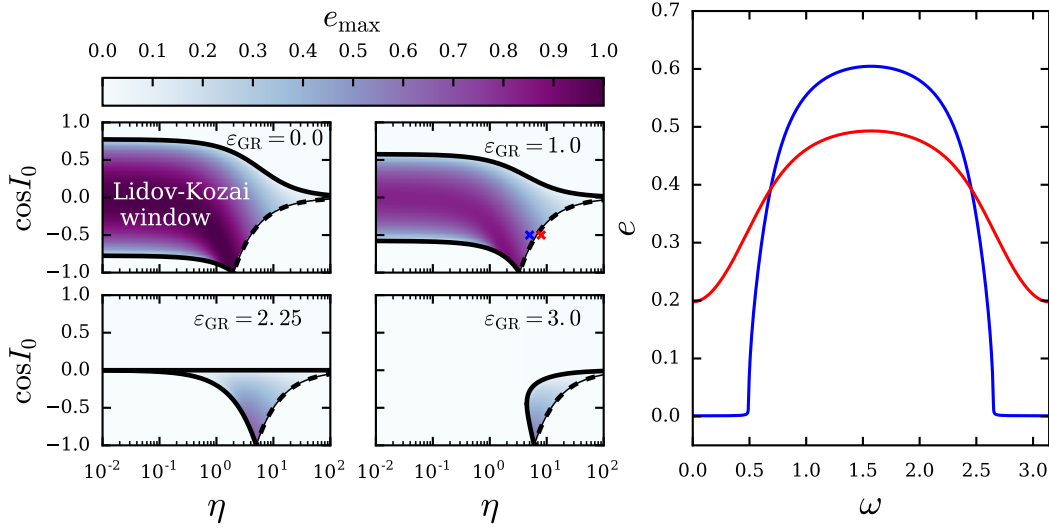


Figure 6.1: *Left and center panels:* The “window” of inclinations (shaded regions) that allow LK oscillations, versus the angular momentum ratio η , for various values of ε_{GR} (we have set $\varepsilon_{\text{Tide}} = \varepsilon_{\text{Rot}} = 0$). The solid lines are obtained from Eq. (6.19), and the dashed line from Eq. (6.23). Inside the window, the LK maximum eccentricity is also shown, as calculated in Section 6.2.3, Eq. (6.24). Combinations of $\cos I_0$ and η below the dashed line allow LK eccentricity oscillations, but these oscillations are not connected to the $e_0 \simeq 0$ trajectory. This is illustrated in the rightmost panel, where we show example phase space trajectories (ω, e) for energies corresponding to the colored crosses in the neighboring uppermost panel (with $\varepsilon_{\text{GR}} = 1.0$).

For $e > 0$, Eq. (6.14) becomes

$$ae^4 + be^2 + c = 0. \quad (6.16)$$

This equation determines e as a function of ω for various parameters $I_0, \eta, \varepsilon_{\text{GR}}, \varepsilon_{\text{Tide}}$, and ε_{Rot} . The maximum eccentricity occurs at $\omega = \pi/2$ and $3\pi/2$. In order for this $e_{\text{max}} \neq 0$ be reachable from $e_0 \simeq 0$, we require that Eq. (6.16) admit $e = e_0 \simeq 0$ as a solution for some value of $\omega_0 \equiv \omega(e_0)$. Evaluating Eq. (6.16) at $e = e_0 = 0$ yields

$$\cos^2 \omega_0 = -\frac{5 \cos^2 I_0 + \eta \cos I_0 - 3 + \varepsilon_{\text{SRF}}}{5 \sin^2 I_0}, \quad (6.17)$$

where we have defined

$$\varepsilon_{\text{SRF}} \equiv \frac{4}{3}\varepsilon_{\text{GR}} + 2\varepsilon_{\text{Rot}} + \frac{4}{3}\varepsilon_{\text{Tide}}. \quad (6.18)$$

Requiring that $\cos^2 \omega_0 \geq 0$ translates into the condition

$$(\cos I_0)_- \leq \cos I_0 \leq (\cos I_0)_+, \quad (6.19)$$

where

$$(\cos I_0)_{\pm} = \frac{1}{10} \left(-\eta \pm \sqrt{\eta^2 + 60 - 20\varepsilon_{\text{SRF}}} \right). \quad (6.20)$$

In order for $(\cos I_0)_{\pm}$ to be real, η and ε_{SRF} must satisfy

$$\eta^2 + 60 - 20\varepsilon_{\text{SRF}} \geq 0. \quad (6.21)$$

If $\varepsilon_{\text{SRF}} < 3$ then Eq. (6.21) is satisfied for all values of η . If $\varepsilon_{\text{SRF}} > 3$ and Eq. (6.21) is not satisfied, eccentricity oscillations cannot be induced for any value of $\cos I_0$.

Note that while $(\cos I_0)_+$ is less than unity for all values of η and ε_{SRF} (provided that Eq. [6.21] is satisfied), $(\cos I_0)_- > -1$ only when

$$\eta < 2 + \varepsilon_{\text{SRF}} \quad \text{and} \quad \eta < 10. \quad (6.22)$$

On the other hand, requiring that $\cos^2 \omega_0 \leq 1$ implies that

$$\cos I_0 \geq -\frac{2}{\eta} \left(1 + \frac{1}{2}\varepsilon_{\text{SRF}} \right). \quad (6.23)$$

Thus, if $\eta > 2\varepsilon_{\text{SRF}}$, then the condition $\cos I_0 \geq (\cos I_0)_-$ (in Eq. [6.19]) must be replaced by Eq. (6.23). If $\varepsilon_{\text{SRF}} = 0$, the requirement that $\cos I_0 \geq -2/\eta$ is recovered, as identified by Lidov & Ziglin (1976).

The above conditions (Eqs. [6.19] and [6.23]) guarantee that energy conservation Eq.(14) has a physical solution $(e, \omega) = (0, \omega_0)$. Requiring $e^2 = e_{\max}^2 > 0$ at $\omega = \pi/2$ implies that $c(\cos \omega = 0) < 0$, which translates into the condition (6.19).

Figure 6.1 shows the “LK window” of inclinations allowing eccentricity oscillations, determined by Eqs (6.20) and (6.23), as a function of η , for several illustrative values of ε_{GR} (and with $\varepsilon_{\text{Tide}}, \varepsilon_{\text{Rot}} = 0$). At moderate eccentricities, the SRF contribution due to GR dominates over the tidal contribution (since $\varepsilon_{\text{Tide}} \ll \varepsilon_{\text{GR}}$), and for solar-type stars, GR also dominates over the rotational distortion (since $\varepsilon_{\text{Rot}} \ll \varepsilon_{\text{GR}}$). As a result, adopting the approximation $\varepsilon_{\text{Tide}}, \varepsilon_{\text{Rot}} = 0$ is often a valid approximation, except for eccentricities near unity, or for large values of the stellar radius and spin rate, see Eqs. (6.12) and (6.13).

Inside the LK window, the maximum eccentricity is also shown, as calculated in Section 6.2.3, Eq. (6.24). When $\varepsilon_{\text{GR}} = 0$ and $\eta = 0$, the window of inclinations allowing LK oscillations is given by the well known form $-\sqrt{3/5} \leq \cos I_0 \leq \sqrt{3/5}$. For increasing ε_{GR} , the window narrows for most values of η . When $\varepsilon_{\text{GR}} > 2.25$, the window closes and eccentricity oscillations are completely suppressed for small values of η . For larger ($\gtrsim 1$) values of η , LK oscillations remain possible, but occur only within a very narrow range of inclinations, and are limited to retrograde ($\cos I_0 < 0$) configurations. We find that for $\varepsilon_{\text{GR}} \gtrsim 5$, the LK window is so narrow for all values of η , that LK oscillations are for all practical purposes completely suppressed. The rightmost panel of Fig. 6.1 shows phase-space trajectories (contours of constant energy) for two representative points. The trajectory located just inside the LK window shows that the eccentricity can increase to a large value, starting from $e_0 \simeq 0$. In contrast, the trajectory just outside of the LK window does not connect to $e_0 \simeq 0$. As a result, for $(\eta, \cos I_0)$ located below the dashed curves in Fig. 6.1, LK oscillations starting from $e_0 \simeq 0$ are completely suppressed.

6.2.3 Maximum and Limiting Eccentricities

Evaluating the eccentricity at $e_0 = 0$ (where $I = I_0$) and $e = e_{\max}$ (where $\omega = \pi/2$), allows energy and angular momentum conservation to be expressed as

$$\frac{3j_{\min}^2 - 1}{8j_{\min}^2} \left[5 \left(\cos I_0 + \frac{\eta}{2} \right)^2 - \left(3 + 4\eta \cos I_0 + \frac{9}{4}\eta^2 \right) j_{\min}^2 + \eta^2 j_{\min}^4 \right] + \left(\frac{\Phi_{\text{SRF}}}{\Phi_0} \right) \Big|_{e_{\max}} = 0, \quad (6.24)$$

where $j_{\min} \equiv \sqrt{1 - e_{\max}^2}$. When the effects of SRFs are negligible, and in the limit $\eta \rightarrow 0$, the solution of Eq. (6.24) yields the well-known relation $e_{\max} = \sqrt{1 - (5/3) \cos^2 I_0}$. Note that the properties of the tertiary companion ($a_{\text{out}}, e_{\text{out}}, m_2$) enter Eq. (6.24) only through the combination $a_{\text{out,eff}}/m_2^{1/3}$ and η .

For general $\eta, \varepsilon_{\text{GR}}, \varepsilon_{\text{Tide}}$, and ε_{Rot} , Eq. (6.24) must be solved numerically for e_{\max} . Fig. 6.2 shows an example of e_{\max} versus I_0 , for an equal-mass inner binary ($m_0 = m_1 = 1M_\odot$) with an orbital period of 15 days, a low-mass outer companion ($m_2 = 0.1M_\odot$), and outer binary separations, $a_{\text{out}} = 10a_{\text{in}}, 30a_{\text{in}}, 65a_{\text{in}}$ as labeled.

Inspection of Fig. 6.2 reveals that there is a maximum (limiting) achievable value of e_{\max} , denoted here as e_{\lim} , which occurs at a critical initial inclination $I_{0,\lim}$. This limiting eccentricity e_{\lim} occurs when the initial inclination satisfies the condition $de_{\max}/dI_0 = 0$, or when $dj_{\min}/dI_0 = 0$. Defining $j_{\lim} \equiv \sqrt{1 - e_{\lim}^2}$, and differentiating Eq. (6.24) with respect to I_0 , we find that $I_{0,\lim}$ is given by

$$\cos I_{0,\lim} = \frac{\eta}{2} \left(\frac{4}{5} j_{\lim}^2 - 1 \right), \quad (6.25)$$

Obviously, the existence of $I_{0,\lim}$ requires $\eta < 2/(1 - 4j_{\lim}^2/5)$. Notice that $I_{0,\lim}$ depends on both η , and on the strength of the SRFs (through e_{\lim}). When $\eta \rightarrow 0$, $I_{0,\lim} \rightarrow 90^\circ$. As η increases, the critical inclination is shifted to progressively

retrograde values ($I_{0,\text{lim}} > 90^\circ$).

Substituting Eq. (6.25) into Eq. (6.24), we find that the limiting eccentricity e_{lim} is determined by

$$\frac{3}{8}(j_{\text{lim}}^2 - 1) \left[-3 + \frac{\eta^2}{4} \left(\frac{4}{5} j_{\text{lim}}^2 - 1 \right) \right] + \left(\frac{\Phi_{\text{SRF}}}{\Phi_0} \right) \Big|_{e=0}^{e=e_{\text{lim}}} = 0. \quad (6.26)$$

Equation (6.26) may sometimes permit a physical solution for $j_{0,\text{lim}}$, but imply unphysical values for $\cos I_{0,\text{lim}}$. In such cases, e_{lim} cannot be achieved. As a result, any solution obtained from Eq. (6.26) must also be substituted into Eq. (6.25) to ensure that $\cos I_{0,\text{lim}}$ exists.

Figure 6.3 shows e_{lim} and $I_{0,\text{lim}}$ as determined from Eq. (6.25) and Eq. (6.26), along with the ranges of inclinations allowing LK oscillations of any amplitude, from Eqs. (6.19) and (6.23), as a function of $a_{\text{out,eff}}/m_2^{1/3}$. In this example, we have set $a_{\text{in}} = 0.17$ AU and $e_{\text{out}} = 0$, and adopted two values of the tertiary mass: a solar-type perturber ($m_2 = 1M_\odot$) and a brown dwarf perturber ($m_2 = 0.1M_\odot$). Since Eq. (6.26) depends on η only through η^2 , e_{lim} is nearly degenerate in terms of $a_{\text{out}}/m_2^{1/3}$ for the adopted parameters in Fig. 6.3. For the solar-mass tertiary, $I_{0,\text{lim}} \simeq 90^\circ$ for all values of $a_{\text{out,eff}}$, because $\eta \ll 1$ is always satisfied. For the brown dwarf tertiary, $I_{0,\text{lim}} > 90^\circ$ for small values of $a_{\text{out,eff}}$, because $\eta \sim 1$.

6.2.4 Constraints on Hidden Tertiary Companions from Inner Binary Eccentricities

For an observed binary system with eccentricity e_{obs} , we can derive constraints on a possible unseen tertiary companion driving the eccentricity from $e_0 \simeq 0$ to $e = e_{\text{obs}}$ through LK cycles. The LK maximum eccentricity must satisfy

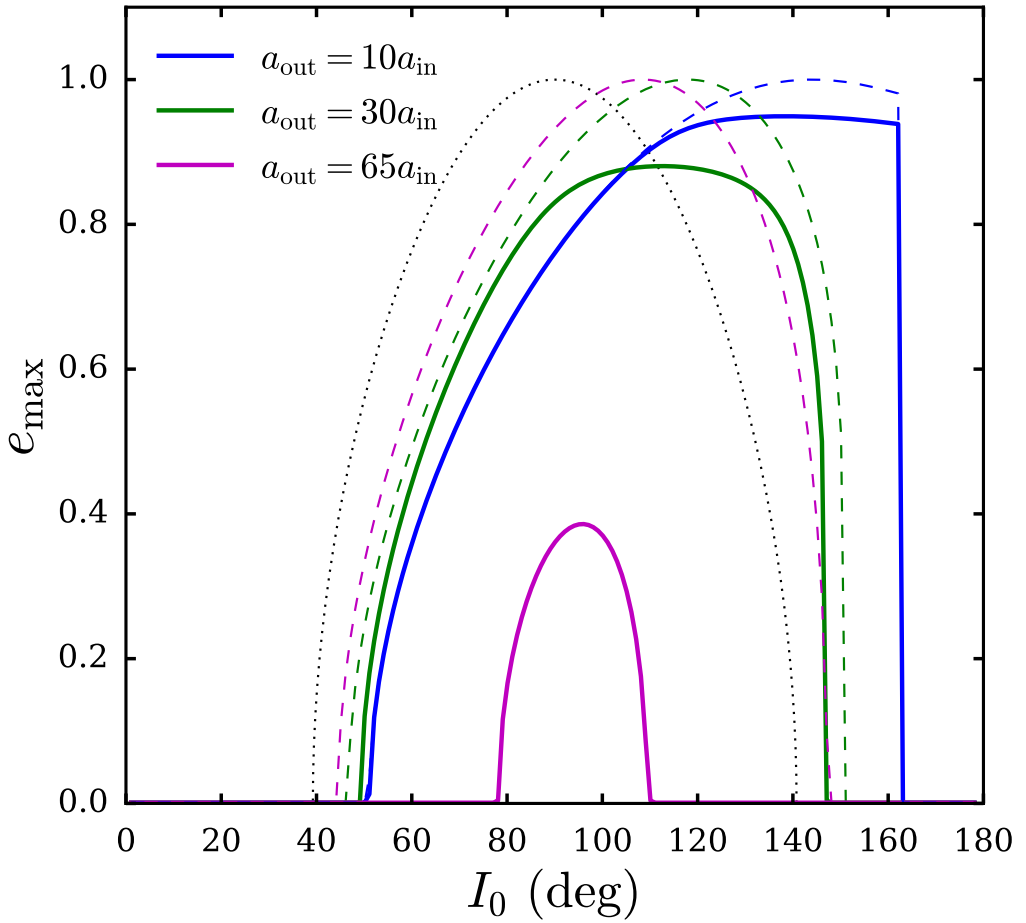


Figure 6.2: The maximum eccentricity of the inner binary, versus the initial inclination I_0 . We have fixed $m_0 = m_1 = 1M_\odot$, $m_2 = 0.1M_\odot$, $a_{\text{in}} = 0.17$ AU (so that the orbital period is ~ 15 days), $e_{\text{out}} = 0$, and varying a_{out} , as labeled. The solid curves show results with SRFs included, and the dashed curves show results without SRFs. The dotted curve depicts the standard result $e_{\text{max}} = \sqrt{1 - (5/3) \cos^2 I_0}$, applicable in the limit $\eta \rightarrow 0$ and $\varepsilon_{\text{GR}}, \varepsilon_{\text{Rot}}, \varepsilon_{\text{Tide}} \rightarrow 0$.

$e_{\max} \geq e_{\text{obs}}$; this places constraints on the mass of the perturber, and the range of mutual inclinations I_0 and effective outer separations $a_{\text{out,eff}}$. In Fig. 6.4, we plot curves of constant $e_{\max} = 0.2, 0.5, 0.8$ in (I_0, a_{out}) space assuming an equal mass inner binary ($m_0 = m_1 = 1M_\odot$) with orbital period $P_{\text{orb}} = 15$ days, $e_{\text{out}} = 0$, and adopting both solar-type and brown-dwarf perturbers. The curves were obtained by solving Eq. (6.24). For a given e_{\max} contour, the regions inside the curve indicate the parameter space able to produce $e \geq e_{\max}$. For example, if an observed binary system has $e_{\text{obs}} = 0.8$, a solar-mass perturber must be located within ~ 10 AU in order to produce the observed eccentricity, and the necessary inclination is restricted to the range $60^\circ \lesssim I_0 \lesssim 120^\circ$. Similarly, a brown-dwarf companion must be located within ~ 6 AU, most likely in a retrograde orbit ($I_0 \gtrsim 90^\circ$).

For $\eta \ll 1$, the properties of the outer perturber required to produce a given eccentricity can be explicitly calculated, without having to resort to numerical root-finding in Eq. (6.24) or Eq. (6.26). Neglecting the SRF contribution from rotational and tidal distortion (so that $\varepsilon_{\text{Rot}} = \varepsilon_{\text{Tide}} = 0$), the LK window (Eq. [6.20]) is

$$|\cos I_0| \leq \frac{1}{5} \sqrt{15 - \frac{20}{3} \varepsilon_{\text{GR}}}. \quad (6.27)$$

Thus, LK oscillations are completely suppressed ($e_{\max} = 0$) when ε_{GR} satisfies (see also Liu et al. 2015)

$$\varepsilon_{\text{GR}} > \frac{9}{4} \left(1 - \frac{5}{3} \cos^2 I_0 \right) \quad \text{for } \eta \ll 1. \quad (6.28)$$

For an inner binary with specified properties, this translates into a maximum effective perturber distance for LK oscillations (of any amplitude) to occur:

$$a_{\text{out,eff}} < 19.6 \text{ AU} \left(\frac{\bar{m}_2}{\bar{m}_{01}^2} \right)^{1/3} \left(\frac{a_{\text{in}}}{0.1 \text{ AU}} \right)^{4/3} \left(1 - \frac{5}{3} \cos^2 I_0 \right)^{1/3}. \quad (6.29)$$

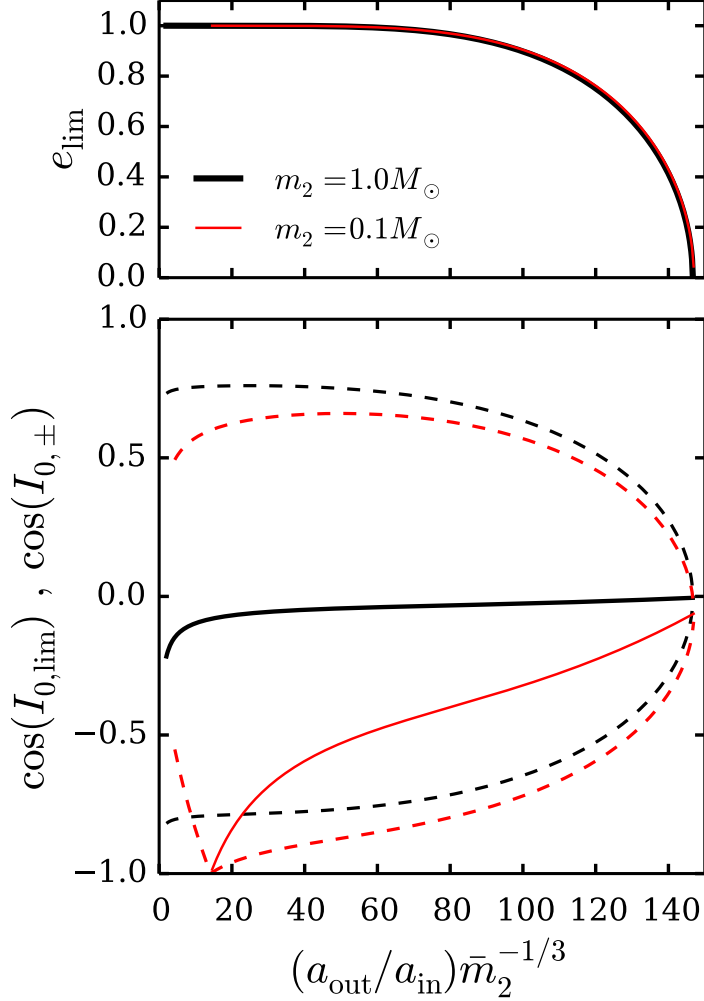


Figure 6.3: Limiting eccentricity e_{lim} and critical inclination $I_{0,\text{lim}}$, as a function of $(a_{\text{out}}/a_{\text{in}})\bar{m}_2^{-1/3}$. The black curves show $m_2 = 1M_\odot$, and the red curves show $m_2 = 0.1M_\odot$. The other parameters are $m_0 = m_1 = 1M_\odot$, $a_{\text{in}} = 0.17$ AU, and $e_{\text{out}} = 0$. In the lower panel, the solid lines indicate $I_{0,\text{lim}}$, and the dashed lines show the range of inclinations capable of exciting LK oscillations ($I_{0,\pm}$), as determined from Eqs. (6.19) and (6.23). As L_{out} decreases relative to L_{in} (i.e. $\eta \gtrsim 1$), $I_{0,\text{lim}}$ is shifted to progressively retrograde values. For the brown dwarf tertiary, $\cos I_{0,\text{lim}}$ does not exist for small values of $a_{\text{out}}m_2^{-1/3}$; as a result e_{lim} cannot always be achieved. Notice that e_{lim} is nearly degenerate in terms of $(a_{\text{out}})\bar{m}_2^{-1/3}$ (thus the red and black curves nearly coincide in the top panel).

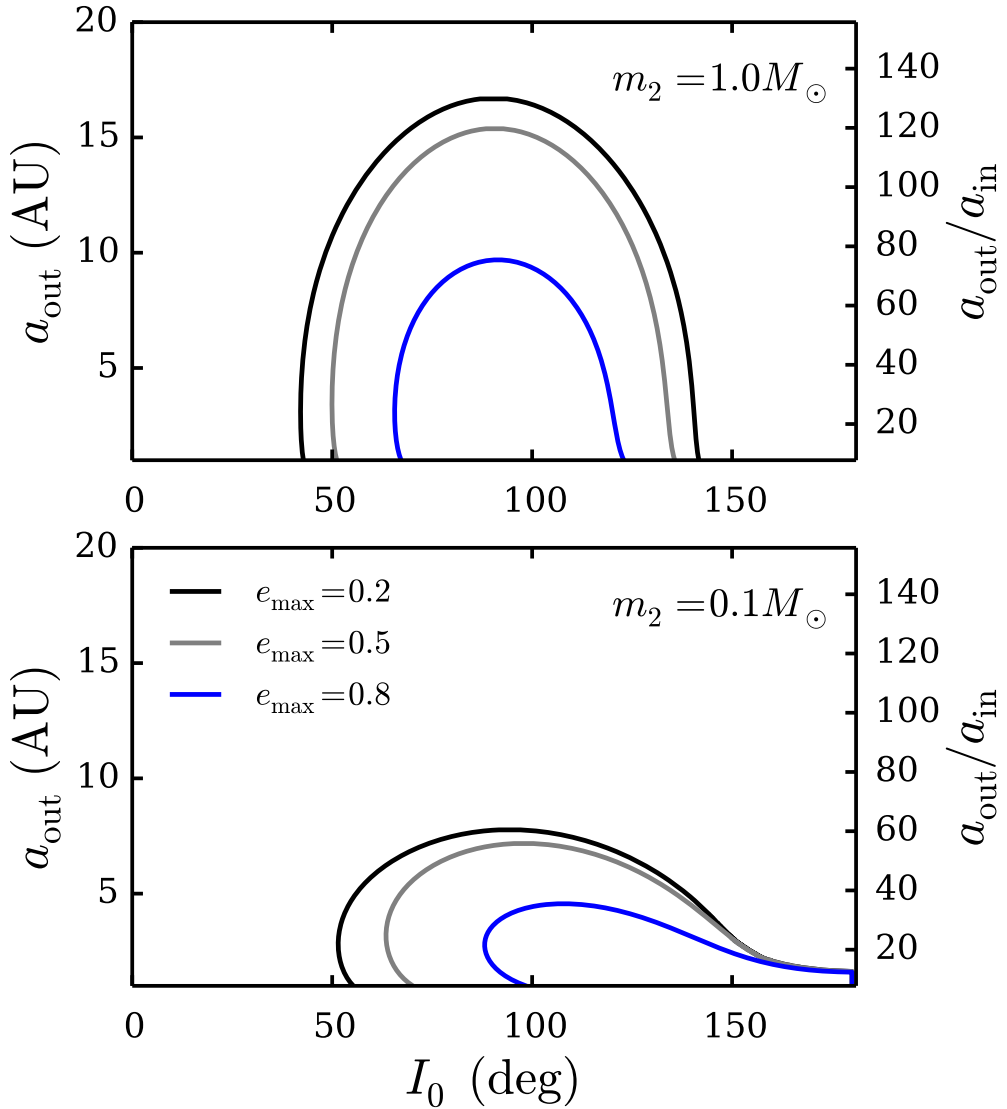


Figure 6.4: Curves in (I_0, a_{out}) parameter space able to produce a given value of e_{max} , as labeled. For each contour of e_{max} , the region bounded by the curve and the x -axis indicates combinations of (I_0, a_{out}) that will yield even higher maximum eccentricities. Results are shown for a solar-mass outer companion (top), and a brown-dwarf outer companion (bottom). The inner binary properties are fixed at $m_0 = m_1 = 1 M_\odot$, $P_{\text{orb}} = 15$ days ($a_{\text{in}} = 0.17$ AU), and $e_{\text{out}} = 0$. See also Fig. 6.13 where we show similar calculations applied to the eclipsing binary system DI Herculis.

Setting $I_0 = I_{0,\text{lim}} = 90^\circ$ yields the absolute maximum effective distance $a_{\text{out,eff}}$ for LK oscillations to occur (for any inclination).

For $\eta \ll 1$, the limiting perturber distance able to drive the eccentricity to e_{obs} can be solved explicitly by setting $e_{\text{max}} = e_{\text{obs}} = e_{\text{lim}}$, and neglecting the terms in Eq. (6.26) proportional to η^2 ,

$$a_{\text{out,eff}} \simeq 15.5 \text{ AU} \left(\frac{a_{\text{in}}}{0.1 \text{ AU}} \right)^{4/3} \left(\frac{\bar{m}_2}{\bar{m}_{01}^2} \right)^{1/3} \times \left[\mathcal{F}_1 + \mathcal{F}_2 \frac{\bar{m}_1 \bar{R}_0^5}{\bar{m}_0 \bar{m}_{01}} \left(\frac{a_{\text{in}}}{0.1 \text{ AU}} \right)^{-4} \right]^{-1/3}, \quad (6.30)$$

where we have defined

$$\mathcal{F}_1 = \frac{1}{j_{\text{lim}}(j_{\text{lim}} + 1)} \quad (6.31)$$

$$\mathcal{F}_2 = \frac{2.02 \times 10^{-2}}{1 - j_{\text{lim}}^2} \left[\frac{1 + 3e_{\text{lim}}^2 + (3/8)e_{\text{lim}}^4}{j_{\text{lim}}^9} - 1 \right]. \quad (6.32)$$

Expanding \mathcal{F}_1 and \mathcal{F}_2 appropriately, and setting $e_{\text{lim}} = 0$, recovers Eq. (6.29) evaluated at $I_0 = 90^\circ$.

In Fig. 6.5, we plot the maximum effective separation required to generate an eccentricity $e_{\text{obs}} = 0.2$ and 0.8 , by solving Eq. (6.26). We also compare this with the approximate ($\eta \ll 1$ limit) expression given in Eq. (6.30). The exact solution agrees well with Eq. (6.30), because the criterion for determining the limiting eccentricity (Eq. 6.26) depends on the angular momentum ratio only as η^2 . Therefore, only when $\eta \rightarrow 1$ does the approximate solution deviate from the exact expression.

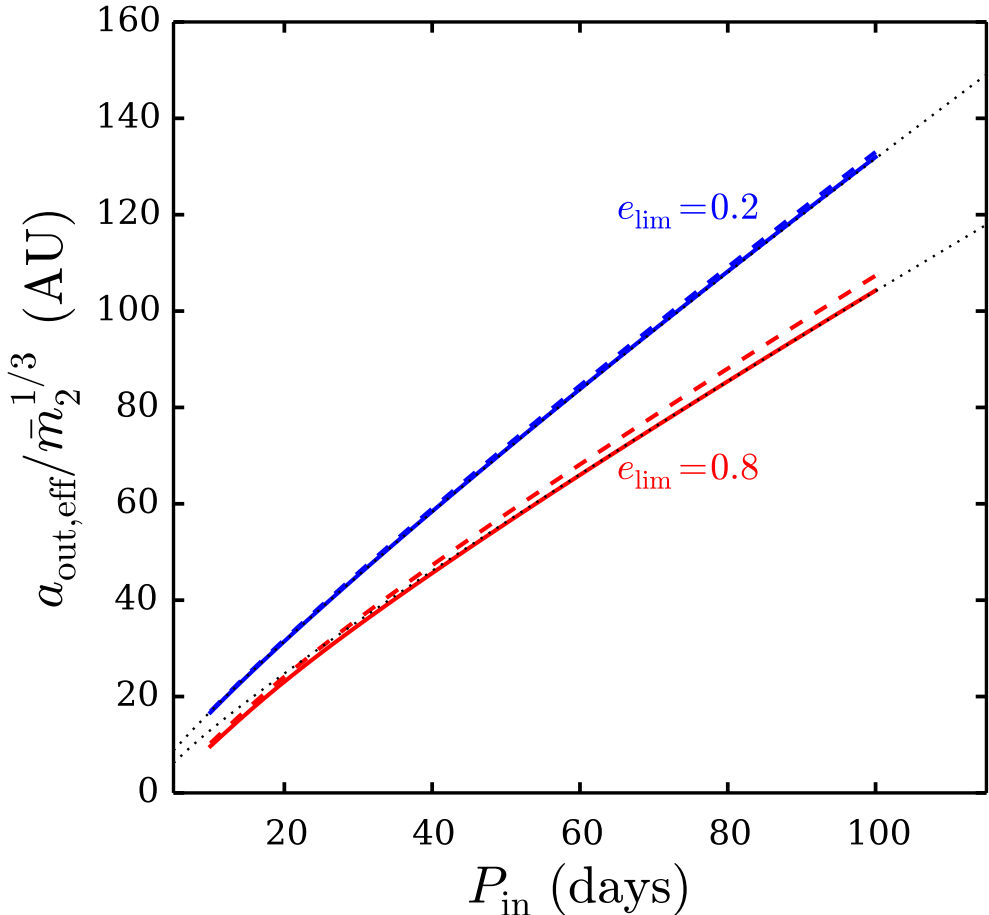


Figure 6.5: Effective perturber distance required to generate a limiting eccentricity e_{lim} , as labeled, as a function of the inner binary orbital period. The solid lines depict a solar-mass outer perturber ($m_2 = 1M_\odot$), whereas the dashed lines depict a low mass brown dwarf perturber ($m_2 = 0.05M_\odot$). The dashed lines correspond to the expression (6.30), valid in the $\eta \rightarrow 0$ limit. For a given inner binary period P_{in} , in order for an unseen perturber to generate an eccentricity $e_{\text{obs}} = 0.2$ (0.8), the perturber must have an effective separation lower than the black (blue) value. Note that the y-axis has been scaled by $(m_2/M_\odot)^{-1/3}$.

6.2.5 Eccentricity Excitation in Coplanar Systems

If the inner and outer orbits are coplanar, and the octupole contribution is non-vanishing ($\varepsilon_{\text{oct}} \neq 0$), the inner and outer binaries can exchange angular momentum, thereby periodically exciting the eccentricity of the inner binary. In the case of exact coplanarity, the maximum eccentricity can be calculated algebraically (Lee & Peale, 2003).

The general interaction potential up to octupole order is given in, e.g. Ford et al. (2000), Naoz et al. (2013a), and Liu et al. (2015). If the orbits are exactly coplanar, the interaction energy simplifies to

$$\begin{aligned}\Phi_{\text{Int}} &= \Phi_{\text{Quad}} + \Phi_{\text{Oct}} \\ &= \frac{\Phi_0}{8} \left[-2 - 3e^2 + \frac{15}{8} e(3e^2 + 4)\varepsilon_{\text{oct}} \cos \Delta\varpi \right],\end{aligned}\tag{6.33}$$

where $\Delta\varpi = \varpi_{\text{in}} - \varpi_{\text{out}}$, with ϖ the longitude of periapsis. The total angular momentum $L_{\text{tot}} = L_{\text{in}} + L_{\text{out}}$ is also conserved. For a given set of orbital geometries (so that both Φ and L_{tot} are fully specified), e_{in} and e_{out} as a function of $\Delta\varpi$ can be obtained. The maximum value of e_{in} , e_{max} occurs at either $\Delta\varpi = 0$ or π , depending on the initial value of $\Delta\varpi$, and whether $\Delta\varpi$ librates or circulates.

If either the inner or outer orbit is initially circular, the interaction energy is independent of the initial orientation ($\Delta\varpi$) of the two orbits. The procedure for calculating e_{max} is as follows: we specify the initial total energy Φ , including the effects of SRFs ($\Phi = \Phi_{\text{Int}} + \Phi_{\text{SRF}}$), and the angular momentum (L_{tot}), calculate e as a function of $\Delta\varpi$, and determine the maximum value of e (see also Petrovich, 2015b). As before, we neglect the contribution to Φ_{SRF} from rotational distortion ($\Phi_{\text{Rot}} = 0$).

In Fig. 6.6 we fix the properties of the inner binary ($m_0 = 1M_\odot$, $m_1 = 0.5M_\odot$,

$P_{\text{orb}} = 15$ days), and plot the maximum eccentricity for the two fiducial masses for the perturber ($1M_{\odot}$ and $0.1M_{\odot}$), and varying initial values of e_{out} . The solar mass perturber must be sufficiently close (~ 1 AU) and eccentric to excite a substantial eccentricity in the inner binary. In such configurations, the secular approximation is in danger of breaking down. The brown dwarf perturber is able to excite higher eccentricities, with a sharp peak. The sharp peak of e_{max} at specific value of a_{out} coincides when the angle $\Delta\varpi$ changes from circulating to librating. The existence of librating solutions allows for higher maximum eccentricities (Lee & Peale, 2003), and can be understood in terms of an “apsidal precession resonance” (Liu et al., 2015b). This “resonance” occurs when the apsidal precession of the inner binary (driven by GR and the outer binary) matches that of the outer binary (driven by the inner binary). However, note that this does not qualify as a “true resonance” (see Laskar & Robutel, 1995; Correia et al., 2010; Laskar et al., 2012, for further discussion on the nature of this “resonance”).

6.3 Spin-Orbit Dynamics in Systems Undergoing LK Oscillations

Due to rotational distortion, each member of the inner binary possesses a quadrupole moment, causing a torque and mutual precession of the spin axis S and the orbital axis L_{in} . Here we discuss the precession of the primary member of the inner binary (m_0). Similar results for the spin precession of m_1 are obtained by switching the indices 0 and 1 in the following expressions.

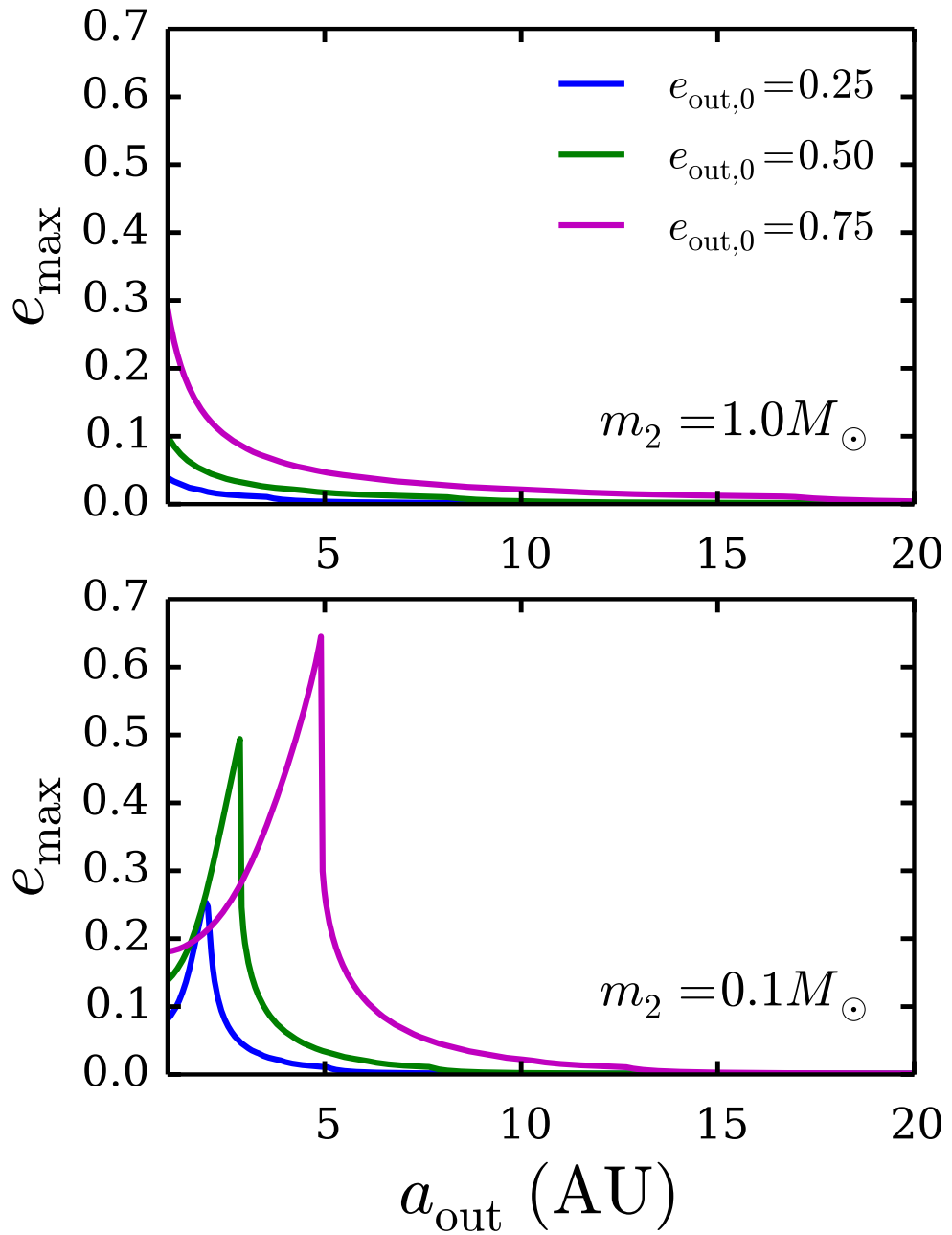


Figure 6.6: Maximum eccentricity e_{\max} for coplanar ($I = 0$) hierarchical triple systems, versus the outer binary semi-major axis. The properties of the inner binary are fixed, with masses $m_0 = 1M_{\odot}$, $m_1 = 0.5M_{\odot}$, and $P_{\text{orb}} = 15$ days.

The spin axis of m_0 precesses around $\hat{\mathbf{L}}_{\text{in}} = \hat{\mathbf{L}}$ according to

$$\frac{d\hat{\mathbf{S}}}{dt} = \Omega_{\text{ps}} \hat{\mathbf{L}} \times \hat{\mathbf{S}}, \quad (6.34)$$

where the symbol $\hat{\cdot}$ denotes unit vectors, and where the precession frequency Ω_{ps} is given by

$$\Omega_{\text{ps}} = -\frac{3Gm_1(I_3 - I_1) \cos \theta_{\text{sl}}}{2a_{\text{in}}^3 j^3 S}. \quad (6.35)$$

In Eq. (6.35), the spin-orbit angle is defined by $\cos \theta_{\text{sl}} = \hat{\mathbf{S}} \cdot \hat{\mathbf{L}}$, and $I_3 - I_1$ are the principle moments of inertia of m_0 .⁵

Meanwhile, the orbital axis of the inner binary precesses and nutates around the total orbital angular momentum axis $\mathbf{J} = \mathbf{L}_{\text{in}} + \mathbf{L}_{\text{out}}$, with frequency $\Omega_L = |d\hat{\mathbf{L}}/dt|$. In general, Ω_L is a complicated function of eccentricity, but takes the approximate form (Anderson et al., 2016).

$$\Omega_L \simeq \frac{3(1+4e^2)}{8t_k \sqrt{1-e^2}} |\sin 2I|. \quad (6.36)$$

Eq. (6.36) is exact at $e = 0$ and $e = e_{\text{max}}$. Both Ω_{ps} and Ω_L are strong functions of eccentricity, and thus can undergo large variation during a single LK cycle.

As described in Storch et al. (2014), the dynamical behavior of $\hat{\mathbf{S}}$ under the influence of a secondary body undergoing LK oscillations depends on the ratio $|\Omega_{\text{ps}}/\Omega_L|$. Here we summarize the key aspects of the dynamics (see also Storch & Lai 2015; Anderson et al. 2016):

If $|\Omega_{\text{ps}}| \ll |\Omega_L|$ throughout the LK cycle, denoted as the “non-adiabatic regime,” $\hat{\mathbf{S}}$ cannot “keep up” with $\hat{\mathbf{L}}$ as $\hat{\mathbf{L}}$ precesses around $\hat{\mathbf{J}}$. As a result, $\hat{\mathbf{S}}$

⁵There is also a spin-spin interaction, of order GQ_0Q_1/r^5 , where $Q_{0,1} = (J_2 mR^2)_{0,1}$ is the rotation-induced quadrupole moment. This is much smaller than the S - L terms, of order $GQ_{0,1}m_{1,0}/r^3$. In addition, spin-spin resonances may occur when the precession frequencies of the spin axes (Eq. [6.35]) become equal (Correia et al., 2016). However, although this latter effect is captured by our numerical integrations in Section 4, such spin-spin interactions do not play an important dynamical role in the systems of interest here.

effectively precesses around $\hat{\mathbf{J}}$, so that $\theta_{sj} \equiv \cos^{-1}(\hat{\mathbf{S}} \cdot \hat{\mathbf{J}}) \simeq \text{constant}$. On the other hand, if $|\Omega_{ps}| \gg |\Omega_L|$ throughout the LK cycle, denoted as the “adiabatic regime,” $\hat{\mathbf{S}}$ “follows” $\hat{\mathbf{L}}$, and the spin-orbit angle $\theta_{sl} \simeq \text{constant}$. Finally, if $|\Omega_{ps}| \sim |\Omega_L|$ at some point during the LK cycle, the dynamical behavior is complicated due to secular resonances, and chaotic evolution of $\hat{\mathbf{S}}$ can ensue (Storch & Lai, 2015). We denote this as the “trans-adiabatic regime.”

In some cases, inclusion of the backreaction torque from the oblate star on the orbit can considerably complicate this simple classification. In particular, our previous work, beginning with Storch et al. (2014), focused on systems in which the secondary member of the inner binary was a planet. In such cases, L_{in} and S are often comparable during the high-eccentricity phases of the LK cycles, and the backreaction torque from the oblate star on the orbit can be significant. In contrast, here we consider a stellar mass secondary body, so that $L_{\text{in}} \gg S$ is well satisfied. As a result, the torque on the orbital axis from the oblate star is negligible⁶, resulting in simplified behavior.

We introduce an “adiabaticity parameter” that characterizes the degree to which the stellar spin axis $\hat{\mathbf{S}}$ “follows” the precession of $\hat{\mathbf{L}}$ around $\hat{\mathbf{J}}$, defined as

$$\begin{aligned}\mathcal{A} &= \left| \frac{\Omega_{ps} t_k j^3}{\cos \theta_{sl}} \right| \\ &\simeq 58 \frac{\bar{k}_{q,0} \bar{m}_1 \bar{m}_{01}^{1/2} \bar{R}_0^3}{\bar{k}_* \bar{m}_0 \bar{m}_2} \left(\frac{P_*}{5 \text{ d}} \right)^{-1} \left(\frac{a_{\text{in}}}{0.1 \text{ AU}} \right)^{-9/2} \left(\frac{a_{\text{out,eff}}}{10 \text{ AU}} \right)^3.\end{aligned}\quad (6.37)$$

In Eq. (6.37), $k_* = S/m_0 R_0^2 \Omega_*$ describes the mass distribution of m_0 , which we set to $k_* = 0.06$ (Claret & Gimenez, 1992). See Section 6.2.1 for definitions and canonical values of the other quantities in Eq. (6.37). Since P_* , a_{in} , $a_{\text{out,eff}}$ can all span wide ranges, \mathcal{A} can vary by many orders of magnitude among possible

⁶However, note that, although the expression for $d\mathbf{L}_{\text{in}}/dt$ is negligible here, the oblate star still causes additional pericenter precession of the orbit.

types of hierarchical stellar triples.

Except for the $\sin 2I$ factor, \mathcal{A} is of order the ratio of $|\Omega_{\text{ps}}|$ and $|\Omega_L|$, both evaluated at $e = 0$. Note that the definition (6.37) differs from the adiabaticity parameter in Storch et al. (2014) and Storch & Lai (2015), and in Anderson et al. (2016). This “fuzziness” and multiple possible ways in defining such a parameter arises because, from a theoretical point of view, the dynamical behavior of the spin axis relative to $\hat{\mathbf{L}}$ depends on two distinct (but related) parameters, as shown by Storch et al. (2017). These two parameters relate to the LK-averaged stellar precession rate, and requires a knowledge of $e(t)$ during the LK cycle to evaluate. For this paper, our goal is to adopt an adiabaticity parameter that is convenient to evaluate for various triple systems, without requiring prior knowledge of $e(t)$.

If the adiabaticity parameter \mathcal{A} is greater than a critical value $\mathcal{A}_{\text{crit}}$, then the system is always in the “adiabatic regime” and θ_{sl} will undergo little variation. As a result, if the inner binary is formed with $\hat{\mathbf{S}}$ and $\hat{\mathbf{L}}$ aligned, then the spin-orbit angle θ_{sl} will remain small for all time. On the other hand, if $\mathcal{A} \lesssim \mathcal{A}_{\text{crit}}$, large spin-orbit misalignment is possible. In Section 6.4, we undertake numerical integrations to determine the behavior of the spin-orbit misalignment angle for different values of \mathcal{A} , and identify the value of $\mathcal{A}_{\text{crit}} \simeq 3$.

6.4 Numerical Experiments

6.4.1 Setup and Computational Procedure

In this section, we present numerical integrations of the full secular equations of motion of hierarchical stellar triples, and examine the maximum achieved eccentricity of the inner binary (e_{\max}) and maximum spin-orbit angle ($\theta_{\text{sl,max}}$) over the integration timespan. We include both the quadrupole and octupole terms for the inner and outer orbits, as well as the effects of SRFs on the inner orbit (pericenter precession due to GR, and tidal and rotational distortion of m_0 and m_1). The full equations of motion can be found in Liu et al. (2015). In the absence of octupole ($\varepsilon_{\text{oct}} = 0$), the evolution of the outer orbit consists of precession of the eccentricity vector \mathbf{e}_{out} (with e_{out} constant), and precession and nutation of $\hat{\mathbf{L}}_{\text{out}}$ around the fixed total angular momentum axis.

We simultaneously evolve the spin axis $\hat{\mathbf{S}}$ of m_0 due to the torque from m_1 , as well as the spin axis of m_1 due to the torque from m_0 (Eq. [6.34]). We also include the backreaction torques from both spins on the orbit. Each spin axis is always placed initially parallel to the orbital axis ($\theta_{\text{sl},0} = 0$). Both spin periods are given the same initial value (P_{\star}), and held constant throughout the integration. The spin-behavior of m_0 and m_1 is qualitatively identical for comparable mass binaries, and we only present results for m_0 (but consider the evolution of both spins in the numerical integrations).

Equal mass inner binaries (for which $\varepsilon_{\text{oct}} = 0$), and unequal mass inner binaries are considered separately, in Sections 6.4.2 and 6.4.3 respectively. In each case, we adopt a Monte Carlo approach, and generate a large number of sys-

tems with the stellar spin periods and orbital parameters uniformly sampled in the following ranges: $P_\star = 1 - 30$ days, $a_{\text{in}} = 0.1 - 1$ AU, $a_{\text{out}} = (10 - 1000)a_{\text{in}}$, $e_{\text{out}} = 0 - 0.9$, and $I_0 = 0^\circ - 180^\circ$. We conduct separate experiments for a stellar mass perturber ($m_2 = 1M_\odot$), and a brown dwarf perturber ($m_2 = 0.1M_\odot$). Systems that satisfy any of the following conditions are discarded:

1. To ensure stability, systems that do not satisfy

$$\frac{a_{\text{out}}}{a_{\text{in}}} > 2.8 \left(1 + \frac{m_2}{m_{01}}\right)^{2/5} \frac{(1 + e_{\text{out}})^{2/5}}{(1 - e_{\text{out}})^{6/5}} \left[1 - 0.3 \frac{I_0}{180^\circ}\right] \quad (6.38)$$

are rejected (Mardling & Aarseth, 2001).

2. In order to reduce the number of cases where the range of eccentricity variation is low (or where LK oscillations are completely suppressed), systems with limiting eccentricities that satisfy $e_{\text{lim}} < 0.3$ are rejected, where e_{lim} is determined by Eq. (6.26). As discussed in Section 6.2.3, for specified inner and outer binary properties, e_{max} depends on the mutual inclination I_0 , and e_{lim} is the maximum possible value of e_{max} , occurring at a critical inclination $I_{0,\text{lim}}$. Due to the full range of inclinations considered ($I_0 = 0^\circ - 180^\circ$), most systems will not be initialized with $I_0 \sim I_{0,\text{lim}}$, and will satisfy $e_{\text{max}} \ll e_{\text{lim}}$. Requiring that $e_{\text{lim}} \geq 0.3$ thus eliminates many systems that will never undergo excursions to high eccentricity.
3. We do not include the effects of tidal dissipation in the inner binary. This is justifiable because the focus of this paper is on binaries with pericenter distances large enough such that tidal dissipation has not occurred, thereby preserving the initial semi-major axis of the system. However, some systems do achieve pericenter distances small enough such that changes in both the orbital and spin angular momentum will occur. As discussed in

Anderson et al. (2016), the tidal decay rate in a system undergoing LK oscillations (starting from $e_0 \simeq 0$) is reduced by roughly a factor $\sim \sqrt{1 - e_{\max}^2}$ (see also Petrovich, 2015b, for a discussion of the orbital decay rate in LK systems). The decay rate of the semi-major axis in a solar-type inner binary undergoing LK oscillations with maximum eccentricity e_{\max} can be approximated by

$$\left| \frac{1}{a_{\text{in}}} \frac{da_{\text{in}}}{dt} \right|_{\text{Tide,Lk}} \sim \frac{1.3 \times 10^{-10}}{\text{yr}} \frac{\bar{m}_1 \bar{m}_{01} \bar{R}_0^5}{\bar{m}_0 \bar{a}_{\text{in}}} \times \left(\frac{\Delta t_{\text{lag}}}{0.1 \text{ s}} \right) \left(\frac{a_F}{0.08 \text{ AU}} \right)^{-7}, \quad (6.39)$$

(Anderson et al. 2016), where the equilibrium tide model was assumed (Darwin, 1880; Singer, 1968; Alexander, 1973; Hut, 1981), Δt_{lag} is the (constant) tidal lag time, and we have defined

$$a_F \equiv a_{\text{in}}(1 - e_{\max}^2). \quad (6.40)$$

The timescale for changing the spin rate of m_0 due to tides is roughly

$$\left| \frac{1}{S} \frac{dS}{dt} \right|_{\text{Tide,LK}} \sim \frac{3 \times 10^{-9}}{\text{yr}} \frac{\bar{m}_1^2 \bar{m}_{01}^{1/2} \bar{R}_0^3}{\bar{m}_0 \bar{a}_{\text{in}}^2} \left(\frac{P_\star}{10 \text{ days}} \right) \times \left(\frac{\Delta t_{\text{lag}}}{0.1 \text{ s}} \right) \left(\frac{a_F}{0.08 \text{ AU}} \right)^{-11/2}. \quad (6.41)$$

This also gives the timescale that tidal dissipation changes the spin-orbit misalignment angle. Systems where this timescale is shorter than $\sim 10^9$ years are affected by tides in terms of their stellar obliquities. We therefore discard systems that achieved $a_{\text{in}}(1 - e_{\max}^2)$ satisfying

$$a_{\text{in}}(1 - e_{\max}^2) < 0.08 \text{ AU}. \quad (6.42)$$

Although this numerical choice is somewhat arbitrary, we have experimented with slightly higher and lower values, and do not find an appreciable effect on our results. Note Eq. (6.42) corresponds to rejecting

systems that achieve pericenter distances in the range $0.04 \text{ AU} \lesssim a_{\text{in}}(1 - e_{\text{max}}) \lesssim 0.08 \text{ AU}$. As a result, adopting the rejection condition in Eq. (6.42) automatically removes systems that are tidally disrupted, i.e. those systems with pericenter distances less than the tidal disruption radius

$$a(1 - e_{\text{max}}) \lesssim 2.5R_0 \left(\frac{m_{01}}{m_0} \right)^{1/3} \simeq 0.01 \text{ AU}. \quad (6.43)$$

For each combination of (m_0, m_1) and m_2 , we generate an initial sample of triples large enough such that, after applying the immediate rejection conditions (i) and (ii), ~ 2000 systems remain. We then integrate each system for a timespan $10^3 t_k$ (in Section 6.4.2), and $30t_k/\varepsilon_{\text{oct}}$ (in Section 6.4.3), and discard any systems that satisfy Eq. (6.42). We record the maximum eccentricity (e_{max}), and the maximum spin-orbit angle ($\theta_{\text{sl,max}}$) achieved over the entire integration.

6.4.2 Equal Mass Inner Binary

To start, we focus on equal mass inner binaries ($m_0 = m_1 = 1M_\odot$), so that $\varepsilon_{\text{oct}} = 0$. In this situation, the maximum achievable eccentricity is specified by the algebraic expression Eq. (6.24).

After discarding systems that were expected to have undergone tidal dissipation, we are left with 1779 and 1742 systems with a stellar and brown dwarf outer companion respectively. These systems have initial angular momentum ratios (see Eq. 6.6) in the range $\eta \sim 0.04 - 0.2$ for the solar-mass tertiary, and $\eta \sim 0.5 - 1.9$ for the brown dwarf tertiary ($m_2 = 0.1M_\odot$). Therefore, triples with stellar mass tertiaries can sometimes be qualitatively understood by the test-particle approximation ($\eta = 0$), whereas the brown dwarf tertiary cannot

(however, the dynamical effects of the inner orbit on the outer orbit are always included in our numerical integrations, regardless of perturber mass).

As discussed in Section 6.3, the qualitative behavior of the spin axis of m_0 , due to the forcing of m_1 depends on the “adiabaticity parameter” \mathcal{A} (see Eq. [6.37]). When \mathcal{A} is greater than a critical value $\mathcal{A}_{\text{crit}}$, the evolution of the spin-axis is strongly coupled to the orbital evolution, and the spin-orbit angle $\theta_{\text{sl}} \simeq \text{constant}$. Thus, for systems that begin with $\hat{\mathbf{S}}$ and $\hat{\mathbf{L}}$ aligned, generating spin-orbit misalignment requires that $\mathcal{A} \lesssim \mathcal{A}_{\text{crit}}$. Here we identify the numerical value of $\mathcal{A}_{\text{crit}}$.

Results of our numerical integrations are depicted in Fig. 6.7. Given the wide ranges in orbital geometries and stellar spin rates sampled, the maximum eccentricities range from $e_{\text{max}} \simeq 0 - 0.96$, and \mathcal{A} varies by 5 – 6 orders of magnitude. The results in Fig. 6.7 can be qualitatively understood using the arguments presented in Section 3:

(i) For $\mathcal{A} \lesssim 0.1$, the system is in the non-adiabatic regime (see Section 3), and the precession rate of $\hat{\mathbf{S}}$ around $\hat{\mathbf{L}}_{\text{in}}$ is slow compared to the precession of $\hat{\mathbf{L}}_{\text{in}}$ around the total angular momentum axis $\hat{\mathbf{J}}$. As a result, $\hat{\mathbf{S}}$ effectively precesses around $\hat{\mathbf{J}}$. If any nutation of $\hat{\mathbf{L}}_{\text{in}}$ relative to $\hat{\mathbf{J}}$ is neglected, the maximum possible spin-orbit misalignment is approximately $\sim 2I_0$. We have confirmed that for $\mathcal{A} \lesssim 0.1$, $\theta_{\text{sl,max}} \simeq 2I_0$.

(ii) For $0.1 \lesssim \mathcal{A} \lesssim 3$, the evolution of the system is trans-adiabatic (and often chaotic), and $\theta_{\text{sl,max}}$ can momentarily reach 180° .

(iii) Systems that satisfy $\mathcal{A} \gtrsim 3$ all maintain low spin-orbit misalignment for the entire integration timespan (with $\theta_{\text{sl,max}} \lesssim 30^\circ$). This is in spite of the fact that

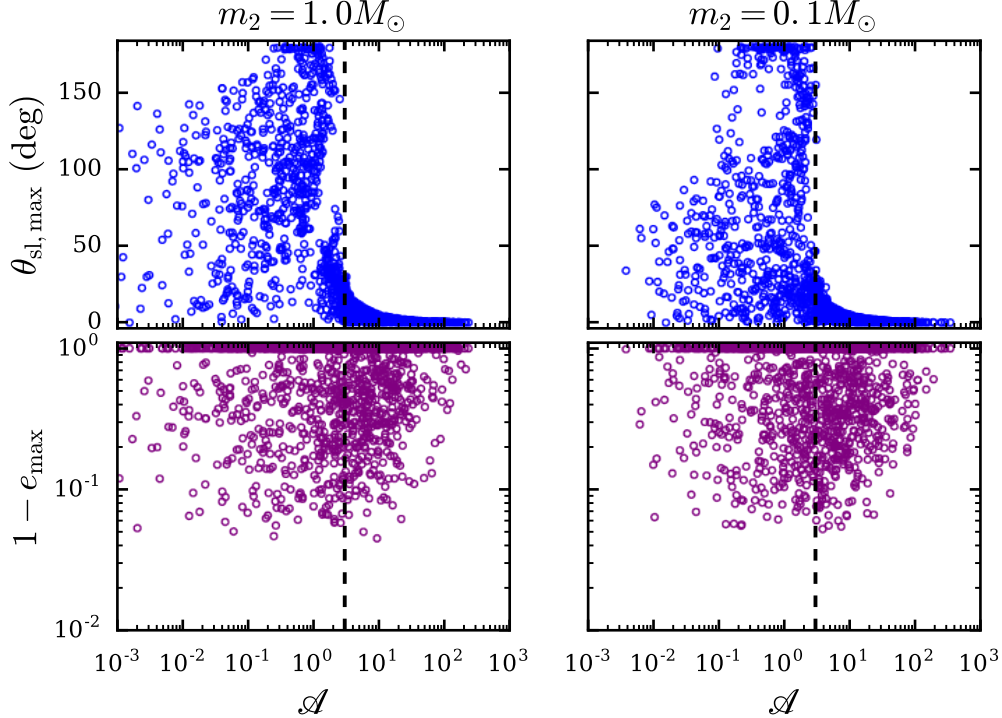


Figure 6.7: Maximum spin-orbit angle θ_{sl} and eccentricity e_{max} of the inner binary as a function of the adiabaticity parameter, defined in Eq. (6.37). The results are obtained by numerical integrations of systems with an equal mass inner binary ($m_0 = m_1 = 1M_\odot$), and other parameters randomly sampled as follows: $P_* = 1 - 30$ days, $a_{\text{in}} = 0.1 - 1$ AU, $a_{\text{out}} = (10 - 1000)a_{\text{in}}$, $e_{\text{out}} = 0 - 0.9$, and $I_0 = 0^\circ - 180^\circ$. Lefthand panels show results for a stellar mass ($m_2 = 1M_\odot$) tertiary, and righthand panels show results for a brown-dwarf tertiary ($m_2 = 0.1M_\odot$). We integrated each system for a period of $10^3 t_k$. Systems with $\mathcal{A} \gtrsim 3$ maintain low spin-orbit misalignment for the entire integration span (top panels), despite undergoing substantial eccentricity variation (bottom panels).

many of these systems reached sufficiently high eccentricities (see the bottom panels of Fig. 6.7) such that the change in orbital inclination is also large. Note that the transition from trans-adiabatic to fully adiabatic evolution, in terms of \mathcal{A} , occurs abruptly (see also Storch et al., 2014; Storch & Lai, 2015).

We conclude from these experiments that a reasonable estimate is $\mathcal{A}_{\text{crit}} \simeq 3$. In order to for substantial spin-orbit misalignment to be generated, the inner

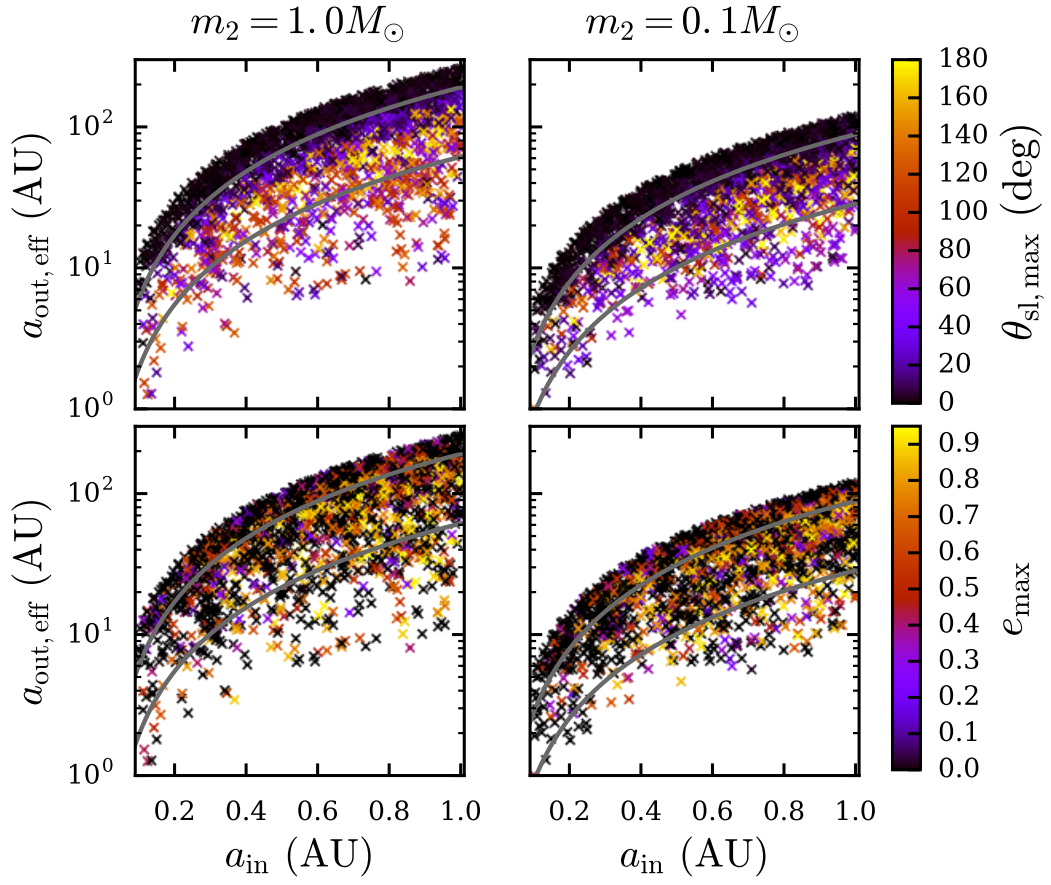


Figure 6.8: Orbital parameters $a_{\text{out,eff}} = a_{\text{out}}\sqrt{1 - e_{\text{out}}^2}$ versus a_{in} for the same sets of triples as in Fig. 6.7. The colors indicate the value of $\theta_{\text{sl,max}}$ (top panels), and e_{max} (bottom panels). We plot curves of constant $\mathcal{A} = 3$ for reference (see Eq. [6.37]), with two stellar spin periods selected ($P_\star = 1, 30$ days, grey curves from bottom to top).

and outer binaries must have parameters (i.e. $P_\star, a_{\text{in}}, a_{\text{out,eff}}$; see Eq. [6.37]) such that $\mathcal{A} \lesssim 3$ is satisfied.

Figure 6.8 depicts the results of the same experiments as shown in Fig. 6.7, in terms of the parameter space $(a_{\text{in}}, a_{\text{out,eff}})$ that we have sampled, with $\theta_{\text{sl,max}}$ and e_{max} indicated by the color. For a fixed a_{in} and P_\star , it is clear that in order to generate substantial spin-orbit misalignment, the perturber must have a sufficiently small effective separation $a_{\text{out,eff}}$ so that the orbital precession is fast compared to

the spin axis precession. Indeed, from Eq. (6.37), the condition $\mathcal{A} \lesssim 3$ translates into

$$\frac{a_{\text{out,eff}}}{\bar{m}_2^{1/3}} \lesssim 3.7 \text{ AU} \left(\frac{\bar{m}_0}{\bar{m}_1 \bar{m}_{01}^{1/2} \bar{R}_0^3} \right)^{1/3} \left(\frac{a_{\text{in}}}{0.1 \text{ AU}} \right)^{3/2} \left(\frac{P_\star}{5 \text{ d}} \right)^{1/3}. \quad (6.44)$$

6.4.3 Unequal Mass Inner Binary: Octupole Results

Next we consider unequal mass inner binaries, with $m_0 = 1M_\odot$ and $m_1 = 0.5M_\odot$. If the octupole potential of the tertiary companion is non-vanishing, i.e. if $\varepsilon_{\text{oct}} \neq 0$ (which occurs if $m_0 \neq m_1$ and $e_{\text{out}} \neq 0$), the eccentricity of the inner binary can undergo excursions to more extreme values, and under some conditions the orbital inclination can flip (cross 90°). The orbital dynamics can be considerably more complicated compared to systems with only the quadrupole potential included. Here, we examine whether the results of Section 6.4.2 remain valid for non-zero ε_{oct} .

First, we show how the maximum eccentricity is affected. With $\varepsilon_{\text{oct}} \neq 0$, e_{max} is no longer specified by Eq. (6.24), and determining e_{max} always requires full numerical integrations. Liu et al. (2015) showed that when considering systems with octupole and SRFs, the maximum achieved eccentricity e_{max} depends on both I_0 and ε_{oct} , but that e_{max} does not exceed the quadrupole limiting eccentricity e_{lim} , as determined by Eq. (6.26). In other words, even with octupole included, $e_{\text{max}} \leq e_{\text{lim}}$. We have confirmed this finding through numerical integrations of the full secular equations of motion (including SRFs). To demonstrate, Fig. 6.9 shows the maximum achieved eccentricity over the integration timespan versus the initial inclination (see also Liu et al., 2015, for similar results), for the two fiducial values of the perturber mass. In these examples, the

inner binary orbital period is fixed at $P_{\text{in}} = 15$ days, and the orbital parameters chosen so that $\varepsilon_{\text{oct}} = 0.01$, and $a_{\text{out,eff}}/\bar{m}_2^{1/3} \simeq 6.28$ AU. We confirm that e_{max} can have a complicated dependence on I_0 , especially if $\eta \sim 1$ (bottom panel). In Fig. 6.9, e_{max} at $I_0 = 0$ can be calculated using the result of Section 2.4. The spike in the lower panel (around $I_0 \sim 30^\circ$) may be the result of a secular resonance, but a detailed characterization is beyond the scope of this paper. In general, the degree of deviation of e_{max} (with octupole) from the quadrupole prediction depends on ε_{oct} , as well as on the relative “strengths” of the SRFs (ε_{GR} , and $\varepsilon_{\text{Tide}}$)⁷. We do not attempt to characterize this behavior here (see Liu et al. 2015 for such a characterization in the test-mass limit [$m_1 \ll m_0, m_2$]), and simply present Fig. 6.9 as illustrative examples. Despite the complicated dependence of e_{max} on inclination, Fig. 6.9 shows that e_{max} does not exceed e_{lim} .

To check whether this result is robust across a wide variety of systems, we repeat the previous Monte Carlo experiment conducted in Section 6.4.2 with $m_0 = 1M_\odot$ and $m_1 = 0.5M_\odot$. All other parameters are sampled identically, with the additional selection criterion that $\varepsilon_{\text{oct}} > 0.001$. We integrate each system for $\sim 30t_{\text{k}}/\varepsilon_{\text{oct}}$, i.e. ~ 30 octupole LK timescales. In Fig. 6.10 we plot $e_{\text{max}}/e_{\text{lim}}$ versus ε_{oct} , where e_{max} is the maximum eccentricity achieved over the entire numerical integration timespan, while e_{lim} is calculated from Eq. (6.26). Inspection of Fig. 6.10 reveals that $e_{\text{max}} \leq e_{\text{lim}}$. As a result, while knowledge of e_{max} for an arbitrary inclination require a full numerical integration, the algebraic expression for the upper limit on e_{max} (Eq. [6.26]) remains valid for systems with non-zero octupole terms.

Second, we examine whether the adiabaticity parameter \mathcal{A} remains a useful

⁷Although the effects of SRFs generally suppress e_{max} , under some circumstances, including the effects of GR precession can give rise to eccentricity excitation, yielding e_{max} that is much higher relative to the case without GR precession included (Ford et al., 2000; Naoz et al., 2013b).

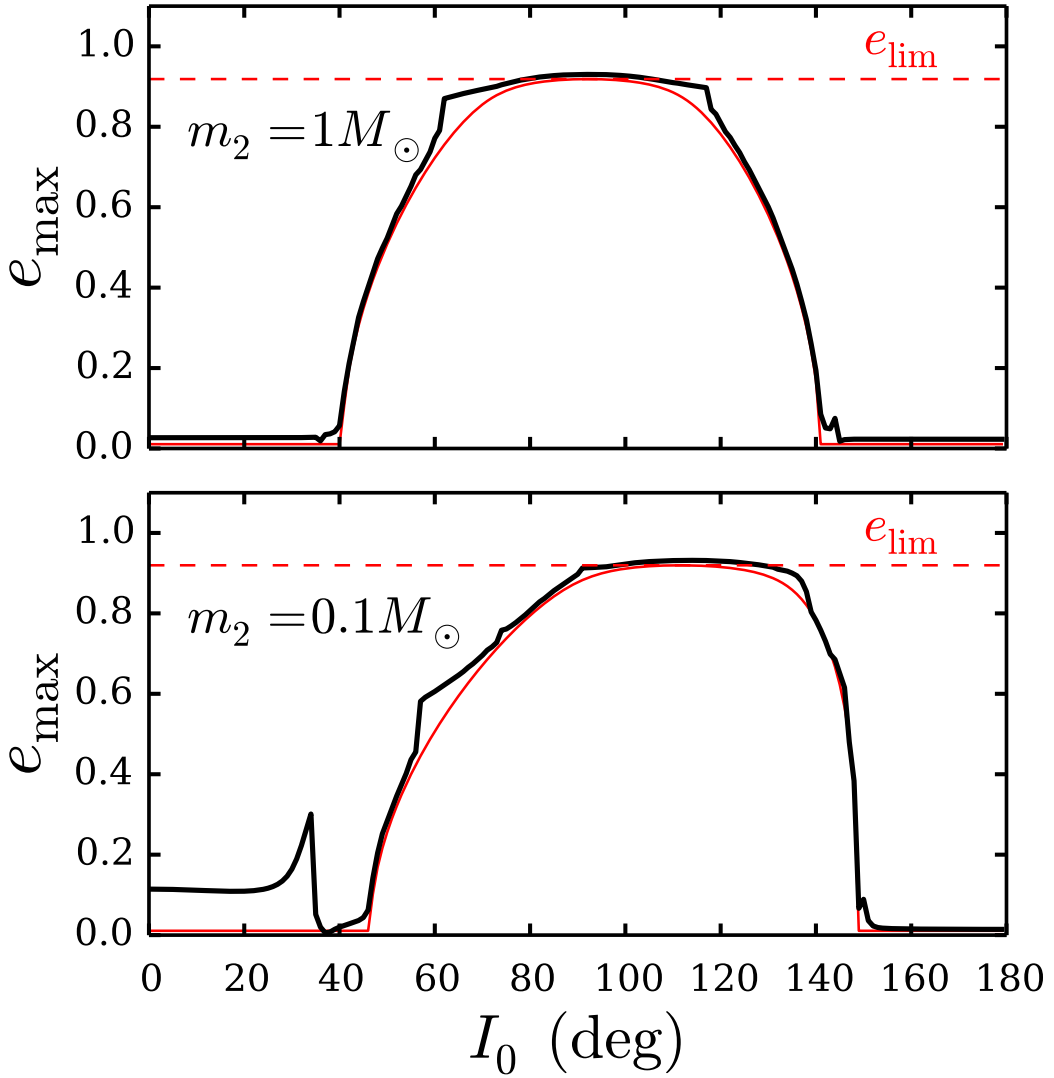


Figure 6.9: Maximum eccentricity e_{\max} achieved over the integration timespan (black curves), compared to the algebraically-determined quadrupole estimate (red curves) from Eq. (6.24). The numerical integrations include quadrupole + octupole contributions, stellar spin-orbit coupling, and all SRFs. Results are depicted for a stellar mass perturber (top panel), and a brown-dwarf perturber (bottom panel). To illustrate the role of the angular momentum ratio η in determining e_{\max} , we have fixed $\varepsilon_{\text{oct}} = 0.01$, as well as the quantity $a_{\text{out,eff}}/\bar{m}_2^{1/3} \simeq 6.28$ AU for both panels. The top panels have $a_{\text{out}} \simeq 10.3$ AU, $e_{\text{out}} \simeq 0.79$, and the bottom panels have $a_{\text{out}} \simeq 3.4$ AU, $e_{\text{out}} \simeq 0.51$. Other parameters (identical for both panels) are: $m_0 = 1M_\odot$, $m_1 = 0.5M_\odot$, $P_{\text{orb}} = 15$ days, $P_* = 10$ days, $\omega_{\text{in}} = 0$, $\Omega_{\text{in}} = 0$, $\omega_{\text{out}} = 0$.

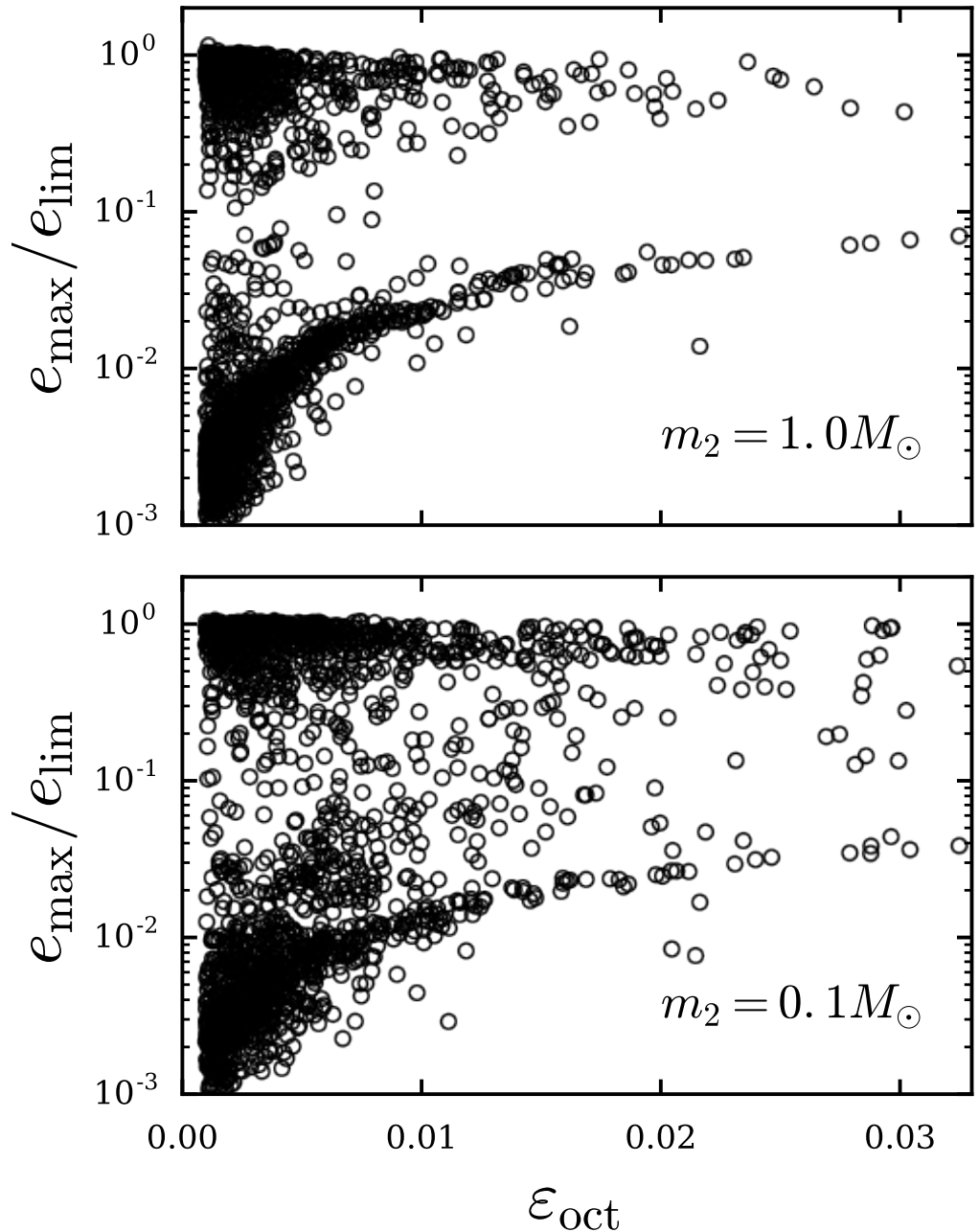


Figure 6.10: Maximum eccentricity e_{\max} achieved over the integration timespan, compared to the analytically determined (quadrupole) limiting eccentricity e_{\lim} . For a given value of ε_{oct} , a wide range of e_{\max}/e_{\lim} is achieved depending on the chosen orbital configuration, but $e_{\max}/e_{\lim} \leq 1$ is always satisfied.

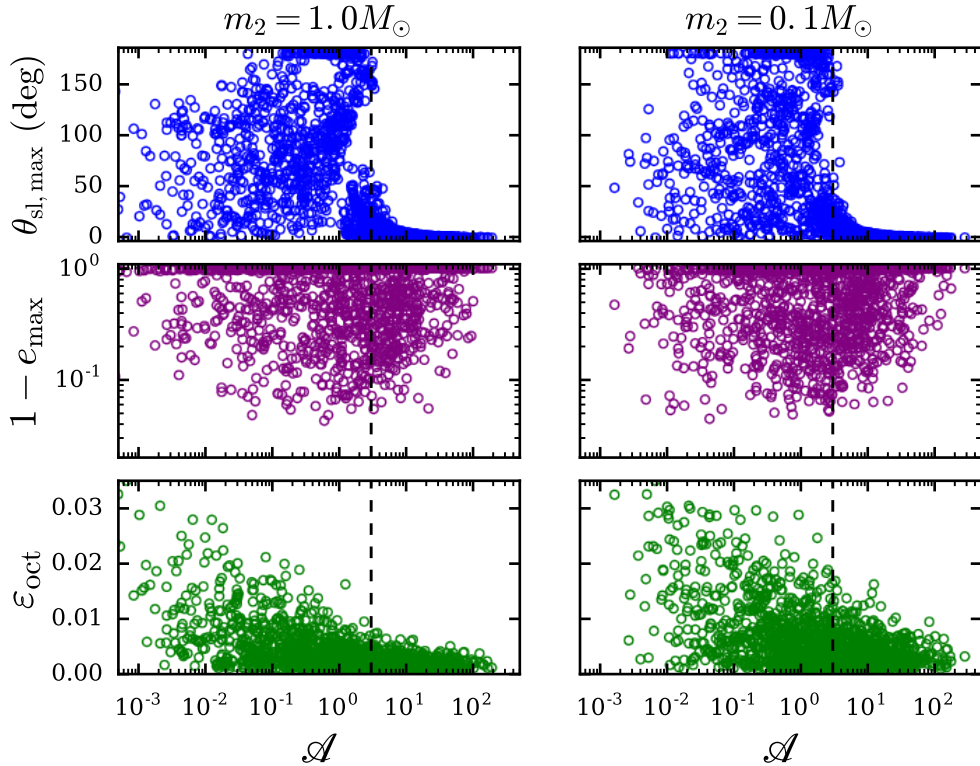


Figure 6.11: Same experiment as depicted in Fig. 6.7, except that the inner binary has unequal mass ($m_0 = 1M_\odot$, $m_1 = 0.5M_\odot$), so that $\varepsilon_{\text{oct}} \neq 0$ (shown in the bottom panel). Same set of simulations as in Fig. 6.10. As found previously (for $\varepsilon_{\text{oct}} = 0$), systems with $\mathcal{A} \gtrsim 3$ all maintain low spin-orbit misalignment for the entire integration.

quantity in predicting the ability to generate spin-orbit misalignment. The results are shown in Fig. 6.11 (compare with Fig. 6.7). We find again that systems with $\mathcal{A} > A_{\text{crit}} \simeq 3$ all maintain low spin-orbit misalignment, while systems with $\mathcal{A} \lesssim 3$ do not. A possible reason is that systems with the largest ε_{oct} tend to have $\mathcal{A} \lesssim 3$ (due to the strong dependence of \mathcal{A} on $a_{\text{out,eff}}$), and therefore lie in the non-adiabatic (low \mathcal{A}) regime. As a result, octupole-level dynamics do not affect the existence or numerical value of A_{crit} , because the octupole contribution for systems near A_{crit} is negligible.

To summarize Sections 6.4.2 and 6.4.3: By conducting a series of numerical integrations, with orbital parameters and stellar spin periods sampled over wide ranges, and considering both a solar-mass and brown dwarf tertiary companion, we have identified a condition necessary for generating substantial spin-orbit misalignment ($\theta_{\text{sl}} \gtrsim 30^\circ$) of the inner binary. The orbital geometries of the inner and outer binaries ($a_{\text{in}}, a_{\text{out,eff}}$), and the stellar spin period (P_*) must satisfy $\mathcal{A} \lesssim 3$, where \mathcal{A} is given in Eq. (6.37). This result also holds for $\varepsilon_{\text{oct}} \neq 0$. We have also shown that the maximum achieved eccentricity of the inner binary in systems with octupole never exceeds the quadrupole limiting value, as determined by the algebraic expression in Eq. (6.26). Therefore, the analytical results in Section 2.3, constraining the maximum perturber distance capable of raising the eccentricity from $e \sim 0$ to e_{obs} (through LK oscillations), remain valid for $\varepsilon_{\text{oct}} \neq 0$.

Taken together, these findings shed insight into the dynamical behavior of hierarchical stellar triples, without undertaking full numerical integrations.

6.5 Application: DI Herculis

As an application of the results presented in previous sections, we consider the eclipsing binary DI Herculis. DI Herculis consists of two B stars, with masses $m_0 = 5.15M_\odot$ and $m_1 = 4.52M_\odot$, orbital period $P \simeq 10.55$ days, and eccentricity $e \simeq 0.49$ (Popper, 1982). DI Herculis has been an object of interest, due to an observed pericenter precession rate too low compared with predicted rate due to general relativity (Martynov & Khaliullin, 1980). Both the primary and secondary components of this system were recently confirmed to have signif-

icant projected spin-orbit misalignments (Albrecht et al., 2009), leading to an additional source of precession (with the opposite direction compared to GR), thereby resolving the anomalously low observed rate. The projected obliquity of the primary is $\lambda_{\text{pri}} \simeq 72^\circ$ and that of the secondary is $\lambda_{\text{sec}} \simeq -84^\circ$. Here, we consider the possibility that the large obliquities and eccentricity arose from secular perturbations from an undetected tertiary companion, and provide constraints that the hypothetical companion must satisfy.

If a tertiary companion is responsible for raising the eccentricity from ~ 0 to the observed value $e_{\text{obs}} \simeq 0.5$, then the LK maximum eccentricity must satisfy $e_{\text{max}} \gtrsim 0.5$. Considering ranges of inclinations and semi-major axes for hypothetical perturbers, the colormap in Fig. 6.12 shows the analytically-determined maximum eccentricity, calculated using the procedure described in Section 2. To ensure that the analytic treatment properly captures the dynamics of DI Herculis, we have also undertaken full numerical integrations, depicted as solid circles. In the analytic determination of e_{max} (Section 2), we have considered the SRF contributions from GR, along with tidal and rotation distortion of both m_0 and m_1 . In contrast to solar-type stars, effects of rotational distortion are important in both members of DI Herculis, because the large radii and rapid rotation rates lead to large rotation-induced quadrupole moments. Recall that rotational distortion may only be incorporated in the analytic treatment of the LK maximum eccentricity in an approximate manner, and in Section 2 alignment of the rotation and orbital axes was assumed. A precise determination of e_{max} thus requires full numerical integrations over a large number of LK cycles. Despite the approximation of aligned spin and orbital axes, the analytic treatment is in near perfect agreement with results from numerical integrations.

Inspecting Fig. 6.12, a solar-mass perturber must be located within ~ 12 AU, with a wide range of possible inclinations. In contrast, the required properties of a brown dwarf perturber are much more restrictive. A brown dwarf perturber must be located within ~ 5 AU in a retrograde orbit. Different choices for the outer binary’s eccentricity will modify these constraints. However, given that $m_0 \simeq m_1$, the DI Herculis system is unlikely to be significantly affected by octupole contributions, so the perturber’s eccentricity can be absorbed into the definition of the “effective” semi-major axis $a_{\text{out,eff}} = a_{\text{out}} \sqrt{1 - e_{\text{out}}^2}$ (unless the angular momentum ratio satisfies $\eta \gtrsim 1$).

If a tertiary companion is responsible for raising the spin-orbit angle of either member of DI Herculis from ~ 0 to the observed values, the adiabaticity parameter must satisfy $\mathcal{A} \lesssim 3$ (see Sections 3 and 4, and Eq. [6.37]). The rapid rotation rates of both stars ($v \sin i > 100$ km s $^{-1}$), combined with the large stellar radii, implies that a perturber must be extremely close and/or massive to achieve $\mathcal{A} \lesssim 3$. Figure 6.13 depicts the combinations of m_2 and $a_{\text{out,eff}}$ that lead to $\mathcal{A} < 3$ for the primary member (shaded region). Note that we have assumed a primary stellar spin period $P_\star = 1.25$ days – this rapid rotation rate is consistent with the observed $v \sin i$, and the estimated value by Philippov & Rafikov (2013) using gravity darkening. Inspecting Fig. 6.13, we see that a perturber with $m_2 \sim 1M_\odot$ must have an effective separation $a_{\text{out,eff}} \lesssim 3$ AU, and if $m_2 \sim 0.1M_\odot$, $a_{\text{out,eff}} \lesssim 1$ AU. Note that such triple systems are only marginally stable – the Mardling & Aarseth (2001) stability criterion (see Eq. 6.38) yields a minimum separation of $a_{\text{out}} \sim 1$ AU.

The requirement that a solar-mass perturber be located within ~ 3 AU in order to generate the observed spin-orbit misalignment may be problematic,

given that no additional bodies have been observed. A low-mass (e.g. brown dwarf) perturber is much more compelling than a solar-mass perturber, because it is more likely to have hitherto escaped detection. However, the requirement that it be located within ~ 1 AU would place it uncomfortably close to the stability limit.

To summarize: we have considered the possibility that the observed eccentricity and/or spin-orbit misalignment in the DI Herculis system result from secular perturbations from a tertiary companion. The perturber must be located within $\sim 5 - 15$ AU to generate the observed eccentricity. The constraints on based on the obliquity are much more stringent, and the perturber must be located within $\sim 1 - 3$ AU (depending on perturber mass), very close to the stability limit.

6.6 Conclusion

6.6.1 Summary of Key Results

This paper has examined the secular dynamics of hierarchical stellar triples, with the goal of identifying the requirements for the tertiary body to induce spin-orbit misalignment and/or eccentricity in the inner binary through Lidov-Kozai cycles in concert with stellar spin-orbit coupling. We have considered the orbital evolution of both the inner and outer binaries, combined with the dynamics of mutual spin-orbit nodal precession, as well as pericenter precession from various short range-forces (SRFs), such as general relativity and stellar tides. The results of this paper allow constraints to be placed on hidden tertiary

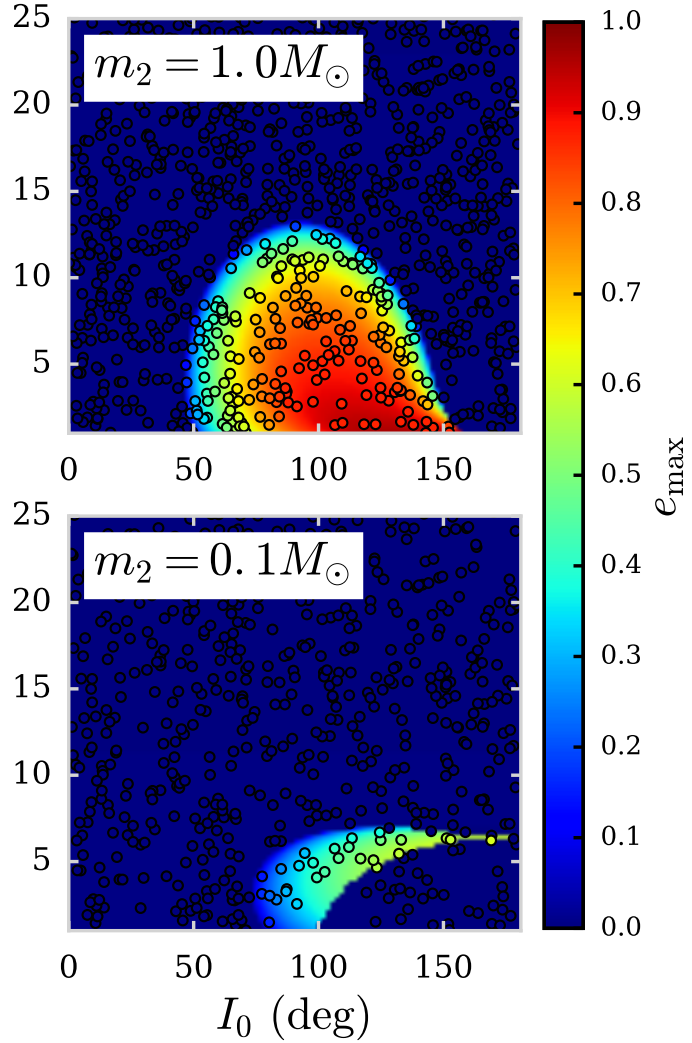


Figure 6.12: Similar to Fig. 6.4, but applied to the DI Herculis system, which has an inner binary with $m_0 \simeq 5.15M_{\odot}$, $m_1 \simeq 4.52M_{\odot}$, eccentricity $e_{\text{obs}} \sim 0.5$, $P_{\text{orb}} \simeq 10.55$ days, and estimated spin periods of $P_{\star} \sim 1$ day. In order for the eccentricity of DI Herculis to have been increased from ~ 0 to 0.5 by LK cycles from a tertiary companion, the LK maximum eccentricity must satisfy $e_{\text{max}} \geq e_{\text{obs}} \simeq 0.5$. We show results for a stellar mass and brown dwarf perturber, as labeled, and have set $e_{\text{out}} = 0$ in this example. The colored circles depict the results of numerical integrations of the full equations of motion, as discussed in Section 6.4. The colormap depicts the analytic estimate of e_{max} as discussed in Sections 6.2.2 and 6.2.3. In order to produce the observed eccentricity, a brown-dwarf perturber must be in a retrograde orbit.

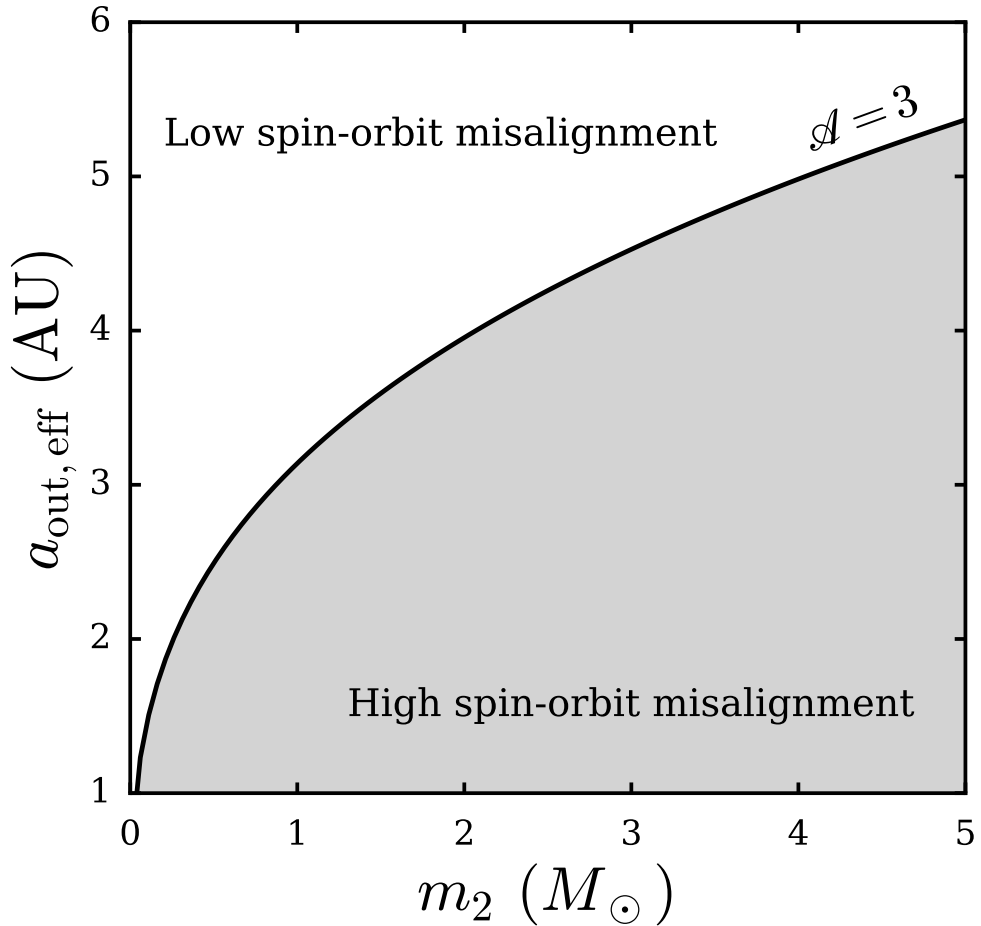


Figure 6.13: Required effective separation $a_{\text{out,eff}} = a_{\text{out}} \sqrt{1 - e_{\text{out}}^2}$ versus mass of a tertiary companion m_2 in the DI Herculis system, to generate the large inferred spin-orbit misalignment of the primary member. In order to produce the misalignment, the inner and outer binaries must satisfy $\mathcal{A} \lesssim 3$, as indicated by the shaded region. As a result, the outer binary must have $a_{\text{out,eff}} \lesssim 1 - 5$ AU, depending on the tertiary mass. Note that the minimum semi-major axis necessary for stability is (~ 1 AU, Mardling & Aarseth, 2001).

companions in stellar binaries that exhibit spin-orbit misalignment or eccentricity. The key results of this paper are:

- We derive new analytic expressions for the maximum eccentricity achieved by the inner binary (Eq. [6.24]) and the “LK window” for eccentricity excitation (see Eqs. [6.19], [6.23], and Fig. 6.1) due to the secular quadrupolar forcing of an external companion. The quadrupole approximation is exact when the inner binary has equal masses, or when the outer binary orbit is circular. Note that these calculations assume an initial inner binary eccentricity $e_0 \simeq 0$. Our expressions for e_{\max} and the LK window are valid for general masses of the triples and include the effects of SRFs. Our analysis generalizes previous work, which was restricted to small mass ratios and/or neglect SRFs. These results shed light on the dynamical behaviors of hierarchical triples with a wide range of parameters, without undertaking full numerical integrations.
- For an observed binary system with eccentricity e_{obs} , constraints on unseen tertiary companions can be made, by requiring $e_{\max} \geq e_{\text{obs}}$, assuming the inner binary has an initial eccentricity $e_0 \simeq 0$. Although the assumption $e_0 \simeq 0$ may not always hold (since the inner binary may form with a range of eccentricities), this constraint ($e_{\text{obs}} \leq e_{\max}$) nonetheless provides useful information on the required masses and separation of an undetected tertiary companion (see Section 6.2.4). See Appendix B for a brief consideration of $e_0 \neq 0$.
- In cases where the octupole contribution is important (when $m_0 \neq m_1$ and $e_{\text{out}} \neq 0$), we carry out numerical experiments to determine e_{\max} (see Figs. 6.9 and 6.10). As first noted by Liu et al. (2015), and confirmed in this paper under general conditions (e.g., arbitrary mass ratios for the hierarchical triples), the maximum eccentricity (with octupole) never exceeds the analytic quadrupole

limiting eccentricity e_{lim} (see Section 6.2.3, Eq. [6.26]). Without octupole this limiting eccentricity is only achieved ($e_{\text{max}} = e_{\text{lim}}$) at a specific value of the initial inclination $I_{0,\text{lim}} \geq 90^\circ$ (see Eq. [6.25]), but including octupole allows $e_{\text{max}} = e_{\text{lim}}$ to be realized for a wider range of inclinations. Since $e_{\text{max}} \leq e_{\text{lim}}$, constraints can be placed on the required perturber properties ($m_2, a_{\text{out}}, e_{\text{out}}$) needed to generate eccentricity even in systems with octupole contributions, without undertaking numerical integrations.

- From numerical integration of the full secular equations of motion (including the dynamics of the orbits and stellar spins) for a variety of triples and stellar parameters, we have identified a robust, necessary condition for generating spin-orbit misalignment in the inner binary due to perturbations from a tertiary companion: Large ($\gtrsim 30^\circ$) misalignment can be generated only if the stellar masses, spin period, and the orbital parameters of the triples are such that the “adiabaticity parameter” \mathcal{A} , defined by Eq. (6.37), satisfies $\mathcal{A} \lesssim 3$ (see Figs. 6.7 and 6.11).

Physically, \mathcal{A} is the ratio of the precession rate of the stellar spin (driven by the secondary) and the orbital precession rate of the inner binary (driven by the tertiary), evaluated at inner binary zero eccentricity. This finding ($\mathcal{A} \lesssim 3$ for producing misalignment) holds across wide ranges of orbital architectures and stellar spin periods. Although theoretical work on spin-orbit dynamics in binaries undergoing LK oscillations shows that the dynamics of the spin axis depends on more than a single parameter (Storch et al., 2017), we find empirically that $\mathcal{A} \lesssim 3$ is highly effective in predicting whether large spin-orbit misalignment will occur, and has the advantage that it is easily evaluated for observed binaries. For a specified inner binary separation, $\mathcal{A} \lesssim 3$ translates

into the requirement that the outer binary must have a small effective separation $a_{\text{out,eff}} = a_{\text{out}} \sqrt{1 - e_{\text{out}}^2}$, and/or the stellar rotation period must be short (see Fig. 6.8). Although the main focus of this paper has been on inclined tertiary companions, we note that nearly coplanar tertiaries can also increase spin-orbit misalignment and eccentricity, provided that the outer orbit is sufficiently eccentric, and the adiabaticity parameter satisfies $\mathcal{A} \sim 3$.

- In Section 5 we apply our general results to the eclipsing binary system DI Herculis, and identify the properties that an undetected tertiary companion must satisfy, in order to be responsible for the observed eccentricity and spin-orbit misalignments.

6.6.2 Discussion

As noted in Section 1, this paper has neglected the effects of tidal dissipation in the inner binary. Therefore, when applying our results (analytic expressions and various constraints) to observed binaries, it is important to make sure that the system under consideration has a sufficiently large pericenter distance so that its eccentricity and spin-orbit misalignment angle have not been affected by tidal dissipation within the lifetime of the system.

Another physical effect ignored in this paper is stellar spin-down by magnetic braking. Our previous works (Storch et al., 2014; Anderson et al., 2016) have shown that stellar spin-down can significantly influence the final spin-orbit misalignments of hot Jupiter systems formed through Lidov-Kozai migration. Although the integration timespans considered in this paper have been sufficiently short so that $P_* = \text{constant}$ is a valid approximation, the decrease in

the stellar spin rate over Gyr timescales could be significant (depending on stellar type), and can reduce \mathcal{A} by ~ 10 for solar-mass stars. As stellar spindown takes place, the adiabaticity parameter may cross $\mathcal{A} \sim 3$, so that substantial misalignment is generated only late in the binary's evolution. As a result, stellar triples where tidal decay does not occur in the inner binary may exhibit an increase in spin-orbit misalignment with stellar age.

As noted above, the analytic results presented in this paper are valid for hierarchical triples with arbitrary masses. Thus, they also have applications in exoplanetary systems consisting of two well-separated planets. While numerous planets within ~ 1 AU of their host stars have been discovered from both transit and radial velocity searches, detection of more distant planets has proceeded more slowly. Many observed planets within 1 AU have substantial eccentricities, and a possible explanation is secular interactions with additional undetected distant planets. In systems containing an eccentric planet, the method developed in this paper can be used to place constraints on additional external planetary companions. We plan to study these issues in a future paper.

CHAPTER 7

**SPIN-ORBIT MISALIGNMENTS IN STELLAR BINARIES WITH
CIRCUMBINARY DISKS: APPLICATION TO DI HERCULIS**

7.1 Introduction

A natural expectation of stellar binary formation is an orbital axis that is aligned with the stellar spin axes, reflecting the rotation axis of the proto-stellar cloud. Indeed, stellar binaries with semi-major axes less than about 40 AU tend to be aligned with their orbital axes, whereas wider binaries are more randomly oriented (Hale, 1994). As a result, the existence of several close (< 1 AU) stellar binaries with significantly misaligned sky-projected spin and orbital axes is of great interest. Such misalignments may suggest a slight anomaly in the usual star formation process, or post-formation dynamical interactions. This paper focuses on the latter process.

One of the most well known spin-orbit misaligned stellar binaries is DI Herculis, a pair of B-type stars with a 10.5 day orbital period and sky-projected obliquities of 72° and -84° for the primary and secondary respectively (Albrecht et al., 2009). In this paper, we suggest a possible mechanism for the nearly perpendicular spins of DI Herculis, due to the presence of a circumbinary disk. An inclined circumbinary disk introduces nodal precession of the binary orbital axis. Meanwhile, the oblate stellar bodies experience torques, causing precession of the spin axes around the binary orbital axis. As the circumbinary disk

This chapter is adapted from Anderson & Lai (2019), in preparation.

mass decreases due to a combination of winds and accretion, a secular resonance may be encountered, in which the spin axis precession is comparable to the binary orbital axis precession. The spin axes may become captured into Cassini states (equilibrium states), causing the obliquities to approach 90° , as the disk mass becomes negligible.

This paper is organized as follows: In Section 7.2 we present the secular equations of motion for the star-binary-disk system, encapsulating the precession of the spin, binary, and disk angular momentum axes due to mutual torques, and review Cassini states. In Section 7.3 we discuss how allowing mass accretion onto the binary may under some circumstances suppress obliquity growth.

7.2 Obliquity Excitation in Stellar Binaries

7.2.1 Torques and Mutual Precession

We consider an equal-mass binary with total mass $M_b = m_0 + m_1$, semi-major axis a_b and angular momentum $L_b = \mu_b \sqrt{GM_b a_b}$. An inclined circumbinary disk has mass M_d , and inner and outer radii r_{in} and r_{out} , with $a_b < r_{\text{in}} < r_{\text{out}}$. Assuming the disk has a density profile $\Sigma(r) = \Sigma_{\text{in}}(r_{\text{in}}/r)$, the disk has mass M_d and angular momentum L_d , with

$$M_d = 2\pi\Sigma_{\text{in}} r_{\text{in}} (r_{\text{out}} - r_{\text{in}}) \quad (7.1)$$

and

$$L_d = \frac{2M_d \sqrt{GM_b r_{\text{out}}}}{3(r_{\text{out}} - r_{\text{in}})} \left[r_{\text{out}} - \sqrt{\frac{r_{\text{in}}^3}{r_{\text{out}}}} \right]. \quad (7.2)$$

We allow the disk mass to decrease with time according to

$$M_d(t) = \frac{M_{d,0}}{(1 + t/t_{\text{disk}})}, \quad (7.3)$$

where t_{disk} is a free parameter. The total mass-loss rate of the disk is therefore

$$\dot{M}_d = -\frac{M_{d,0}}{t_{\text{disk}}(1 + t/t_{\text{disk}})^2}. \quad (7.4)$$

Due to the binary-disk inclination, the unit vectors $\hat{\mathbf{l}}_b = \mathbf{L}_b/L_b$ and $\hat{\mathbf{l}}_d = \mathbf{L}_d/L_d$ undergo mutual precession around their total angular momentum axis $\hat{\mathbf{j}}$, defined by $\mathbf{J} = \mathbf{L}_b + \mathbf{L}_d$. The binary precesses around $\hat{\mathbf{l}}_b$ at a rate ω_{bd} , with

$$\omega_{\text{bd}} = \frac{3M_d}{8M_b} \frac{a_b^3}{r_{\text{in}}^2(r_{\text{out}} - r_{\text{in}})} \left[1 - \frac{r_{\text{in}}^2}{r_{\text{out}}^2} \right] n_b, \quad (7.5)$$

where $n_b = \sqrt{GM_b/a_b^3}$. The precession rate of $\hat{\mathbf{l}}_d$ around $\hat{\mathbf{l}}_b$ is denoted as $\omega_{\text{db}} = (L_b/L_d)\omega_{\text{bd}}$. The precession frequency of $\hat{\mathbf{l}}_b$ around $\hat{\mathbf{j}}$ has the rate

$$\begin{aligned} \omega_{\text{bj}} &= \left(1 + 2 \frac{L_b}{L_d} \cos I + \frac{L_b^2}{L_d^2} \right)^{1/2} \omega_{\text{bd}} \\ &\simeq \frac{9}{16} \frac{\mu_b}{M_b} \left(\frac{a_b}{r_{\text{in}}} \right)^{7/2} \left(\frac{r_{\text{in}}}{r_{\text{out}}} \right)^{3/2} n_b \quad \text{for } r_{\text{out}} \gg r_{\text{in}}, L_b \gg L_d. \end{aligned} \quad (7.6)$$

Due to stellar oblateness, the spin axis of m_0 ($\hat{\mathbf{s}} = \mathbf{S}/S$) experiences a torque from m_1^2 , and precesses around $\hat{\mathbf{l}}_b$ with frequency

$$\omega_{\text{sb}} = \frac{3k_q}{2k_*} \frac{m_1}{m_0} \left(\frac{R_0}{a_b} \right)^3 \Omega_*. \quad (7.7)$$

The binary orbit experiences a backreaction torque from m_0 , and precesses with much lower frequency $\omega_{\text{bs}} = (S/L_b)\omega_{\text{sb}}$.

The secular equations of motion for the binary, disk, and spin unit vectors,

²Throughout this paper, we consider only the torque on the oblate m_0 ; identical expressions for m_1 are obtained by switching the indices “0” and “1”.

encapsulating the precessional dynamics are thus

$$\begin{aligned}\frac{d\hat{s}}{dt} &= \omega_{sb}(\hat{s} \cdot \hat{l}_b)(\hat{s} \times \hat{l}_b), \\ \frac{d\hat{l}_b}{dt} &= \omega_{bd}(\hat{l}_b \cdot \hat{l}_d)(\hat{l}_b \times \hat{l}_d) + \omega_{bs}(\hat{s} \cdot \hat{l}_b)(\hat{l}_b \times \hat{s}), \\ \frac{d\hat{l}_d}{dt} &= \omega_{db}(\hat{l}_b \cdot \hat{l}_d)(\hat{l}_d \times \hat{l}_b)\end{aligned}\quad (7.8)$$

7.2.2 Cassini States

Cassini states are equilibrium states of the vector trio \hat{s} , \hat{l}_b and \hat{l}_d . Dissipative processes such as tides may drive the system to an equilibrium state. We orient \hat{l}_b along the z-axis and place the disk axis in the \hat{x} - \hat{z} plane. The unit vectors \hat{l}_d and \hat{s} have the coordinates

$$\hat{l}_d = \sin \theta_{bd} \hat{x} + \cos \theta_{bd} \hat{z} \quad (7.9)$$

$$\hat{s} = \sin \theta_{sb} \cos \phi \hat{x} + \sin \theta_{sb} \sin \phi \hat{y} + \cos \theta_{sb} \hat{z}, \quad (7.10)$$

where the angles are defined through $\cos \theta_{sb} = \hat{s} \cdot \hat{l}_b$ and $\cos \theta_{bd} = \hat{l}_b \cdot \hat{l}_d$, and ϕ is the phase of \hat{s} relative to \hat{l}_b . The equilibrium states occur when the relative orientations of all three axes are fixed (e.g. Boué & Laskar, 2006; Fabrycky et al., 2007; Correia et al., 2016; Anderson, & Lai, 2018), and are given by

$$\begin{aligned}[\hat{s} \cdot (\hat{l}_b \times \hat{l}_d)] &= 0 \\ \frac{d}{dt} [\hat{s} \cdot (\hat{l}_b \times \hat{l}_d)] &= 0.\end{aligned}\quad (7.11)$$

The first condition implies that $\phi = 0, \pi$. The second condition specifies the Cassini state angles, which becomes (Anderson, & Lai, 2018)

$$\begin{aligned} & \frac{\omega_{bd}}{\omega_{sb}} \cos \theta_{bd} \left[\cos \theta_{bd} \cos(\theta_{sb} - \theta_{bd}) - \cos \theta_{sb} \right] \\ & + \frac{S}{L_b} \cos \theta_{sb} \left[\cos \theta_{bd} - \cos(\theta_{sb} - \theta_{bd}) \right] \\ & - \sin \theta_{bd} \sin \theta_{sb} \left[\cos \theta_{sb} - \frac{L_b \omega_{bd}}{L_d \omega_{sb}} \cos \theta_{bd} \right]. \end{aligned} \quad (7.12)$$

Given values of the angular momentum ratios and either θ_{sb} or θ_{bd} , equation (7.12) may be numerically solved to calculate the Cassini states. Alternatively, the Cassini states can be thought of as an ordered pair of the obliquity and binary-disk inclination $(\theta_{sb}, \theta_{bd})$, which depends on the total angular moment of the system and precession frequencies. Following Correia (2015), we define the angular momentum constant K_0 :

$$K_0 = S L_b \cos \theta_{sb} + S L_d \cos \theta_{sd} + L_b L_d \cos \theta_{bd} = \frac{1}{2} (K^2 - S^2 - L_b^2 - L_d^2). \quad (7.13)$$

where $\mathbf{K} = \mathbf{S} + \mathbf{L}_b + \mathbf{L}_d$. Since

$$\cos \theta_{sd} = \sin \theta_{sb} \sin \theta_{bd} + \cos \theta_{sb} \cos \theta_{bd}, \quad (7.14)$$

$K_0 = K_0(\theta_{sb}, \theta_{bd}, S, L_b, L_d)$, and is a quadratic in $\cos \theta_{bd}$, which can be solved as (Correia et al. (2016), equations 78-80)

$$\cos \theta_{bd} = \frac{Z(L_b + S \cos \theta_{sb}) \pm S \sin \theta_{sb} \sqrt{1 - Z^2}}{G}, \quad (7.15)$$

where

$$Z = \frac{K_0 - S L_b \cos \theta_{sb}}{L_d G} \quad (7.16)$$

$$G = \sqrt{(L_b + S \cos \theta_{sb})^2 + S^2 \sin^2 \theta_{sb}} = (\mathbf{S} + \mathbf{L}_b)^2 \quad (7.17)$$

Together, equations (7.12) and (7.15) specify the ordered pair of Cassini state angles $(\theta_{sb}, \theta_{bd})$ as a function of $\omega_{sb}, \omega_{bd}, S, L_b, L_d, K_0$, and can be solved using numerical root-finding methods.

The number of Cassini states depends on several factors: The precession rates ω_{sb} and ω_{bd} , the angular momentum ratios S/L_b , L_b/L_d , and the binary-disk inclination. In the classical Cassini state problem (with $S/L_b = 0$), four states exist, two of which are stable, denoted as (θ_1, I_1) and (θ_2, I_2) . In the limit of strong spin-orbit coupling ($\omega_{\text{bd}}/\omega_{\text{sb}} \ll 1$), $\theta_1 \rightarrow 0$ and $\theta_2 \rightarrow \pi/2$. In the limit of weak spin-orbit coupling ($\omega_{\text{bd}}/\omega_{\text{sb}} \gg 1$) only one stable state exists (θ_2, I_2) , with $\theta_2 \rightarrow I_2$. Cassini state 1 ceases to exist when the ratio $\omega_{\text{bd}}/\omega_{\text{sb}}$ is of order unity.

Beginning with a sufficiently massive disk, the spin and orbit will initially be weakly coupled, so that the system may be driven towards the only stable Cassini state (θ_2, I_2) . As the disk mass decreases, the obliquity and binary-disk inclination will track (θ_2, I_2) as the ratio $\omega_{\text{bd}}/\omega_{\text{sb}}$ decreases. Following the dispersal of the disk, the obliquity will remain at a fixed value, corresponding to the asymptotic value of θ_2 , in the limit of $\omega_{\text{bd}}/\omega_{\text{sb}} \ll 1$.

In order for the system to become captured into Cassini state 2 without fine-tuning, the star-binary system must initially be sufficiently weakly coupled, so that Cassini state 1 does not exist. As a result, an approximate requirement is $\omega_{\text{bd}}/\omega_{\text{sb}} \gtrsim 1$ initially. This places constraints on the necessary disk properties, with a minimum disk mass (in units of binary mass) given by

$$\frac{M_d}{M_b} \gtrsim 4 \frac{k_q}{k_\star} \frac{\Omega_0}{n_b} \frac{R_0^3 r_{\text{in}}^2 r_{\text{out}}}{a_b^6}. \quad (7.18)$$

7.2.3 Relevant Timescales

We will fix the binary properties to values appropriate for a DI Herculis type system, choosing for simplicity $m_0 = m_1 = 5M_\odot$, $R_0 = 2.5R_\odot$, $P_\star = 1.25$ day, and $a_b = 0.2$ AU.

Figure 7.1 shows the precession frequencies ω_{sb} and ω_{bd} as a function of M_d/M_b , for the binary properties as specified above, fixed $r_{\text{in}} = 2a_b$ and various values of $r_{\text{out}}/r_{\text{in}}$. We see the condition $\omega_{\text{bd}}/\omega_{\text{sb}} \gtrsim 1$ is satisfied for disk masses initially of order the binary mass and a range of $r_{\text{out}}/r_{\text{in}}$. In the following examples and numerical integrations in this paper, we will fix the canonical disk properties to $r_{\text{in}} = 2a_b$, $r_{\text{out}} = 30r_{\text{in}}$, and initial mass $M_{d,0} = 0.5M_b = 5M_\odot$.

Fig. 7.2 illustrates the system properties and relevant timescales for the binary and disk parameters stated previously as a function of time, in units of the disk dispersal timescales t_{disk} . Inspecting the lefthand panel, the disk angular momentum is initially greater than the binary angular momentum by a factor of ~ 10 . As the disk dissipates, the ratio L_b/L_d increases and reaches unity after a time $10t_{\text{disk}}$ has elapsed. The spin angular momentum is much less than the binary angular momentum. We note that the assumption of a fixed disk profile may be an oversimplification at times beyond \sim a few t_{disk} . However, a more complex model is not justified in this situation, given uncertainties on the details of disk dispersal.

The righthand panel of Fig. 7.2 shows the relevant precession timescales. Initially, the binary precession frequency around the disk axis is greater than the stellar spin precession frequency around the binary axis ($\omega_{\text{bd}}/\omega_{\text{sb}} > 1$), so that the spin is weakly coupled to the orbit. When the disk mass becomes very small, the spin is very strongly coupled to the binary orbit ($\omega_{\text{bd}}/\omega_{\text{sb}} \ll 1$). Due to the backreaction torque on the binary orbit from the oblate star, the disk axis precesses with a very low frequency $\omega_{\text{bs}} = (S/L_b)\omega_{\text{sb}} \ll \omega_{\text{sb}}$.

In order for the system to be permanently captured into Cassini state 2, the mass loss must be “adiabatic,” with M_d/\dot{M}_d sufficiently slow. Inspecting the

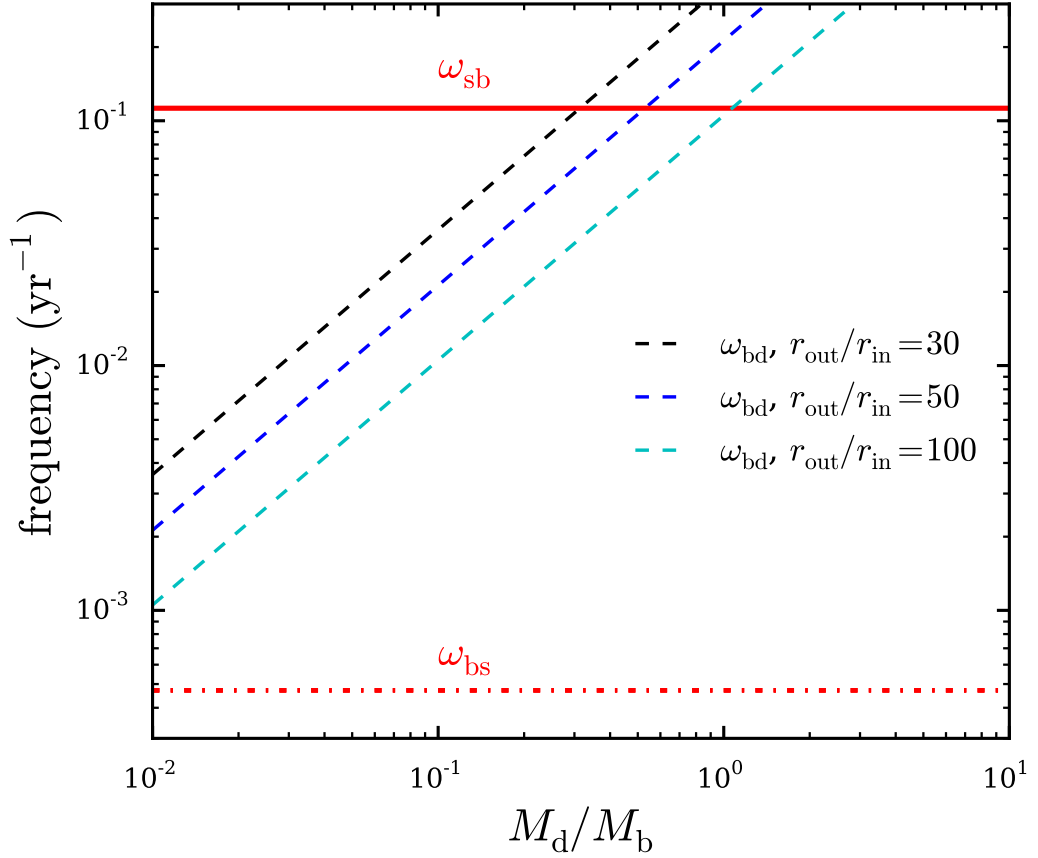


Figure 7.1: Relevant frequencies as a function of disk mass in units of the binary mass. The binary properties have been chosen to be similar to the observed properties of DI Herculis, with $m_0 = m_1 = 5M_\odot$, $R_0 = R_1 = 2.5R_\odot$, $a_b = 0.2$ AU, $P_\star = 1.25$ days. The solid red line indicates the precession frequency of \hat{s} due to \hat{l}_b (ω_{sb}) and the dash-dot line indicates the precession of \hat{l}_b due to \hat{s} (ω_{bs}). The three dashed lines indicate ω_{bd} , the precession frequency of \hat{l}_b due to \hat{l}_d , assuming an inner disk edge $r_{\text{in}} = 2a_b$ and varying values of $r_{\text{out}}/r_{\text{in}}$, as labeled. For initial disk masses of order the binary mass, $\omega_{\text{bd}}/\omega_{\text{sb}} \gtrsim 1$ initially, so that the system may be captured into Cassini state 2.

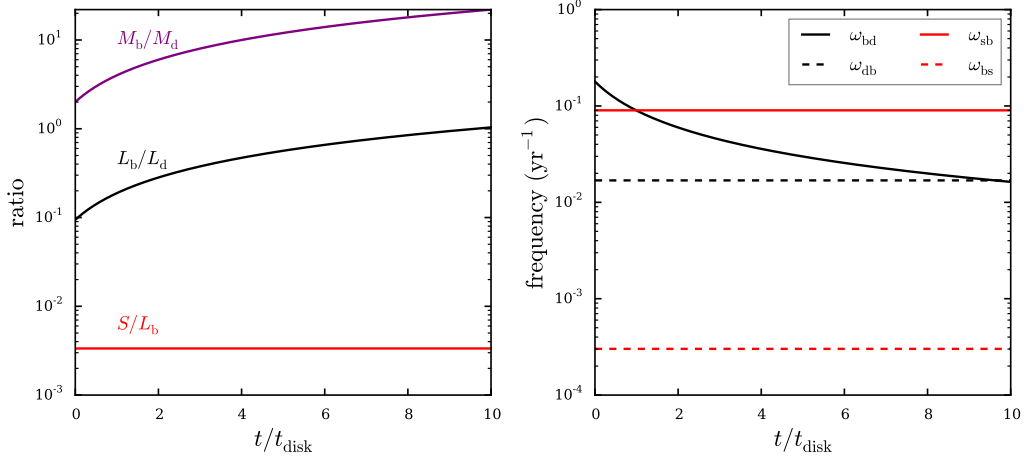


Figure 7.2: Relevant ratios and precession frequencies. The binary parameters shown here are the same as in Fig. 7.1 as well as all numerical integrations shown in this paper, and the disk properties are $r_{\text{in}} = 2a_b$, $r_{\text{out}} = 30r_{\text{in}}$, and initial mass $M_{d,0} = 0.5M_b = 5M_\odot$.

precession frequencies in the right panel of Fig. 7.2 shows that the disk mass loss timescale will be the slowest timescale in the problem for $t_{\text{disk}} \lesssim 10^4$ yrs.

7.2.4 Importance of Spin Feedback

Next, we conduct numerical integrations of a binary-disk system with the canonical disk and binary parameters (as listed in Fig. 7.2), with a disk dispersal timescale $t_{\text{disk}} = 10^5$ yr. Since $S/L_b \ll 1$, we will begin by neglecting the spin-feedback on the binary orbit (setting $S/L_b = 0$ in the equations of motion, so that $\omega_{\text{bs}} = 0$). The left panels of Fig. 7.3 shows examples starting with an initial binary-disk inclinations $\theta_{\text{bd},0} = 2^\circ$. Compare with the timescales and ratios shown in Fig. 7.2. The system is quickly captured into libration around Cassini state 2, and steadily tracks the state to a large final obliquity $\sim 70^\circ$. The binary-disk inclination remains constant, due to the fact that the binary experiences no

torque from the star, and simply precesses due to the disk. Note that this example has been integrated for a time $10t_{\text{disk}}$. The obliquity may continue to evolve slightly at later times and may eventually approach 90° , but the assumption of a fixed disk profile is almost certainly invalid at this point, and we do not attempt to precisely predict the final obliquity.

The right-hand panels of Fig. 7.3 show the same system, but including the spin feedback on the binary orbit ($S/L_b \neq 0$, so that $\omega_{\text{bs}} \neq 0$). Including the spin feedback has a profound effect on the Cassini state ordered pair $(\theta_{\text{sb}}, \theta_{\text{bd}})$, causing the binary-disk inclination to damp to less than 0.5° and the obliquity to settle at a final value of 31° . Thus, the spin feedback on the binary cannot be ignored for these parameters and initial conditions, in spite of the fact that $S/L_b \ll 1$.

Figure 7.4 presents the final obliquity and inclination for a set of numerical integrations conducted identical to the integrations shown in Fig. 7.3, but varying the initial binary-disk inclination in the range $1^\circ - 10^\circ$. We compare the results with and without spin feedback included. For initial inclinations $\theta_{\text{bd},0} \lesssim 4.5^\circ$, the spin-feedback dramatically reduces the binary-disk inclination, leading to a reduced final obliquity.

In summary, we have demonstrated that at small inclinations, the back-reaction torque of the oblate star on the orbit plays an essential role in the spin-binary-disk dynamics, leading to damping of the mutual inclination, and a final obliquity that can be far less than 90° .

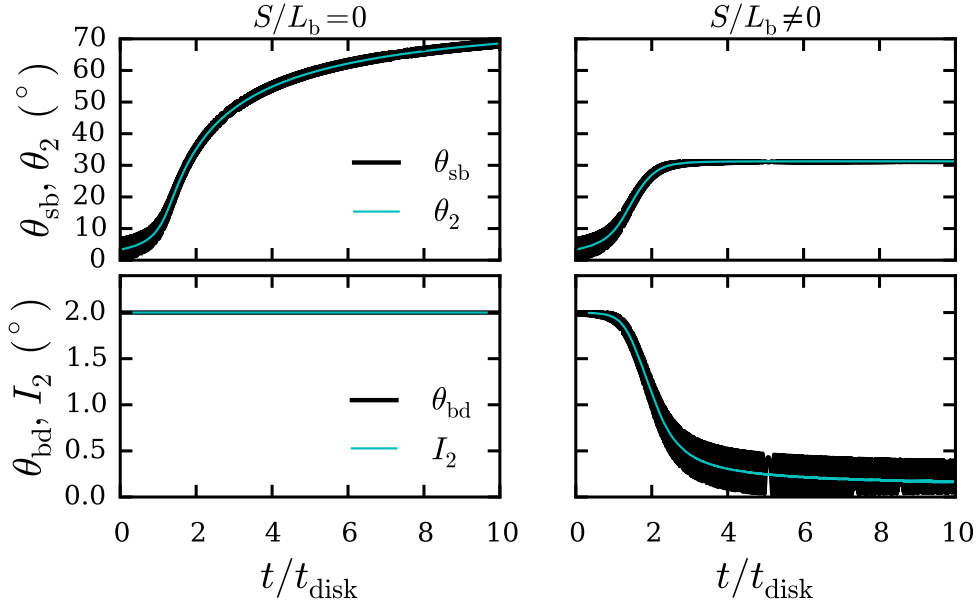


Figure 7.3: Example of obliquity and inclination evolution (θ_{sb} and θ_{bd}) for the canonical parameters (same as in Fig. 7.2). The results from the integration are shown in black. The Cassini state 2 angles (θ_2, I_2) are calculated analytically from the total angular momentum K_0 obtained from the numerical integration, and are shown in cyan. The left panels show an example with the spin feedback neglected (setting $S/L_b = 0$ in the equations of motion), and the right panels show the same example with the spin feedback included ($S/L_b \neq 0$). Despite the fact that $S/L_b \ll 1$ (see Fig. 7.2), the spin feedback on the orbit has a dramatic effect, causing the θ_{bd} to damp to nearly zero, and the final obliquity to settle to a value far below 90° .

7.3 Effects of Accretion onto the Binary

We now allow the possibility for accretion onto the binary. The total mass accretion onto the binary is specified as

$$\dot{M}_{\text{acc,b}} = f_b \dot{M}_d, \quad (7.19)$$

with f_b a free parameter between 0 – 1. The mass accretion rate onto each of the stars is

$$\dot{M}_{\text{acc,s}} = \frac{f_s f_b}{2} \dot{M}_d, \quad (7.20)$$

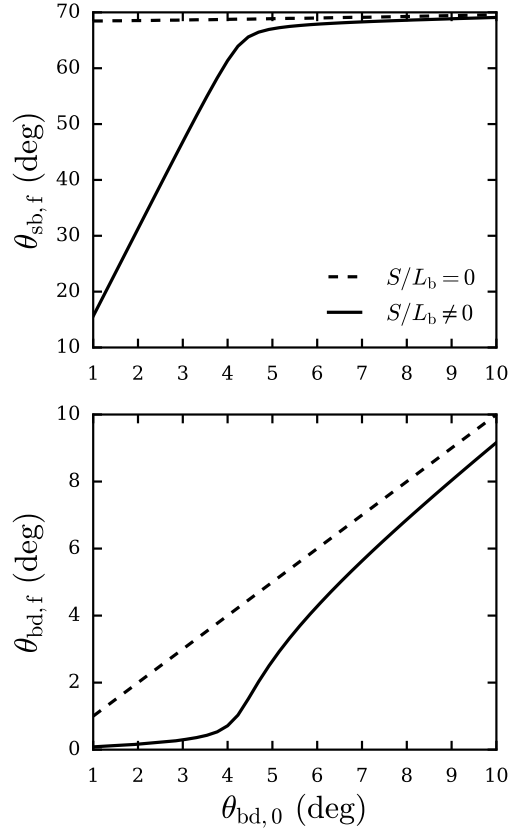


Figure 7.4: “Final” obliquity (top panel) and binary-disk inclination (bottom panel) after the disk has lost the majority of its initial mass (when $t = 10t_{\text{disk}}$). The solid lines show results of numerical integrations with the spin feedback on the orbit included (finite S/L_b , and the dashed lines show results with spin feedback neglected, by setting $S/L_b = 0$. For small initial inclinations ($\theta_{bd,0} \lesssim 5^\circ$), inclusion of feedback can drastically damp the inclination, thereby reducing the final obliquity.

with f_s a free parameter between 0 – 1 quantifying the total amount of mass accreted onto the stars.

Accretion from the circumbinary disk onto the binary introduces accretion torques, which act to align both the disk and binary, and the spin axis and bi-

nary. The accretion torques take the form

$$\begin{aligned} \left(\frac{d\mathbf{L}_b}{dt} \right)_{acc} &= N_{bd} \hat{\mathbf{l}}_d \\ \left(\frac{d\mathbf{S}}{dt} \right)_{acc} &= N_{sb} \hat{\mathbf{l}}_b. \end{aligned} \quad (7.21)$$

with

$$\begin{aligned} N_{bd} &\simeq \dot{M}_{acc,b} \sqrt{GM_b a_b}, \\ N_{sb} &\simeq \dot{M}_{acc,s} \sqrt{Gm_0 R_0}. \end{aligned} \quad (7.22)$$

The interaction between an accreting binary and disk is a complicated problem, with significant uncertainties in how the binary responds to the accreting mass. As a result, in this paper, we will consider the effects of accretion only on the directions of \mathbf{S} and \mathbf{L}_b , which yields alignment torques

$$\begin{aligned} \left(\frac{d\hat{\mathbf{l}}_b}{dt} \right)_{acc} &= \frac{N_{bd}}{L_b} \left(\hat{\mathbf{l}}_d - \cos \theta_{bd} \hat{\mathbf{l}}_b \right) \\ \left(\frac{d\hat{\mathbf{s}}}{dt} \right)_{acc} &= \frac{N_{sb}}{S} \left(\hat{\mathbf{l}}_b - \cos \theta_{sb} \hat{\mathbf{s}} \right). \end{aligned} \quad (7.23)$$

We add equations (7.23) to the system of precessional equations (7.8) and numerically integrate.

For an equal mass binary, the alignment timescale for the star-binary ($t_{sb,align} \sim S/N_{sb}$) compared to the alignment timescale for the binary-disk ($t_{bd,align} \sim L_b/N_{bd}$) is

$$\frac{t_{bd,align}}{t_{sb,align}} \simeq 41.7 f_s \left(\frac{k_*}{0.06} \right)^{-1} \left(\frac{\hat{\Omega}_0}{0.1} \right)^{-1}. \quad (7.24)$$

where $\hat{\Omega}_0 = \Omega_0 / \sqrt{Gm_0/R_0^3}$. Since $t_{bd,align}/t_{sb,align} \simeq 40$, we will first neglect the alignment of $\hat{\mathbf{l}}_b$ and $\hat{\mathbf{l}}_d$ (artificially setting $N_{bd} = 0$). In the following examples, we integrate the equations for the binary, disk, and spin unit vectors according to equations (7.8) and (7.23), with $f_s = f_b = 1$ in calculating N_{sb} . Figure 7.5

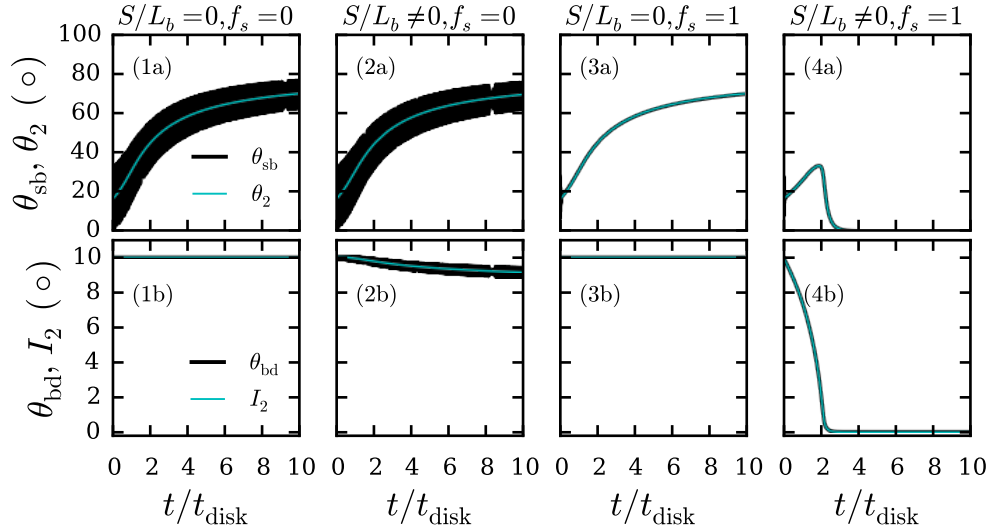


Figure 7.5: Similar to Fig. 7.3, illustrating how the combination of spin feedback and accretion torques can dramatically reduce the final obliquity. The top panels, labeled “(a)” show obliquity and the bottom panels, labeled “(b)” show the binary-disk inclination. All panels have the same disk and binary properties as in the previous figures. *Panels (1) and (2):* No accretion ($f_s = 0$). Panel 1 shows an idealized example neglecting the spin-feedback on the binary orbit, by artificially setting $S/L_b = 0$ (so that $\omega_{bs} = 0$), as in the left panels of Fig. 7.3. Panel (2) shows the same result, but with feedback included, so that $\omega_{bs} \neq 0$. Since the initially inclination is $\theta_{bd} = 10^\circ$, the feedback torque has a very small effect on the obliquity and inclination evolution. *Panels (3) and (4):* Effects of the accretion torque N_{sb} (with $f_s = f_b = 1$), but neglecting N_{bd} , since the time for accretion to align \hat{s} and \hat{l}_b is shorter than the time to align \hat{l}_b and \hat{l}_d (see equation [7.24]). Including the accretion torque but neglecting the spin feedback (Panel 3) causes the system to become captured into Cassini state 2 early, and the obliquity grows to $\sim 70^\circ$. Including both the accretion torque and spin feedback (Panel 4) also results in quick capture into Cassini state 2, but causes both the obliquity and inclination to damp to small values. These examples show that the spin feedback in conjunction with accretion torques is an important ingredient in this problem.

systematically presents how the combined effects of accretion and spin feedback act to suppress obliquity growth, in spite of tight capture into Cassini state 2.

Next we include both alignment torques, N_{sb} and N_{bd} . Figure 7.6 compares the obliquity and inclination evolution for highly suppressed accretion ($f_b = 0.1$), and moderate accretion ($f_b = 0.5$). Suppressed accretion causes

the system to retain a binary-disk inclination above a few degrees, leading to a $\sim 70^\circ$ final obliquity. In contrast, although moderate accretion leads to initial obliquity excitation, eventually the accretion torques act to align the entire star-binary-disk system.

Sustained obliquity excitation requires that the binary and disk maintain a sufficiently high inclination. In order to prevent alignment of \hat{l}_b and \hat{l}_d due to accretion torques requires that the alignment timescale to be greater than the disk mass loss timescale: $L_b/N_{bd} \gtrsim M_d/\dot{M}_d \simeq t_{disk}$. This implies a maximum disk mass in order to prevent alignment:

$$M_{d,max} \lesssim \frac{\mu_b}{f_b}. \quad (7.25)$$

There also exists a minimum initial disk mass necessary for capture into Cassini state 2 (equation [7.18]). Together, these conditions specify a range of initial disk masses allowing sustained obliquity excitation, due to capture into Cassini state 2, but preventing star-binary-disk alignment due to accretion from the disk. This range of disk masses is shown in Fig. 7.7, assuming the canonical binary and disk parameters. At large f_b , the available parameter space narrows, indicating that accretion must be at least partially suppressed in order for sustained obliquity excitation. Also included for reference are the combinations of $(f_b, M_{d,0})$ used in the numerical integrations depicted in Fig. 7.6. The example shown in the lefthand panels of Fig. 7.6 (resulting in a high obliquity) lie comfortably within the parameter space for resonant excitation, while the example shown in the right panels of Fig. 7.6 lies right at the upper mass limit.

Figure 7.7 delineates the parameter space for obliquity excitation, but does not yield information on the actual degree of obliquity growth. Fig. 7.8 shows results of numerical integrations with varying f_b (and assuming $f_s = 1$), and

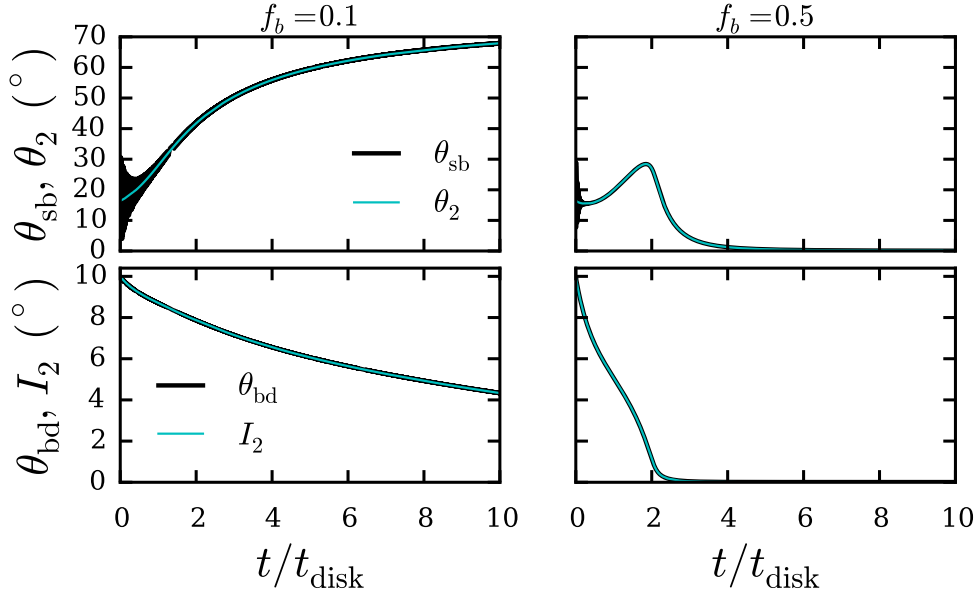


Figure 7.6: Similar to Figs. 7.3 and 7.5, showing the effects of including both N_{bd} and N_{sb} . Both examples have the spin feedback on the orbit included. The left panels show highly suppressed accretion ($f_b = 0.1$), and the right panels show moderate accretion ($f_b = 0.5$).

several different initial binary-disk inclinations spanning $5^\circ - 30^\circ$. Higher initial inclinations are more favorable for obliquity growth because the fractional degree of binary-disk realignment is lower. An initial inclination $\theta_{\text{bd}} = 30^\circ$ requires moderately suppressed accretion ($f_b \lesssim 0.5$) in order to produce substantial obliquity. In contrast, $\theta_{\text{bd}} = 5^\circ$ requires highly suppressed accretion ($f_b \lesssim 0.15$).

Thus far, we have assumed binary properties fixed to similar values as the observed DI Herculis system. However, since the obliquity growth must occur early (when the disk mass is of order the binary mass), the initial binary properties may have been substantially different from the observed values. For example, the stellar radii are expected to be larger, the disk morphology may have differed, and the binary semi-major axis may have been larger or smaller.

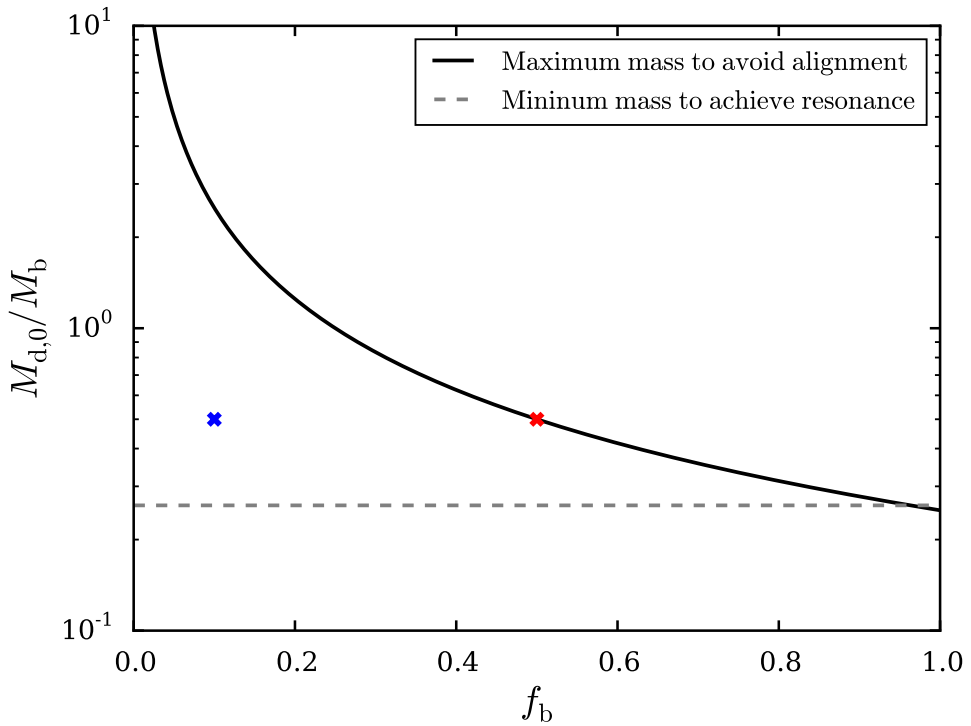


Figure 7.7: Parameter space allowing sustained obliquity excitation. The dashed grey line indicates the minimum disk mass (in units of the binary mass) needed for efficient obliquity growth due to capture into Cassini state 2 (see equation [7.18]). The solid black line indicates the maximum disk mass to avoid binary-disk realignment due to accretion (see equation [7.25]). In calculating these lines, we have assumed the canonical binary properties (similar to the observed values in DI Herculis), as specified in Fig. 7.1, and disk inner and outer radii $r_{\text{in}} = 2a_b$ and $r_{\text{out}} = 30r_{\text{in}}$. The blue and red crosses indicate the values of $M_{d,0}$ and f_b used in Fig. 7.6.

Figure 7.9 shows how the parameter space for sustained obliquity excitation widens or narrows with varying properties of the binary or disk. Enlarging the binary semi-major axis widens the available parameter space for sustained obliquity excitation. Enlarging the stellar radius and inner and outer disk edges narrows the available parameter space.

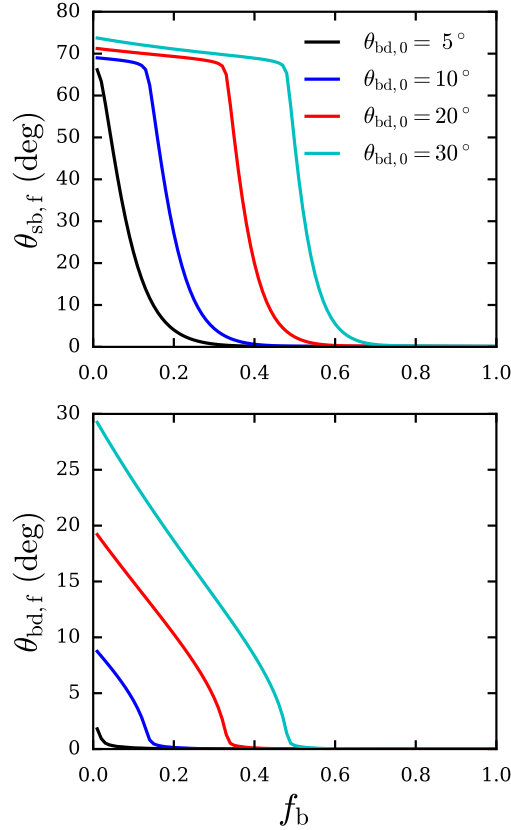


Figure 7.8: “Final” obliquity (top) and binary-disk inclination (bottom), obtained when $t = 10t_{\text{disk}}$, illustrating the affects of accretion torques and initial binary-disk inclination $\theta_{bd,0}$, as labeled. The binary and disk parameters are the canonical values as in previous figures, and the accretion efficiency parameter onto the stellar masses is $f_s = 1$. In order to prevent binary-disk alignment, the accretion efficiency parameter (onto the binary) must satisfy $f_b \lesssim 0.5$ for the range of $\theta_{bd,0}$ shown here.

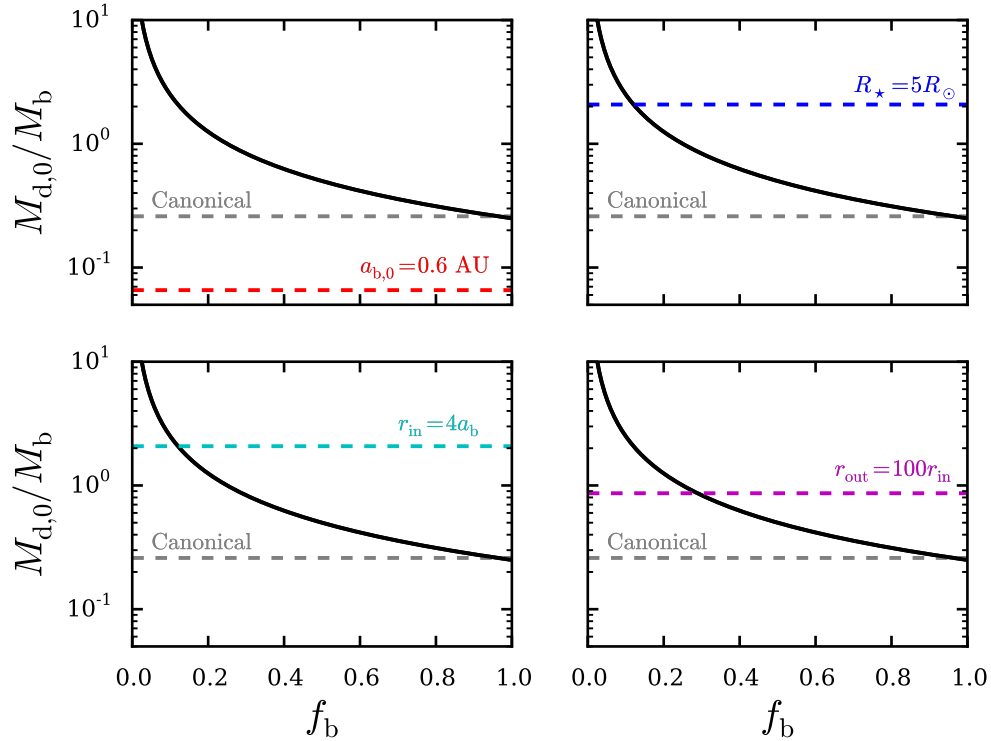


Figure 7.9: Similar to Fig. 7.7, illustrating how differing binary and disk properties widen or narrow the available parameter space for sustained obliquity excitation. In all panels, the grey lines show the canonical parameters (as in Fig. 7.7), and the colored lines show the effects of changing a given property, as labeled. Enlarging the binary semi-major axis widens the available parameter space for sustained obliquity excitation (top left panel). Enlarging the stellar radius (top right panel), and inner and outer disk edges (bottom left and right panels) narrows the available parameter space.

CHAPTER 8

CONCLUSION AND FUTURE WORK

This dissertation has examined the spin and orbital dynamics of giant planets and stellar binaries in a variety of contexts, with the broad goal of better understanding formation and migration histories of closely-orbiting systems. Important observational motivation for many of the dynamical studies this dissertation is the existence of close-in giant planets (hot and warm Jupiters) with a range of eccentricities and stellar spin-orbit misalignments (obliquities). In Chapter 2, I study orbital migration and obliquity excitation of giant planets in stellar binaries, and subsequent hot Jupiter formation. Chapter 3 presents a method for resonantly exciting stellar obliquities in both hot and warm Jupiter systems with inclined companions. Chapters 4 and 5 present mechanisms for producing eccentric warm Jupiters, starting from a low-eccentricity state consistent with either in-situ formation, or migration within the protoplanetary disk. In addition to these planetary studies, this dissertation has studied two mechanisms for exciting stellar obliquities, starting from an initially aligned state (Chapters 6 and 7).

There are several opportunities for future work. For example, the giant planet tidal migration model presented in Chapter 2 may be adapted to explore different mass regimes. “Hot” brown dwarfs (with orbital periods of several days) are observed, especially orbiting F-type stars. Similar to hot Jupiters, the presence of such closely orbiting brown dwarf companions raises questions regarding the migration mechanism. While several studies of high-eccentricity tidal migration of giant planets and stellar binaries exist, complementary migration studies of brown dwarfs have not been conducted.

The treatment of planet-planet collisions in the N-body scattering experiments presented in Chapter 5 may be refined. The present treatment assumes perfect inelastic mergers, so that mass and momentum are conserved. Such a treatment is a standard assumption in previous N-body exoplanet studies, but in reality additional physical ingredients such as tidal capture and mass loss may play a role in determining the final properties of the collision product. The finding in this dissertation that many planet-planet collisions are grazing, rather than head-on, serves as further motivation for further study.

Some of the secular problems explored in this dissertation (Chapters 3 and 4) require significant mutual inclinations in multi-planet systems. Mutual inclinations of observed giant planet pairs are almost entirely unconstrained, with measurements existing only in a few special systems (Dawson et al., 2014; Mills & Fabrycky, 2017). Knowledge of mutual inclinations in observed systems is of utmost importance in the future of exoplanet dynamics, and will help to identify the relevance of theoretical studies with much larger inclinations than observed in the solar system. Mutual inclinations in transiting planetary systems may be inferred due to nodal precession of the orbital plane, leading to transit duration variations. In addition, *Gaia* astrometry will allow for some constraints on mutual inclinations. Exploiting these techniques, as well as developing new methods will yield a more complete picture of exoplanetary system architectures and dynamical evolution.

APPENDIX A

ORBITAL & SPIN SECULAR EQUATIONS OF MOTION

In this Appendix we present the secular equations of motion governing the planetary orbit and stellar spin axis. The reader is referred to Table 2.1 for a concise summary of the notation used in this paper.

A.0.1 Lidov-Kozai Oscillations

The hierarchical triple systems studied in this paper consist of an inner binary M_\star (host star) and M_p (planet), with total mass $M_{\text{tot}} = M_\star + M_p$, with an outer stellar mass binary companion M_b . The planet has semi-major axis a and eccentricity e , and the binary companion has semi-major axis a_b and eccentricity e_b . The inner binary is characterized by the unit vectors $\hat{\mathbf{L}}$ and $\hat{\mathbf{e}}$, where $\hat{\mathbf{L}}$ is in the direction of the orbital angular momentum vector \mathbf{L} , and $\hat{\mathbf{e}}$ is in the direction of the eccentricity vector \mathbf{e} . Similarly, the outer binary is characterized by the unit vectors $\hat{\mathbf{L}}_b$ and $\hat{\mathbf{e}}_b$. Since we are considering systems in the regime $M_p \ll M_b$, the effect of the planet on the outer binary is negligible, and $\hat{\mathbf{L}}_b$ and $\hat{\mathbf{e}}_b$ are held constant. The inclination of the planetary orbit relative to the outer binary is specified by $\cos \theta_{lb} = \hat{\mathbf{L}} \cdot \hat{\mathbf{L}}_b$. If the outer binary companion has $\theta_{lb} \gtrsim 40^\circ$, the planet undergoes periodic variations in its orbital eccentricity and inclination (Lidov, 1962; Kozai, 1962), denoted in this paper as Lidov-Kozai (LK) oscillations. The secular equations of motion for \mathbf{L} and \mathbf{e} are, to octupole order in the

disturbing potential of the binary (Liu et al. 2015, see also Petrovich 2015b),

$$\begin{aligned}
\frac{d\mathbf{L}}{dt} \Big|_{\text{LK}} &= \frac{d\mathbf{L}}{dt} \Big|_{\text{LK, quad}} + \frac{d\mathbf{L}}{dt} \Big|_{\text{LK, oct}} \\
&= \frac{3}{4} \frac{L}{t_k(1-e^2)^{1/2}} \left[(\mathbf{j} \cdot \hat{\mathbf{L}}_b) \mathbf{j} \times \hat{\mathbf{L}}_b - 5(\mathbf{e} \cdot \hat{\mathbf{L}}_b) \mathbf{e} \times \hat{\mathbf{L}}_b \right] \\
&\quad - \frac{75}{64} \frac{\varepsilon_{\text{oct}} L}{t_k(1-e^2)^{1/2}} \left\{ \left[2 \left[(\mathbf{e} \cdot \hat{\mathbf{L}}_b)(\mathbf{j} \cdot \hat{\mathbf{L}}_b) \right. \right. \right. \\
&\quad \left. \left. \left. + (\mathbf{e} \cdot \hat{\mathbf{L}}_b)(\mathbf{j} \cdot \hat{\mathbf{e}}_b) \right] \mathbf{j} + 2 \left[(\mathbf{j} \cdot \hat{\mathbf{e}}_b)(\mathbf{j} \cdot \hat{\mathbf{L}}_b) \right. \right. \\
&\quad \left. \left. - 7(\mathbf{e} \cdot \hat{\mathbf{L}}_b)(\mathbf{e} \cdot \hat{\mathbf{L}}_b) \right] \mathbf{e} \right] \times \hat{\mathbf{L}}_b \\
&\quad + \left[2(\mathbf{e} \cdot \hat{\mathbf{L}}_b)(\mathbf{j} \cdot \hat{\mathbf{L}}_b) \mathbf{j} + \left[\frac{8}{5} e^2 - \frac{1}{5} \right. \right. \\
&\quad \left. \left. - 7(\mathbf{e} \cdot \hat{\mathbf{L}}_b)^2 + (\mathbf{j} \cdot \hat{\mathbf{L}}_b)^2 \right] \mathbf{e} \right] \times \hat{\mathbf{e}}_b \left. \right\}, \tag{A.1}
\end{aligned}$$

and

$$\begin{aligned}
\frac{d\mathbf{e}}{dt} \Big|_{\text{LK}} &= \frac{d\mathbf{e}}{dt} \Big|_{\text{LK, quad}} + \frac{d\mathbf{e}}{dt} \Big|_{\text{LK, oct}} \\
&= \frac{3}{4} \frac{L}{t_k} \left[(\mathbf{j} \cdot \hat{\mathbf{L}}_b) \mathbf{e} \times \hat{\mathbf{L}}_b + 2 \mathbf{j} \times \mathbf{e} - 5(\mathbf{e} \cdot \hat{\mathbf{L}}_b) \mathbf{j} \times \hat{\mathbf{L}}_b \right] \\
&\quad - \frac{75\varepsilon_{\text{oct}}}{64} \left\{ \left[2(\mathbf{e} \cdot \hat{\mathbf{L}}_b)(\mathbf{j} \cdot \hat{\mathbf{L}}_b) \mathbf{e} \right. \right. \\
&\quad \left. \left. + \left[\frac{8}{5} e^2 - \frac{1}{5} - 7(\mathbf{e} \cdot \hat{\mathbf{L}}_b)^2 + (\mathbf{j} \cdot \hat{\mathbf{L}}_b)^2 \right] \mathbf{j} \right] \times \hat{\mathbf{e}}_b \right. \\
&\quad + \left[2 \left[(\mathbf{e} \cdot \hat{\mathbf{e}}_b)(\mathbf{j} \cdot \hat{\mathbf{L}}_b) + (\mathbf{e} \cdot \hat{\mathbf{L}}_b)(\mathbf{j} \cdot \hat{\mathbf{e}}_b) \right] \mathbf{e} \right. \\
&\quad \left. \left. + 2 \left[(\mathbf{j} \cdot \hat{\mathbf{L}}_b)(\mathbf{j} \cdot \hat{\mathbf{e}}_b) - 7(\mathbf{e} \cdot \hat{\mathbf{L}}_b)(\mathbf{e} \cdot \hat{\mathbf{e}}_b) \right] \mathbf{j} \right] \times \hat{\mathbf{L}}_b \right. \\
&\quad \left. + \frac{16}{5} (\mathbf{e} \cdot \hat{\mathbf{e}}_b) \mathbf{j} \times \mathbf{e} \right\}, \tag{A.2}
\end{aligned}$$

where we have defined $\mathbf{j} = \sqrt{1-e^2} \hat{\mathbf{L}}$. The terms in braces describe the octupole-level perturbation of the binary companion, where the relative “strength” of the octupole term is quantified through the parameter ε_{oct} , defined by Eq. (2.4). Note that in Eqs. (A.1) and (A.2) we have introduced a characteristic

(quadrupole) timescale for LK oscillations t_k , given by Eq. (6.1). Focusing only on the quadrupole terms, we note that the binary companion induces simultaneous precession and nutation of the orbital axis $\hat{\mathbf{L}}$ at a rate $\Omega_L \equiv |d\hat{\mathbf{L}}/dt_{\text{quad}}| = [(\Omega_{\text{pl}} \sin \theta_{\text{lb}})^2 + \dot{\theta}_{\text{lb}}^2]^{1/2}$, see Eq. (2.5). From the standard equations for LK oscillations (in terms of orbital elements) to quadrupole order (e.g. Innanen et al., 1997),

$$\begin{aligned}\Omega_{\text{pl}} \sin \theta_{\text{lb}} &= \frac{3}{8t_k} \sin 2\theta_{\text{lb}} \frac{(5e^2 \cos^2 \omega - 4e^2 - 1)}{\sqrt{1 - e^2}} \\ \dot{\theta}_{\text{lb}} &= -\frac{15}{16t_k} e^2 \frac{\sin 2\theta_{\text{lb}} \sin 2\omega}{\sqrt{1 - e^2}}.\end{aligned}\quad (\text{A.3})$$

The value of Ω_L therefore depends on the argument of pericenter ω . A good approximation to Ω_L is

$$\Omega_L \simeq \frac{3(1 + 4e^2)}{8t_k \sqrt{1 - e^2}} |\sin 2\theta_{\text{lb}}|. \quad (\text{A.4})$$

This expression is exact at both $e = 0$ and $e = e_{\text{max}}$ (when $\omega = \pi/2$).

A.0.2 Spin Evolution Due to the Stellar Quadrupole

We denote the spin angular momentum of the host star as $\mathbf{S}_* = I_* \Omega_* \hat{\mathbf{S}}_*$, where $I_* = k_* M_* R_*^2$ is the moment of inertia, Ω_* is the spin frequency, and $\hat{\mathbf{S}}_*$ is a unit vector along the spin axis. Note that we have introduced a coefficient k_* , describing the interior mass distribution, where $k_* = 0.1$ is used throughout this paper.

Due to the rotational distortion of the star, the stellar spin axis \mathbf{S}_* precesses around the orbital axis $\hat{\mathbf{L}}$ according to

$$\left. \frac{d\mathbf{S}_*}{dt} \right|_{\text{SL}} = \Omega_{\text{ps}} \hat{\mathbf{L}} \times \mathbf{S}_*, \quad (\text{A.5})$$

with the spin precession frequency Ω_{ps} (see Section 2.2.1) given by Eq. (6.35).

The effects on the planetary orbit due to the stellar quadrupole are

$$\frac{d\mathbf{L}}{dt}\Big|_{\text{SL}} = -\frac{d\mathbf{S}_*}{dt}\Big|_{\text{SL}} = \Omega_{\text{ps}} \mathbf{S}_* \times \hat{\mathbf{L}}, \quad (\text{A.6})$$

and

$$\frac{d\mathbf{e}}{dt}\Big|_{\text{SL}} = -\dot{\omega}_* \left[\cos \theta_{\text{sl}} \hat{\mathbf{S}}_* \times \mathbf{e} + \frac{1}{2} (1 - 5 \cos^2 \theta_{\text{sl}}) \hat{\mathbf{L}} \times \mathbf{e} \right], \quad (\text{A.7})$$

where $\dot{\omega}_*$ quantifies the rate of apsidal precession due to the oblate star, and is given by

$$\dot{\omega}_* = -\frac{S_*}{L} \frac{\Omega_{\text{ps}}}{\cos \theta_{\text{sl}}} = \frac{3}{2} k_{q*} \left(\frac{R_*}{a} \right)^2 \frac{\hat{\Omega}_*^2}{(1 - e^2)^2} n. \quad (\text{A.8})$$

A.0.3 Pericenter Precession Due to Short Range Forces

Besides the pericenter precession induced by the oblate host star, given in Eq. (A.7), additional short range forces (SRFs), due to general relativistic corrections, the (static) tidal bulge in the planet, and rotational distortion of the planet, induce precession of the eccentricity vector, given by (e.g. Correia et al., 2011; Liu et al., 2015)

$$\begin{aligned} \frac{d\mathbf{e}}{dt}\Big|_{\text{SRF}} &= \frac{d\mathbf{e}}{dt}\Big|_{\text{GR}} + \frac{d\mathbf{e}}{dt}\Big|_{\text{Tide}} + \frac{d\mathbf{e}}{dt}\Big|_{\text{rot}} \\ &= (\dot{\omega}_{\text{GR}} + \dot{\omega}_{\text{Tide}} + \dot{\omega}_{\text{rot}}) \hat{\mathbf{L}} \times \mathbf{e}, \end{aligned} \quad (\text{A.9})$$

where the precession frequencies take the form

$$\dot{\omega}_{\text{GR}} = \frac{3GM_{\text{tot}}}{c^2 a (1 - e^2)} n, \quad (\text{A.10})$$

$$\dot{\omega}_{\text{Tide}} = \frac{15}{2} k_{2p} \frac{M_*}{M_p} \left(\frac{R_p}{a} \right)^5 \frac{f_4(e)}{j^{10}} n, \quad (\text{A.11})$$

and

$$\dot{\omega}_{\text{rot}} = \frac{3}{2} k_{qp} \left(\frac{R_p}{a} \right)^2 \frac{\hat{\Omega}_p^2}{(1 - e^2)^2} n, \quad (\text{A.12})$$

where $f_4(e)$ in Eq. (A.11) is a dimensionless function of eccentricity, given in Eq. (A.21), and in Eq. (A.12) we have introduced a “planetary rotational distortion coefficient” $k_{qp} = 0.17$, analogous to the stellar rotational distortion coefficient.

A.0.4 Dissipative Tides in the Planet

The planet has spin angular momentum $\mathbf{S}_p = I_p \Omega_p \hat{\mathbf{S}}_p$, where $I_p = k_p M_p R_p^2$ is the moment of inertia, Ω_p is the rotation rate, and where $k_p = 0.25$ throughout this paper. Averaged over an eccentricity precession timescale, the change in the planet spin due to tidal dissipation is (Correia et al., 2011)

$$\frac{1}{S_p} \frac{d\mathbf{S}_p}{dt} = -\frac{1}{2t_a j^{13}} \frac{L}{S_p} \left[j^3 f_5(e) (\hat{\mathbf{S}}_p + \cos \theta_p \hat{\mathbf{L}}) \frac{\Omega_p}{2n} - f_2(e) \hat{\mathbf{L}} \right], \quad (\text{A.13})$$

where $\cos \theta_p = \hat{\mathbf{S}}_p \cdot \hat{\mathbf{L}}$, and $f_2(e)$ and $f_5(e)$ are given in Eqs. (A.19) and (A.22). The timescale t_a is

$$\begin{aligned} \frac{1}{t_a} &= 6k_{2p} \Delta t_L \frac{M_*}{M_p} \left(\frac{R_p}{a} \right)^5 n^2 \\ &\approx \frac{7.3 \times 10^{-21}}{\text{yr}} \chi \bar{k}_{2p} \frac{\bar{M}_* \bar{M}_{\text{tot}}}{\bar{M}_p} \frac{\bar{R}_p^5}{\bar{a}^8}, \end{aligned} \quad (\text{A.14})$$

where Δt_L is the lag time, k_{2p} is the tidal Love number, and where we have introduced a tidal enhancement factor χ (relative to Jupiter), defined such that $\Delta t_L = 0.1\chi$ sec. In this paper we assume $\mathbf{S}_p = S_p \hat{\mathbf{L}}$ (see Section 2.3.3 for a justification of this approximation), so that Eq. (A.13) becomes

$$\frac{1}{S_p} \frac{dS_p}{dt} = -\frac{1}{2t_a j^{13}} \frac{L}{S_p} \left[j^3 f_5(e) \frac{\Omega_p}{n} - f_2(e) \right]. \quad (\text{A.15})$$

The effect of tidal dissipation on the orbit is

$$\left. \frac{d\mathbf{L}}{dt} \right|_{\text{Tide}} = -\frac{d\mathbf{S}_p}{dt} = -\dot{S}_p \hat{\mathbf{L}}, \quad (\text{A.16})$$

The change in the eccentricity vector due to tidal dissipation takes the form

$$\frac{d\mathbf{e}}{dt} \Big|_{\text{Tide}} = -\frac{1}{2t_a j^{13}} \left[j^3 f_4(e) \frac{\Omega_p}{2n} (\mathbf{e} \cdot \hat{\mathbf{S}}_p) \hat{\mathbf{L}} - \left(\frac{11}{2} j^3 f_4(e) \frac{\Omega_p}{n} - 9 f_3(e) \right) \mathbf{e} \right], \quad (\text{A.17})$$

where the first term inside the brackets vanishes if $\hat{\mathbf{S}}_p = \hat{\mathbf{L}}$. The dimensionless functions of eccentricity used to describe the tidal evolution take the form

$$f_1(e) = 1 + \frac{31e^2}{2} + \frac{255e^4}{8} + \frac{185e^6}{16} + \frac{25e^8}{64} \quad (\text{A.18})$$

$$f_2(e) = 1 + \frac{15e^2}{2} + \frac{45e^4}{8} + \frac{5e^6}{16} \quad (\text{A.19})$$

$$f_3(e) = 1 + \frac{15e^2}{4} + \frac{15e^4}{8} + \frac{5e^6}{64} \quad (\text{A.20})$$

$$f_4(e) = 1 + \frac{3e^2}{2} + \frac{e^4}{8} \quad (\text{A.21})$$

$$f_5(e) = 1 + 3e^2 + \frac{3e^4}{8}. \quad (\text{A.22})$$

A.0.5 Stellar Spin-down due to Magnetic Braking

We use the Skumanich law (Skumanich, 1972), given by

$$\frac{d\boldsymbol{\Omega}_*}{dt} = -\alpha_{\text{MB}} \Omega_*^2 \boldsymbol{\Omega}_*, \quad (\text{A.23})$$

where we set $\alpha_{\text{MB}} = 1.5 \times 10^{-14}$ yr to model G-type stars, and $\alpha_{\text{MB}} = 1.5 \times 10^{-15}$ yr to model F-type stars (from Barker & Ogilvie, 2009). See also Section 2.2.1.

APPENDIX B

LK MAXIMUM ECCENTRICITY FOR NON-ZERO INITIAL ECCENTRICITY

In this Appendix, we demonstrate how the analytic results of Section 2 may be modified when the initial eccentricity $e_0 \neq 0$. In the following results, we restrict the initial eccentricity to moderate values, $e_0 \lesssim 0.3$. This is justified because our goal is to identify the required properties of tertiary companions in raising the eccentricity of binaries starting from low or moderate initial values.

For general values of the initial eccentricity e_0 , e oscillates between a minimum value e_{\min} and a maximum value e_{\max} , with $e_{\min} \leq e_0 \leq e_{\max}$. Both e_{\max} and e_{\min} depend on the initial pericenter angle $\omega_0 \equiv \omega(e_0)$. If $\omega_0 = 0, \pi$ or $\omega_0 = \pi/2, 3\pi/2$, then either $e_0 = e_{\min}$ or $e_0 = e_{\max}$. For other values of ω_0 , we have $e_{\min} \leq e_0 \leq e_{\max}$.

When $e_0 \neq 0$, the minimum and maximum eccentricities may occur either at $\omega = 0, \pi$ or $\omega = \pi/2, 3\pi/2$, and ω may either circulate or librate. To determine e_{\max} from a given set of initial conditions, we calculate $\omega(e)$ using energy conservation, given by:

$$\Phi_{\text{Quad}}(e, \omega) + \Phi_{\text{SRF}}(e) = \Phi_{\text{Quad}}(e_0, \omega_0) + \Phi_{\text{SRF}}(e_0). \quad (\text{B.1})$$

See Section 6.2.1 for definitions of Φ_{Quad} and Φ_{SRF} . Requiring $0 \leq \cos^2 \omega \leq 1$ allows the maximum and minimum eccentricities to be determined, and are given by $\max[e(\omega)]$ and $\min[e(\omega)]$.

For specified (e_0, ω_0) , along with the orbital geometry and physical properties of m_0 , m_1 , and m_2 (which enter through η , ε_{GR} , $\varepsilon_{\text{Tide}}$ and ε_{Rot} ; see Eqs. [6.6] and [6.11]), the value of e_{\max} depends on the initial inclination I_0 . In the case of

$e_0 \simeq 0$, the “LK window,” (i.e. the range of inclinations that allow eccentricity oscillations) may be explicitly calculated (see Section 6.2.2), and takes the simple form of Eqs. (6.20) and (6.23). When $e_0 \neq 0$, the LK window is modified, and becomes somewhat fuzzier. In Fig. B.1 we demonstrate how non-zero e_0 affects the LK window, by calculating e_{\max} as function of η and $\cos I_0$, for a fiducial value of ε_{GR} and several different combinations of (e_0, ω_0) . Compare with Fig. 6.1. For reference, the explicit expressions for the LK window when $e_0 \simeq 0$ (Eqs. [6.20] and [6.23]) are also shown. For $\eta \lesssim 1$, Eqs. (6.20) remain an excellent prediction of whether eccentricity excitation may occur, regardless of the values of e_0 and ω_0 . When $\eta \gtrsim 1$ and $\omega_0 \neq 0$, the range of inclinations allowing eccentricity increases is modified compared to the $e_0 \simeq 0$ case.

Figure B.2 depicts e_{\max} and e_{\min} versus I_0 for several different values of e_0 and ω_0 , assuming the same orbital and physical parameters as in Fig. 6.2. As discussed in Section 6.2.3, there is a value of I_0 that yields a maximum value of e_{\max} (the “limiting eccentricity”), denoted as $I_{0,\text{lim}}$ and e_{lim} respectively. Regardless of e_0 and ω_0 , e_{lim} and $I_{0,\text{lim}}$ have nearly the same values.

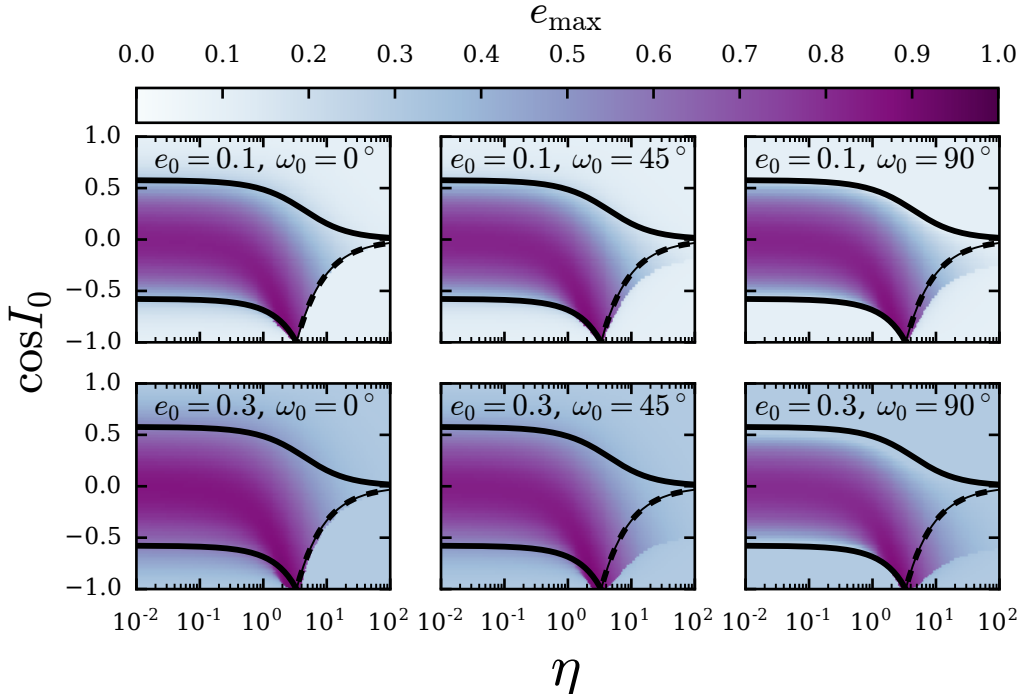


Figure B.1: e_{\max} , in terms of η and $\cos I_0$, for various combinations of e_0 and ω_0 . We have fixed $\varepsilon_{\text{GR}} = 1$, and have set $\varepsilon_{\text{Tide}}, \varepsilon_{\text{Rot}} = 0$. Compare with Fig. 6.1. For reference, the black curves show the analytic expressions for the range of $\cos I_0$ allowing eccentricity increases from $e_0 \simeq 0$ (the “LK window”), derived in Section 6.2.2 (Eqs. [6.20] and [6.23]). Non-zero e_0 does not substantially modify the LK window unless $\eta \gtrsim 1$.

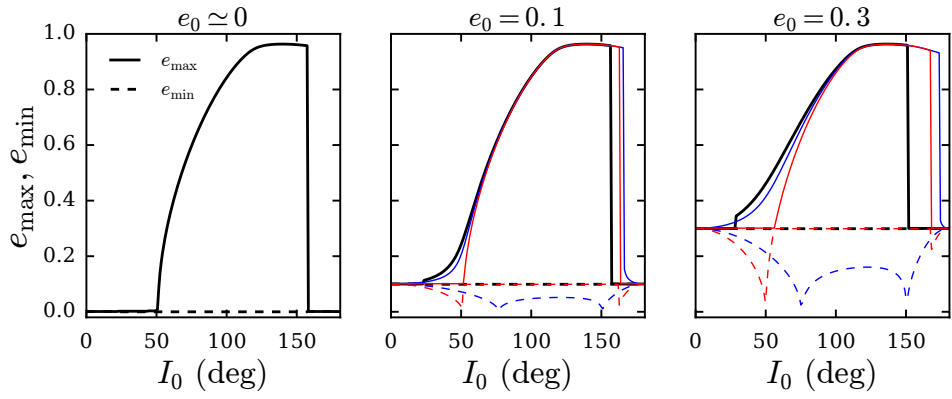


Figure B.2: Maximum and minimum eccentricities as a function of initial inclination, for various initial eccentricities e_0 and phase angles ω_0 . We show $\omega_0 = 0^\circ$ (black curves), $\omega_0 = 45^\circ$ (blue curves), and $\omega_0 = 90^\circ$ (red curves). The solid curves depict e_{\max} and the dashed curves depict e_{\min} . Compared to the $e_0 \simeq 0$ case, non-zero e_0 can lead to eccentricity oscillations for a wider range of I_0 , depending on the value of ω_0 . The lower inclination boundary for eccentricity growth $(\cos I_0)_+$ approaches zero, but the upper boundary corresponding to $(\cos I_0)_-$ remains. The orbital and physical parameters are the same as in Fig. 6.2. I_{\lim} and e_{\lim} (see Section 6.2.3) are nearly independent of e_0 and ω_0 .

APPENDIX C

TREATMENT OF PLANET-PLANET COLLISIONS

As in previous N-body works, this paper has assumed completely inelastic collisions, so that once the distance between two planets becomes less than the sum of their physical radii, the planets merge conserving mass and momentum. Such a treatment is clearly a simplification. In reality, giant planets will tidally interact upon close encounters, leading to mass loss, and other physical effects not captured. In addition, head-on versus grazing collisions may result in very different outcomes. Although expanding on this treatment is beyond the scope of this paper, here we discuss some of the caveats and limitations by assuming such a collision treatment.

We define the collision impact parameter, $b_{\text{coll}} = |\mathbf{r} \times \hat{\mathbf{v}}|$ where \mathbf{r} is the relative distance between the center of mass of each planet, and $\hat{\mathbf{v}}$ is the relative velocity unit vector. The top left panel of Fig. C.1 shows that many planet-planet collisions (from `fiducial`) are grazing, with $b_{\text{coll}}/(2R_p) \sim 1$.

Next we discuss some aspects of the collision of two planets m_1 and m_2 , with radii R_1 and R_2 . Once the planet-planet gravitational interaction becomes sufficiently strong so that the tidal gravity from the host star can be ignored, the scattering process up to just before merging can be modeled approximately as a parabolic encounter. Denote v_∞ as the relative velocity of the reduced mass μ as it enters the Hill sphere of the “primary” mass $M = m_1 + m_2$, and v_{coll} as the relative velocity just before collision. Energy conservation yields

$$v_\infty^2 = v_{\text{coll}}^2 - v_0^2, \quad (\text{C.1})$$

where $v_0^2 = 2GM/(R_1 + R_2)$. Angular momentum conservations yields

$$b_\infty v_\infty = b_{\text{coll}} v_{\text{coll}}, \quad (\text{C.2})$$

where b_∞ is the impact parameter as the secondary particle μ enters the hill sphere of the primary M .

The upper right panel of Fig. C.1 shows v_{coll}/v_0 . As expected, the majority of collisions have $v_{\text{coll}}/v_0 \sim 1$. The lower left panel of Fig. C.1 shows v_∞^2/v_0^2 . Typically $v_\infty^2/v_0^2 \ll 1$. Negative values of v_∞^2 indicate that equation (C.1) does not adequately describe the scattering dynamics. Finally, the lower right panel of Fig. C.1 shows b_∞ in units of the Hill radius of M . These result will be useful as initial conditions for future numerical simulations (e.g. SPH simulations) of planet-planet collisions.

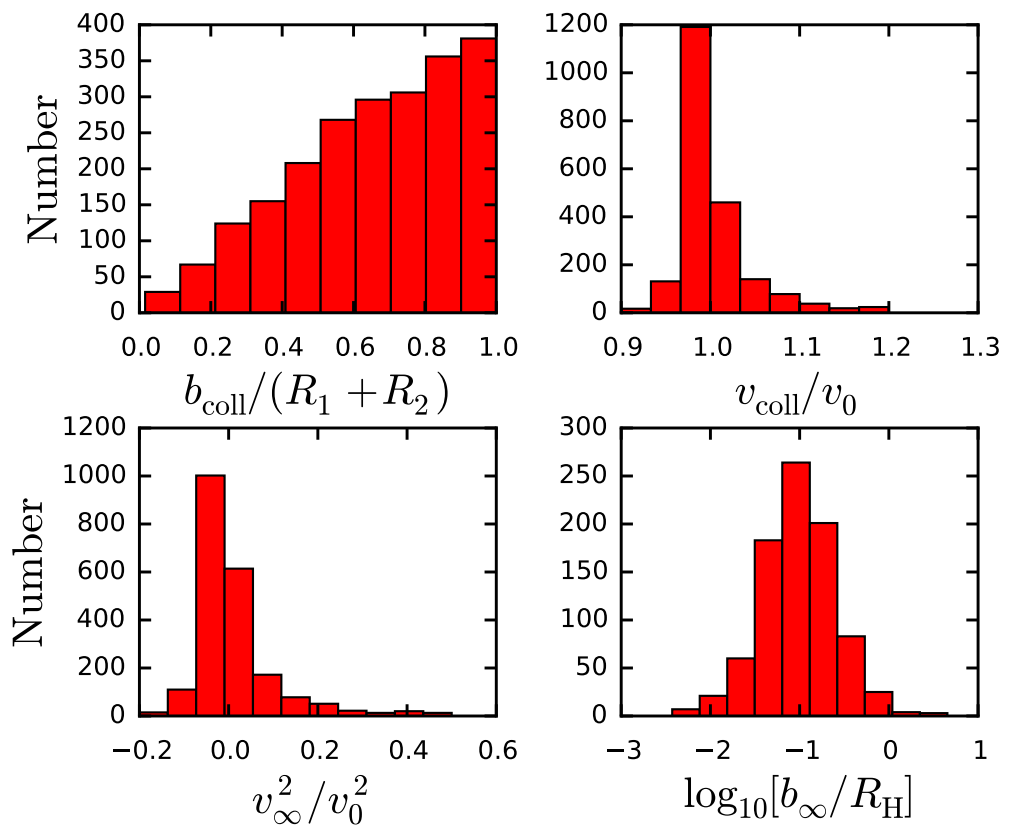


Figure C.1: Properties of scattering outcomes, showing that most collisions are grazing (upper left panel). The remaining panels are useful in establishing initial conditions for future numerical simulations of planet-planet collisions.

APPENDIX D

DISCRETE MIXTURE MODEL FOR PLANET ECCENTRICITIES

In this Appendix we outline the mixture model mentioned in Section 5.3.1. In this model, we augment the sample of one-planet systems obtained from `fiducial` with a population of low-eccentricity planets (that did not undergo scattering), in order to better match the observed distribution of solitary WJs with the scattering calculations. This model allows us to obtain a quantitative estimate of the extent to which in-situ scattering may have contributed to the population of observed solitary eccentric WJs. We note that this calculation neglects the uncertainties of observed eccentricities. Accounting for uncertainties of observed eccentricities in this calculation is not a simple task, because no standard procedure has been adopted in eccentricity uncertainty estimates.

We assume a mixture model such that the probability distribution function for eccentricities takes the form

$$f(e) = \mathcal{F}f_{\text{circ}}(e) + (1 - \mathcal{F})f_{\text{scat}}(e), \quad (\text{D.1})$$

where f_{circ} is the injected probability density function of low-eccentricity planets, and f_{scat} is the empirical probability density function of eccentricities of one-planet systems obtained from `fiducial`. The free parameter $\mathcal{F} = [0, 1]$ quantifies the number of injected low-eccentricity planets N_{circ} relative to the total number of planets $N_{\text{circ}} + N_{\text{scat}}$, so that

$$\mathcal{F} = \frac{N_{\text{circ}}}{N_{\text{circ}} + N_{\text{scat}}}. \quad (\text{D.2})$$

Clearly, $\mathcal{F} = 0$ corresponds to all of the eccentricities arising from scattering, while $\mathcal{F} = 1$ corresponds to none of the eccentricities arising from scattering.

We adopt a half-Gaussian for $f_{\text{circ}}(e)$ peaked at $e = 0$ and truncated at $e = 1$, and a range of characteristic widths σ . This accounts for the fact that modest eccentricities may be generated by factors other than scattering, e.g. by planet-disk interactions. To construct a smooth probability density function for $f_{\text{scat}}(e)$, we employ a Gaussian Kernel-density estimate. Armed with $f_{\text{circ}}(e)$ and $f_{\text{scat}}(e)$, we explore a grid of values for the parameters \mathcal{F}, σ , and calculate the likelihood function for the observed eccentricities e_i , with $i = 1, n_{\text{obs}} = 83$,

$$\mathcal{L} = \prod_{i=1}^{n_{\text{obs}}} \left[\mathcal{F} f_{\text{circ}}(e_i) + (1 - \mathcal{F}) f_{\text{scat}}(e_i) \right]. \quad (\text{D.3})$$

We explore the ranges $\mathcal{F} = 0 - 1$ and $\sigma = 0 - 0.2$. We restrict σ to a relatively small range because we are considering that the injected population experienced only modest eccentricity excitation. Maximizing \mathcal{L} yields the parameter values $\mathcal{F} \approx 0.35$ and $\sigma = 0.07$. In other words, the observed eccentricity distribution of single WJs is consistent with scattering having occurred in $\sim 65\%$ of all systems. This estimate, alongside $1, 2, 3 - \sigma$ contours is shown in Fig. D.1. Taking the 95% contour as the uncertainty, we find that \mathcal{F} lies in the range $18\% - 54\%$. In other words, the observed eccentricity distribution of solitary WJs is consistent with scattering having contributed to roughly half or more of systems.

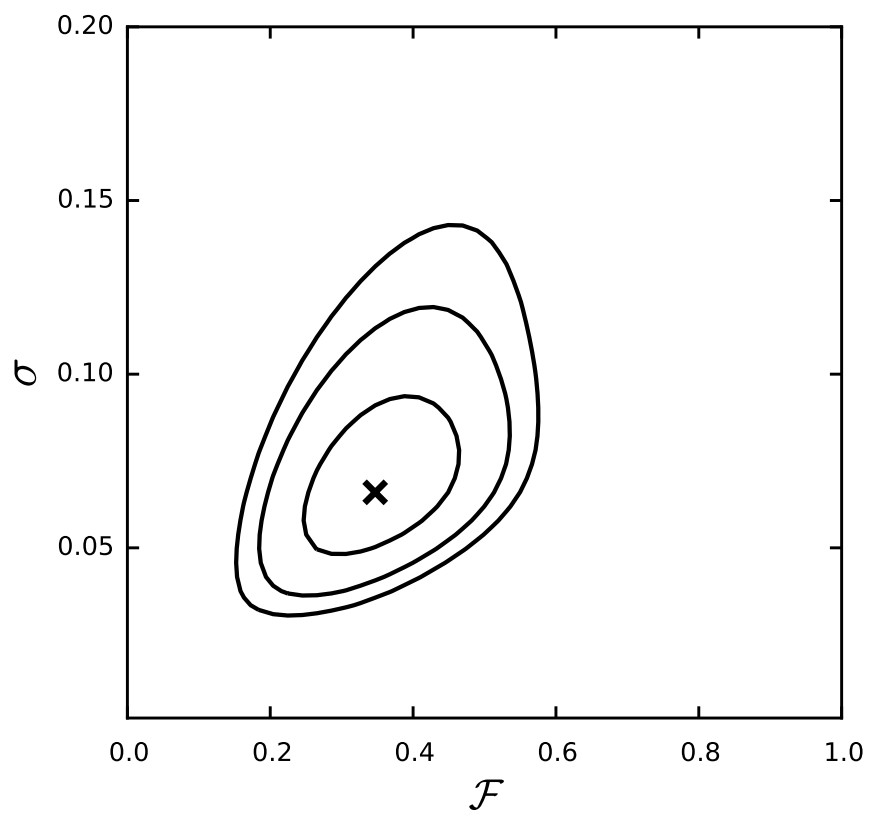


Figure D.1: Estimated parameters of the mixing model discussed in Appendix D, using maximum likelihood estimation. The cross indicates the maximum likelihood, and the contours indicate the 68%, 95% and 99% confidence intervals.

BIBLIOGRAPHY

- Adams, F. C., & Laughlin, G. 2003, *Icarus*, 163, 290
- Addison, B. C., Tinney, C. G., Wright, D. J., et al. 2013, *ApJL*, 774, L9
- Albrecht, S., Reffert, S., Snellen, I., Quirrenbach, A., & Mitchell, D. S. 2007, *A & A*, 474, 565
- Albrecht, S., Reffert, S., Snellen, I. A. G., & Winn, J. N. 2009, *Nature*, 461, 373
- Albrecht, S., Winn, J. N., Carter, J. A., Snellen, I. A. G., & de Mooij, E. J. W. 2011, *ApJ*, 726, 68
- Albrecht, S., Winn, J. N., Johnson, J. A., et al. 2012a, *ApJ*, 757, 18
- Albrecht, S., Winn, J. N., Butler, R. P., et al. 2012b, *ApJ*, 744, 189
- Albrecht, S., Setiawan, J., Torres, G., Fabrycky, D. C., & Winn, J. N. 2013, *ApJ*, 767, 32
- Albrecht, S., Winn, J. N., Torres, G., et al. 2014, *ApJ*, 785, 83
- Alexander M. E., 1973, *ASS*, 23, 459
- Anderson, K. R., Storch, N. I., & Lai, D. 2016, *MNRAS*, 456, 3671
- Anderson, K. R., Lai, D., & Storch, N. I. 2017, *MNRAS*, 467, 3066
- Anderson, K. R., & Lai, D. 2017, *MNRAS*, 472, 3692
- Anderson, K. R., & Lai, D. 2018, *MNRAS*, 480, 1402
- Anderson, K. R., Lai, D., & Pu, B. 2019, to be submitted
- Anderson, K. R., & Lai, D. 2019, in preparation

- Antonini, F., Hamers, A. S., & Lithwick, Y. 2016, AJ, 152, 174
- Barker, A. J., & Ogilvie, G. I. 2009, MNRAS, 395, 2268
- Baruteau, C., Crida, A., Paardekooper, S.-J., et al. 2014, Protostars and Planets VI, 667
- Bate, M. R., Lodato, G., & Pringle, J. E. 2010, MNRAS, 401, 1505
- Batygin, K. 2012, Nature, 491, 418
- Batygin, K., & Adams, F. C. 2013, ApJ, 778, 169
- Batygin, K., Bodenheimer, P. H., & Laughlin, G. P. 2016, ApJ, 829, 114
- Beaugé, C., & Nesvorný, D. 2012, ApJ, 751, 119
- Becker, J. C., Vanderburg, A., Adams, F. C., Rappaport, S. A., & Schwengeler, H. M. 2015, ApJL, 812, L18
- Becker, J. C., Vanderburg, A., Adams, F. C., Khain, T., & Bryan, M. 2017, AJ, 154, 230
- Boley, A. C., Granados Contreras, A. P., & Gladman, B. 2016, ApJL, 817, L17
- Bolmont, E., & Mathis, S. 2016, Celestial Mechanics and Dynamical Astronomy, 126, 275
- Boué, G., & Laskar, J. 2006, Icarus, 185, 312
- Boué, G., & Fabrycky, D. C. 2014, ApJ, 789, 111
- Bouvier, J. 2013, EAS Publications Series, 62, 143
- Bryan, M. L., Knutson, H. A., Howard, A. W., et al. 2016, ApJ, 821, 89

- Chambers, J. E., Wetherill, G. W., & Boss, A. P. 1996, *Icarus*, 119, 261
- Chatterjee, S., Ford, E. B., Matsumura, S., & Rasio, F. A. 2008, *ApJ*, 686, 580
- Ciceri, S., Lillo-Box, J., Southworth, J., et al. 2015, *A & A*, 573, L5
- Claret, A., & Gimenez, A. 1992, *A&AS*, 96, 255
- Colombo, G. 1966, *AJ*, 71, 891
- Correia, A. C. M., Couetdic, J., Laskar, J., et al. 2010, *A&A*, 511, A21
- Correia, A. C. M., Laskar, J., Farago, F., & Boué, G. 2011, *Celestial Mechanics and Dynamical Astronomy*, 111, 105
- Correia, A. C. M. 2015, *A&A*, 582, A69
- Correia, A. C. M., Boué, G., & Laskar, J. 2016, *Celestial Mechanics and Dynamical Astronomy*, 126, 189
- Cumming, A., Butler, R. P., Marcy, G. W., et al. 2008, *PASP*, 120, 531
- Darwin, G. H. 1880, *Philosophical Transactions of the Royal Society of London Series I*, 171, 713
- Dawson, R. I., & Murray-Clay, R. A. 2013, *ApJL*, 767, L24
- Dawson, R. I., & Chiang, E. 2014, *Science*, 346, 212
- Dawson, R. I., & Murray-Clay, R. A. 2013, *ApJL*, 767, L24
- Dawson, R. I., Johnson, J. A., Fabrycky, D. C., et al. 2014, *ApJ*, 791, 89
- Dawson, R. I., Murray-Clay, R. A., & Johnson, J. A. 2015, *ApJ*, 798, 66
- Dawson, R. I., & Johnson, J. A. 2018, *ARA&A*, 56, 175

Dong, S., Katz, B., & Socrates, A. 2013, ApJL, 763, L2

Dong, S., Katz, B., & Socrates, A. 2014, ApJL, 781, L5

Duffell, P. C., & Chiang, E. 2015, ApJ, 812, 94

Eggleton, P. P., & Kiseleva-Eggleton, L. 2001, ApJ, 562, 1012

Fabrycky, D., & Tremaine, S. 2007, ApJ, 669, 1298

Fabrycky, D. C., Johnson, E. T., & Goodman, J. 2007, ApJ, 665, 754

Feng, Y. K., Wright, J. T., Nelson, B., et al. 2015, ApJ, 800, 22

Fielding, D. B., McKee, C. F., Socrates, A., Cunningham, A. J., & Klein, R. I. 2015, MNRAS, 450, 3306

Ford, E. B., Kozinsky, B., & Rasio, F. A. 2000, ApJ, 535, 385

Ford, E. B., Havlickova, M., & Rasio, F. A. 2001, Icarus, 150, 303

Ford, E. B., & Rasio, F. A. 2008, ApJ, 686, 621

Foucart, F., & Lai, D. 2011, MNRAS, 412, 2799

Gallet, F., & Bouvier, J. 2013, A&A, 556, A36

Goldreich, P., & Sari, R. 2003, ApJ, 585, 1024

Guillochon, J., Ramirez-Ruiz, E., & Lin, D. 2011, ApJ, 732, 74

Hale, A. 1994, AJ, 107, 306

Hamers, A. S., Antonini, F., Lithwick, Y., Perets, H. B., & Portegies Zwart, S. F. 2017, MNRAS, 464, 688

Hamers, A. S. 2017, MNRAS, 466, 4107

- Han, E., Wang, S. X., Wright, J. T., et al. 2014, PASP, 126, 827
- Harrington, R. S. 1968, AJ, 73, 190
- Hébrard, G., Bouchy, F., Pont, F., et al. 2008, A&A, 488, 763
- Heller, R. 2018, arXiv:1806.06601
- Henrard, J., & Murigande, C. 1987, Celestial Mechanics, 40, 345
- Holman, M., Touma, J., & Tremaine, S. 1997, Nature, 386, 254
- Huang, C., Wu, Y., & Triaud, A. H. M. J. 2016, ApJ, 825, 98
- Hut P., 1981, A&A, 99, 126
- Innanen, K. A., Zheng, J. Q., Mikkola, S., & Valtonen, M. J. 1997, AJ, 113, 1915
- Jackson, B., Barnes, R., & Greenberg, R. 2009, ApJ, 698, 1357
- Jones, H. R. A., Butler, R. P., Tinney, C. G., et al. 2003, MNRAS, 341, 948
- Jurić, M., & Tremaine, S. 2008, ApJ, 686, 603
- Kaib, N. A., Raymond, S. N., & Duncan, M. J. 2011, ApJL, 742, L24
- Kley, W., & Nelson, R. P. 2012, ARAA, 50, 211
- Knutson, H. A., Fulton, B. J., Montet, B. T., et al. 2014, ApJ, 785, 126
- Kozai, Y. 1962, AJ, 67, 591
- Lai, D., Foucart, F., & Lin, D. N. C. 2011, MNRAS, 412, 2790
- Lai, D. 2012, MNRAS, 423, 486
- Lai, D. 2014, MNRAS, 440, 3532

- Lai, D., & Pu, B. 2017, AJ, 153, 42
- Lai, D., Anderson, K. R., & Pu, B. 2018, MNRAS, 475, 5231
- Laskar, J., & Robutel, P. 1995, Celestial Mechanics and Dynamical Astronomy, 62, 193
- Laskar, J., Boué, G., & Correia, A. C. M. 2012, A&A, 538, A105
- Laughlin, G., Crismani, M., & Adams, F. C. 2011, ApJL, 729, LL7
- Law, N. M., Morton, T., Baranec, C., et al. 2014, ApJ, 791, 35
- Lee, M. H., & Peale, S. J. 2003, ApJ, 592, 1201
- Lee, E. J., Chiang, E., & Ormel, C. W. 2014, ApJ, 797, 95
- Lee, E. J., & Chiang, E. 2016, ApJ, 817, 90
- Li, G., Naoz, S., Holman, M., & Loeb, A. 2014, ApJ, 791, 86
- Li, G., Naoz, S., Kocsis, B., & Loeb, A. 2014, ApJ, 785, 116
- Lidov, M. L. 1962, Planet. Space Sci., 9, 719
- Lidov, M. L., & Ziglin, S. L. 1976, Celestial Mechanics, 13, 471
- Lin, D. N. C., Bodenheimer, P., & Richardson, D. C. 1996, Nature, 380, 606.
- Lin, D. N. C., & Ida, S. 1997, ApJ, 477, 781
- Lithwick, Y., & Naoz, S. 2011, ApJ, 742, 94
- Lithwick, Y., & Wu, Y. 2011, ApJ, 739, 31
- Lithwick, Y., & Wu, Y. 2014, Proceedings of the National Academy of Science, 111, 12610

- Liu, B., Muñoz, D. J., & Lai, D. 2015, MNRAS, 447, 751
- Liu, B., Lai, D., & Yuan, Y.-F. 2015, Phys. Rev. D, 92, 124048
- Mardling, R. A., & Aarseth, S. J. 2001, MNRAS, 321, 398
- Mardling, R. A. 2010, MNRAS, 407, 1048
- Martin, D. V., & Triaud, A. H. M. J. 2016, MNRAS, 455, L46
- Martynov, D. I., & Khaliullin, K. F. 1980, Ap & SS, 71, 147
- Marzari, F., & Nagasawa, M. 2019, arXiv e-prints , arXiv:1904.01420
- Masuda, K. 2017, AJ, 154, 64
- Mathis, S. 2015, A&A, 580, L3
- Matsumura, S., Peale, S. J., & Rasio, F. A. 2010, ApJ, 725, 1995
- Mayor, M., & Queloz, D. 1995, Nature, 378, 355
- Mazeh, T., & Shaham, J. 1979, A&A, 77, 145
- McArthur, B. E., Benedict, G. F., Barnes, R., et al. 2010, ApJ, 715, 1203
- McLaughlin, D. B. 1924, ApJ, 60, 22
- McQuillan, A., Mazeh, T., & Aigrain, S. 2014, ApJS, 211, 24
- Mills, S. M., & Fabrycky, D. C. 2017, AJ, 153, 45
- Moutou, C., Díaz, R. F., Udry, S., et al. 2011, A&A, 533, A113
- Muñoz, D. J., Lai, D., & Liu, B. 2016, submitted
- Muñoz, D. J., & Perets, H. B. 2018, AJ, 156, 253

- Mustill, A. J., Davies, M. B., & Johansen, A. 2017, MNRAS, 468, 3000
- Nagasawa, M., Ida, S., & Bessho, T. 2008, ApJ, 678, 498
- Nagasawa, M., & Ida, S. 2011, ApJ, 742, 72
- Naoz, S., Farr, W. M., & Rasio, F. A. 2012, ApJL, 754, LL36
- Naoz, S., Farr, W. M., Lithwick, Y., Rasio, F. A., & Teyssandier, J. 2013, MNRAS, 431, 2155
- Naoz, S., Kocsis, B., Loeb, A., & Yunes, N. 2013, ApJ, 773, 187
- Naoz, S., & Fabrycky, D. C. 2014, ApJ, 793, 137
- Narita, N., Hirano, T., Sato, B., et al. 2009, PASJ, 61, 991
- Neveu-VanMalle, M., Queloz, D., Anderson, D. R., et al. 2015, arXiv:1509.07750
- Ngo, H., Knutson, H. A., Hinkley, S., et al. 2015, ApJ, 800, 138
- Ogilvie, G. I. 2013, MNRAS, 429, 613
- Ortiz, M., Gandolfi, D., Reffert, S., et al. 2015, A & A, 573, L6
- Peale, S. J. 1969, AJ, 74, 483
- Peale, S. J. 1974, AJ, 79, 722
- Perryman, M., Hartman, J., Bakos, G. Á., & Lindegren, L. 2014, ApJ, 797, 14
- Petrovich, C., Tremaine, S., & Rafikov, R. 2014, ApJ, 786, 101
- Petrovich, C. 2015a, ApJ, 805, 75
- Petrovich, C. 2015b, ApJ, 799, 27

- Petrovich, C. 2015, *ApJ*, 808, 120
- Petrovich, C., & Tremaine, S. 2016, *ApJ*, 829, 132
- Petrovich, C., Wu, Y., & Ali-Dib, M. 2019, *AJ*, 157, 5.
- Philippov, A. A., & Rafikov, R. R. 2013, *ApJ*, 768, 112
- Popper, D. M. 1982, *ApJ*, 254, 203
- Pu, B., & Lai, D. 2018, *MNRAS*, 478, 197
- Queloz, D., Anderson, D. R., Collier Cameron, A., et al. 2010, *A&A*, 517, L1
- Quinn, S. N., White, T. R., Latham, D. W., et al. 2015, *ApJ*, 803, 49
- Raghavan, D., McAlister, H. A., Henry, T. J., et al. 2010, *ApJS*, 190, 1
- Raymond, S. N., Barnes, R., Veras, D., et al. 2009, *ApJ*, 696, L98
- Rasio, F. A., & Ford, E. B. 1996, *Science*, 274, 954
- Rein, H., & Liu, S.-F. 2012, *A & A*, 537, A128
- Rein, H., & Spiegel, D. S. 2015, *MNRAS*, 446, 1424
- Rein, H., & Tamayo, D. 2015, *MNRAS*, 452, 376
- Ricker, G. R., Winn, J. N., Vanderspek, R., et al. 2014, Space Telescopes and Instrumentation: Optical, Infrared, and Millimeter Wave, 9143, 914320
- Rogers, T. M., & Lin, D. N. C. 2013, *ApJL*, 769, L10
- Rossiter, R. A. 1924, *ApJ*, 60, 15
- Santerne, A., Moutou, C., Tsantaki, M., et al. 2016, *A & A*, 587, A64

- Simpson, E. K., Pollacco, D., Cameron, A. C., et al. 2011, MNRAS, 414, 3023
- Singer, S. F. 1968, Geophys. J. R. Astron. Soc., 15, 205
- Skumanich, A. 1972, ApJ, 171, 565
- Socrates, A., Katz, B., Dong, S., & Tremaine, S. 2012, ApJ, 750, 106
- Spalding, C., & Batygin, K. 2014, ApJ, 790, 42
- Storch, N. I., Anderson, K. R., & Lai, D. 2014, Science, 345, 1317
- Storch, N. I., & Lai, D. 2015, MNRAS, 448, 1821
- Storch, N. I., Lai, D., & Anderson, K. R. 2017, MNRAS, 465, 3927
- Sybilska, P., Pawłaszek, R. K., Sybilska, A., et al. 2018, MNRAS, 478, 1942
- Tanaka, H., Takeuchi, T., & Ward, W. R. 2002, ApJ, 565, 1257
- Teyssandier, J., Lai, D., & Vick, M. 2019, MNRAS, 486, 2265.
- Thies, I., Kroupa, P., Goodwin, S. P., Stamatellos, D., & Whitworth, A. P. 2011, MNRAS, 417, 1817
- Tokovinin, A., Thomas, S., Sterzik, M., & Udry, S. 2006, A & A, 450, 681
- Tokovinin, A., & Kiyaeva, O. 2015, arXiv:1512.00278
- Triaud, A. H. M. J., Collier Cameron, A., Queloz, D., et al. 2010, A&A, 524, A25
- Triaud, A. H. M. J., Hebb, L., Anderson, D. R., et al. 2013, A & A, 549, A18
- Tsang, D., Turner, N. J., & Cumming, A. 2014, ApJ, 782, 113
- Udry, S., Mayor, M., & Santos, N. C. 2003, A & A, 407, 369

- Valsecchi, F., Rasio, F. A., & Steffen, J. H. 2014, *ApJL*, 793, L3
- Vick, M., Lai, D., & Anderson, K. R. 2019, *MNRAS*, 484, 5645
- Ward, W. R., Burns, J. A., & Toon, O. B. 1979, *Geophys. Res.*, 84, 243
- Ward, W. R., & Hamilton, D. P. 2004, *AJ*, 128, 2501
- Wang, J., Xie, J.-W., Barclay, T., & Fischer, D. A. 2014, *ApJ*, 783, 4
- Wang, J., Fischer, D. A., Horch, E. P., & Xie, J.-W. 2015, *ApJ*, 806, 248
- Weiss, L. M., & Marcy, G. W. 2014, *ApJL*, 783, L6
- Winn, J. N., Noyes, R. W., Holman, M. J., et al. 2005, *ApJ*, 631, 1215
- Winn, J. N., Johnson, J. A., Albrecht, S., et al. 2009, *ApJL*, 703, L99
- Winn, J. N., Fabrycky, D., Albrecht, S., & Johnson, J. A. 2010, *ApJL*, 718, L145
- Winn, J. N., & Fabrycky, D. C. 2015, *ARAA*, 53, 409
- Winn, J. N., Petigura, E. A., Morton, T. D., et al. 2017, *AJ*, 154, 270
- Wright, J. T., Marcy, G. W., Howard, A. W., et al. 2012, *ApJ*, 753, 160
- Wu, Y., & Murray, N. 2003, *ApJ*, 589, 605
- Wu, Y., Murray, N. W., & Ramsahai, J. M. 2007, *ApJ*, 670, 820
- Wu, Y., & Lithwick, Y. 2011, *ApJ*, 735, 109
- Xue, Y., Suto, Y., Taruya, A., et al. 2014, *ApJ*, 784, 66
- Zahn, J.-P. 1977, *A&A*, 57, 383
- Zanazzi, J. J., & Lai, D. 2018, *MNRAS*, 478, 835